



# Optical absorption and electronic properties of individual carbon nanotubes

Jean-Christophe Blancon

## ► To cite this version:

Jean-Christophe Blancon. Optical absorption and electronic properties of individual carbon nanotubes. Physics [physics]. Université Claude Bernard - Lyon I, 2013. English. NNT : 2013LYO10164 . tel-01171001

**HAL Id: tel-01171001**

**<https://theses.hal.science/tel-01171001>**

Submitted on 2 Jul 2015

**HAL** is a multi-disciplinary open access archive for the deposit and dissemination of scientific research documents, whether they are published or not. The documents may come from teaching and research institutions in France or abroad, or from public or private research centers.

L'archive ouverte pluridisciplinaire **HAL**, est destinée au dépôt et à la diffusion de documents scientifiques de niveau recherche, publiés ou non, émanant des établissements d'enseignement et de recherche français ou étrangers, des laboratoires publics ou privés.

THESE DE L'UNIVERSITÉ DE LYON

Délivré par

L'UNIVERSITÉ CLAUDE BERNARD LYON 1

Ecole Doctorale Matériaux

DIPLÔME DE DOCTORAT

(arrêté du 7 août 2006)

Spécialité Physique

Soutenue publiquement le 17 Octobre 2013

par

**M. Jean-Christophe BLANCON**

# Propriétés optiques d'absorption et électroniques de nanotubes de carbone individuels

Directeurs de Thèse : M. Anthony AYARI  
M. Alfonso SAN MIGUEL

M.	Anthony	AYARI	<i>Directeur de Thèse</i>
Mme	Natalia	DEL FATTI	<i>Examineur</i>
M.	Tobias	HERTEL	<i>Examineur</i>
M.	Pascal	PUECH	<i>Rapporteur</i>
M.	Alfonso	SAN MIGUEL	<i>Directeur de Thèse</i>
M.	Christophe	VOISIN	<i>Rapporteur</i>



À Aneso,  
*pour son éternel soutien.*





# Résumé

---

L'obtention des propriétés optiques intrinsèques d'absorption des nanotubes de carbone, et plus particulièrement leur section efficace d'absorption, reste un challenge expérimental. Pourtant, la majorité des nanotubes de carbone sont identifiés par des méthodes de spectroscopie optique, telles que la diffusion Raman et la photoluminescence, qui s'appuient directement sur ces propriétés d'absorption. Il en va de même pour beaucoup d'études s'attachant à obtenir des propriétés intrinsèques autres des nanotubes, telles que leur conductivité et leur diffusion thermique.

Au cours de ce travail de thèse à caractère expérimental, nous nous sommes attachés à mesurer les spectres absolus de section efficace d'absorption de nanotubes de carbone individuels placés dans différents environnements. Pour ce faire, nous avons développé un dispositif expérimental basé sur la technique de spectroscopie à modulation spatiale qui permet d'accéder de manière directe à la section efficace d'absorption de nano-objets individuels. Cette méthode ne requière aucun a priori sur les propriétés des nanotubes, et très important nous affranchit des effets d'ensemble. Ainsi, nous avons pu étudier les propriétés d'absorption de nanotubes individuels simple et double parois dans les environnements suivants : suspendus librement, agrégés en petit fagot, et déposés sur substrat. Plus précisément, l'évolution de l'absorption excitonique des nanotubes est analysée en fonction des paramètres structuraux (diamètre, nombre de parois, chiralité) et de l'environnement de ces derniers.

Un autre aspect de cette thèse a pour objet l'analyse des propriétés de transport électronique des nanotubes de carbone soumis à des pressions hydrostatiques de gaz de l'ordre du gigapascal, avec la possibilité d'accéder au régime des basses températures. Ici, nous nous sommes concentrés sur l'étude de transistors à effet de champ composés de petits fagots de nanotubes de carbone contactés à leurs extrémités par des électrodes en palladium. Dans ce cadre, nous avons notamment réalisé la première observation de l'effet de blocage de Coulomb sous pression.

Au final, ce travail de thèse a permis d'analyser les propriétés optiques et électroniques intrinsèques aux nanotubes de carbone et leur évolution sous l'effet de différents environnements (écranage diélectrique, dopage chimique, contrainte mécanique et pression hydrostatique). Ce travail a pu être réalisé grâce au développement de nouvelles techniques permettant de sonder ces propriétés au niveau du nanotube individuel.



# Optical absorption and electronic properties of individual carbon nanotubes

A dissertation submitted to  
UNIVERSITÉ DE LYON  
Université Claude Bernard Lyon 1

for the degree of  
Doctor of Sciences

Presented by  
Jean-Christophe BLANCON

October 17, 2013

M.	Anthony	AYARI	<i>PhD supervisor</i>
Mme	Natalia	DEL FATTI	<i>Co-referee</i>
M.	Tobias	HERTEL	<i>Co-referee</i>
M.	Pascal	PUECH	<i>Referee</i>
M.	Alfonso	SAN MIGUEL	<i>PhD supervisor</i>
M.	Christophe	VOISIN	<i>Referee</i>



# Abstract

---

In this dissertation, we report on the experimental investigation of the optical properties of single- and double-wall carbon nanotubes. Despite numerous studies performed using photoluminescence or Raman and Rayleigh scattering, knowledge of their optical response is still partial. In particular direct quantitative measurement of their absorption cross-section has not been achieved yet.

Using spatial modulation spectroscopy we have determined, over a broad optical spectral range, the spectrum and amplitude of the absorption cross-section of identified individual single- and double-wall carbon nanotubes. These quantitative measurements permit the determination of the oscillator strength of the different excitonic resonances, and their dependencies on the excitonic transition and type of nanotube. Furthermore, investigation of the same nanotube, either a single-wall or double-wall nanotube, free-standing or deposited on a substrate shows large broadening with increase of oscillator strength of the excitonic resonances, as well as stark weakening of polarization-dependent antenna effects, due to nanotube-substrate interaction. Similar study on nanotube bundles and double-wall nanotubes demonstrate the importance of inter-tube and inter-wall exciton coupling effects which seem to be of different nature in these two types of sample.

The second part of this thesis studies electrical transport in carbon nanotube bundles under high pressure condition and low temperature. The behavior of nanotube-based field-effect transistors has been investigated, in the classical and Coulomb blockade regime, under gas-pressure up to 0.9 GPa.

Overall, this dissertation communicates on the quantitative analysis of the absorption and electronic properties of carbon nanotubes and how they are influenced by various environmental effects such as dielectric screening, stress-induced strain, hydrostatic pressure, or chemical doping. The novelty of this work is to address these issues at the single nanotube level.



# Contents

---

<b>Titre</b>	<b>i</b>
<b>Résumé</b>	<b>v</b>
<b>Title</b>	<b>vii</b>
<b>Abstract</b>	<b>ix</b>
<b>Contents</b>	<b>xiv</b>
<b>Introduction</b>	<b>1</b>
<b>1 Fundamentals</b>	<b>5</b>
<b>I Basics of carbon nanotubes</b>	<b>7</b>
I-1 General description . . . . .	7
I-1.1 Carbon-based materials . . . . .	7
I-1.2 Structure and geometrical considerations . . . . .	8
I-1.2.a Carbon nanotubes from graphene sheet . . . . .	8
I-1.2.b Geometry of carbon nanotubes . . . . .	10
I-1.2.c Single- and multi-wall carbon nanotubes . . . . .	11
I-2 Electronic structure . . . . .	12
I-2.1 $sp^2$ hybridization . . . . .	12
I-2.2 Tight-binding model for graphene . . . . .	12
I-2.3 Zone folding approximation . . . . .	14
I-2.4 Semiconducting and metallic nanotubes . . . . .	16
I-2.5 Density of states . . . . .	17
<b>II Optical properties of single-wall carbon nanotubes</b>	<b>21</b>
II-1 First description of absorption in carbon nanotubes . . . . .	21
II-1.1 General concepts . . . . .	21



II-1.2	Absorption transitions <i>vs.</i> nanotube diameter . . . . .	26
II-1.3	Kataura plot (single-particle model) . . . . .	27
II-2	Excitons in carbon nanotubes . . . . .	31
II-2.1	The ratio problem . . . . .	31
II-2.2	Optical transitions arise from excitons . . . . .	32
II-2.2.a	Mott-Wannier excitons . . . . .	32
II-2.2.b	Exciton states . . . . .	33
II-2.2.c	Exciton properties . . . . .	38
II-3	State-of-the-art . . . . .	43
II-3.1	Potpourri of spectroscopy techniques . . . . .	43
II-3.2	Absorption spectroscopy . . . . .	45
II-3.2.a	A deeper insight on Kataura plot(s) . . . . .	45
II-3.2.b	Absolute absorption cross-section . . . . .	47
<b>2</b>	<b>Absorption spectroscopy</b>	<b>51</b>
<b>III</b>	<b>Experimental methods</b>	<b>53</b>
III-1	Sample description . . . . .	53
III-1.1	Carbon nanotubes deposited on substrates . . . . .	54
III-1.1.a	Preparation method . . . . .	54
III-1.1.b	Silicon substrate . . . . .	54
III-1.1.c	Quartz substrate . . . . .	55
III-1.2	Free-standing carbon nanotubes . . . . .	56
III-1.2.a	Environment-free carbon nanotubes . . . . .	56
III-1.2.b	In-lab preparation method . . . . .	58
III-1.3	General comments and sample overview . . . . .	58
III-1.3.a	Synthesis of carbon nanotubes . . . . .	58
III-1.3.b	Sample overview . . . . .	60
III-2	Absorption spectroscopy of individual nanotubes . . . . .	61
III-2.1	Spatial modulation spectroscopy . . . . .	61
III-2.1.a	Principle . . . . .	61
III-2.1.b	Absolute absorption cross-section in carbon nanotubes . . . . .	63
III-2.1.c	Experimental setup . . . . .	68
III-2.1.d	Calibration of the experimental parameters . . . . .	69
III-2.1.e	Absorption spectroscopy of individual carbon nanotubes . . . . .	71
III-2.1.f	SMS imaging of carbon nanotubes . . . . .	75
III-2.2	Reflective spatial modulation spectroscopy . . . . .	75
III-2.2.a	Principle and theoretical background . . . . .	75
III-2.2.b	Imaging of carbon nanotubes on opaque substrates . . . . .	80
<b>IV</b>	<b>Absorption spectroscopy of single-wall carbon nanotubes</b>	<b>85</b>
IV-1	Free-standing SWNTs . . . . .	85
IV-1.1	Broadband absorption cross-section . . . . .	85

IV-1.2 Semiconducting SWNTs of family type I . . . . .	86
IV-1.2.a Structure assignment . . . . .	86
IV-1.2.b Exciton, phonon-assisted and non-resonant absorption . . . . .	88
IV-1.2.c Measurements uncertainties . . . . .	91
IV-1.3 Semiconducting SWNTs of family type II . . . . .	92
IV-1.4 Interpretation and oscillator strength . . . . .	92
IV-1.5 Optical conductivity . . . . .	96
IV-2 Single-wall carbon nanotube bundles . . . . .	98
IV-2.1 Absorption and Raman spectroscopy . . . . .	99
IV-2.2 Interpretation of absorption in bundles . . . . .	103
IV-3 Substrate interactions . . . . .	105
IV-3.1 Absorption spectroscopy of SWNT on Si/SiO <sub>2</sub> substrate: first measurement . . . . .	105
IV-3.2 Comparison of the absorption response between free-standing and substrate-supported SWNT . . . . .	108
IV-3.2.a Absorption spectroscopy . . . . .	108
IV-3.2.b Polarization-dependent absorption . . . . .	110
IV-3.2.c Raman scattering . . . . .	110
IV-3.2.d Substrate effects on the absorption response of SWNTs . . . . .	110
IV-3.3 SWNTs on quartz substrate . . . . .	114
IV-3.3.a AFM and Raman spectroscopy . . . . .	114
IV-3.3.b Absorption spectroscopy . . . . .	116
IV-4 General comments on the absorption of SWNT . . . . .	117
<b>V Absorption spectroscopy of double-wall carbon nanotubes</b>	<b>119</b>
V-1 State-of-the-art . . . . .	119
V-2 Raman spectroscopy . . . . .	123
V-2.1 Breathing-like modes . . . . .	123
V-2.2 Tangential modes . . . . .	124
V-3 Absorption spectroscopy of free-standing DWNT . . . . .	126
V-3.1 Double-wall nanotube of type SC@SC . . . . .	126
V-3.1.a DCNT 1 . . . . .	127
V-3.1.b DCNT 2 . . . . .	130
V-3.2 Double-wall nanotube of type SC@M . . . . .	133
V-3.3 Double-wall nanotube of type M@SC . . . . .	136
V-4 Environment effects on double-wall nanotubes absorption properties . . . . .	137
V-4.1 Substrate effects on the absorption response of a DWNT . . . . .	137
V-4.1.a Freely suspended . . . . .	137
V-4.1.b Substrate supported . . . . .	139
V-4.2 Bundling effects on the absorption response of a DWNT . . . . .	141
V-4.2.a Results . . . . .	141
V-4.2.b Discussion . . . . .	145
V-5 Discussion on the absorption of DWNTs . . . . .	146
V-5.1 Excitonic energy transitions . . . . .	146

V-5.2 Non-resonant absorption . . . . .	147
<b>3 Electrical transport</b>	<b>149</b>
<b>VI Electronic transport in individual carbon nanotube bundles under pressure</b>	<b>151</b>
VI-1 Carbon nanotubes under pressure . . . . .	151
VI-2 Experimental details . . . . .	152
VI-2.1 Sample preparation . . . . .	152
VI-2.2 Characterization of the device at ambient pressure . . . . .	152
VI-2.3 High pressure measurements . . . . .	154
VI-3 Results . . . . .	155
VI-4 Discussion . . . . .	159
VI-5 Coulomb blockade under pressure . . . . .	161
<b>Conclusion</b>	<b>163</b>
<b>4 Appendix</b>	<b>167</b>
<b>A Structure assignment of SWNT</b>	<b>169</b>
<b>B Model for the absorption cross-section</b>	<b>175</b>
II-1 Nanowire and hollow cylinder models . . . . .	175
II-2 Results and interpretation . . . . .	177
<b>C Absorption of mono- and bi-layers graphene</b>	<b>181</b>
III-1 Sample preparation and characterization . . . . .	181
III-2 High-contrast imaging of graphene flakes . . . . .	182
III-3 Absorption spectroscopy . . . . .	182
<b>Bibliography</b>	<b>187</b>
<b>List of figures</b>	<b>205</b>
<b>Acronyms</b>	<b>207</b>
<b>List of notations</b>	<b>209</b>

# Introduction

---

After the observation of the first carbon nanotubes [1, 2], several research groups have been motivated by their promising electrical properties (high conductivity, stability of metallic tubes, FET response of semiconducting nanotubes), and have put a lot of effort in the fabrication of nanotube-based electronic devices [3, 4]. Since then, several routes have been explored for the integration of these nanometer-scale materials in molecular electronics, which recently led to the conception of new prototype devices, e. g. for logic technology [5] or transparent/flexible electronics [6]. These materials are not only interesting for applications in transistor devices. Indeed, the unique optical properties of carbon nanotubes (CNTs), especially few-wall carbon nanotubes, are appealing for the development of novel applications in optoelectronics [7], all optical integrated circuits [8], and biology. Despite numerous studies performed using photoluminescence or Raman and Rayleigh scattering, knowledge of their optical response is still partial. Scarcely any studies have attempted to assess one of their most fundamental attribute: their absorption cross-section.

For nanometric size objects, as single and double-wall carbon nanotubes (SWNTs and DWNTs), the dominant interaction with light is due to their optical absorption. Understanding and quantitative characterization of the absorption processes and of the modifications due to the nanotube environment are crucial for their applications and, more generally, for fundamental understanding of light-matter interaction in quasi one-dimensional nanomaterials [7]. The richness of the carbon nanotube nature (semiconducting or metallic) and structural parameters usually complicates their precise investigation when carried out on synthesized CNT ensemble. Avoiding these averaging effects and assessing the intrinsic properties of structure-assigned CNTs is achievable by addressing their optical properties at the single nanotube level. During the last ten years, such an approach has been developed for the investigation of the photo-physics of SWNTs. The three most widespread techniques, photoluminescence and Raman or Rayleigh scattering, have yielded optical imaging of individual CNTs and precious information on their excitonic resonant energies and linewidths [9–21]. However, they have failed to systematically determine the absolute amplitude of CNTs absorption cross-section, except at specific wavelengths [14, 22, 23]. Still the absorption process was only indirectly addressed, which explains the dispersion of the values of absorption cross-sections found in the literature (see Tab. II.1). A major experimental challenge is thus to directly analyze the absorption of an individual carbon nanotube, quantitatively and

over a large spectral range.

**In the main body of this thesis**, using (reflective) spatial modulation spectroscopy we determine, over a broad spectral range, the spectrum and absolute amplitude of the absorption cross-section of individual SWNTs and DWNTs. For incident light polarized along the nanotubes, this approach allows quantitative determination of the oscillator strength associated with the different excitonic resonances, and their dependencies on the excitonic transition and type of nanotube. Beforehand, we address the issue of the excitonic nature of high-order energy transitions in semiconducting and metallic CNTs. The non-resonant absorption background, identified in previous studies on CNTs ensembles, is examined and compared to the frequency-independent ideal sheet optical conductivity of graphene. Furthermore, environment effects on the nanotubes absorption properties are quantified by investigating identical structure-identified CNTs in different situations: freely suspended, supported on a substrate, and/or bundled with metallic SWNTs. Finally, the dependence of the absorption cross-section on the incident light polarization is addressed for each type of nanotube as well as in the different environments.

Besides their original electrical and optical properties, carbon nanotubes also possess unique mechanical characteristics [24]. As for silicon micro- and nanotechnologies, the development of strain engineering can have an important impact in the CNT context. Recently, a pressure nano-sensing system based on pristine CNTs was developed that aims at utilizing high pressure to tune either the Schottky barriers at the contacts between CNTs and patterned electrodes [25], or the interwall coupling in DWNTs [26]. In this context, and considering the richness of this material, pressure is a relevant tool to investigate either the influence of mechanical stress on the properties of carbon nanotubes [27–29] or the interactions of CNTs with their environment [30–32].

**Also in this thesis**, the pressure evolution of the electrical transport properties of field-effect transistors (CNT-FETs) based on individual carbon nanotube bundles with reduced Schottky barriers is investigated under hydrostatic gas-pressure (up to 0.9 GPa), either in the classical regime or, for the first time, in the Coulomb blockade regime. The pressure evolution of the CNT-FETs response is addressed by probing changes of the nanotubes cross-sections, as well as nanotube-electrode contact barriers and environment interactions.

This dissertation is organized in three parts, each sub-divided into chapters: fundamentals (two chapters), absorption spectroscopy (three chapters), and electrical transport (one chapter).

*In the first chapter*, general concepts on carbon nanotubes are introduced regarding their structure and electronic properties. The general electronic properties of CNTs are described with a simple but conceptual tight binding model.

*The second chapter* focuses on the optical properties of single-wall carbon nanotubes. A general overview of the state-of-the-art is provided regarding more specifically the absorption properties of CNTs. In particular, construction of the Kataura plot is explained

into detail, as well as the characteristics of excitons in nanotubes.

*The third chapter* describes the CNTs synthesis techniques and the experimental methods, spatial modulation spectroscopy or reflective spatial modulation spectroscopy, developed to directly access the absolute absorption cross-section of individual carbon nanotubes.

*The fourth and fifth chapters* address the absorption of individual single- and double-wall carbon nanotubes either free-standing or subject to various environments (substrate, other nanotubes). The core results of this work are analyzed and discussed regarding both the CNTs structural parameters and their environment.

*The sixth and last chapter* reports the pressure evolution electrical transport response of field-effect transistor devices based on individual carbon nanotubes bundles. Preliminary measurements in the Coulomb blockade regime are also discussed.



# **Part 1**

## **Fundamentals**





# Basics of carbon nanotubes



*In this chapter, I introduce general concepts on carbon nanotubes (CNTs). Structural and geometrical considerations are discussed, defining the notations that will be used throughout this thesis. In a second section, the electronic properties of CNTs are addressed within a tight binding model. The discussion is kept short as these subjects are covered by a vast literature. Several reviews and text books present detailed description of carbon nanotubes, e. g. the reader is advised to refer to the books of S. Reich et al. and R. Saito et al. [33, 34].*

## I–1 General description

### I–1.1 Carbon-based materials

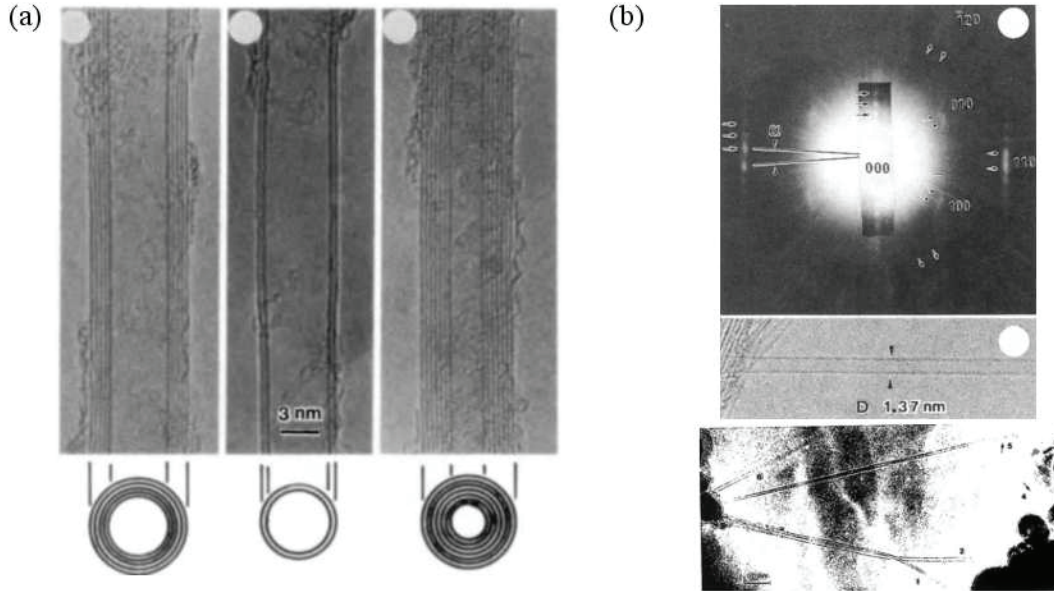


**Figure I.1:** First observation of carbon nanotubes by Sumino Ijima. (a) Electron micro-graphs of multi-wall carbon nanotubes from [1]. b) Electron micrographs showing single-wall carbon nanotubes as reported in [1, 2].

Carbon-based materials, bulk or nano-structured, have been subject to intense research in the last decades. Their bulk forms, diamond and graphite, already present different arrangement and hybridization ( $sp^3$  and  $sp^2$ , respectively) of the carbon atoms, which results in fundamentally different electrical, optical and thermal properties. In nano-structures these properties are extraordinarily enhanced which justify the important research developed by the carbon community. The first carbon nano-structured material, the  $sp^2$ -hybridized carbon cage named fullerene, was discovered by Richard E. Smalley in 1985.<sup>a</sup> In 1991, Sumio Iijima reported the observation of ‘Helical microtubules of graphitic carbon’, nowadays called multi-wall carbon nanotubes (Fig. I.1.a). Two years latter, he synthesized the first single-wall carbon nanotube (Fig. I.1.b). Finally, in 2005, Kostya Novoselov and Andrei Geim performed the first electric field effect study of graphene [35].<sup>b</sup>

These carbon nano-structures, exhibit unique physical properties, and provide support for the investigation of nanometer-size materials with low dimensionality: 0D (fullerene), 1D (nanotube), and 2D (graphene). In particular, carbon nanotubes have been studied for their impressive electrical properties, with the possibility to obtain field-effect transistors with high mobility compared to silicon. More recently, optical properties of nanotubes have drawn a lot of interest in the international community, as their one dimensional character and their diversity open wide opportunities for future optoelectronic applications.

Another more general difference of carbon nanotubes with respect to conventional crystalline materials is their characteristic dimensions: their diameters are on the order of a few nanometers or less while their lengths are typically of a few micrometers. Because of this small size and large aspect-ratio, carbon nanotubes exhibit unique physical and chemical properties. Properties originating from this one dimensional character are dominant in single- and few-wall nanotubes, in particular, and become more pronounced as their diameter become smaller. CNTs properties are also controlled by the tubes nature (metallic or semiconducting) and the arrangement of the carbon atoms.

## I–1.2 Structure and geometrical considerations

### I–1.2.a Carbon nanotubes from graphene sheet

Many of the nanotubes properties can be obtained from the study of rolled up sheets of carbon atoms arranged in a honey comb lattice – or mono-layer graphene. The way the sheet is rolled up, defined by the chiral vector or circumferential vector  $\mathbf{C}$ , determines the geometrical characteristics of the tube, as well as most of its physical properties. The graphene is a two-dimensional carbon structure, where carbon atoms are arranged on a honeycomb network (Fig. I.2.a). The honeycomb network is described by a Bravais lattice with two atoms in the unit-cell. The triangular lattice is generated by the primitive basis vectors  $\mathbf{a}_1$  and  $\mathbf{a}_2$ , as shown in Fig. I.2.b. The primitive unit-cell spanned by these two vectors exhibits a the lattice constant  $a_0 = \sqrt{3}a_{CC}$ , where the

---

<sup>a</sup>He obtained the Nobel prize in Chemistry in 1996 for his work.

<sup>b</sup>They share the Nobel prize in Physics 2010.

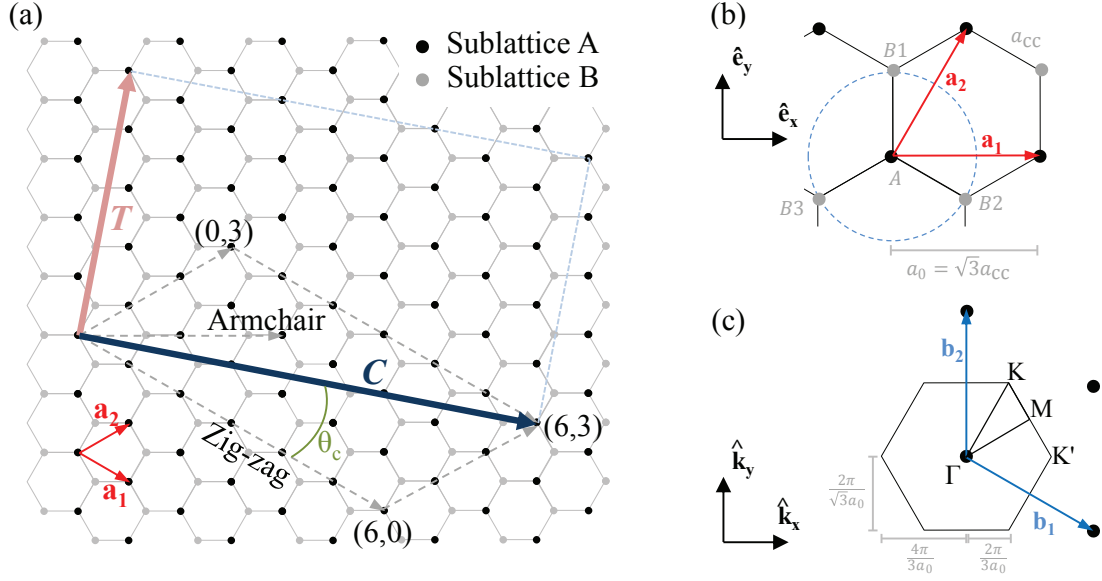


**Figure I.2:** Graphene honeycomb lattice. (a) Real-space lattice with the two sublattices A and B. The chiral (circumferential) vector  $\mathbf{C}$  links two atoms of sub-lattice A, and determines the direction the graphene is rolled-up to obtain a nanotube with defined chiral indices  $(n, m)$  and chiral angle  $\theta_c$ . The unit cell of the nanotube  $(6, 3)$  is defined by the parallelogram spanned by  $\mathbf{C}$  and the translational vector  $\mathbf{T}$ . Definition of primitive basis vectors in (b) real space, and (c) reciprocal space. (dashed blue circle) Interaction range of atom A within the first-neighbor approximation.

carbon-carbon bound length  $a_{CC}$  is 1.42 Å. In the coordinate system  $(\hat{\mathbf{e}}_x, \hat{\mathbf{e}}_y)$ , the basis vectors are

$$\mathbf{a}_1 = \begin{pmatrix} 1 \\ 0 \end{pmatrix} a_0, \quad \mathbf{a}_2 = \begin{pmatrix} \frac{1}{2} \\ \frac{\sqrt{3}}{2} \end{pmatrix} a_0, \quad (\text{I.1})$$

and the two atoms in the basis are at positions

$$\mathbf{a}_A = \begin{pmatrix} 0 \\ 0 \end{pmatrix}, \quad \mathbf{a}_B = \begin{pmatrix} 1 \\ \frac{1}{\sqrt{3}} \end{pmatrix} a_0. \quad (\text{I.2})$$

The chiral vector, shown in Fig. I.2.a, links two atoms of the same sub-lattice. The length and orientation of  $\mathbf{C}$  are defined by the chiral indices  $(n, m)$  such that  $\mathbf{C} = n\mathbf{a}_1 + m\mathbf{a}_2$  ( $n$  and  $m$  are integers). On the figure, the example of a  $(6, 3)$  nanotube is presented. The angle between  $\mathbf{C}$  and  $\mathbf{a}_1$  is called chiral angle  $\theta_c$ , with

$$\cos \theta_c = \frac{\mathbf{a}_1 \cdot \mathbf{C}}{\|\mathbf{a}_1\| \|\mathbf{C}\|} = \frac{n + m/2}{\sqrt{n^2 + nm + m^2}}. \quad (\text{I.3})$$

Because of the six-fold rotational symmetry of graphene, all nanotubes can be constructed with chiral angle smaller than  $60^\circ$ . Moreover, for each tube with  $\theta_c$  between  $0$  and  $30^\circ$  an equivalent tube can be found for  $\theta_c$  in the range  $30^\circ - 60^\circ$ , but the helix of the

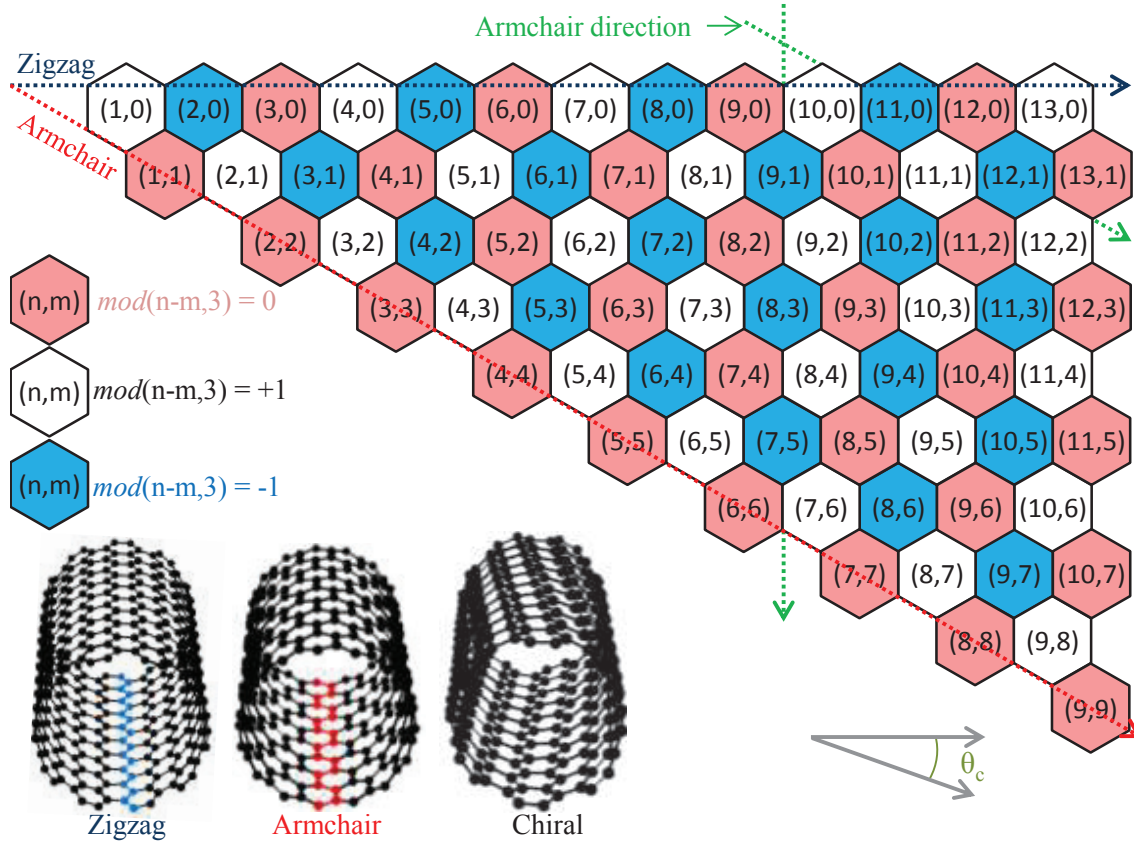


**Figure I.3:** Carbon nanotube classification depending on the chiral indices  $(n, m)$ .

honeycomb lattice around the tube changes from right-handed to left-handed. Hence, in the following, we consider only nanotubes with  $0^\circ \leq \theta_c \leq 30^\circ$ , corresponding to  $n < m$ , as shown in Fig. I.3. The tubes are classified in three groups based on their chiral angle:

- zig-zag nanotubes (non-chiral), with  $\theta_c = 0^\circ$  or  $m = 0$ ,
- armchair nanotubes (non-chiral), with  $\theta_c = 30^\circ$  or  $n = m$ ,
- chiral nanotubes, otherwise.

Examples of CNTs of each group are presented in Fig. I.3. On the figure, the color code defines another classification method which consider the result of  $\bmod(n - m, 3)$ . We will see later that this parameter defines the nature of the nanotube, i. e. its semiconducting (SC) or metallic (M) character.

### I-1.2.b Geometry of carbon nanotubes

The structure of each nanotube (diameter, unit cell, number of carbon atoms, Brillouin zone) is derived from the chiral vector and the geometry of graphene.  $\mathbf{C}$  defines the

circumference of the nanotube, giving the expression of its diameter

$$d = \frac{\|\mathbf{C}\|}{\pi} = \frac{a_0}{\pi} \sqrt{n^2 + nm + m^2}. \quad (\text{I.4})$$

The translational vector  $\mathbf{T}$  is the smallest vector perpendicular to  $\mathbf{C}$  and linking atoms of sublattice A (Fig. I.2.a); its expression is

$$\mathbf{T} = -\frac{n+2m}{N_R} \mathbf{a}_1 + \frac{2n+m}{N_R} \mathbf{a}_2, \quad (\text{I.5})$$

and

$$\|\mathbf{T}\| = \frac{a_0 \sqrt{3(n^2 + nm + m^2)}}{N_R}, \quad (\text{I.6})$$

where  $N_R$  is the greatest common divisor of  $(2n+m)$  and  $(2m+n)$ . The unit cell of the nanotube, with cylinder shape, is defined by the tube's diameter and the length of the translational vector. Doing the calculation shows that chiral nanotubes often have longer unit cells.

The formulas giving the number of carbon atoms per unit length and in the unit cell, are of prior importance in the following chapters. Considering the graphene lattice, the area of its primitive unit cell is defined by  $\|\mathbf{a}_1 \times \mathbf{a}_2\| = a_0^2 \sin(\pi/3) = 0.05245 \text{ nm}^2$ , and contains two atoms. Hence, the number of atoms per unit length of the nanotube is given by

$$N_L = \frac{2\|\mathbf{C}\|}{\|\mathbf{a}_1 \times \mathbf{a}_2\|} = 119.8 d \text{ [nm}^{-1}\text{]}, \quad (\text{I.7})$$

and the number of atoms in the tube's cylindrical unit cell is

$$N_C = \frac{2d\|\mathbf{T}\|}{\|\mathbf{a}_1 \times \mathbf{a}_2\|} = \frac{4\sqrt{(n^2 + nm + m^2)}}{a_0 N_R}. \quad (\text{I.8})$$

The symmetry of carbon nanotubes are described by line groups, which include the translations to the point groups, which are different for different chirality  $(n,m)$  [33]. In practice, only point groups  $D_q$  (for chiral nanotubes) and  $D_{2nh}$  (for armchair and zig-zag tubes) have to be consider for the study of optical properties.

### I-1.2.c Single- and multi-wall carbon nanotubes

So far, nanotubes have been obtained by rolling-up a piece of mono-layer graphene, thus creating tubes with one wall or so-called single-wall carbon nanotubes (SWNTs). Although this chapter concentrates on the description of SWNTs, multi-wall carbon nanotubes (MWNTs) are more commonly used especially for industrial applications since their fabrication is more adapted to mass production (Fig. I.1.a). Fundamental research, which aims at studying nanotubes intrinsic properties, usually concentrate on few-wall carbon nanotubes. Hence, in this thesis we focus on single-wall, double-wall (DWNT) carbon nanotubes individualized or in small bundles. They are characterized by the chiral indices of each of their walls:

- $(n,m)$  in SWNT,
- $(n,m)@(n',m')$  corresponding in DWNT to the inner and outer walls, respectively,
- $(n,m)@(n',m')@(n'',m'')$  from the inner to the outer wall in TWNT.

To simplify the description of the electronic and optical properties of nanotubes, the discussion is limited to SWNTs in this chapter and the next one.

## I–2 Electronic structure

### I–2.1 $sp^2$ hybridization

Graphene and carbon nanotubes are characterized by two types of bounds, arranged in the well-know  $sp^2$  planar hybridization. Carbon atom possesses four valence orbitals:  $2s$ ,  $2p_x$ ,  $2p_y$ ,  $2p_z$  –  $z$ -axis is defined perpendicular to the graphene sheet. In-plane covalent bounds  $\sigma$  (bounding) and  $\sigma^*$  (anti-bounding) are formed by orbitals  $(s, p_x, p_y)$ ; they determine the binding energy and elastic properties of graphene. Out-of-plane orbitals  $p_z$ , which cannot couple to the  $\sigma$  states due to their opposite symmetry, interact with each other and create delocalized  $\pi$  (bounding) and  $\pi^*$  (anti-bounding) orbitals. In carbon nanotubes, these  $\pi$  states are influenced by the tubes curvature which impact on the band structure. They are also responsible for the weak interaction between nanotubes in bundle, as well as the interaction with substrates [30, 33, 36].<sup>c</sup>

As previously shown, nanotubes are defined by their chiral indices  $(n,m)$  constructed from graphene sheet. The next paragraphs aim at describing the CNT electronic structure starting from the band structure of graphene.

### I–2.2 Tight-binding model for graphene

The Brillouin zone of graphene is shown in Fig. I.2.c, and presents a hexagonal structure with two nonequivalent  $K$  and  $K'$  points at the corner of the Wigner-Seitz cell. The first Brillouin zone is defined by the high-symmetry points  $(\Gamma, M, K)$ . The primitive vectors of the reciprocal space, expressed in the coordinate system  $(\hat{\mathbf{k}}_x, \hat{\mathbf{k}}_y)$ , are

$$\mathbf{b}_1 = \begin{pmatrix} \frac{2\pi}{a_0} \\ -\frac{2\pi}{\sqrt{3}a_0} \end{pmatrix}, \quad \mathbf{b}_2 = \begin{pmatrix} \frac{4\pi}{\sqrt{3}a_0} \\ 0 \end{pmatrix}. \quad (\text{I.9})$$

As mentioned in the previous paragraph, electronic properties of  $p_z$  orbitals forming the  $\pi$  states can be treated independently in graphene, and to some extend also in relatively large diameter carbon nanotubes which present not too important wall curvature. The electronic band structure of graphene  $\pi$  states is derived from the Schrödinger's equation

$$H\Psi(\mathbf{k}) = E_g(\mathbf{k})\Psi(\mathbf{k}), \quad (\text{I.10})$$

---

<sup>c</sup>This is similar to the van der Waals interaction between layers in graphite.



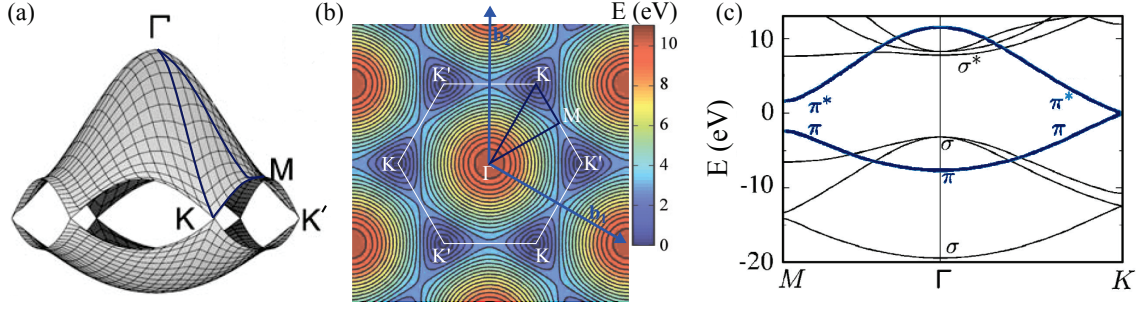


**Figure I.4:** Nearest-neighbor tight-binding band structure of graphene. Calculation in the first-neighbor approximation with transfer integral  $\gamma_0 = 2.9$  eV. (a) 3D view showing the valence and conduction bands of  $\pi$  states (from [37]). (b) 2D colormap of the graphene  $\pi^*$  conduction band dispersion. (c) Band structure in the first Brillouin zone showing the  $\pi$  and  $\sigma$  states (adapted from [38]). The  $\pi^*$ -band first Brillouin high symmetry projections are highlighted in dark blue on the three figures.

where  $H$  is the Hamiltonian,  $E_g(\mathbf{k})$  the eigenvalues, and  $\Psi(\mathbf{k})$  the eigenfunctions at wave-vector  $\mathbf{k}$ . From the periodicity of the atom network, the eigenfunctions are written as a linear combination of Bloch functions of each sublattice ( $\Phi_j$ ):

$$\Psi(\mathbf{k}) = \sum_{j=A,B} c_j(\mathbf{k}) \Phi_j(\mathbf{k}, \mathbf{r}). \quad (\text{I.11})$$

In the tight-binding model, the Bloch functions are expressed as a linear combination of the atomic wave functions. Within this  $\pi$ -band approximation, the  $p_z$  electrons are described by the wave functions  $\varphi_z(\mathbf{r} - \mathbf{R}_A)$  and  $\varphi_z(\mathbf{r} - \mathbf{R}_B)$ , respectively, in sub-lattice A and B. Therefore, the Bloch functions for sublattices A and B are

$$\Phi_A(\mathbf{k}, \mathbf{r}) = \frac{1}{\sqrt{N_{\text{cells}}}} \sum_{\mathbf{R}_A} e^{i\mathbf{k} \cdot \mathbf{R}_A} \varphi_z(\mathbf{r} - \mathbf{R}_A), \quad (\text{I.12a})$$

$$\Phi_B(\mathbf{k}, \mathbf{r}) = \frac{1}{\sqrt{N_{\text{cells}}}} \sum_{\mathbf{R}_B} e^{i\mathbf{k} \cdot \mathbf{R}_B} \varphi_z(\mathbf{r} - \mathbf{R}_B), \quad (\text{I.12b})$$

where  $N_{\text{cells}}$  is the number of unit cells in the graphene plane associated with positions  $\|\mathbf{R}_A\|$  ( $\|\mathbf{R}_B\|$ ). By substituting the expression of the eigenfunctions  $|\Psi\rangle$  (Dirac's notation is conveniently used from this point) in the Schrödinger equation (I.10), and multiplying the left side by  $\langle \Phi_A|$  or  $\langle \Phi_B|$ , the eigenstates are derived by solving the system

$$\begin{pmatrix} H_{AA}(\mathbf{k}) - E_g(\mathbf{k})S_{AA}(\mathbf{k}) & H_{AB}(\mathbf{k}) - E_g(\mathbf{k})S_{AB}(\mathbf{k}) \\ H_{BA}(\mathbf{k}) - E_g(\mathbf{k})S_{BA}(\mathbf{k}) & H_{BB}(\mathbf{k}) - E_g(\mathbf{k})S_{BB}(\mathbf{k}) \end{pmatrix} \begin{pmatrix} c_A(\mathbf{k}) \\ c_B(\mathbf{k}) \end{pmatrix} = 0, \quad (\text{I.13})$$

where the matrix elements are defined as

$$H_{ij} = \langle \Phi_i | H | \Phi_j \rangle, \quad (\text{I.14a})$$

$$S_{ij} = \langle \Phi_i | \Phi_j \rangle, \text{ with } i, j = (A, B). \quad (\text{I.14b})$$



The carbon atoms in sublattices  $A$  and  $B$  are equivalent, thus  $H_{AB} = H_{BA}^*$ ,  $H_{AA} = H_{BB}^*$ ,  $S_{AB} = S_{BA}^*$ , and  $S_{AA} = S_{BB}$ . The expression (I.13) is further simplified within the nearest-neighbor approximation, i.e. by considering interactions of each atom with its nearest neighbor only. Moreover, the overlap matrix element between wavefunctions centered at different atoms  $S_{AB}$  is neglected.<sup>d</sup> Setting the element  $S_{AA}$  to unity, the solution of (I.13) gives the eigenvalues

$$E_g^\pm(\mathbf{k}) = H_{AA}(\mathbf{k}) \mp H_{AB}. \quad (\text{I.15})$$

The first term express the self-interaction of each atom in sublattice  $A$ , which is a constant term reflecting the properties of the  $A$  (set as energy reference in the following,  $H_{AA} = 0$ ). The second term represents the interaction of each  $A$  atom with its nearest neighbors in sublattice  $B$  at positions (see also the dashed blue circle on Fig. I.2.b)

$$\mathbf{R}_{B1} = a_0 \begin{pmatrix} 0 \\ \frac{1}{\sqrt{3}} \end{pmatrix}, \quad \mathbf{R}_{B2} = a_0 \begin{pmatrix} \frac{1}{2} \\ -\frac{1}{2\sqrt{3}} \end{pmatrix}, \quad \mathbf{R}_{B3} = a_0 \begin{pmatrix} -\frac{1}{2} \\ -\frac{1}{2\sqrt{3}} \end{pmatrix}. \quad (\text{I.16})$$

Therefore, the matrix elements reduce to

$$H_{AB}(\mathbf{k}) = -\gamma_0 (e^{-i\mathbf{k}\cdot\mathbf{R}_{B1}} + e^{-i\mathbf{k}\cdot\mathbf{R}_{B2}} + e^{-i\mathbf{k}\cdot\mathbf{R}_{B3}}), \quad (\text{I.17})$$

where  $-\gamma_0$  is the carbon-carbon interaction energy or transfer integral (typically,  $\gamma_0 = 2.9$  eV, cf. refs. [33, 38]). Finally, solving the eigenvalue equation (I.15) gives the valence (−) and conduction (+) bands of graphene (Fig. I.4):

$$E_g^\pm(\mathbf{k}) = \pm\gamma_0 \sqrt{1 + 4 \cos\left(\frac{a_0 k_x}{2}\right) \sin\left(\frac{\sqrt{3}a_0 k_y}{2}\right) + 4 \cos^2\left(\frac{a_0 k_x}{2}\right)}. \quad (\text{I.18})$$

The valence and conduction bands cross at the  $K$ - and  $K'$ -points, where the Fermi energy  $E_F = 0$ . Development of the cosines around these high-symmetry points yields

$$E_g^\pm(\mathbf{k} + K) = E_g^\pm(\mathbf{k} + K') = \pm \frac{\sqrt{3}\gamma_0 a_0}{2} \sqrt{k_x^2 + k_y^2}, \quad (\text{I.19})$$

showing a peculiar quasi-linear dispersion of graphene band structure in the  $K$  and  $K'$  valleys (so-called Dirac cones). The electrons behave like mass-less particles or Dirac fermions close to  $K$  and  $K'$ .

### I–2.3 Zone folding approximation

The band structure of carbon nanotubes is nowhere built from the one of graphene. As shown previously, a nanotube is constructed from the graphene sheet by defining its chiral vector  $\mathbf{C}$ . Along  $\mathbf{C}$ , a periodic boundary condition imposed on the graphene wave function yields  $\Phi(\mathbf{r} + \mathbf{C}) = \Phi(\mathbf{r})$ , which is satisfied if and only if  $\exp(i\mathbf{k}\cdot\mathbf{C}) = 1$ . Along

<sup>d</sup>This approximation defines the so-called orthogonal tight-binding schemes.

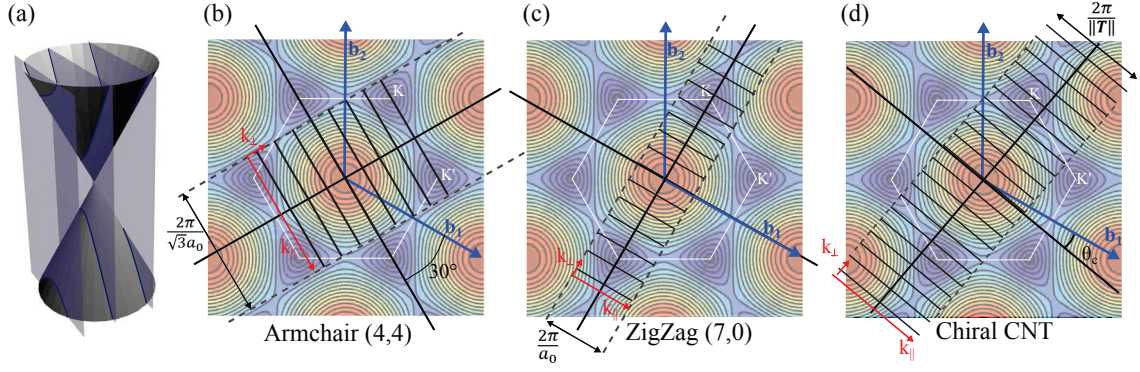


**Figure I.5:** Construction of the nanotubes band structure: zone-folding approximation. (a) Sketch of the zone folding approximation and cutting of the graphene conduction and valence bands close to the Dirac point. (b-d) The background color map is the graphene  $\pi^*$  conduction band dispersion as shown in Fig. I.4. The Brillouin zone of a carbon nanotube is composed of  $u_{\text{cell}}$   $k$ -lines parallel to the continuous wave vector  $\mathbf{k}_{\parallel}$ , i. e. oriented along the nanotube main axis. The  $k$ -lines are separated by  $k_{\perp} = 2/d$ , and indexed by the band-index  $p$ . Within the zone folding approximation, the nanotube bandstructure is obtained by cutting the graphene dispersion according to the  $k$ -lines. The nanotube is metallic if one of the  $k$ -line crosses the  $K$ -point of the graphene Brillouin zone (b), otherwise it is semiconducting (c,d).

the main axis of the nanotube, the reciprocal lattice wave vector  $\mathbf{k}_{\parallel}$  is determined by the translational vector.  $\mathbf{k}_{\parallel}$  remains continuous in the approximation of infinitely long tube, and its length falls in the interval  $]-\pi/\|\mathbf{T}\|, \pi/\|\mathbf{T}\|]$ . Along the circumference of the nanotube, i. e. parallel to  $\mathbf{C}$ , the wave vector  $\mathbf{k}_{\perp}$  is quantized according to the periodic boundary condition

$$k_{\perp,q} = q \frac{2\pi}{\|\mathbf{C}\|} = q \frac{2}{d}, \quad (\text{I.20})$$

where  $q$  is an integer taking the values  $-u_{\text{cell}}/2 + 1, \dots, 0, 1, \dots, u_{\text{cell}}/2$ .  $u_{\text{cell}}$  is the number of graphene hexagons in the nanotube unit cell ( $u_{\text{cell}} = N_C/2$ ). In the reciprocal space of graphene, the couple  $(\mathbf{k}_{\perp}, \mathbf{k}_{\parallel})$  defines 1D cutting lines corresponding to the 1D energy subbands of nanotubes. This method, so-called zone-folding, is sketched in Fig. I.5 for armchair, zig-zag, and chiral nanotubes. The quantized wave vector  $\mathbf{k}_{\perp}$  and the reciprocal lattice vector  $\mathbf{k}_{\parallel}$  are derived from

$$\mathbf{k}_{\perp} \cdot \mathbf{C} = 2\pi, \quad \mathbf{k}_{\perp} \cdot \mathbf{T} = 0, \quad (\text{I.21a})$$

$$\mathbf{k}_{\parallel} \cdot \mathbf{C} = 0, \quad \mathbf{k}_{\parallel} \cdot \mathbf{T} = 2\pi, \quad (\text{I.21b})$$

which yield [33]

$$\mathbf{k}_{\perp} = \frac{1}{u_{\text{cell}}} \left( \frac{n+2m}{N_R} \mathbf{b}_1 - \frac{2n+m}{N_R} \mathbf{b}_2 \right) \quad (\text{I.22a})$$

$$\mathbf{k}_{\parallel} = \frac{1}{u_{\text{cell}}} (n\mathbf{b}_1 - m\mathbf{b}_2). \quad (\text{I.22b})$$

The first Brillouin zone of carbon nanotube consists of  $u_{\text{cell}}$  k-lines (Fig. I.5), of length  $2\pi/\|\mathbf{T}\|$ , parallel to the transnational vector, and separated by  $k_{\perp} = 2/d$ . In other words, the cutting lines in the graphene conduction and valence bands are defines by

$$\mathbf{k}_q = q\mathbf{k}_{\perp} + k \frac{\mathbf{k}_{\parallel}}{\|\mathbf{k}_{\parallel}\|}, \quad (\text{I.23})$$

with discrete band index  $q \in [-u_{\text{cell}}/2 + 1, u_{\text{cell}}/2]$  and continuous  $k \in [-\pi/\|\mathbf{T}\|, \pi/\|\mathbf{T}\|]$  parallel to the nanotube's main axis. Finally the one-dimensional dispersion of the band  $q$  is obtained by inserting (I.23) in the dispersion of graphene (I.18)

$$E_q^{\pm}(k) = E_g^{\pm} \left( q\mathbf{k}_{\perp} + k \frac{\mathbf{k}_{\parallel}}{\|\mathbf{k}_{\parallel}\|} \right). \quad (\text{I.24})$$

Close to the Fermi level, i.e. close to the  $K$ -point, the energy dispersion is linear in a first approximation. Hence, the dispersion of subband  $q$  can be expressed as

$$E_q^{\pm}(k) \approx \pm \frac{\sqrt{3}\gamma_0 a_0}{2} |\mathbf{k}_q - \mathbf{k}_F|, \quad (\text{I.25})$$

where  $\mathbf{k}_F$  is the Fermi wave vector. Further details on the zone-folding method can be found in [33,37,38]. In the following, the discussion focused on the behavior close to the Dirac points which is crucial for nanotubes properties.

## I-2.4 Semiconducting and metallic nanotubes

One remarkable property of carbon nanotubes is their ability to adopt a semiconducting or metallic character, depending on their chirality  $(n,m)$ . The nature of a nanotube depends on the position of the cutting k-lines (in the zone folding approximation) with respect to the  $K$  (or  $K'$ ) point. If one of the k-lines crosses exactly the Dirac point of graphene, the nanotube is metallic (Fig. I.5).<sup>e</sup> Otherwise, a region where no energy state is available appears between the valence and conduction bands, and the nanotube is semiconducting. We showed earlier that the electronic states are restricted to wave vectors that fulfill the condition  $\mathbf{k} \cdot \mathbf{C} = 2\pi q$  ( $q$  integer). Since the Dirac point of graphene is at the position  $\mathbf{K} = (\mathbf{b}_1 - \mathbf{b}_2)/3$ , a nanotube is metallic if

$$\mathbf{K} \cdot \mathbf{C} = 2\pi q \Leftrightarrow \mathbf{K} \cdot \mathbf{C} = \frac{2\pi}{3}(n - m), \quad (\text{I.26})$$

i.e. when  $\nu = \text{mod}(n - m, 3) = 0$ . In the following, the carbon nanotubes are also classified based on the result of  $\text{mod}(n - m, 3)$ , defining the so-called **nanotube families**

- $\nu = 0 \rightarrow$  metallic (M),
- $\nu = +1 \rightarrow$  semiconducting of family type I,

---

<sup>e</sup>To be exact, the graphene is a semimetal as its valence and conduction bands cross only at  $K$  and  $K'$  points.

- $\nu = -1 \rightarrow$  semiconducting of family type II.

More precisely, armchair CNTs are always metallic, whereas zig-zag and chiral CNTs can be either metallic or semiconducting. This point is addressed in detail in the next chapter (see for instance Fig. II.4).

Fig. I.6 shows typical dispersion diagrams of both semiconducting and metallic nanotubes computed from (I.25). The metallic tube presents one valence and one conduction band crossing the Fermi energy, whereas in the case of the semiconducting CNT the highest energy valence subband and the lowest energy conduction subband define an energy bandgap. In both cases, each subband is associated with a discrete value of  $k_{\perp}$  corresponding itself to a quantum number  $q$  set as band index.

The energy dispersion diagrams of the three nanotube families ( $\nu = 0, \pm 1$ ) are sketched in Fig. I.6 where the origin of the phase of the wave functions has been shifted such that the valence and conduction bands the closest to  $E_F$  are associated with the circumferential wave vector  $k_{\perp,q} = 0$  (or  $q = 0$  from (I.20)). In metallic tubes ( $\nu = 0$ ), subband indices ( $q = 0, \pm 1, \pm 2, \dots$ ) are identical in the  $K$  and  $K'$  valleys. On the contrary, in semiconducting CNT, subband quantum numbers are opposite at the  $K$  and  $K'$  valleys, as well they are opposite between family I ( $\nu = +1$ ) and family II ( $\nu = -1$ ). Each subband is fourfold degenerated due to both the intervalley ( $K$  and  $K'$  valleys are equivalent) and spin degeneracy. The simple nanotube band structures shown in Fig. I.6 serve our purpose and capture the main differences between the three types of CNT family. Still, the reader should be aware that reality involves different types of nanotubes leading to various electronic band structures, i.e. subbands are not always centered at  $k_{\parallel} = 0$  and the quantum numbers of the valence and conduction subbands the closest to  $E_F$  are not necessarily zero.

## I-2.5 Density of states

Carbon nanotubes are one-dimensional systems. Consequently, the density of states (DOS) associated with each energy band varies as  $1/\sqrt{E}$ , and presents characteristic diverging values called Van-Hove singularities (VHS) [33,34]. The contribution of energy band of index  $q$  to the density of states is

$$\rho_q(E) = \frac{2}{l_{BZ}} \sum_{k, E=E_q^{\pm}(k)} \left| \frac{dE_q^{\pm}(k)}{dk} \right|^{-1}, \quad (\text{I.27})$$

where  $l_{BZ}$  is the size of the first Brillouin zone, and the term 2 in the numerator comes from the spin degeneracy of the band.

An analytic expression of the DOS can be derived close to the Dirac point using (I.25). In particular, for a given subband  $q$ , the energy of the minimum of the conduction band and maximum of the valence band are simply [33]

$$E_q^{\pm} = \pm \frac{a_0 \gamma_0}{\sqrt{3}d} |3q - n - m| = \pm E_0 |3q - n - m|, \quad (\text{I.28})$$

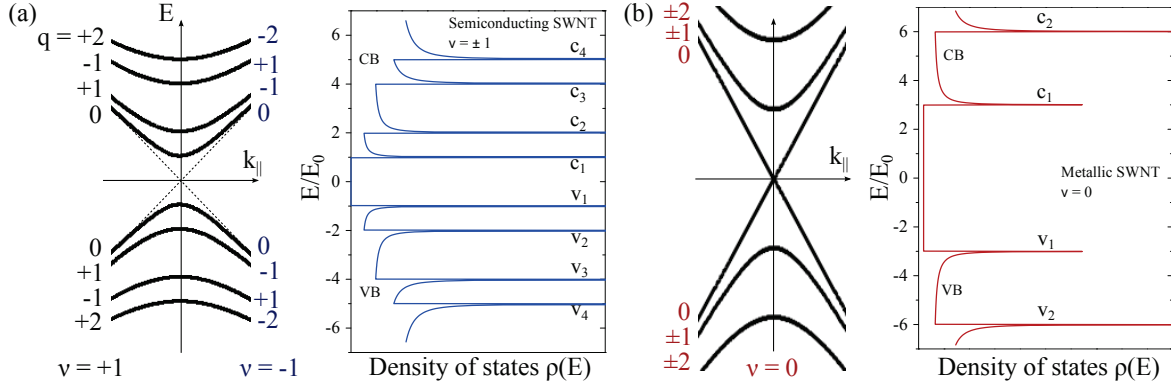


**Figure I.6:** Density of states of carbon nanotubes in the approximation of linear dispersion of graphene. Energy is in unit of  $E_0 = a_0\gamma_0/\sqrt{3}d$ , the Fermi level  $E_F$  is set to zero. Positive and negative energy regions correspond to the conduction and valence bands, respectively. The dispersion diagrams are computed from (I.25).  $q$  are the band indices labeled for: the metallic at  $K$  and  $K'$  points, the SC nanotube type I ( $\nu = +1$ ) or type II ( $\nu = -1$ ) at  $K$  point (labels at  $K'$  point is opposite). (see text for more details) (a) Semiconducting nanotube showing Van-Hove singularities at positions  $E/E_0 = 1, 2, 4, 5, \dots$ , as well as the bandgap where no states are available. (b) Metallic nanotube present no bandgap (available states at the Fermi energy), but Van-Hove singularities are observed at  $E/E_0 = 3, 6, \dots$

where the Fermi energy is set to zero as mentioned previously. Then, the total density of states is expressed by

$$\rho(E) = \frac{4a_0}{\pi^2 d \gamma_0} \sum_q g(E, E_q), \quad (\text{I.29})$$

with

$$g(E, E_q) = \begin{cases} |E|/\sqrt{E^2 - E_q^2} & \text{if } |E| > |E_q| \\ 0 & \text{if } |E| < |E_q|. \end{cases} \quad (\text{I.30})$$

The function  $g(E, E_q)$  diverges at the band-edges of the conduction and valence subbands, i.e. for  $E = E_q$ . This behavior is expected at the Van-Hove singularities in 1D systems. Fig. I.6 shows the density of states of semiconducting and metallic carbon nanotubes from (I.29) and (I.30). For the sake of clarity, on the same figure, we show the nanotubes band structure computed from (I.25).

In the case of SC nanotubes, the bandgap is defined as the region around the Fermi energy where no states are available; its expression is given by

$$S_{11} = 2 E_0 = \frac{2a_0\gamma_0}{\sqrt{3}d}. \quad (\text{I.31})$$

This simple model catches the main physics of semiconducting nanotubes: the bandgap varies as  $d^{-1}$  to a first approximation. The Van-Hove singularities are located at  $E/E_0 = \pm 1, \pm 2, \pm 4, \pm 5, \dots$ . For metallic nanotubes, the DOS at the Fermi energy is

non-zero where the valence and conduction band are merging.<sup>f</sup> Van-Hove singularities are observed at  $E/E_0 = \pm 3, \pm 6, \dots$ , thus a pseudo bandgap is defined for metallic CNTs between the first singularities in the valence and conduction bands, i. e.

$$M_{11} = 6 E_0 = \frac{6a_0\gamma_0}{\sqrt{3}d}. \quad (\text{I.32})$$

The electronic density of states in single-wall carbon nanotubes was successfully confirmed by scanning tunneling spectroscopy at the end of the last century [39, 40]. Since then, many experiments, most of the time based on optical spectroscopy, have been able to observe this DOS for various nanotube species.

---

<sup>f</sup>To be exact the so-called metallic nanotubes are semi-metals in the zone-folding approximation.



# Optical properties of single-wall carbon nanotubes

## II

*In the previous chapter, the general electronic properties of carbon nanotubes were introduced within the framework of tight binding models. Although this approach is rather simple, it is a very powerful tool to describe the most important electronic properties of nanotubes, and to some extent is used in this chapter to introduce their optical properties. More precisely, in the first section, we go one step beyond the zone-folding approximation and analyze the optical response of nanotubes versus their characteristics (nature, geometry), from which the so-called Kataura plot is drawn. The second section addresses the many body interactions and the important idea that exciton prevail in the optical properties of CNTs. Finally, I present my personal interpretation of the state-of-the-art, meaning that a potpourri of selected results is discussed rather than trying to cover all the literature on the subject which is well documented in several textbooks and reviews. In this last section, state-of-the-art of the very active field of absorption spectroscopy in carbon nanotubes is presented as well, out of which we draw some of the issues which will be addressed in this work.*

## II–1 First description of absorption in carbon nanotubes

In this section, optical properties of carbon nanotubes are drawn from the band structure obtained in the previous chapter with the zone folding method. General notations are introduced and will be directly used also in more advanced analysis. Starting from the density of states in (I.29), light absorption and emission processes are introduced along with optical selection rules and the joint density of states (JDOS). Then, the concepts of trigonal warping and family behavior are discussed in order to explain advanced features of the Kataura plot. The latter, introduced by Kataura et al. in 1999 [41], regroups all absorption transitions  $E_{ii}$  of carbon nanotubes and plots their energy as a function of the nanotubes diameter.

### II–1.1 General concepts

#### Absorption transition rate

The main body of this thesis studies the absorption phenomenon in carbon nanotubes,



i. e. the promotion of an electron from the valence band (VB) to the conduction band (CB) via the absorption of one photon of energy  $\hbar\omega$ . To clarify this process, one can start from the band structures and density of states shown in Fig. I.6, where the different Van-Hove singularities are labeled  $v_j$  and  $c_j$  in the valence and conduction subbands, respectively. An electron in a subband is described by the quantum numbers  $q$  and its momentum  $k$  introduced in (I.23), hence the electron wavefunction is written  $|-, q, k\rangle$  and  $|+, q', k'\rangle$  in the valence and conduction bands, respectively. Therefore, the absorption process, characterized by its absorption rate  $W_{\text{abs}}$ , consists in the excitation of an electron from an occupied state  $|-, q, k\rangle$  to an unoccupied state  $|+, q', k'\rangle$ .<sup>a</sup>

The interaction of an electron and the radiation field is addressed with perturbation theory and a semiclassical treatment of the electromagnetic field (EM). In the approximation of weak EM field (linear optics regime), and in the Coulomb gauge, the single particle Hamiltonian reads [42]

$$H = H_{el} + H_{em}, \text{ with } H_{em} = -\frac{e}{m_e} \mathbf{p} \cdot \mathbf{A}, \quad (\text{II.1})$$

where  $H_{el}$  is the unperturbed electronic Hamiltonian of the system,  $\mathbf{p}$  the electron momentum, and  $\mathbf{A}$  the potential vector. The electron charge and mass are denoted by  $e$  and  $m_e$ , respectively. Within this framework, the probability to absorb one photon  $\hbar\omega$  per time unit, and promote one electron from the valence state  $|-, q, k\rangle$  of energy  $E_q^-(k)$  to the conduction state  $|+, q', k'\rangle$  of energy  $E_{q'}^+(k')$ , is given by the Fermi golden rule:

$$W_{\text{abs}} \sim \sum_{q, q'} \frac{1}{l_{BZ}} \int_{BZ} dk \delta(E_{q'}^+(k') - E_q^-(k) - \hbar\omega) |\langle +, q', k' | H_{em} | -, q, k \rangle|^2 f_q^-(k) (1 - f_{q'}^+(k')). \quad (\text{II.2})$$

The occupation probability of the initial state  $f_q^-(k)$  or final state  $1 - f_{q'}^+(k')$  is derived from the Fermi-Dirac distribution. The total absorption rate depends on the optical transition matrix  $H_{qq'}^{\text{abs}}(k, k') = \langle +, q', k' | H_{em} | -, q, k \rangle$  and the joint density of states  $J_{q, q'}(\hbar\omega) = \sum_{q, q'} \frac{1}{l_{BZ}} \int_{BZ} dk \delta(E_{q'}^+(k') - E_q^-(k) - \hbar\omega)$ . In the approximation of large radiation wavelength  $\lambda$  as compared to the characteristic size of the lattice  $a_0$ , the photon momentum is negligible with respect to the size of the Brillouin zone. Therefore, for energy inter-band transitions, the first condition holds:

$$k' - k = 0. \quad (\text{II.3})$$

It allows us to drop the momentum dependency in both the optical transition matrix and in the JDOS, such that

$$W_{\text{abs}} = J_{q, q'}(\hbar\omega) |H_{qq'}^{\text{abs}}|^2 f_q^-(k) (1 - f_{q'}^+(k')). \quad (\text{II.4})$$

---

<sup>a</sup>The emission process corresponds to the recombination of an excited electron in the conduction band and a vacant state in the valence band, accompanied by the emission of a photon at the energy difference between the two states.

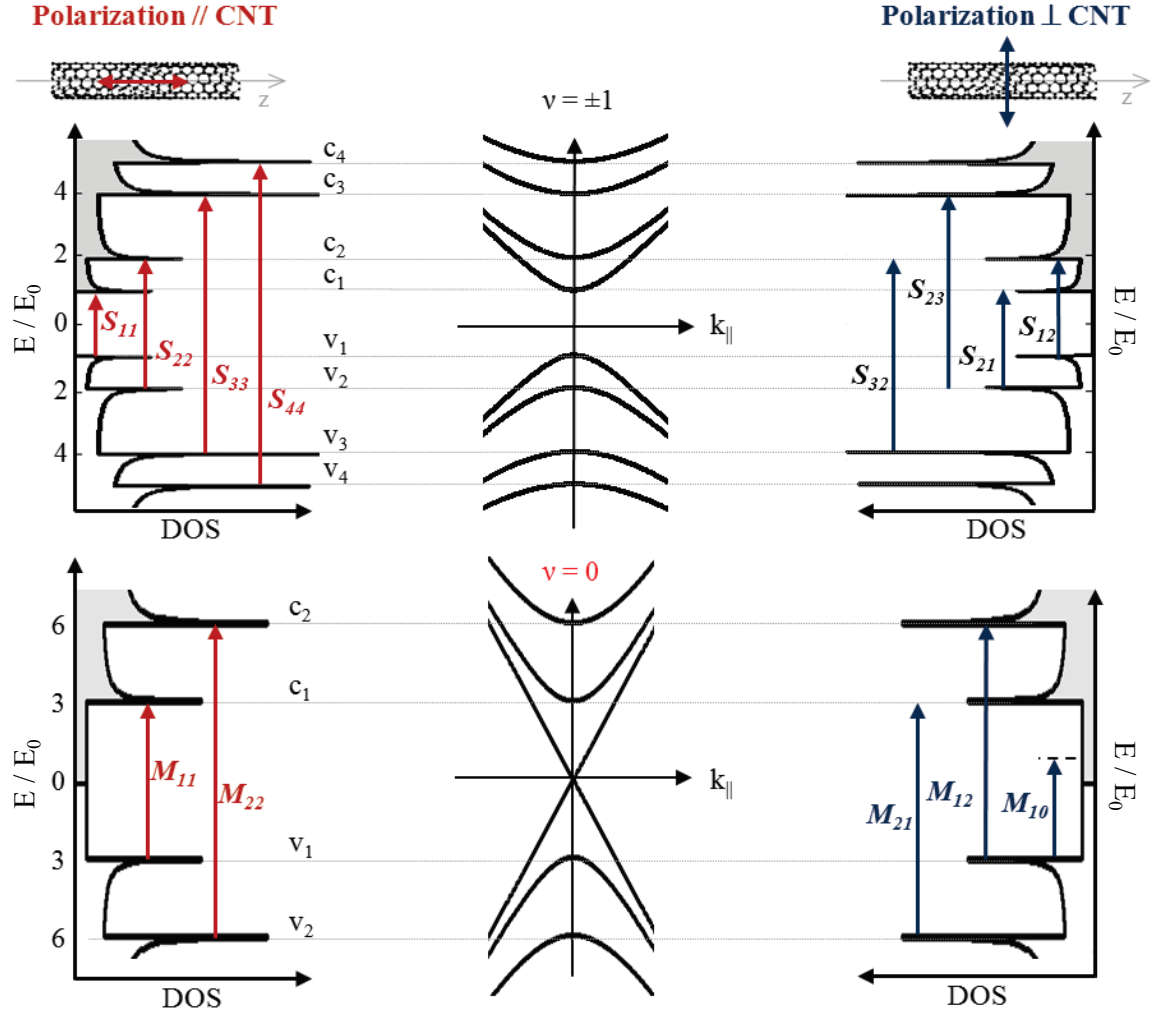


**Figure II.1:** Sketch of the absorption energy transitions in carbon nanotubes for parallel (//) and perpendicular ( $\perp$ ) light polarization, also called parallel and cross-polarized configuration, respectively. Band structures and density of states are recalled from Fig. I.6.

### Selection rules and joint density of states

The transition between the two states  $|-, q, k\rangle$  and  $|+, q', k\rangle$  is optically allowed if and only if the representation of the photon polarized excitation  $\Gamma_{ph}$  is included in the transition matrix representation  $\Gamma_{q'}^+ \otimes \Gamma_H \otimes \Gamma_q^-$  [43]. For incident light polarization parallel to the nanotube main axis, which is set parallel to  $z$ -axis, the transition matrix is non-zero only for absorption between the VB and CB subbands of same index (concomitantly the same quantum number):

$$q' - q = 0, \quad \mathbf{E} // z. \quad (\text{II.5})$$

On the contrary, for cross-polarization, i. e. EM field perpendicular to the nanotube axis, energy transitions are allowed only between valence and conduction subbands with unity absolute index difference:

$$q' - q = \pm 1, \quad \mathbf{E} \perp z. \quad (\text{II.6})$$

The absorption energy transitions, including the selection rules, are sketched in Fig. II.1 where both conduction and valence bands are labeled with  $i$  (or  $j$ ) starting from the Fermi level. For sake of clarity; this notation system is preferred over the subband index  $q$ .<sup>b</sup> In general, these energy transitions are denoted  $E_{ij}$  with  $i, j = \{1, 2, 3, 4, \dots\}$  corresponding to the transitions between the  $v_i$  valence subband and the  $c_j$  conduction subband. More particularly, in semiconducting and metallic tubes they are labeled  $S_{ij}$  and  $M_{ij}$ , respectively. In the following, the absorption transitions for parallel polarization are also denoted by  $p$  with:  $p = 1, 2, 4, 5, 7, \dots$  corresponding to  $S_{11}, S_{22}, S_{33}, S_{44}, S_{55}, \dots$ ; and  $p = 3, 6, \dots$  standing for  $M_{11}, M_{22}, \dots$

The second parameter which determines the strength of the absorption process is the JDOS. It includes the dispersion of both the initial and final subbands involved in the transition process, and  $J_{q,q'}$  is maximum when the two subbands run parallel one to each other creating Van-Hove singularities in the JDOS. This is the case conjointly at the top of the VB and the bottom of the CB, i. e. at the VHS of the DOS. In summary, maximum absorption is observed between Van-Hove singularities of the nanotube DOS (Fig. II.1). The resulting spectrum yields absorption peaks forming Van-Hove singularities too [44].

### Depolarization field and antenna effect

Based on the analysis of the selection rules and JDOS, absorption spectra of a nanotube present Van-Hove singularities in both parallel and cross-polarization configurations. To be exact, perpendicular optical absorption is strongly suppressed by the depolarization effect, also called antenna effect. Assimilating the CNT to an infinite cylinder, this phenomenon can be understood in the static approximation: the incident  $\mathbf{E}$ -field creates surface charges as shown in Fig. II.2 (inset), and consequently a depolarization field opposing the incident one is induced in the  $x$ - $y$  plane. In other words, the effective electric field in the cylinder is strongly reduced resulting in the strong damping of cross-

<sup>b</sup>As demonstrated in Sec. I-2.4, for a given subband the quantum number  $q$  may differ from one nanotube to another. For sake of clarity, we choose to label the subbands in a way which is more adapted for the discussion of the absorption processes.

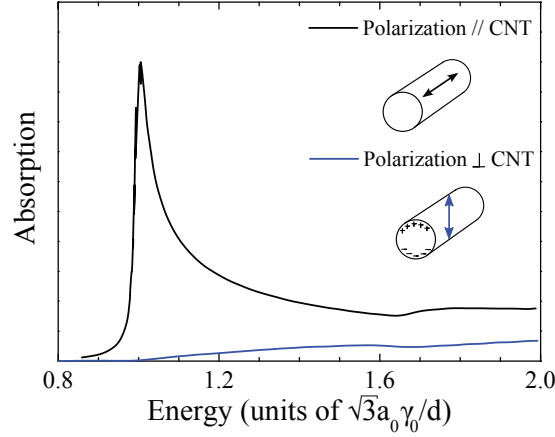


**Figure II.2:** Calculated absorption for parallel and perpendicular polarization. Computed for a tight-binding model, the perpendicular absorption is strongly damped due to charges at the nanotube surface creating a depolarization field opposing the excitation EM field. Adapted from [45].

polarized absorption Fig. II.2. The cylinder (nanowire) model is discussed to a more extent in Appx. B.

The depolarization effect was first described theoretically combining a tight-binding model and the electrostatic argument [46, 47]. In 2004, Islam et al. observed this phenomenon via absorption measurements on assemblies of aligned nanotubes [48]. They have shown that, to a first approximation, the screened polarizability  $\alpha_{\perp}(\omega)$  can be expressed as a function of the unscreened polarizability  $\alpha_{0,\perp}(\omega)$  as

$$\alpha_{\perp} = \left( \frac{1}{\alpha_{0,\perp}} + \frac{1}{2Ld^2} \right)^{-1}, \quad (\text{II.7})$$

where  $L$  is the nanotube length. The polarizability at frequency  $\omega$  (wave vector  $k = \omega/c$ ) is directly related to the absorption cross-section  $C_{\text{abs}} = k \text{Im}(\alpha)$ .

Rayleigh experiments at the single nanotube level have confirmed the strong antenna effect in CNTs [49]. On the contrary, some photoluminescence experiments have detected weak absorption peaks for perpendicular excitation [15, 50]. These features are described by advanced theory including excitonic effects [51–54]. More recently, few research groups have reported the observation of weaker antenna effect when nanotubes are deposited on various substrates [12, 55–57]. This point is discussed in Chap. IV and Chap. V. In the following of this chapter, we focus on light excitation linearly polarized parallel to the carbon nanotubes.

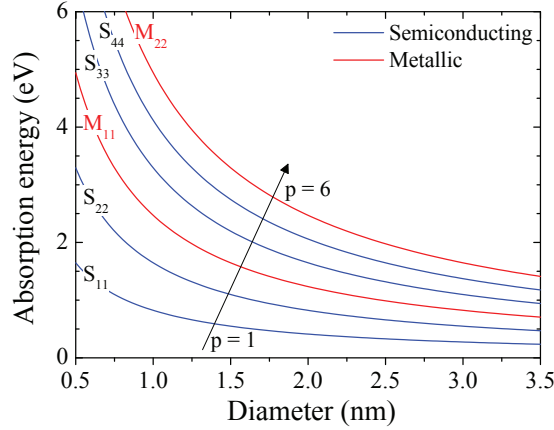


**Figure II.3:** Absorption energy transitions vs. diameter: simplified Kataura plot. First model addressing the diameter dependence of the absorption energy transitions in carbon nanotubes. These results were computed within the zone folding approximation and considering linear dispersion of the graphene bands in the  $K$  and  $K'$  valleys (see Sec. I–2.5).  $p = 1, 2, 4, 5$  corresponds to the semiconducting nanotube transitions  $S_{11}, S_{22}, S_{33}, S_{44}, S_{55}$ ; and  $p = 3, 6$  stand for metallic tube energy transitions  $M_{11}, M_{22}$ . These results are valid for light polarization along the nanotubes.

## II–1.2 Absorption transitions vs. nanotube diameter

Close to the Dirac points, within the tight-binding model described in Secs. I–2.3 and I–2.5, the absorption energy transitions yield

$$E_{ii} = p E = \frac{p a_0 \gamma_0}{\sqrt{3} d}, \quad p = 1, 2, 3, \dots \quad (\text{II.8})$$

Despite the simplicity of this model, a general picture of the absorption in carbon nanotubes can be drawn from the plain Kataura plot presented in Fig. II.3.

(i) First, the metallic and semiconducting energy transitions appear in the order  $S_{11}, S_{22}, M_{11}, S_{33}, S_{44}, M_{22}, S_{55}, \dots$ , which will be conserved even in more advanced models.

(ii) Second, bandgap in semiconducting CNTs ( $S_{11}$ ) scales with the inverse of nanotubes diameter. This behavior is verified for all absorption transitions in both semiconducting and metallic tubes (see  $S_{ii}$  and  $M_{ii}$  curves in Fig. II.3). This property motivates the development of an absorption-based characterization tool to discriminate nanotubes of different diameter. Despite recent developments, synthesis methods have not achieved control over the chirality of the nanotubes produced yet, which is a significant drawback for the development of new industrial applications. Nowadays, the challenge stays in the elaboration of efficient characterization methods to overcome the lack of control in the fabrication process. A large panel of techniques have been developed in this direction: atomic force microscopy, transmission electron microscopy [2], electron diffraction,

Raman spectroscopy [58], photoluminescence (PL) [59], absorption/photoluminescence excitation (PLE) [60], and Rayleigh scattering [49].

(iii) Finally, Fig. II.3 shows also that the  $E_{ii}$  come closer to each other for larger diameter, thus the analysis of the absorption spectra can become tedious for big nanotubes.

### II-1.3 Kataura plot (single-particle model)

The electronic and optical properties of CNTs have been described within a single particle model. In the zone folding approximation, for linear and isotropic dispersion of the graphene bands near the  $K$  and  $K'$  points, the absorption energy of each transition  $E_{ii}$  simply scales with  $d^{-1}$  (Fig. II.3). One can go one step beyond the zone folding approximation by including curvature effects and many-body interactions. The latter is further discussed in the next section. The former concerns the possible mixing of  $\pi$  and  $\sigma$  orbital states resulting from the curvature of nanotube walls, which leads to the formation of hybrids with partly  $sp^2$  and partly  $sp^3$  characters [33].<sup>c</sup> Curvature effects are in fact more pronounced for small diameter tubes [44].

#### Trigonal warping and family behavior

Chirality dependence, i. e. including both diameter and chiral angle, of the nanotubes band structure and absorption energy transitions find its origin in the deviation of the graphene dispersion from the ideal Dirac cone dispersion [20, 61]. More precisely, band dispersion in graphene is not perfectly linear even at the  $K$  and  $K'$  valleys, as well as it shows dependence with directions in the Brillouin zone (particularly visible along the high-symmetric lines). This effect, so-called **trigonal warping**, accounts for the energy shifts of the absorption band-edges, i. e. the absorption energy transitions, depending on the nanotubes chirality. More precisely, trigonal warping explains:

- the splitting of  $M_{ii}$  transitions into  $M_{ii(-)}$  and  $M_{ii(+)}$ , in the case of chiral and zig-zag metallic CNTs,
- the different ratio  $S_{p+1,p+1}/S_{ii}$  observed for semiconducting nanotubes of type I and type II, referred as **family behavior**.

This effect is illustrated in Fig. II.4 for armchair, zig-zag, and chiral nanotubes. The background 2D energy colormap is the graphene  $\pi$  conduction band dispersion close to the  $K$  point (the same behavior is observed at the  $K'$  point as a consequence of the twofold valley degeneracy of each subband). The thick cutting lines, defined in the zone folding approximation (see Fig. I.5), are orientated perpendicular to  $\mathbf{k}_\perp$  and separated by  $2/d$ . All lines (thick and thin) are parallel and each line is separated from its two neighbors by a distance  $2/3d$ . The minimum (resp. maximum) of the nanotubes conduction (resp. valence) subbands determine the position of the band-edge absorption  $E_{ii}$  or Van-Hove singularities in the JDOS. Hence, the energy minimum of each cutting

<sup>c</sup>In graphene,  $\pi$  states are strictly perpendicular to in plane  $\sigma$  states, hence mixing between these orbitals is forbidden and the bounds have  $sp^2$  character.



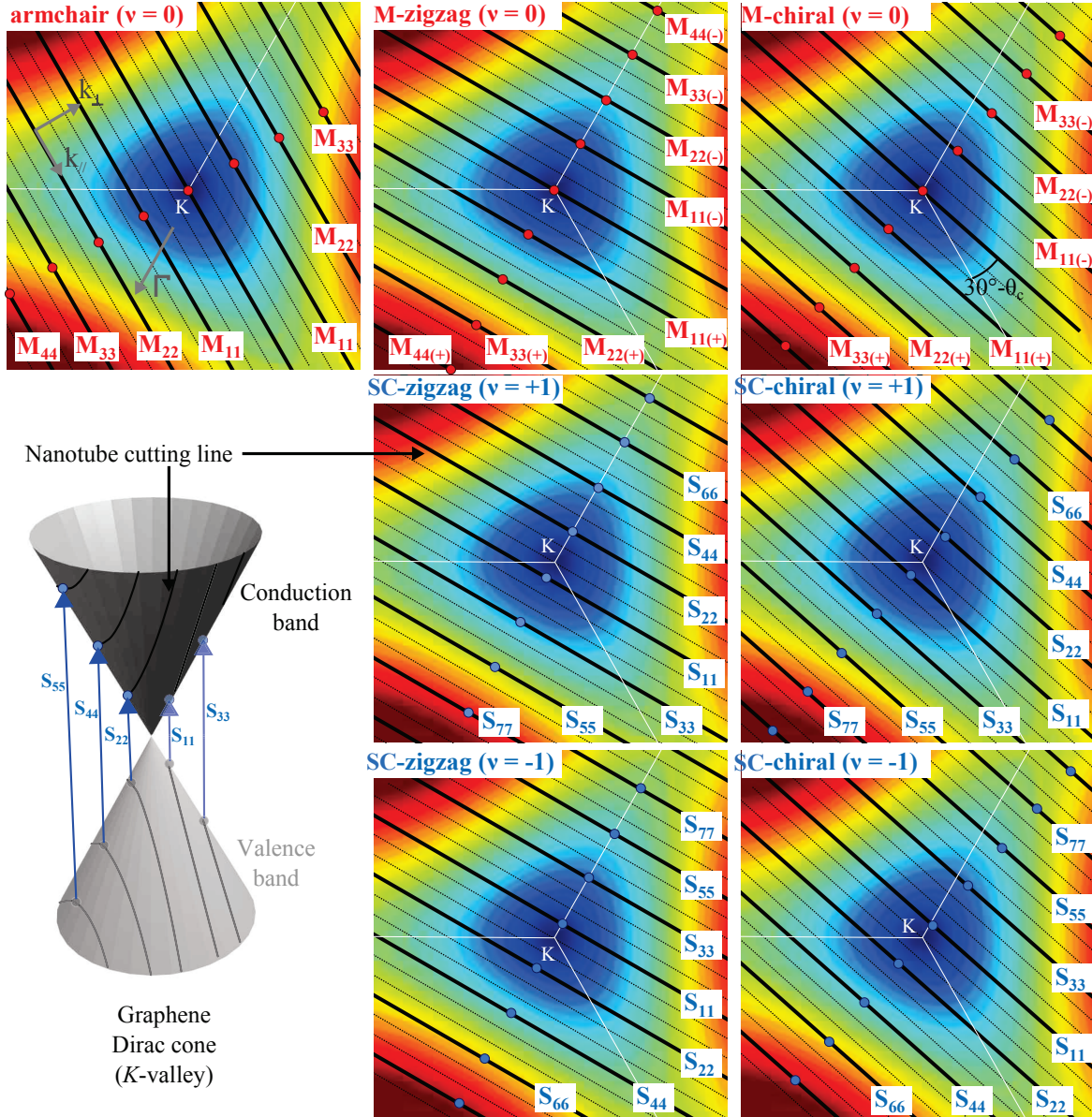


**Figure II.4:** Sketch of trigonal warping effect in carbon nanotubes. The background colormap is the graphene conduction band close to the  $K$ -valley. The energy transitions take place between band edges of the conduction (blue and red dots) and valence subbands. The notations are identical to those shown in Fig. I.5. The thick lines recall the cutting lines defined in the zone folding approximation (period  $2/d$ ). Thin lines, separated by  $2/3d$ , are added to clarify the difference between M, SCI, SCII nanotubes. Due to the asymmetry on the two sides of  $K$  point for finite chiral angle  $\theta_c$ , non-armchair metallic tubes have two  $M_{ii}$  subbands with differing energies. The same asymmetry leads to a systematic variation of transitions energies for semiconducting tubes of different chirality: odd bands ( $S_{11}, S_{33}, S_{55}, \dots$ ) with  $\nu = +1$  have lower energies than their counterparts with  $\nu = -1$  for tubes of the same diameter, whereas even bands ( $S_{22}, S_{44}, S_{66}, \dots$ ) have higher energies. The differences increase with the asymmetry level and  $\theta_c$ . These trends give rise to the family behavior in SWNTs.

line (indicated with blue or red dots in Fig. II.4) is associated with a transition  $E_{ii}$  as labeled directly in Fig. II.4.

**Metallic nanotubes ( $\nu = 0$ )** One cutting line crossed the  $K$  point giving the semi-metallic character. The two nearest-neighbor cutting lines on each side of the  $K$  point define the  $M_{11}$  transition, they are both at  $2/d$  from the  $K$  point. In the case of armchair tubes the  $M_{11}$  energies defined for the two subbands are identical. On the contrary, they are different for chiral and zig-zag nanotubes, i.e.  $M_{11}$  transition splits into  $M_{11(-)}$  and  $M_{11(+)}$  [20, 62]. The same behavior is observed also for higher-energy transitions. The upper and lower branches are referred to as  $M_{ii(+)}$  and  $M_{ii(-)}$ , respectively. The energy splitting  $\Delta M_{ii} = M_{ii(+)} - M_{ii(-)}$  increases while decreasing the chiral angle  $\theta_c$ , and reach its maximum for zig-zag nanotubes (Fig. II.5.c).

**Semiconducting nanotubes ( $\nu = +1$ )** The cutting line defining the bandgap energy  $S_{11}$  is at  $2/3d$  from the  $K$  point. The transition  $S_{22}$  is on the opposite side of the  $K$  valley. The other transitions  $S_{ii}$  ( $i > 3$ ) are alternatively on one side or the other of the Dirac point.

**Semiconducting nanotubes ( $\nu = -1$ )** The  $S_{ii}$  are at the same distance from the  $K$  point as for semiconducting tubes of type I ( $\nu = +1$ ), except that for each cutting line (associated with  $S_{ii}$ ) is on the opposite side of the Dirac point. In other words, due to trigonal warping the  $S_{ii}$  transitions behave differently in semiconducting tubes of type I and type II (compare the energy at the band edge of each subband, i.e. the energy of the blue dots). For identical diameter, nanotubes of each family show  $S_{ii}$  at different energies. Moreover, for a given family, the energy separation between adjacent transitions  $S_{ii}$  and  $S_{i+1,i+1}$  depends on the chiral angle.

The effect of trigonal in semiconducting nanotubes is summarized by two simple inequalities derived from the observation of Fig. II.4:

$$S_{ii}^{\text{small } \theta_c}(\nu = +1) > S_{ii}^{\text{large } \theta_c}(\nu = +1) > S_{ii}^{\text{large } \theta_c}(\nu = -1) > S_{ii}^{\text{small } \theta_c}(\nu = -1), \quad i \text{ even}, \quad (\text{II.9a})$$

$$S_{ii}^{\text{small } \theta_c}(\nu = -1) > S_{ii}^{\text{large } \theta_c}(\nu = -1) > S_{ii}^{\text{large } \theta_c}(\nu = +1) > S_{ii}^{\text{small } \theta_c}(\nu = +1), \quad i \text{ odd}. \quad (\text{II.9b})$$

In metallic nanotubes the more simple relation holds (not valid for armchair)

$$M_{ii(+)}^{\text{small } \theta_c} > M_{ii(+)}^{\text{large } \theta_c} > M_{ii(-)}^{\text{large } \theta_c} > M_{ii(-)}^{\text{small } \theta_c}. \quad (\text{II.10})$$

The Kataura plots including the effects of trigonal warping and family behavior are shown in Fig. II.5.b and Fig. II.5.c for semiconducting and metallic nanotubes, respectively. This point is further discussed in the next paragraph.



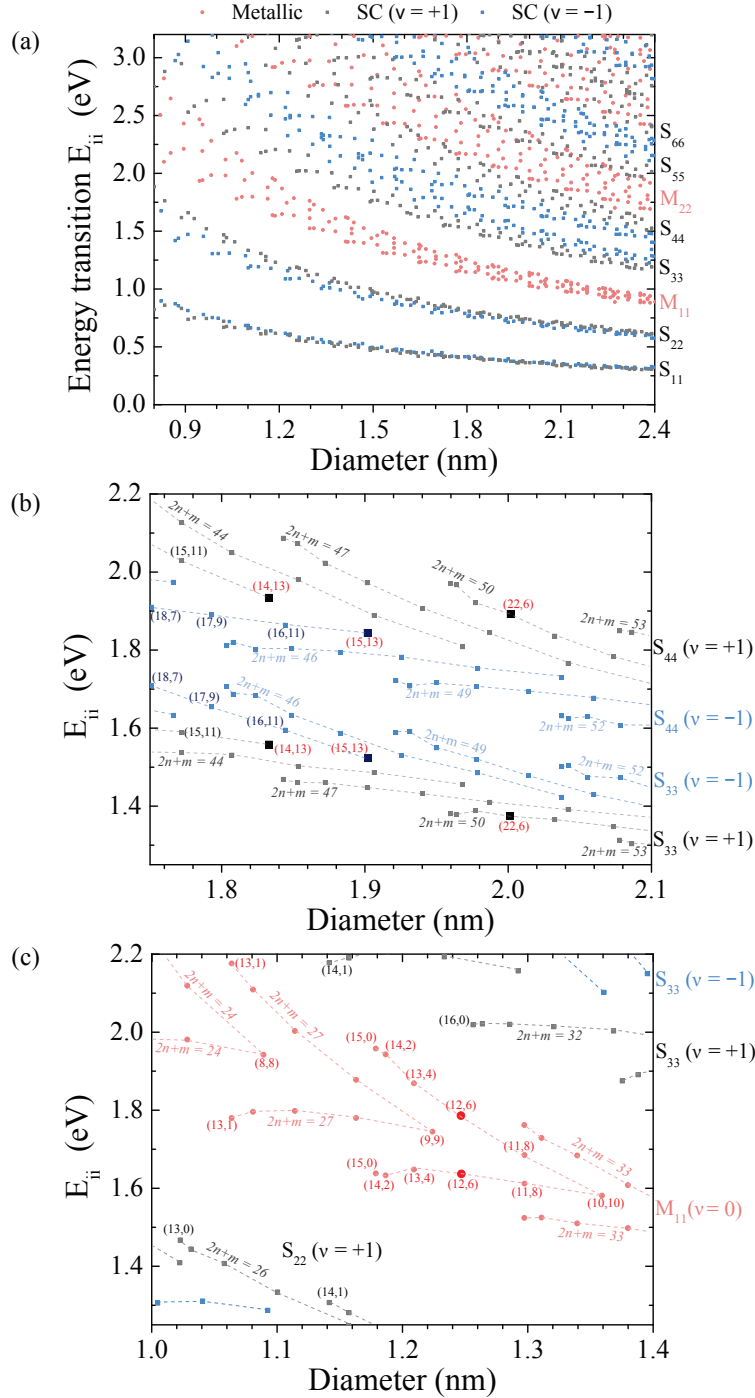


**Figure II.5:** Kataura plot in the single-particle model computed from the theoretical data of V. Popov calculated within the non-orthogonal tight-binding model including curvature corrections [44]. (a) General Kataura plot. (b)  $S_{33}$  and  $S_{44}$  energy transitions for diameter range 1.75 – 2.1 nm. (c)  $M_{11}$  for metallic tubes with  $d \in [1.0, 2.4]$  nm. Nanotubes (14,13), (15,13), (22,6), and (12,6) are investigated by means of absorption spectroscopy in this thesis. Dashed lines link energy transitions of nanotubes with chirality  $(n,m)$  such that  $2n + m$  is constant.

### Kataura plot

At this point, we have all the ingredients to introduce the Kataura plot in Fig. II.5. The optical energy transitions were computed from the theoretical data of V. Popov calculated within an advanced tight-binding model including curvature corrections (non-orthogonal tight binding model) [44].<sup>d</sup> Fig. II.5.a presents energy transitions of semi-conducting and metallic nanotubes over a broad energy range for diameters between 0.8 and 2.4 nm. The transitions of each nanotube of a given chirality  $(n,m)$  form a vertical set of points on the Kataura plot at the tube's diameter. The two lower panels are zoom in regions of interest which show absorption transitions of some of the nanotubes investigated in this thesis. As suggested by the dashed lines, nanotubes transitions can be organized in branches with  $2n + m$  constant following for each  $E_{ii}$  a herringbone pattern. The large chiral angles are at the center of each transition 'band', whereas the small chiral angle tubes are located at the band extremities. Moreover, in the case of semiconducting CNTs, the order of the transitions between SC nanotubes type I and II is reversed in  $S_{44}$  as compared to  $S_{33}$  – this behavior is explained by the effect of trigonal warping described by (II.9a).

## II-2 Excitons in carbon nanotubes

In the last section the optical properties of carbon nanotubes were described in the single particle model. However, charge carriers confined in one-dimensional systems present strong interactions. In this part, we show that the description of nanotubes optical properties requires to take into account many-body effects. Thereafter, we discuss the exciton properties in CNTs and we introduce a corrected Kataura plot accounting for these effects.

### II-2.1 The ratio problem

The pioneer experiment relating CNTs chirality to their optical properties was performed in 2002 by Bachilo et al. [59]. They measured the absorption and emission properties of SWNTs isolated in aqueous surfactant solutions by means of photoluminescence. Fig. II.6.a shows the photoluminescence excitation (PLE) map obtained by Bachilo and coworkers. The semiconducting nanotubes are excited in their  $S_{ii}$  energy transitions and after non-radiation relaxation processes the photo-emission takes place between the first conduction  $c_1$  and valence  $v_1$  sub-bands. In the PLE map, each peak identified one nanotube chirality  $(n,m)$ , hence an empirical Kataura plot can be obtained [59,63]. In the single particle model approximation, a ratio of 2 is expected between the absorption energy  $S_{22}$  and the emission energy  $S_{11}$  (see (II.8)). Fig. II.6.b shows that experimental results strongly deviate from this prediction. In fact, the ratio  $S_{22}/S_{11}$  takes dispersed values between 1.2 and 2.1 with average 1.7. Moreover, tubes of semiconducting family type I (family type II) are exclusively observed above (below) the average ratio. This was

<sup>d</sup>Results of V. Popov are reported here for parallel polarization only, but one can find details about perpendicular absorption transitions in his papers.

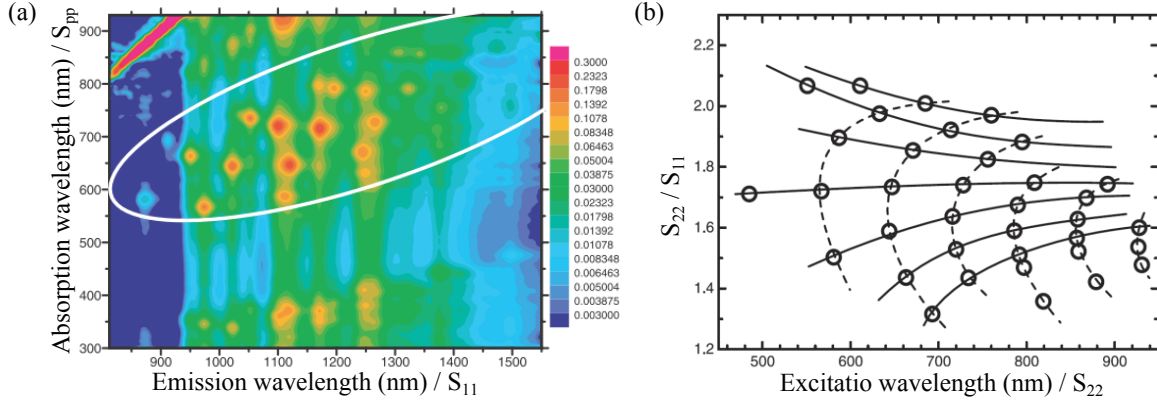


**Figure II.6:** Structure-assigned optical spectra of SWNTs and ratio problem observed by Bachilo et al. . (a) Photoluminescence excitation map (PLE) of SWNTs isolated in aqueous surfactant solutions. Each peak identifies a particular chirality. The white oval encloses the nanotubes excited in their  $S_{22}$  transition. (b) The ratio of the second to first transitions for a large number of nanotube species. Circles are the experimental data and solid lines connect nanotubes with identical  $n - m$ . The points above a ratio 1.7 are semiconducting tubes of type I, and the others belong to the family type II.

the first direct observation of the family behavior. These results are not fully explained by trigonal warping effects, and the Kataura plot introduced in Fig. II.5.a does not account for the positions of the  $E_{ii}$  transitions as well as their shapes. Finally, the failure of the single particle model to explain the ratio problem was overcome by taking into account many-body effects [64–67].

## II–2.2 Optical transitions arise from excitons

### II–2.2.a Mott-Wannier excitons

Including many-body effects have at least two important consequences on the electronic structure of nanotubes:

- electron-electron repulsion induces blue-shifts of the energy bands and renormalizes the bandgap or self energy (energy  $E_{e-e}$ ),
- electron-hole attraction introduces red-shifts of the energy bands and leads to the formation of exciton states ( $E_{e-h}$ ).

The large many-body effect in carbon nanotubes is explained by both low screening of electrostatic interactions and strong confinement of carriers in one dimensional systems. They both result in enhanced Coulomb interactions. Luer et al. investigated exciton size and mobility in (6,5) single carbon nanotubes [68]. They concluded that excitons in CNTs are typically **Mott-Wannier excitons** which are characteristic of covalent inorganic semiconductors. In fact, they measured an exciton size  $l_\chi = 2.0 \pm 0.7$  nm and

a diffusion length smaller than 10 nm in average, meaning that each exciton extend over a large number of carbon atoms.<sup>e</sup>

The exciton wavefunction can be written as a linear combination of the product of quasi-single particle eigenstates in the valence (holes) and conduction (electrons) bands

$$\chi(\mathbf{r}_e, \mathbf{r}_h) = \sum_{q,q'} \mathbf{A}_{qq'} \varphi_{h,q}^-(\mathbf{r}_h) \varphi_{e,q'}^+(\mathbf{r}_e), \quad (\text{II.11})$$

where the sum runs over the valence  $q$  and conduction  $q'$  sub-bands of the nanotube, and  $\varphi_{h,q}^-(\mathbf{r}_h)$  (resp.  $\varphi_{e,q'}^+(\mathbf{r}_e)$ ) is the valence (resp. conduction) single-particle state. Solution of the excitonic eigenfunctions and eigenstates are obtain by solving the Bethe-Salpater equation, which includes many-body interactions and considers the mixing via Coulomb interactions of both electron and hole states with all the different wavevectors of all the sub-bands [64, 66, 69, 70]. The unscreened Coulomb interaction between  $\pi$  orbitals is included in the many-body term. It is described by the Ohno-potential  $V(\mathbf{r}_{ss'})$  which depends on the distance between two orbital sites  $s$  and  $s'$ . Eventually, the environment effects were included by Nugraha et al. via the introduction of a screened Coulomb potential

$$W(\mathbf{r}_{ij}) = V(\mathbf{r}_{ss'}) / \kappa(d, l_\chi) \epsilon(\mathbf{k}_e), \quad (\text{II.12})$$

where  $\epsilon$  describe the dielectric constant of  $\pi$  electrons and  $\kappa$  depends on the surrounding material (cf. [70] for details).

Another possible theoretical approach to the exciton problem was proposed by Malic et al. using the density matrix formalism based on Bloch equation and tight-binding single-particle wave equations [71]. Moreover, this method presents the advantage of describing the dynamics of the photo-absorption processes.

## II-2.2.b Exciton states

### Exciton Rydberg states

Since the Coulomb interaction depends only on the relative distance between the electron and hole, the many-body Hamiltonian is invariant under the symmetry operations of the nanotube [43]. Each excitonic eigenstate will then transform as one of the irreducible representations of the space group of the nanotube. In general the electron-hole interaction mix states with all sub-bands. However, for relatively small nanotubes ( $d < 1.5$  nm), the separation between energy transitions is large enough to consider that only the electronic sub-bands involved in the formation of the exciton mix. Within this approximation, the exciton wavefunction can be expressed in the usual form of bulk semiconductors:

$$\chi(\mathbf{r}_e, \mathbf{r}_h) = \mathbf{B}_{he} \varphi_h^-(\mathbf{r}_h) \varphi_e^+(\mathbf{r}_e) \phi^{\text{env}}(\mathbf{r}_e - \mathbf{r}_h), \quad (\text{II.13})$$

with  $\phi^{\text{env}}$  the envelope function, and the subband index  $q'$  ( $q$ ) in the electron (hole) wavefunctions was dropped for clarity (this points is addressed in the next paragraph). In a

<sup>e</sup>To the opposite, Frenkel excitons show tightly bound electron-hole pairs and are located near a single atom of the lattice.

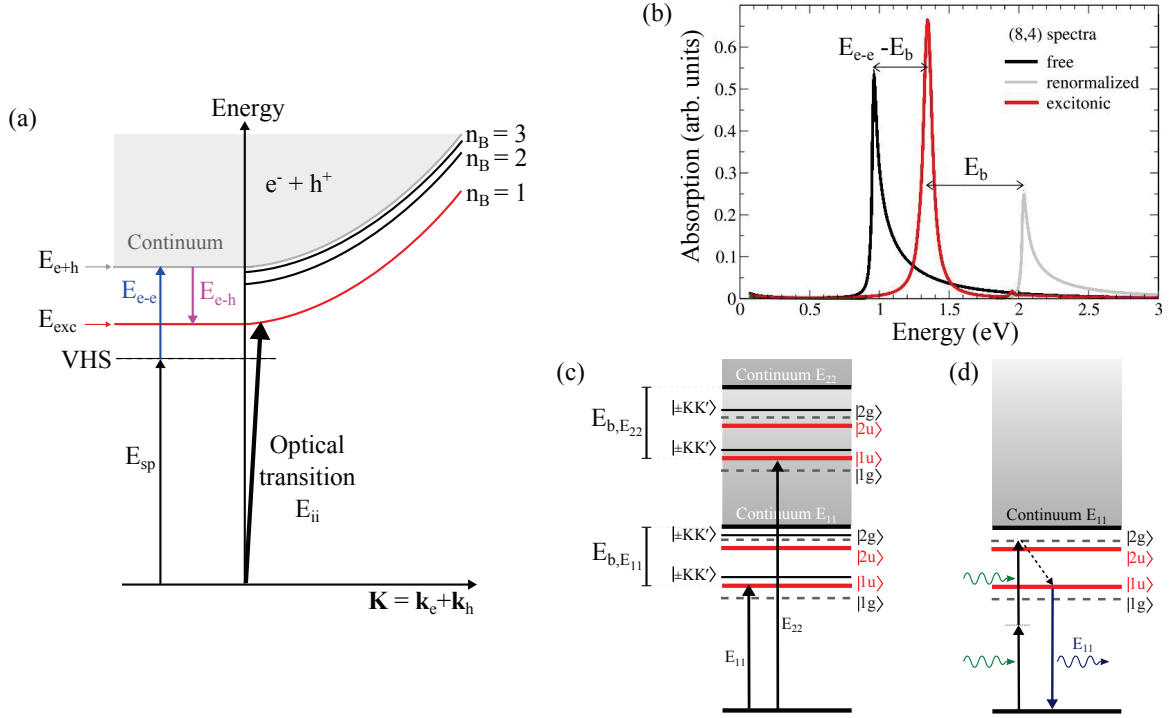


**Figure II.7:** Exciton states in single-wall carbon nanotubes. (a) Rydberg states modeling excitons for one energy transition  $E_{ii}$ . Exciton states are obtained from (II.15) and (II.16). (b) Computed absorption at the transition  $E_{ii}$  for three situations: in the single-particle picture (black), including electron-electron interactions (grey), including electron-electron and electron-hole interactions (red). Adapted from [71]. (c) Energy diagram of the first two transitions  $E_{ii}$  showing the bright and dark states, as well as the allowed dipolar transitions. (d) Two-photon absorption process used by Wang et al. and Maultzch et al. to measure the binding energy of exciton  $S_{11}$  in semiconducting nanotubes.

simple approach neglecting the electron-electron exchange interaction, the exciton states are derived directly from the model of the hydrogen atom. The exciton wavefunction yields

$$\chi(\mathbf{r}_e, \mathbf{r}_h) = \Omega^{-1/2} e^{i\mathbf{K}_{\text{exc}} \cdot \mathbf{R}} \varphi_h^-(\mathbf{r}_h) \varphi_e^+(\mathbf{r}_e) \phi_{n_B, l, m}^{\text{env}}(\mathbf{r}_e - \mathbf{r}_h), \quad (\text{II.14})$$

where  $n_B (= 1, 2, 3, \dots)$ ,  $l$ ,  $m$ , are the quantum numbers of Rydberg or hydrogenic states. The envelope function of the exciton  $\phi_{n_B, l, m}^{\text{env}}(\mathbf{r}_e - \mathbf{r}_h)$  is even or odd upon  $\mathbf{r} \rightarrow -\mathbf{r}$  operations for  $n_B$  odd or even, respectively. The exciton dispersion relation is then

$$E_{\text{exc}}(\mathbf{K}, n_B) = \frac{\hbar^2 \mathbf{K}_{\text{exc}}^2}{2M} + E_{e+h} - \frac{R_y^*}{n_B^2}, \quad (\text{II.15a})$$

$$R_y^* = 13.6 \text{ eV} \frac{\mu}{m_0 \epsilon_{eh}} \quad \text{the exciton binding energy of 1s-state } (n_B = 1). \quad (\text{II.15b})$$

$E_{e+h}$  is the energy of the continuum and  $m_0$  the real electron mass. The excitonic center of mass momentum  $\mathbf{K}_{\text{exc}}$  and the translational mass  $M$  are defined as the sum

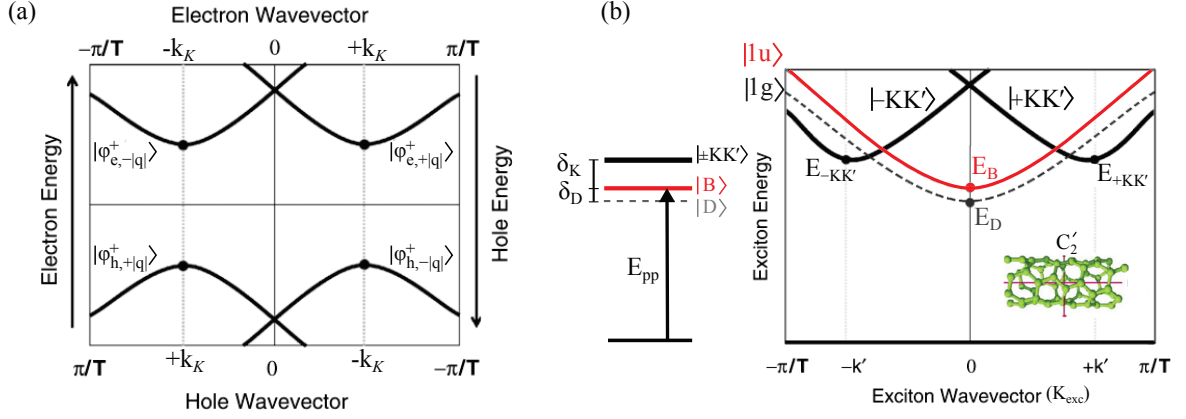


**Figure II.8:** Exciton dispersion in chiral single-wall carbon nanotubes, adapted from [43]. (a) Electron and hole dispersion labeled by their state, as obtained from zone-folding method. (b) Exciton dispersion for the lower-energy Rydberg state  $n_B = 1$  showing the four singlet states.  $|1u\rangle$  is bright state  $|B\rangle$  (dipole allowed transition) and odd under  $C'_2$  rotation, it can couple directly to light excitation.  $|1g\rangle$  is dark state  $|D\rangle$  (dipole forbidden) and even under  $C'_2$  rotation. The two states  $|\pm KK'\rangle$ , with band edge at  $\pm k' = \pm 2k_{||}$ , are dark states that can be probed only with phonon-assisted absorption/photoluminescence. (inset) Symmetry in chiral nanotubes. (middle) Energy diagram showing the energy levels of the four singlet states.

of the individual carrier wave vectors and effective masses, respectively, i.e.  $\mathbf{K}_{\text{exc}} = \mathbf{k}_e + \mathbf{k}_h$  and  $M = m_e + m_h$  (the indices  $e$  and  $h$  stand for electron and hole).  $\mu$  is the reduced mass of the system,  $\mathbf{R}$  is the center of mass, and  $\Omega$  the exciton volume.  $\epsilon_{eh}$  is the phenomenological dielectric constant defined for the environment surrounding the exciton. As shown in Fig. II.7.a, exciton states lie directly below the continuum of free electron-hole pairs. Finally, in carbon nanotubes, the exciton energy is defined as the sum of the single particle energy ( $E_{\text{SP}}$ ) and the self-energy ( $E_{e-e}$ ) reduced by the exciton energy ( $E_{e-h}$ ):

$$E_{\text{exc}} = E_{\text{SP}} + E_{e-e} - E_{e-h}, \quad (\text{II.16})$$

where  $E_{e-h}$  can be understood as  $R_y^*/n_B^2$  in the hydrogenic model. The absorption process in nanotubes is dominated by excitonic transitions, i.e. energy transitions take place between the exciton ground state and exciton states. It is common to use the same notation as in the single particle picture to label the exciton transitions  $E_{ii}$ . The oscillator strength, which is directly proportional to the optical transition matrix of the system, is mainly carried by the lower energy exciton or  $1s$ -like state of the exciton ( $n_B = 1$ ) [72–74]. As a consequence, the absorption spectrum does not show Van-Hove singularities transitions but rather symmetric Lorentzian-like exciton peaks at the position of the  $1s$  exciton. This is illustrated in Fig. II.7.b where the single-particle absorption, the excitonic absorption, and the position of the continuum, are depicted in black, red, and grey, respectively [71]. The **exciton binding energy**  $E_b$  is the energy

between the band edges of the continuum and the lower energy bright exciton (this quantity can be different from the electron-hole binding energy  $E_{e-h}$  in some cases as discussed in the next paragraph).

### Fine structure

At this point, for one energy transitions  $E_{ii}$ , an ensemble of exciton states are available with associated quantum number  $n_B$ . Each exciton is formed of one electron and one hole from  $K$  and  $K'$  valleys associated with the wave vector  $\pm k_0$ , for the valence and conduction subband  $\pm|q|$ . Including the twofold spin degeneracy, each exciton Rydberg state is 16 times degenerated, leading to 12 triplet states and 4 singlet states. Only the latter are accessible for dipole optical transitions, and most of the oscillator strength is carried by the lower energy exciton ( $n_B = 1$ ), hence the discussion is limited to singlet states of the lower energy Rydberg state. Exact analysis of all the exciton states is beyond the scope of this thesis, the reader is advised to refer to the reviews [43, 75], and details on the triplet states can be found in [76, 77]. Furthermore, the fourfold degeneracy of the singlet states is lifted by the electron-hole interactions. Then, the four final exciton states are expressed from the mixing of the conduction electron states  $\{|\varphi_{e,-|q|}^+\rangle, |\varphi_{e,+|q|}^+\rangle\}$  and valence holes states  $\{|\varphi_{h,+|q|}^-\rangle, |\varphi_{h,-|q|}^-\rangle\}$ . As shown in Fig. II.8.a in the case of chiral nanotubes, these states have band edge at  $\pm k_K$  corresponding to the value of the axial component  $k_{\parallel}$  of the wave vector at the closest  $K$  ( $K'$ ) point of the graphene dispersion (see Sec. I-2.3).<sup>f</sup>The resulting four singlet excitons are  $|1u\rangle$ ,  $|1g\rangle$ , and  $|\pm K K'\rangle$  as shown in Fig. II.8.b.

### Bright and dark excitons

Two singlet states  $|1u\rangle$  and  $|1g\rangle$ , with band edge at zero center of mass momentum, combine one electron and one hole from the same  $K$  ( $K'$ ) valley, and the spin state  $S = 0$  (Fig. II.8.b).  $|1u\rangle$  and  $|1g\rangle$  are antisymmetric ( $A_2$ ) and symmetric ( $A_1$ ), respectively, under the  $\pi$  ( $C'_2$ ) rotation around the  $C'_2$  direction perpendicular to the nanotube axis. The expression of these two states are:

$$|1u\rangle = \frac{1}{\sqrt{2}} \left( |\varphi_{e,-|q|}^+, \varphi_{h,+|q|}^- \rangle + |\varphi_{e,+|q|}^+, \varphi_{h,-|q|}^- \rangle \right) \quad (\text{II.17a})$$

$$|1g\rangle = \frac{1}{\sqrt{2}} \left( |\varphi_{e,-|q|}^+, \varphi_{h,+|q|}^- \rangle - |\varphi_{e,+|q|}^+, \varphi_{h,-|q|}^- \rangle \right), \quad (\text{II.17b})$$

where we omitted the cross-product with Hilbert space of the envelop function state  $|\phi^{\text{env}}\rangle$ , and  $|\varphi_{e,-|q|}^+, \varphi_{h,+|q|}^- \rangle$  is the mixed state of a conduction electron of subband  $+|q|$  and a valence hole of subband  $-|q|$ . Linear optical transitions are possible if the representation of the photon polarized excitation  $\Gamma_{ph}$  is included in the representation of

<sup>f</sup>Reference [43] addresses the excitons states in zig-zag and armchair nanotubes. In the latter case, the two electron and hole pairs are degenerated giving three zero-momentum singlet states including one with twofold degeneracy. In the former case, metallic nanotubes still shows exciton states but different states representations need to be considered.



the exciton state  $\Gamma_{\text{env}} \otimes \Gamma_e \otimes \Gamma_h$ . Considering that the Rydberg envelope function of the 1s-exciton ( $n_B = 1$ ) is even, the zero momentum exciton state  $|1u\rangle$  is odd under  $C'_2$  rotation and thus can couple to light (the dipole operator for polarization parallel to the nanotube axis transforms like a vector and is odd under  $C'_2$  rotation). On the contrary,  $|1g\rangle$  is even under  $C'_2$  rotation and cannot couple to parallel excitation light (assuming no symmetry breaking). Finally, light polarized parallel to the nanotube, for dipolar transitions, couples directly to the bright state  $|1u\rangle$  (or  $|B\rangle$ ), whereas the dark state  $|1g\rangle$  (or  $|D\rangle$ ) is dipole forbidden. The splitting between the bright and dark excitons ( $\delta_D$ ) varies to the leading term as  $1/d^2$ , and higher order terms only capture chirality dependency [78]. Experimental values in the range from 1 to 5 meV have been reported for nanotubes diameter between 0.8 and 1.3 nm at the  $S_{11}$  [79–81].<sup>g</sup> The presence of the dark exciton can have drastic consequence on the photoluminescence properties of carbon nanotubes if the energy splitting  $\delta_D$  is too important; in fact the exciton can relax and trap onto the dark state. However, the small value of  $\delta_D$  means that  $|1u\rangle$  and  $|1g\rangle$  are equally populated at room temperature, and its presence explains only partly the low quantum efficiency of nanotubes [81].<sup>h</sup> Recently, the dark state has been accounted for the bi-exponential PL decay that is observed in ‘environment-free’ (or clean) nanotubes [22, 82, 83].

### K-momentum dark states

The two other singlet states  $|\pm KK'\rangle$  show band edge at  $\mathbf{K}_{\text{exc}} = \pm 2k_{\parallel}$ , combine one electron from  $K$  ( $K'$ ) valley and one hole from  $K'$  ( $K$ ) valley, and the spin state is  $S = 0$  (Fig. II.8.b).<sup>i</sup> These states are energy-degenerated, carry opposite angular momentum, and their energy separation  $\delta_K$  with the bright state  $|1u\rangle$  is scaling as  $1/d^2$  [77]. They are both dark states, optically forbidden primarily due in chiral nanotubes to the non-conservation of optical wave vector [43]. Although linear optical absorption is forbidden, indirect processes such as phonon-assisted double resonance can possible take place. It involves the creation of an  $A_2$ -antisymmetric exciton to a virtual state above  $|1u\rangle$  and the coupling with a phonon (excitation of the lattice here) which fulfill wave vector and angular momentum conservation, i. e.  $\mathbf{K}_{\text{exc}} \pm k_{\text{phonon}} = \pm k_{\parallel}$  and  $E_{\text{exc}} - E_{\text{phonon}} = E_{\pm KK'}$ . The double resonance in which both a photon and a phonon are absorbed is less likely to occur since its probability is proportional to the probability to find a phonon  $n_{\text{phonon}}$ . On the contrary, the probability of absorbing a photon and creating a phonon scales as  $n_{\text{phonon}} + 1$ . The phonon-assisted absorption is addressed in details in Sec. IV–1.2.b.

### Higher-order Rydberg states

In the previous paragraph, only the fine structure of the lower lying Rydberg state ( $n_B =$

<sup>g</sup>The splitting  $\delta_D$  is measured using either Aharonov-Bohn effect that brighten the dark exciton  $|1g\rangle$  when a magnetic field is applied parallel to the nanotube [79, 80], or the temperature evolution of the PL intensity showing a drastic drop below few tens of kelvins that attests exciton trapping by the dark exciton state [81].

<sup>h</sup>The role of triplet states remains an open question.

<sup>i</sup>In the case of zig-zag nanotubes,  $|\pm KK'\rangle$  merge in one twofold degenerated state with zone edge at the  $\mathbf{K}_{\text{exc}} = 0$ .



1 and 1s-like) have been discussed since it carries the major part of the oscillator strength. However, in certain situations, the higher order Rydberg states are important, hence a more complete band structure is sketched in Fig. II.7.c where we omitted the dark states  $|KK'\rangle$ . It is clear that light can probe exciton states with both zero center of mass momentum and odd under  $C'_2$  rotation (we are still in the case of chiral nanotubes). The dipolar transition to the  $|1u\rangle$  state of the first Rydberg state dominates the absorption spectrum, whereas the second Rydberg state ( $n_B = 2$ ) shows  $p$ -like envelop function which implies that the bright and dark states are reversed.<sup>j</sup>

These excited exciton states ( $|1u\rangle$  is also called ground exciton state) have been observed experimentally with PLE in small diameter SWNTs [15, 72] and discussed theoretically for resonances  $S_{11}$  &  $S_{22}$  [73, 74]. Their amplitudes and energy positions depend on: the transition order  $E_{ii}$ , the nanotube diameter and chiral angle. They can be distinguished from phonon-assisted absorption from their different temperature behavior [72]. Experimentally, Lefebvre et al. resolved the first excited exciton state ( $|1g\rangle$ ) and the edge of the continuum of states (energy region where the exciton dissociate into a free electron and hole) [15, 72]. These states are expected to behave differently for higher-order energy transitions.

### II-2.2.c Exciton properties

Although many papers have been reported on the subject, I discuss here a limited number of works relevant for the purpose of this thesis. In particular, after presenting the two historical experiments that first observed excitons, I concentrate on the description of exciton properties: binding energy, size, lifetime, and oscillator strength. Particular attention will be given to the higher order energy transitions  $S_{ii}$  ( $i \geq 3$ ) and to the effects of the dielectric environment.

#### Binding energy $S_{11}$ and bandgap

The exciton binding energy of transition  $S_{11}$  (or bandgap) was measured experimentally by two groups in 2005 by means of two-photon absorption technique [17, 21]. The principle of the method is sketched in Fig. II.7.d. The two excitation photons, forming an even state, create an exciton in the  $|2p\rangle$  state which relax non-radiatively to the  $|1u\rangle$  state from which PL signal is measured. In fact, the energy difference between the impinging and detected photon energies  $E^{2g} - E^{1u}$  provides a lower limit for the exciton binding energy  $E_{\text{exc}}$ . Wang et al. measured  $E_{\text{exc}} \approx 420$  meV for nanotubes with diameter 1.8 nm, which corresponds to a third of the bandgap (PL signal with energy 1.3 eV) [21]. Maultzch et al. reported slightly smaller values of 325 meV and 240 meV for nanotubes (6,4) ( $d = 0.68$  nm) and (7,5) ( $d = 0.82$  nm), respectively. These values are very important in comparison to the typical binding energy recorded for other bulk semiconducting materials ( $\leq 100$  meV) [42]. However, the single-particle model gives a bandgap around 0.9 eV in this diameter range, and the self energy  $E_{e-e}$  is about 700 – 800 meV, meaning

---

<sup>j</sup>This is exactly done by changing  $|1u\rangle \rightarrow |2g\rangle$  and  $|1g\rangle \rightarrow |2u\rangle$  in (II.17), and substituting the electron and hole wavefunctions.

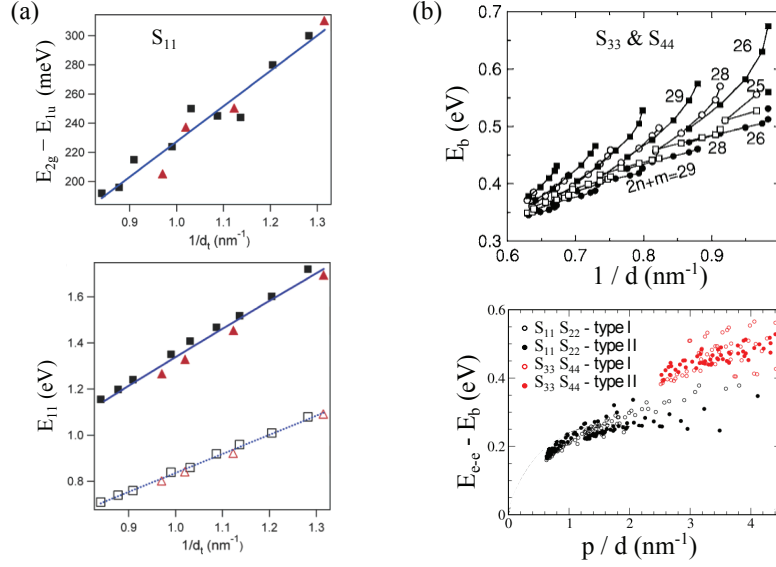


**Figure II.9:** Diameter dependency of exciton binding energy in semiconducting single-wall carbon nanotubes. (a) Binding energy (top panel) and bandgap energy (bottom) measured by Dukovic et al. using two-photon absorption [13]. Open symbols are results from single particle model for comparison. (b) Binding energy (top) for transitions  $S_{33}$  and  $S_{44}$  calculated in refs. [84, 85]. (bottom) Difference between binding and self energy corresponding to the overall energy blueshift (with respect to the single particle Van-Hove singularity) when including many-body interactions. The different nature of lower ( $S_{11}$ ,  $S_{22}$ ) and higher ( $S_{33}$ ,  $S_{44}$ ) is clearly visible on this figure.

that the exciton band is about 350 meV above the single-particle band [44].

After the observation of the ratio problem in 2002 and besides the historical experiments reported above, many theoretical studies tried to describe the optical properties of carbon nanotubes with respect to their structure by including many-body effects [66, 69, 70, 78]. Perebeinos et al. proposed the following expression for the binding energy:

$$E_b = A_b d^{\alpha-2} m_{\text{eff}}^{\alpha-1} \varepsilon_m^{-\alpha}, \quad (\text{II.18})$$

where  $A_b$  and  $\alpha$  are empirical parameters,  $\varepsilon_m$  is the effective dielectric constant in the nanotube's vicinity, and  $m_{\text{eff}}$  the effective mass that depends on the tube chirality [66]. The latter is expressed by  $m_{\text{eff}} = 2\pi\hbar/2\|\mathbf{C}\|v_F$  [38]. Assuming that the Fermi velocity is identical for all nanotubes,  $m_{\text{eff}}$  is inversely proportional to the diameter, . However, recent Rayleigh scattering experiments showed that  $v_F$  depends on the diameter and the energy transition  $S_{ii}$  [16]. Sticking to our first approximation, (II.18) reads  $E_b \propto 1/d\varepsilon_m^{-\alpha}$ . This scaling relation was verified in two experiments: two-photon absorption [13], and Raman spectroscopy [86]. The results of the former are reported in Fig. II.9.a, and show that both the binding energy ( $\approx E_{2g} - E_{1u}$ ) and the bandgap energy

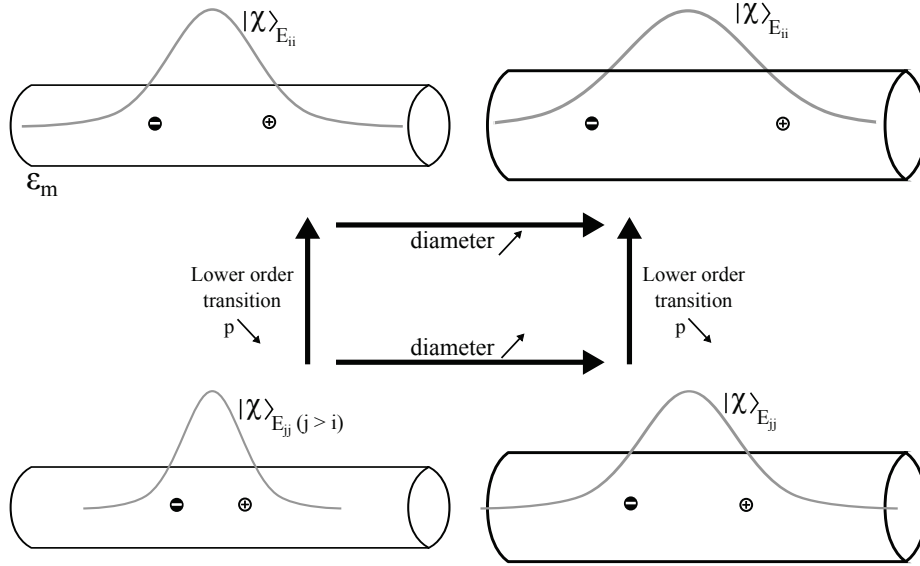


**Figure II.10:** Sketch of the exciton size evolution with diameter and energy transition. The exciton wavefunction  $|\chi\rangle$  is represented in real space by the grey Gaussian-like profile (for the lower lying exciton states with  $n_B = 1$ ) for different resonance  $S_{ii}$  [68]. The strength of Coulomb interactions (binding) is schematized by the tick-ness of the dashed lines. Exciton size  $l_\chi$  is measured at FWHM of  $|\chi\rangle$ . It decreases for smaller nanotube diameter and higher energy transitions.  $\epsilon_m$  is the dielectric constant of the environment in which the nanotube is embedded.

are inversely proportional to the nanotubes diameter (for constant environment). In the 0.8 to 1.3 nm diameter range,  $E_b$  varies from  $\sim 300$  meV down to 200 meV, and the bandgap reduces from 1.7 to 1.2 eV. In comparison to early single particle model (open symbols) [34], the bandgap broadens by more than 400 meV. Hence, again, many-body effects are important for the description of optical properties of carbon nanotubes.

More advanced models include both diameter and chiral angle. In particular, Capaz et al. propose a detailed description of the exciton properties in chiral nanotubes for transitions  $E_{11}$  and  $E_{22}$  [78]. In this case, the binding energy yields<sup>k</sup>

$$E_b = \frac{A}{d} + \frac{B + (-1)^\nu \cos 3\theta_c}{d^2} + D \frac{\cos^2 3\theta_c}{d^3}. \quad (\text{II.19})$$

The first term describe the main diameter dependency and agree with (II.18). The second term and third terms capture the chirality dependence, and the resulting  $E_b$  show the family pattern observed in the Kataura plot. The previous expression of  $E_b$  follow the same scaling law with respect to  $\epsilon_m$  as reported in (II.18) (with  $\alpha = 1.4$ ).

Exciton binding energy for higher transitions  $S_{ii}$  ( $i \geq 2$ ) is more difficult to access experimentally. Recently, scanning tunnelling spectroscopy yield binding energies of 400

<sup>k</sup>Values of parameters

meV and 700 meV for 1.4 nm tubes [87]. Although these descriptions of the binding energy and bandgap energy give a fairly good agreement with experiments for the  $S_{11}$  and  $S_{22}$  exciton transitions, further corrections are required in order to describe the nature of excitons for the higher order transitions ( $p \geq 3$ ).

### Excitons for $S_{33}$ and $S_{44}$ transitions

Early Raman and Rayleigh experiments studied the third and fourth optical transitions in semiconducting nanotubes which show different behavior from the  $S_{11}$  and  $S_{22}$  [20, 88, 89]. They suggest that either these transitions are not excitonic in nature but rather involve the creation of electron-hole pairs, or that they have a weak exciton binding energy. To reach this conclusion, the energy transitions of identified nanotubes are compared to the  $E_{ii}$  computed from the non-orthogonal tight-binding model and including the correction given by Kane et al. [44, 64], i. e. data of  $E_{ii,exp}$  are compared to <sup>1</sup>

$$E_{ii,SP} + 0.67 \frac{2p}{3d} \ln \left( \frac{6d}{2p} \right). \quad (\text{II.20})$$

For the first and second transitions in semiconducting CNTs, this relation is very well verified [13, 88]. In contrast,  $S_{33}$  and  $S_{44}$ , for diameter between 1.5 and 2.5 nm, clearly show a deviation from (II.20). More strikingly, Michel et al. demonstrated that a rigid shift (identical for all chirality) of  $\sim 0.43$  eV exactly describes this difference, i. e.  $E_{ii,exp} = E_{ii,SP} + 0.43(\text{eV})$  for  $i = 3, 4$ . The different scaling law between lower and higher order energy transitions is explained in terms of many body effects [85, 90]. These theoretical works, as well as more recent ones [73], agree that  $S_{33}$  and  $S_{44}$  are of excitonic nature, with binding energies larger than those of the first and second transitions in semiconducting nanotubes.

The debate concerning the photophysics of higher-order optical transitions (as well as the metallic transitions that are addressed later) is of particular importance for applications since these transitions lie in the visible for nanotubes ( $d \sim 1.5 - 3$  nm) synthesized in regular conditions of growth. The excitonic nature of higher transitions were recently confirmed experimentally by resonant Raman scattering [91] and Rayleigh scattering [10] investigations. Berciaud et al. carried out Rayleigh scattering experiments on individual free-standing SWNTs at optical frequencies where they observed  $S_{33}$  and  $S_{44}$  [10]. The scattering profile of each transition fits very well with an exciton model, whereas band-to-band model (free carriers) fails to reproduce the profile. However, transitions linewidths reach up to 80 meV which is two times broader than the values reported for  $S_{11}$  in the same conditions [92]. The linewidths are consistent with time-resolved spectroscopy measurements which observed a very fast relaxation time (few femtosecond) of excitons from the upper transitions [93, 94]. This characteristic can be understood as the coupling of the bright states to lower continuum of states.

In this work absorption spectroscopy in similar conditions as Rayleigh experiments show that energy transitions up to  $S_{77}$  seem to keep their excitonic nature, but with a

<sup>1</sup>The first term  $E_{ii,SP}$  can be found in Fig. II.5.

linewidth broadening trend for the higher-order resonances (see Chap. IV).

One of the few theoretical works addressing the transitions  $S_{33}$  and  $S_{44}$  shows that their binding energy are greater than those of the first and second transitions in semiconducting nanotubes [85]. As shown in Fig. II.9.b,  $E_b$  decreases from  $\sim 500$  meV to  $\sim 350$  meV for diameters in the range 1 to 1.5 nm. Moreover,  $E_b$  presents a similar pattern as in the Kataura plot resulting from trigonal warping effects. More importantly, Sato et al. investigated the energy difference between  $S_{ii}$  (accessible with direct absorption) and  $S_{ii,SP}$  (computed in the single particle model) which presents a clear difference of scaling law between lower and higher orders energy transitions.

In summary, excitonic nature of higher order transitions in semiconducting nanotubes has been confirmed with bigger exciton binding energy in comparison to lower energy transitions ( $S_{11}$ ,  $S_{22}$ ). On the other hand, the broadening of the absorption resonances suggest smaller exciton lifetime.

### Excitons in metallic nanotubes

The question that remains: do metallic energy transitions  $M_{ii}$  model as excitons or band-to-band transitions? In bulk metallic materials, the free carrier screening of the Coulomb potential prevent the formation of a pair electron-hole. This situation is quite different in CNTs due to their one-dimensional geometry and the formation of excitons is predicted by theory [67, 73]. The studies using photoluminescence, which has been widely used for optical characterization of CNTs, are restricted to semiconducting entities. For this reason, the first observation of exciton in metallic nanotubes was reported not before 2007 by Wang et al. [95]. They measured the absorption of a (21,21) armchair nanotube using spatial modulation spectroscopy. The observed  $M_{22}$  transition (due to its armchair nature, no splitting was observed) is optimally fitted by including: a constant background, a Lorentzian (exciton peak with FWHM of about 100 meV), and an approximated continuum profile (account for the high-energy asymmetry of the exciton peak). The difference between the exciton peak central position and the onset of the continuum gives an estimate of the binding energy, and the measured value of  $\sim 50$  meV confirms the weakening of Coulomb interactions in metallic tubes (free carrier screening is orders of magnitude weaker than in bulk). Still, the observation of exciton in a metallic material underline again the unique photophysics occurring in 1D systems.<sup>m</sup>

### Exciton size and oscillator strength

To complete this section on the properties of exciton in CNTs, we focus on their spatial expansion and their oscillator strength  $f_C$ . Exciton size  $l_\chi$  directly affects observable quantities such as the exciton oscillator strength and the radiative lifetime. In 1D materials  $f_C$  is inversely proportional to  $l_\chi$ , and  $l_\chi \propto d$  is expected to the first order approximation (additional correction accounting for the chirality are discussed in refs. [66, 78, 96]), and the lifetime is directly related to the inverse of  $f_C$ . For instance,

---

<sup>m</sup>Exciton in metallic nanotubes were also investigated by means of Rayleigh scattering (see ref. [10] for details).

Capaz et al. calculated exciton sizes between  $\sim 1$  and  $2$  nm for diameters range  $0.5$ - $1.0$  nm [78], and gave a good estimate ( $l_\chi \sim 1$  nm) of the value  $l_\chi = 2.0 \pm 0.7$  nm measured in ref. [68]. Moreover, Nugraha et al. proposed an advanced model for the study of exciton transitions (Kataura plot) including transition-dependent exciton size and environmental dielectric screening [70].<sup>a</sup> Recently, Choi et al. derived an explicit formula for  $f_C$  applicable to relatively large diameter semiconducting nanotubes [96]. The oscillator strength per atom of the  $|1u\rangle$  singlet exciton then reads

$$\frac{f_C}{N_a} = \frac{G(1 + J\xi \cos(3\theta_c)p/d)}{(p + Q)d}, \text{ and} \quad (\text{II.21a})$$

$$l_\chi \sim d(1 + Q/p), \quad (\text{II.21b})$$

where  $N_a$  is the Avogadro's number,  $G = 0.29$  nm,  $J = 0.047$  nm,  $Q = 7.5$ , and  $\xi = (-1)^{\text{mod}(n-m,3)+2p/3+\text{mod}(p,3)/3}$ . The FWHM of the exciton wavefunction in real space scales as  $d/p$  (Fig. II.10). The Coulomb potential is stronger for both high-order energy transitions and larger tubes. However, to a first approximation (not considering chirality),  $f_C$  increases for both small  $d$  and lower transitions  $p$ , i.e. the oscillator strength is damped as the electron-hole Coulomb interaction is enhanced [70, 96]. Chirality is accounted by the second term between brackets in (II.21), and we will see later that the only scaling relation  $f_C \propto d^{-1}p^{-1}$  is not sufficient to describe the evolution of  $f_C$  in SWNTs (see for instance Sec. IV-1.4).

## II-3 State-of-the-art

In the two previous sections, we discussed the processes involved in the absorption of carbon nanotubes. In this part, at first, we draw a more detailed description of the experimental techniques which have been developed for addressing the photo-physics of CNTs. Then, some comments are made on the different Kataura plots which have been proposed in the literature. Finally, we present the state-of-the-art of the absorption spectroscopy of carbon nanotubes and comment on the results reported in the literature.

### II-3.1 Potpourri of spectroscopy techniques

From the beginning of the 21st century, many research groups put a lot of effort towards the understanding of the carbon nanotubes photo-physics. Their exceptional electrical and optical properties made them candidates for applications in optoelectronics. Optical spectroscopy techniques developed in the last decade first aimed at providing fast methods for structural characterization of CNTs. It appeared that the photo-physics of these one-dimensional materials is extremely rich for both fundamental physics and applications. Nowadays, several research groups have developed various approaches for the characterization of the optical properties of nanotubes: photoluminescence spectroscopy, Raman scattering, (resonant) Rayleigh scattering, photocurrent, absorption spectroscopy, and other derived methods (e.g. transient absorption and PL dynamics).

<sup>a</sup>These affects are included in the Bethe-Salpeter scheme through the variable  $\kappa$  in (II.12).



### Photoluminescence

Photoluminescence (PL) and PL excitation (PLE) provide fast and accurate characterization of the structure of ensemble and individual semiconducting carbon nanotubes. This method of choice was applied as early as in 2002 by Bachilo et al. who obtained the first so-called PLE map (see Fig. II.6.a) which allows the identification of nanotube chirality. As PL (resp. PLE) probes the emission (resp. absorption) of energy transition  $S_{11}$  (resp.  $S_{22}$ ), each peak in the PLE map can be associated with a single chirality in the Kataura plot. This method has been applied to measurements on nanotube ensembles [59, 63] as well as studies at the single nanotube level [15, 97]. Two of the main breakthroughs obtained with PL are: the first experimental Kataura plot [59], the first observation of polarization effects ( $S_{ii}$  vs.  $S_{ij}$ ) [15]. Nowadays, this method is widely used for fast characterization of sorted/individualized semiconducting nanotubes in solution or matrix. The main drawbacks of the technique are: its limitation to relatively small diameter semiconducting tubes, probing of  $S_{11}$  and  $S_{22}$  only, as well as constraints on the choice of the dielectric environment.

### (Resonant) Raman scattering

Raman scattering is of particular interest for the structural characterization of carbon nanotubes. The tangential phonon modes (LO and TO phonons) associated with in-plane vibrations of the carbon atoms (similar to the phonon modes in graphene) provide information on the nature of the tubes: semiconducting vs. metallic, ensemble vs. individual, single walled vs. multi-wall. The single radial breathing mode (RBM) of a SWNT, associated with periodic expansion/contraction of its cross-section, is inversely proportional to its diameter. It is observable only for laser excitation energy close to one the nanotube resonances: so-called resonance condition. In other words, the RBM and tangential modes amplitudes dependent directly on the absorption response of nanotubes, i.e. on the position of the energy transitions. In summary, resonant Raman spectroscopy (RRS) gives information on the nature, diameter, and absorption of the nanotubes. A large number of reviews and textbooks discuss this technique in detail [33, 98, 99]. This method is a fast characterization tool well adapted to carbon nanotubes in all environments. Conversely to photoluminescence, RRS is well adapted to the study of the optical properties of metallic nanotubes [62, 100, 101]. However, with few laser excitations available, one is limited to the identification of nanotubes fulfilling the resonance condition (i.e. one  $E_{ii}$  should lie close to  $E_{\text{exc}}$ ), and exact chirality identification is difficult generally.

### Rayleigh scattering

Rayleigh scattering is a method of choice (bright and fast) to study the photo-physics of individual nanotubes.<sup>o</sup> Rayleigh scattering (small particle limit to the Mie scattering) is proportional to  $\omega^3 |\chi(\omega)|^2$ , where absorption probes only the imaginary part of the susceptibility  $\text{Im}(\chi(\omega))$ . Using a continuum or white source, one can obtain a large band spectrum which shows, as in absorption spectroscopy, excitonic resonances.

---

<sup>o</sup>Rayleigh scattering has been developed in Tony Heinz's group around 2004

Some important results have been recently obtained with this method: an experimental Kataura plot for relatively large diameter tubes [16], quantitative estimation of the diffusion and absorption cross-sections [14], and insights in the photo-physics of excitons and carriers [10, 16]. However, these studies are limited to individual nanotubes either freely-suspended or specially prepared on transparent substrates.

### Photocurrent

Recently, different studies combined the unique optical and electrical properties of carbon nanotubes to fabricate opto-electronics devices. The possibility to probe the two characteristics at the same time as well as their inter-dependence is a very active and exciting research field [7]. The first nanotube based p-n junction was fabricated in 2004 [102]. In the past five years many papers focus on such devices. In particular, two studies focused on the photo-current effects in individual nanotubes to probe their absorption properties [55, 56]. The main limitation of this method concerns the device fabrication which includes many processes that can deteriorate/alter the nanotubes optical properties.

## II-3.2 Absorption spectroscopy

All the techniques reported in the previous paragraph are able to probe some of the absorption characteristics of CNTs. However, direct investigation of the absorption properties of nanotubes is desirable in order to directly probe light-matter interaction mechanisms involved in this process. At the beginning of this thesis, a few papers reported absorption measurements on CNT ensembles [41, 48, 103], while only two studies had been carried out on individual nanotubes [22, 95]. Nevertheless, they did not provide quantitative measurements of the absorption cross-section ( $C_{\text{abs}}$ ). The small magnitude of  $C_{\text{abs}}$  in CNTs has been the main difficulty to address in this type of measurement carried out at the single nanotube level. Such study requires structural identification of each nanotube investigated, as well as the control of its environment.

### II-3.2.a A deeper insight on Kataura plot(s)

The Kataura plot is fundamental for the study of the optical properties of carbon nanotubes. As already explained, it allows the structural assignment of CNTs based on their absorption properties [41]. However, as demonstrated in this thesis, absorption characteristics, in particular the positions of the energy transitions  $E_{ii}$ , depend on the tubes environment. In other words, several types of experiment coupled with theoretical studies have proposed different empirical Kataura plots (Fig. II.11):

- Popov calculated the optical energy transitions of SWNTs within the non-orthogonal tight-binding model which includes curvature effects (see also Fig. II.5). The many-body effects are introduced by applying rigid energy shifts to the calculated  $E_{ii}$ . The shifts  $\Delta E_{ii}$  have been determined independently for each resonance order using Raman spectroscopy of structure-identified individual freely suspended SWNTs [18, 19, 89]:  $\Delta E_{ii} = 0.35$  eV for  $p = 1, 2, 3$ , and  $\Delta E_{ii} = 0.43$  eV for  $p \geq 4$ ,



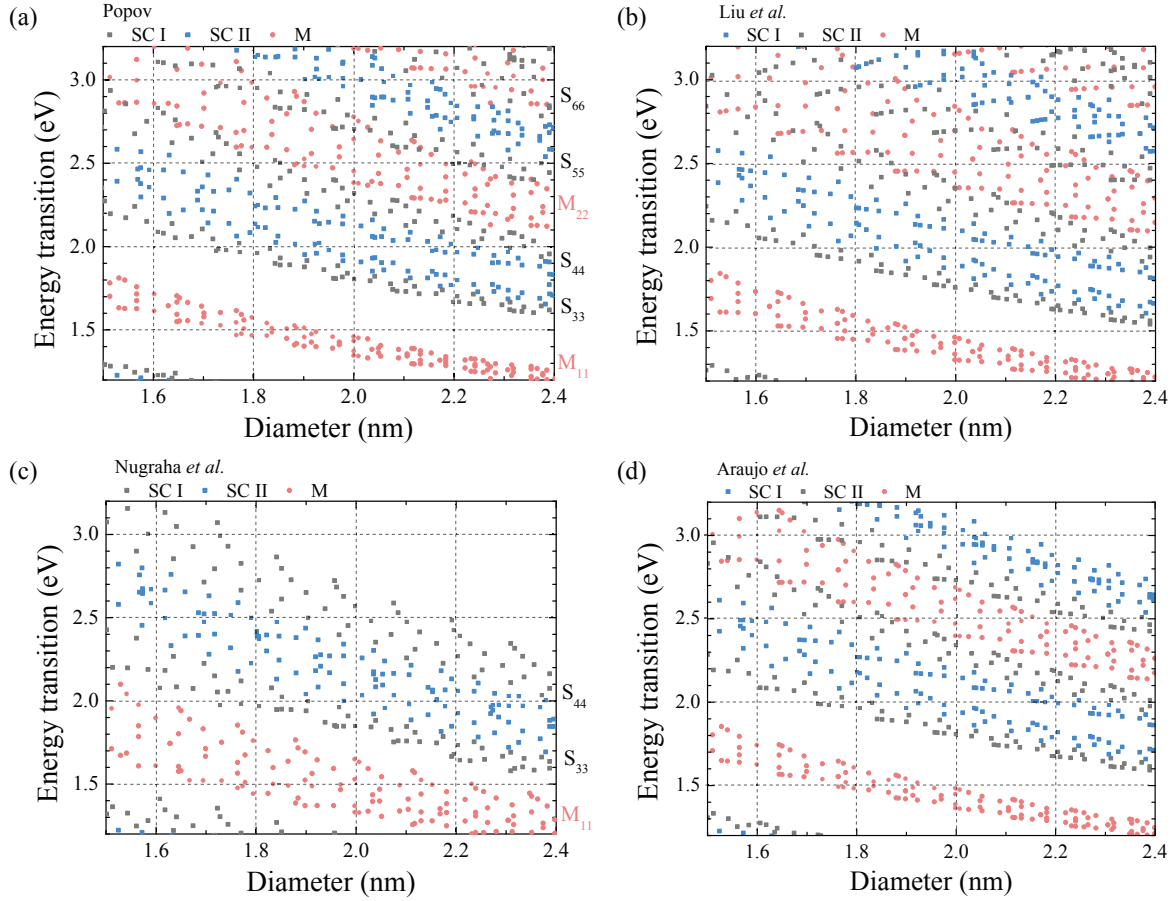


**Figure II.11:** Presentation of different experimental and theoretical Kataura plots. (a) Calculated energy transitions obtained from the non-orthogonal tight-binding model (Popov [44]) including experimental corrections to account for many-body effects [89]. (b) Empirical model obtained from Rayleigh scattering and photoluminescence experiments on structure-identified nanotubes [16, 59]. (c) Theoretical study including many-body interactions for vertically-grown (super-growth) nanotubes [70]. (d) Analytical model derived from Raman scattering experiments [88].

with an uncertainty of the order of 100 meV. This method is applied latter in this thesis to assign the chirality of nanotubes from Raman and absorption measurements.

- Araujo et al. performed an extended Raman study of carbon nanotubes from which they derived an analytic formula for the energy transitions [88]:

$$E_{ii}(p, d, \theta_c) = \frac{p}{d} \left( A + B \log \frac{C}{p/d} \right) + \beta_p \cos(3\theta_c/d^2), \quad (\text{II.22})$$

with  $A = 1.074$  ( $p < 4$ ) or  $1.133$  ( $p \geq 4$ ),  $B = 0.502$ ,  $C = 0.812$ , and  $\beta_p$  takes different values for each  $E_{ii}$  and each family (cf. ref. [88] for the list  $\beta_p$  values).

- Later, Nugraha et al. calculated the optical energy transitions by solving the Bethe-Salpeter equation within the extended tight-binding ETB model. The latter includes curvature and many-body effects [70]. In this study, modified Coulomb potentials consider environmental effects.
- Recently, Liu et al. proposed an empirical formula for the energy transitions obtained from Rayleigh and fluorescence measurements on SWNTs [16, 59, 64]:

$$E_{ii}(p, d, \theta_c) = 2\hbar v_F(p) \frac{2p}{3d} + \beta \left( \frac{2p}{3d} \right)^2 + \nu(p) \cos(3\theta_c) \left( \frac{2p}{3d} \right)^2, \quad (\text{II.23})$$

where the Fermi velocity  $v_F(p)$ , as well as the parameters  $\beta$  and  $\nu(p)$ , are given in ref. [16]. In this equation, the different terms are associated with contributions of: the linear dispersion in the  $K$ -valleys, deviations from the linear dispersion away from the center of the valleys, trigonal warping effects.

The differences between the different Kataura plots are attributed mainly to both the sample preparation methods (HiPco, CoMoCat, CVD-grown, ...) and the tubes environment (pristine, surfactant, substrate, ...). Kataura plots from Popov, Liu et al. , and Araujo et al. (Figs. II.11.a,b,d) are in good agreement within  $\sim 100$  meV, in the diameter range 1.5-2.5 nm. Only the calculated optical energy transitions from Nugraha et al. show more dispersed results (Fig. II.11.c). In the latter case, energy shifts are introduced specifically to each type of sample and environments.

As a matter of fact, most of the tubes investigated in this thesis have been synthesized using the process described in Sec. III-1.2. This type of sample, in the same environment (freely suspended), have been studied by at least three research groups with either electron diffraction/Raman scattering [18, 104, 105] or Rayleigh/Raman spectroscopy [10, 11]. Taking into account all these measurements, the RBM *vs.* diameter relationship

$$\omega_{\text{RBM}} = \frac{204}{d} + 27 \quad (\text{II.24})$$

has been established ( $\omega_{\text{RBM}}$  and  $d$  are in  $\text{cm}^{-1}$  and nm, respectively).<sup>P</sup> Moreover, these results tend to say that the Kataura plot from V. Popov (Fig. II.11.a) is better adapted for our samples.

### II-3.2.b Absolute absorption cross-section

In the following table (Tab. II.1), we list the experimental values of absorption cross-section reported in the literature: The disparity between the values of  $C_{\text{abs}}$  is explained by the dispersion of the samples (synthesis and preparation method, environment, ...) and the measurement techniques (ensemble *vs.* individual nanotube study, indirect *vs.* direct measures). Only the two last studies provide direct access to the absolute absorption

<sup>P</sup>The estimated overall uncertainty, including spectrometer error and deviation from the law (II.24), is about  $3 \text{ cm}^{-1}$ .

1 <sup>st</sup> author (year)	$C_{\text{abs}} (\times 10^{-17})$ $\text{cm}^2/\text{C-atom}$	Type	Sample	$E_{\text{ii}}$	Method(s)
Islam (2004) [48]	0.08	Ensemble	HiPCO in gel $d \approx 1.35$ nm	$S_{22}$	Polarized absorption measurements
Zheng (2004) [103]	0.7	Ensemble	CoMOCAT DNA-suspended (6,5)-enriched	$S_{11}$	Absorption measurements
Berciaud (2008) [22]	$1 \pm 0.3$	Individual	HiPCO in gel (6,5)	$S_{22}$	Luminescence decay (indirect)
Joh (2011) [14]	$\approx 2.5$	Individual	CVD on quartz + glycerol $d \approx 1\text{-}2$ nm	$S_{33}$ $M_{11}$	Rayleigh scattering
Wang (2011) [23]	0.8 (// pol.) 0.2 ( $\perp$ pol.)	Individual	HiPCO in polymer $d \approx 1$ nm	$M_{11}$ $S_{22}$	Thermal conductance + heat transfer model (indirect)
Schöppler (2011) [106]	$1.7 \pm 0.4$	Ensemble	DNA-suspended (6,5)-sorted	$S_{11}$	Absorption Fluorescence labeling + AFM (tube concentration)
Christofilos (2012) [12]	1.8 (// pol.)	Individual	(18,5) deposited on Si/SiO <sub>2</sub> substrate	$S_{33}$	Sample spatial modulation (direct)
Oudjedi (2013) [107]	$3.2 \pm 0.5$	Individual	(6,5) in gel	$S_{22}$	Berm spatial modulation (direct)

**Table II.1:** State-of-the-art of the absorption cross-section of single-wall carbon nanotubes

cross-section of nanotubes, both are based on spatial modulation spectroscopy. The other techniques either assess  $C_{\text{abs}}$  indirectly (indirect measurements at the single tube level) or suffer from averaging effects (or are limited to (6,5)-sorted nanotubes).

A few other approaches to assess the absolute absorption cross-section of SWNTs have been introduced during the 5<sup>th</sup> Workshop on Nanotube Optics and Nanospectroscopy (WONTON'13, Santa Fe (NM), US, June 16–20, 2013) which took place about the end of my thesis. Here I provide a partial record of the techniques presented at the workshop (in addition to spatial modulation spectroscopy). The team of C. Voisin at the ENS Paris, has been putting efforts in assessing the properties of nanotube/porphyrin compounds, i. e. enriched HiPCO nanotubes (diameters in the range  $\sim 0.8\text{-}1.2$  nm) individualized and wrapped in molecules of porphyrin. The absorption cross-section of porphyrin and the efficiency of energy transfer into the nanotube are known parameters [108]. Photoluminescence excitation spectroscopy is used to evaluate the ratio between the PL emission while exciting the energy transfer resonance or the intrinsic  $S_{22}$  transition. Then, both

the dependence on the PL quantum yield and on the species concentration can be eliminated providing access to  $C_{\text{abs}}$  of each species [109]. As a result,  $C_{\text{abs}}$  in the range  $1.7 - 3.7 \times 10^{-17} \text{ cm}^2/\text{C atom}$  are obtained with strong dependency on the nanotube family and chiral angle (parameter  $\nu \cos(3\theta_c)$ ). These results are in good agreement with recent theoretical works [74, 110].

A second method has been developed in the group of R. B. Weisman at the Rice University. HiPCO nanotubes (diameter around 1 nm) are sorted and individualized in solution, then they are transferred into a micro-channel where they are counted down using near-IR fluorescence microscopy. Thereafter, providing the concentration of nanotubes in the micro-channel, absorption measurements yield  $C_{\text{abs}}$  for a single tube chirality [111]. Typical values of absorption cross-section fall in the range  $0.5 - 2.5 \times 10^{-17} \text{ cm}^2/\text{C atom}$  for  $S_{11}$  and  $S_{22}$  resonances, with again strong chirality variations (diameter, family, chiral angle).

New measurements of  $C_{\text{abs}}$  on free-standing SWNTs (around 2 nm) have been reported by the group of F. Wang in Berkeley University. However, no clear statements both on the technique and the results have been made during the workshop [112]. These results have been reported somehow in a recent theoretical paper providing an analytic formula for the exciton oscillator strength in nanotubes [96].

Having discussed the different measurements of the absorption cross-section reported in the literature, I will present the experimental methods and the results of this thesis in the next chapters. The reader will be encouraged to compare the values of  $C_{\text{abs}}$  summarized in Tab. II.1 with our results reported in Chap. IV and Chap. V.



## **Part 2**

### **Absorption spectroscopy**



# Experimental methods III

---

*In the first section of this chapter, I introduce the samples that will be studied by means of absorption spectroscopy in Chaps. IV and V. I describe the growth techniques which employed for synthesizing individual carbon nanotubes on substrates (silicon and quartz), as well as freely suspended across trenches. In the second part I discuss the experimental methods which have been developed to provide direct access to the absorption cross-section  $C_{\text{abs}}$  of individual carbon nanotubes placed in different environments. The procedure to extract  $C_{\text{abs}}$  from the raw signal is described in detail.*

*Throughout this chapter, some samples are characterized with techniques such as atomic force microscopy, transmission or scanning electron microscopy. Furthermore, our optical techniques are applied to the imaging of these samples based on their absorption properties.*

## III–1 Sample description

In this section, I give an overview of the samples that have been investigated by means of (reflective) spatial modulation spectroscopy (RSMS and SMS). I introduce the method of chemical vapor deposition used for the growth of individualized carbon nanotubes either supported on substrates or freely suspended. The discussion is limited to sample imaging and preliminary characterization with different techniques (AFM, SEM, TEM). Eventually, few features of the CNTs are introduced, such as their diameters obtained via AFM. Complete characterization of the nanotubes is addressed in the main discussion of Chaps. IV and V.

We prepared and characterized the samples presented in Sec. III–1.1 (Q-3) at the Institut Lumière Matière. Parts of the experiments on the sample Si-4 were performed by D. Chrisofilos and J. Arvanitidis at the Aristotle University of Thessaloniki.

Synthesis and characterization (Raman spectroscopy, AFM, SEM, TEM) of the free-standing nanotube samples FS-1 & FS-2, presented in Sec. III–1.2.a, were performed by our coworkers:

- Dr. Matthieu Paillet, Huy Nam Tran, Prof. Ahmed-Azmi Zahab, and Prof. Jean-Louis Sauvajol – Université Montpellier 2 & CNRS, Laboratoire Charles Coulomb UMR 5221, F-34095, Montpellier, France.



- Dr. Xuan Tinh Than and Dr. Ngoc-Minh Phan – Laboratory of Carbon Nanomaterials, Institute of Materials Science, VAST, 100000 Hanoi, Vietnam.

### III–1.1 Carbon nanotubes deposited on substrates

#### III–1.1.a Preparation method

During my thesis, carbon nanotubes were synthesized using chemical vapour deposition (CVD). Fig. III.1 shows a schematic view of the method. Iron catalyst nanoparticles are deposited by dipping the substrate first into a solution of  $\text{Fe}(\text{NO}_3)_3$  in isopropanol and then into hexane, 10 s each. The nanotubes are grown in a tube furnace at  $900^\circ\text{C}$  for 10 min, while feedstock gases ( $\text{C}_2\text{H}_4$ ,  $\text{CH}_4$ ,  $\text{H}_2$ ) are flowing inside the tube. Density and size of the CNTs are determined by the density and size of the iron nanoparticles. The nanotubes tend to orientate preferentially in the direction of the gas flow.

CVD-grown carbon nanotubes present a good crystallinity, thus a small defect band in Raman, which is essential for spectroscopy. This synthesis method makes long CNTs, of several microns, which is crucial for the fabrication of free-standing nanotubes. Moreover, the SMS spectroscopy is performed far from the tubes' ends to eliminate possible tip effects on the absorption properties.

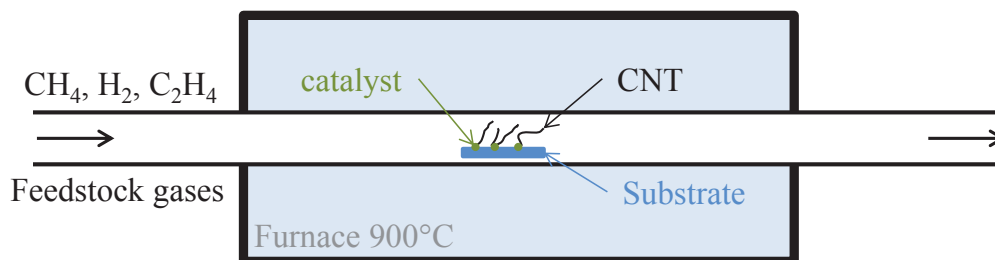


**Figure III.1:** Sketch of the carbon nanotube vapor deposition synthesis technique.

#### III–1.1.b Silicon substrate

The first experiments, that aimed at measuring the absolute absorption cross-section of individual CNTs, were performed on nanotubes grown on commercial degenerated silicon substrates with a 300 nm (or a 100 nm) thick  $\text{SiO}_2$  layer. Alignment markers were fabricated either by optical lithography and gold evaporation before the nanotube growth (Fig. III.20), or by means of silver paint post-growth (Fig. III.19).<sup>a</sup> Fig. III.2 shows an individual CNT grown on a Si/ $\text{SiO}_2$  (300 nm) substrate that was investigated by RSMS. The  $2\ \mu\text{m}$  long tube observed in AFM presents a diameter of  $1.6 \pm 0.1\ \text{nm}$ . Full optical characterization of this CNT (sample Si-4) is discussed in Sec. IV–3.1.

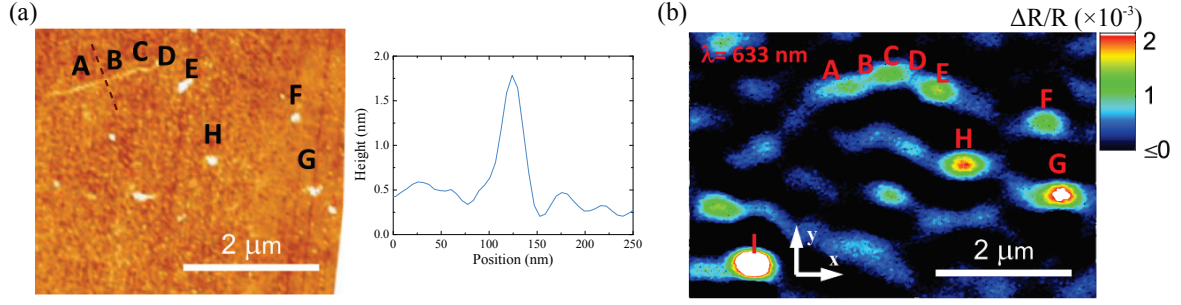


**Figure III.2:** Single-wall carbon nanotube grown on a silicon substrates with a 300 nm thick silicon dioxide layer (sample Si-4). (a-left panel) AFM surface rastering showing an isolated nanotube (A-D) and (a-right panel) height profile along the dashed line yielding a diameter  $d = 1.6 \pm 0.1 \text{ nm}$  for the nanotube. (b) RSMS imaging of the same substrate region.

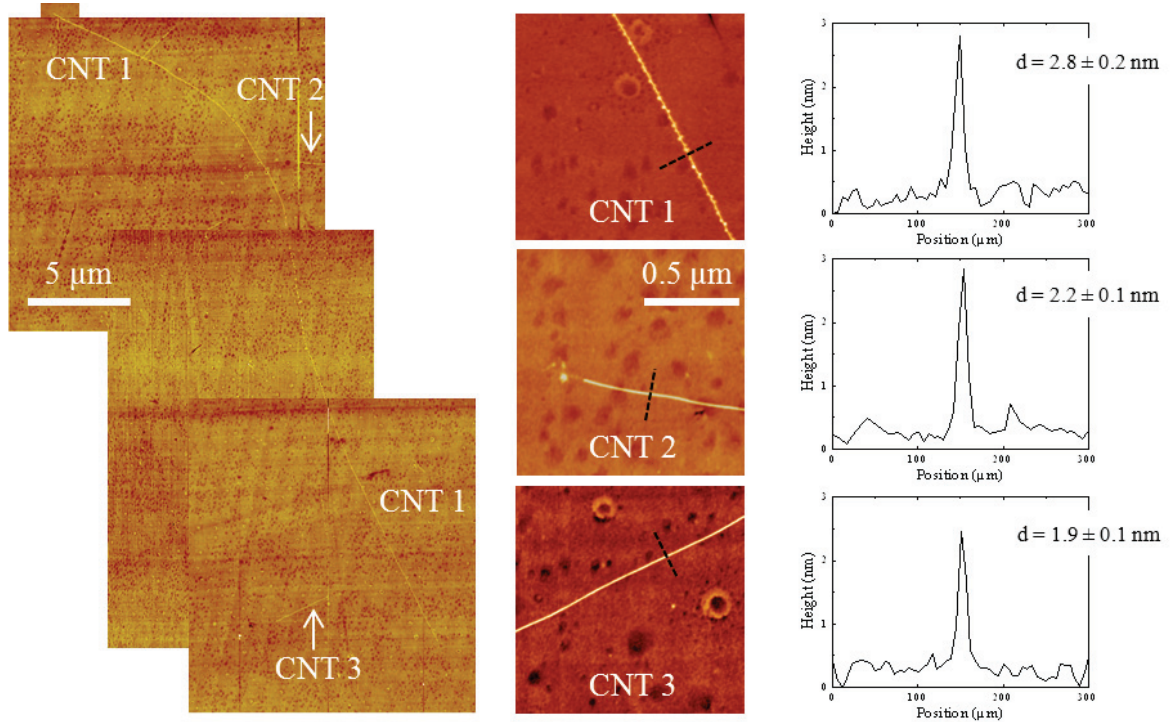


**Figure III.3:** AFM imaging of carbon nanotubes grown on a quartz ST-cut substrate (sample Q-3). Right panels show AFM profiles along the dashed lines.

### III-1.1.c Quartz substrate

The second batch of samples are CVD-grown carbon nanotubes on a quartz ST-cut substrate (sample Q-3, Fig. III.3). Properties of three nanotubes were investigated by SMS, AFM and Raman spectroscopy. Fig. III.3 shows AFM imaging of the samples,

<sup>a</sup>Dust particles are very useful for locating individualized nanotubes in large surface areas.

as well as height profiles measured along the dashed lines which estimate the CNTs diameters. CNT 1, with diameter  $2.8 \pm 0.2$  nm and length  $\sim 40$   $\mu$ m, was investigated only partially by absorption spectroscopy, but was the first to give a significant signal during the preliminary pump-probe experiments that I started during my thesis. The absorption properties of the two other nanotubes, CNT 2 and CNT 3, were investigated using SMS (see Sec. IV–3.3). They were further characterized by means of Raman and AFM: measured diameters for CNT 2 and CNT 3 are  $2.2 \pm 0.1$  nm and  $1.9 \pm 0.1$  nm, respectively.

The quartz substrates are transparent which is advantageous for the absorption measurements, whereas observation of RBM Raman line is challenging due to the presence of important signal originating from the substrate in the RBM frequency range. For this reason, and because of the relative accuracy of AFM measurements, the investigations of this kind of sample were not further pursued during the last year of my PhD.

## III–1.2 Free-standing carbon nanotubes

### III–1.2.a Environment-free carbon nanotubes

Carbon nanotubes optical properties are influenced by the environment in which they are embedded in (see refs. [97, 113, 114] and results for SWNTs/DWNTs in the next two chapters). To minimize these possible environmental effects, we chose also to investigate individual freely suspended nanotubes by means of absorption and Raman spectroscopy.

The suspended nanotubes were synthesized by chemical vapor deposition (CVD) on home-made Si/SiO<sub>2</sub> slit substrates using a method previously reported [115–117]. The catalyst consists of 5 Å Fe thin films deposited by thermal evaporation on Si/SiO<sub>2</sub> substrates. During the CVD, the catalyst substrates were put side by side with the slit substrates. The substrates were oriented with the catalyst side toward the gas inlet. The sample held in a quartz tube was kept outside the heated zone during temperature ramping of the furnace. Before heating, all gas lines and the reactor tube were purged by argon at a flow rate of 800 sccm for 30 minutes. Then the furnace was heated to 950°C or 1000°C at a ramping rate of 20°C/min. To carry ethanol to the furnace, Ar at a flow of 10 or 15 sccm was passed through a bubbler containing ethanol (kept at room temperature 25°C). When the temperature reached the synthesis temperature, argon was replaced by hydrogen and ethanol/argon at flow rates of 10 sccm or 15 sccm. After 5 minutes, the furnace was slid to the sample position to fast heat the sample and to grow CNTs. The synthesis durations were 30 minutes. After that, hydrogen and ethanol vapor were replaced by pure Ar at a flow rate of 30 sccm, the furnace was switched off and was slid to the initial position to fast cool the samples.

Figs. III.4 and III.5 present SEM and TEM images of samples FS-1 (trench  $\sim 100$   $\mu$ m, 100 nm thick SiO<sub>2</sub> layer) and FS-2 (trench  $\sim 20$   $\mu$ m), respectively. In the case of FS-1, freely suspended nanotubes appear as white ropes spanning the trench. SEM imaging is performed at low current and small zoom to avoid sample contamination, this type of image gives a rough idea of the density of free-standing nanotubes. The absorption properties of the nanotubes labeled CNT 2, DCNT 4, and DCNT 5 are investigated into

details in the next chapters (see Chaps. IV and V). With the combination of SMS and RSMS, optical measurements become possible on both freely suspended and supported segments of these nanotubes, giving insights in the influence of environmental conditions on their absorption response. For sample FS-2, absorption and Raman experiments were performed on twelve free standing nanotubes, identified as SWNT or DWNT, isolated or in bundles. Some of them, labeled CNT 1, B2, and DCNT 2 are visualized in Fig. III.5 over their whole freely suspended segments.

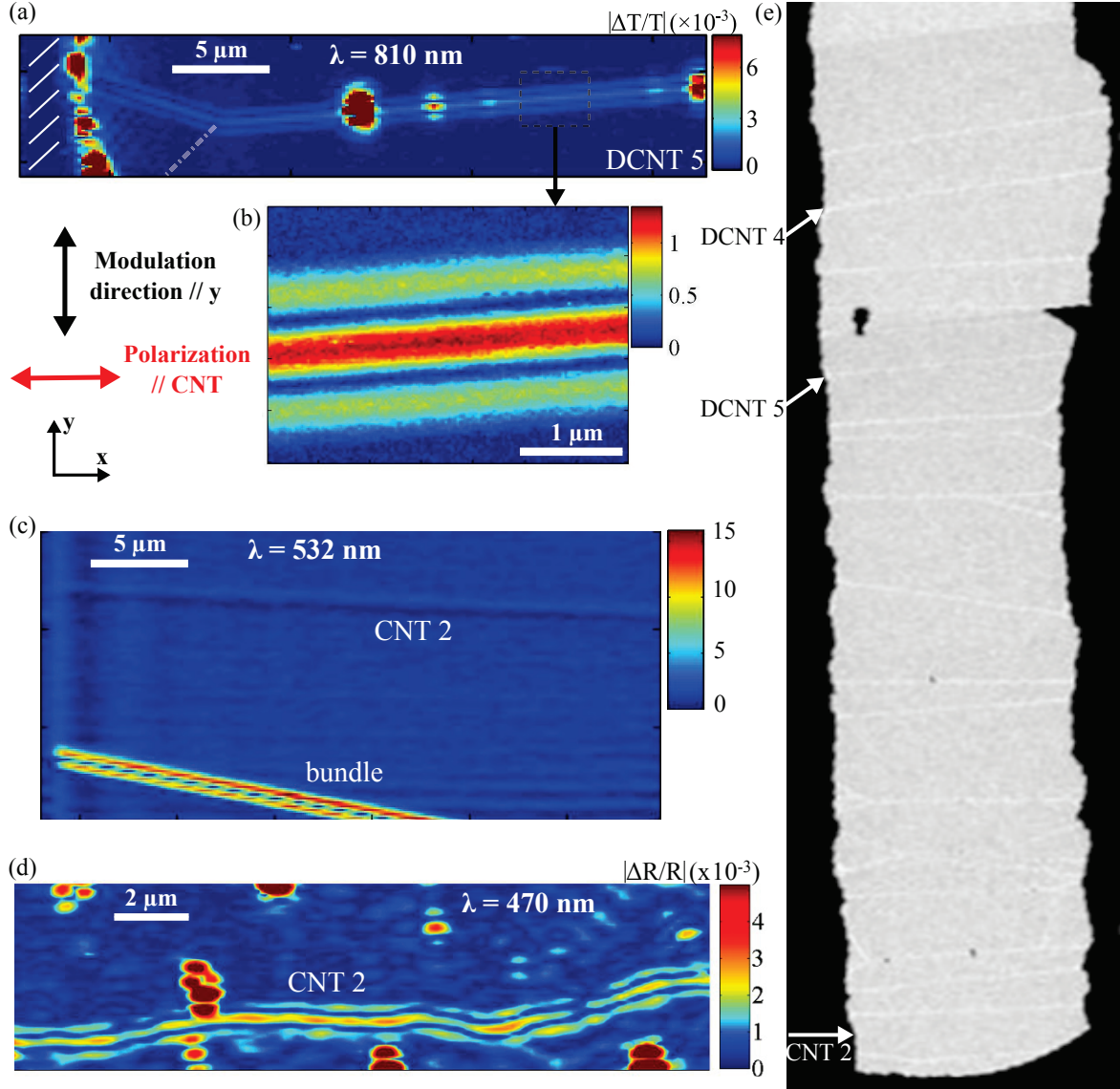


**Figure III.4:** Freely suspended and supported CNTs on the sample FS-1. (a-d) SMS and RSMS imaging. (e) TEM image of the CNTs freely suspended across the slit.



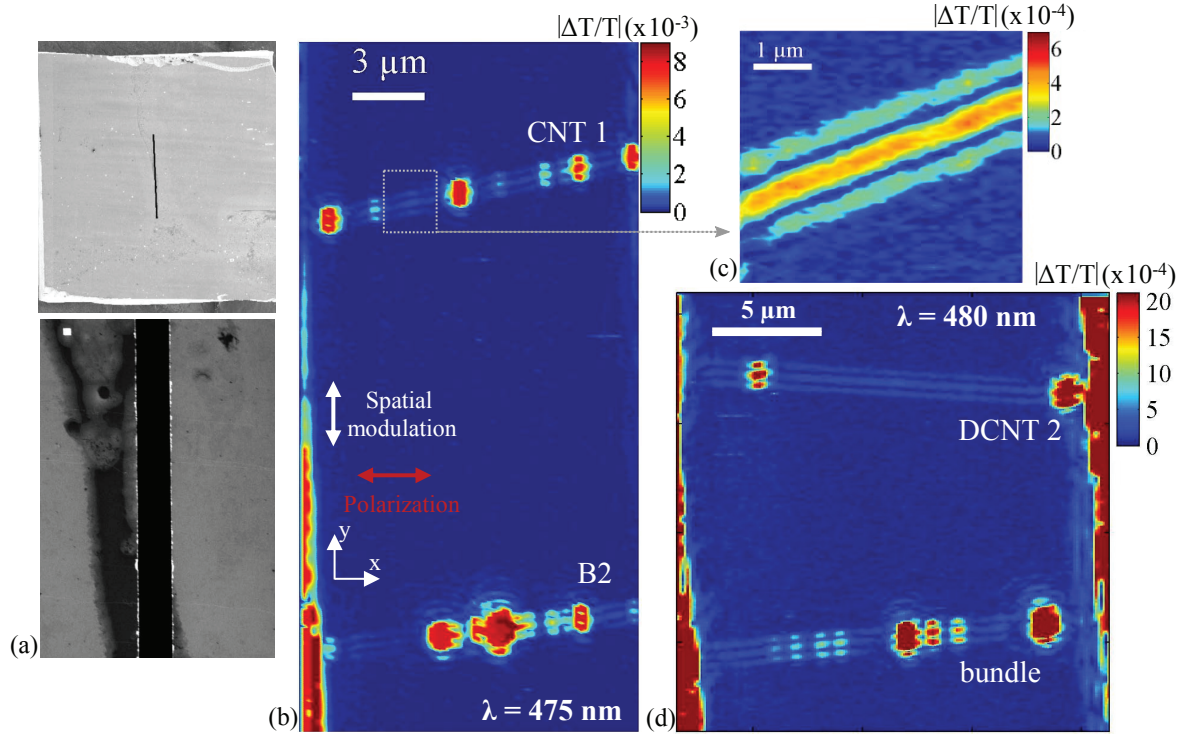


**Figure III.5:** SMS images of selected free-standing nanotubes on sample FS-2. (a) SEM images of the substrate. (b-d) SMS imaging.

### III-1.2.b In-lab preparation method

In this section, I will present some results on my attempts to make individualized free-standing nanotubes for future optical experiments. Beforehand trenches were etched in  $\text{SiN}_4$  or Si TEM grids with a focus ion beam (FIB).<sup>b</sup> Then, nanotubes were grown by CVD using the method presented in Sec. III-1.1.a, and varying the Fe-catalyst density. TEM images of the resulting samples are presented in Fig. III.6. Free-standing individual DWNTs are observed on some images, their diameter is about 3 nm. One of them seems also collapsed at one point, which is quite surprising in this diameter range. It is also possible that this particular DWNT became twisted during the growth.

## III-1.3 General comments and sample overview

### III-1.3.a Synthesis of carbon nanotubes

Although CVD was the only method used for the synthesis of carbon nanotubes in my thesis, several other techniques have been developed in the last two decades: arc discharge, laser ablation, HiPCO method, . . . For both experimental studies and applications, one is interested in a particularly type of nanotube (SWNT, multi-wall CNT, semi-conducting, metallic, . . .) with certain structural characteristics (diameter, length, . . .)

<sup>b</sup>The FIB was operated by Nicolas Blanchard at the Centre Lyonnais de Microscopie.

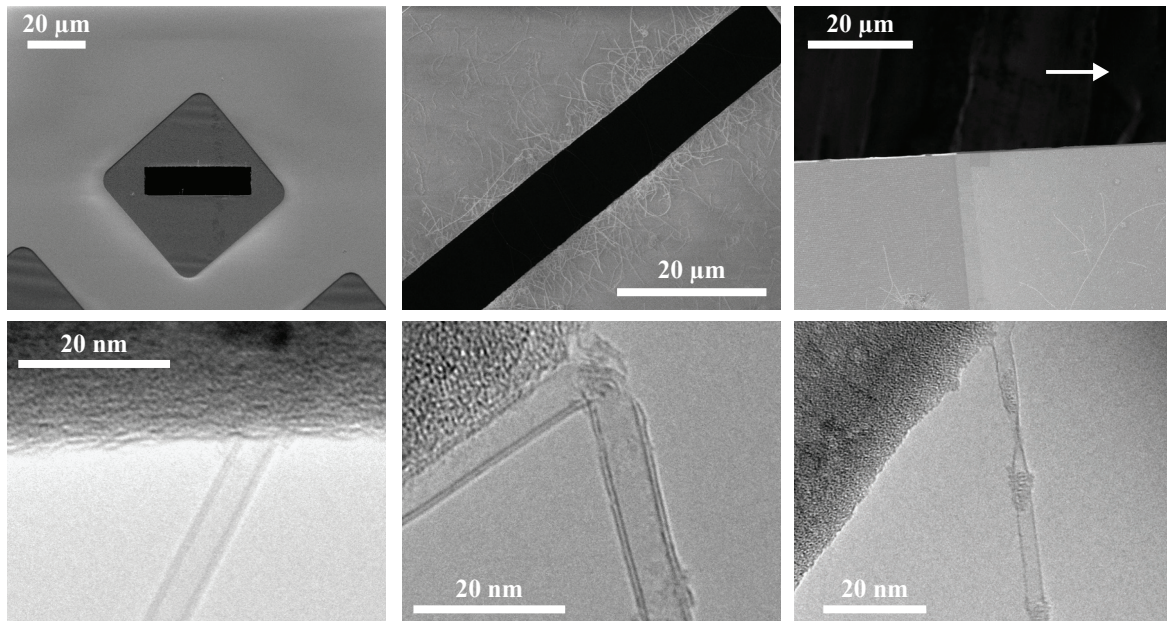


**Figure III.6:** TEM and SEM imaging of home-made free-standing double-wall carbon nanotubes.

and properties (electronic, optical, mechanical). These parameters will generally determine the synthesis method one can choose, each presenting different throughput.

### The different fabrication methods

Arc discharge nanotubes are produced by applying a 100 A current (20 V potential difference) between two graphite electrodes placed under a low pressure helium flux [118]. The carbon contained in the negative electrode sublimates because of the high-discharge temperatures giving a mixture of nanotubes, amorphous carbon, and fullerene. Adjusting the temperature, arc discharge can synthesize small diameter SWNTs ( $< 1.5$  nm) of lengths of the order of  $10\text{ }\mu\text{m}$  [2]. This type of tube usually present few structural defects but several purification steps are necessary to remove byproducts of the growth.

Laser ablation nanotubes are synthesized by vaporizing a graphite/metal catalyst target with a nanosecond-pulsed laser [119]. This method produces SWNTs with narrow diameter dispersion; It shows a good throughput still containing byproducts (amorphous carbon, fullerene,...) and a post-purification process is necessary.

The HiPCO method (and later CoMoCAT) has been developed in the former group of R.E. Smalley at Rice University [120]. SWNTs are produced in a gas-phase catalytic process, consisting in the high-pressure decomposition of iron pentacarbonyl  $\text{Fe}(\text{CO})_5$  in a heated flow of carbon monoxide. This type of nanotube has been widely used for optical studies on nanotube ensembles dispersed (individualized) in a solution (or surfactant, gel,...). In fact, the HiPCO method efficiently produces small diameter SWNTs ( $\sim 0.7 - 1.0$  nm, thus showing absorption/luminescence in the visible and near-IR) free of amorphous carbon and with small quantity of byproducts (mainly residual

metallic catalyst).

### Advantage of CVD-grown nanotubes for optical studies

For most optical studies on nanotube ensembles, tubes are individualized/sorted from bulk materials (mainly commercially purchased powders or suspensions - synthesized with one of the presented methods). They usually have small diameters. The preparation processes often involve several centrifugation steps which can possible damage or break the tubes (water molecules tend to penetrate into open tubes [83]). Moreover, they need to be individualized in a solution/surfactant/gel thus introducing an environment that can alter the nanotubes optical properties. Conversely, CVD-synthesized pristine individual ultralong suspended (or substrate supported) tubes have usually diameters in the range 1.5-3 nm. Only a limited number of research laboratories in the world have the know-how to prepare such samples, which can therefore be exploited for suspending SWNTs over few tens of  $\mu\text{m}$  wide trenches. Most studies of the CNTs photo-physics at the single-particle level on ultralong nanotubes are therefore focused on rather large diameter SWNTs and high-order energy transitions ( $S_{33}$ ,  $S_{44}$ ,  $M_{22}, \dots$ ). For this reason, CVD-synthesized nanotubes are ideal candidates for absorption spectroscopy at the single-tube level.

### III–1.3.b Sample overview

The samples studied in this thesis by absorption spectroscopy are summarized in the following table. The reader is referred to the preceding subsections for more details.

Sample	Substrate	Carbon nanotubes studied	Techniques
FS-1	Si/SiO <sub>2</sub> (100 nm) with a trench 100 $\mu\text{m}$ $\times$ 1 mm	Free-standing and supported 3 CNTs	SMS+RSMS Raman <sup>†</sup> AFM
FS-2	Si/SiO <sub>2</sub> with a trench 20 $\mu\text{m}$ $\times$ 1 mm	Free-standing 8 CNTs	SMS Raman <sup>†</sup>
Q-3	Quartz ST-cut 100 $\mu\text{m}$ $\times$ 1 mm	Supported 3 CNTs	SMS AFM Raman
Si-4	Si/SiO <sub>2</sub> (300 nm) 100 $\mu\text{m}$ $\times$ 1 mm	Supported 1 CNT	RSMS AFM Raman <sup>‡</sup>

**Table III.1:** Overview of the samples studied with (reflective) spatial modulation spectroscopy. <sup>†</sup>Sample fabrication, carbon nanotube synthesis and Raman characterization were performed by Matthieu Paillet, Huy Nam Tran, Xuan Tinh Than, Ngoc-Minh Phan, Ahmed-Azmi Zahab, and Prof. Jean-Louis Sauvajol. <sup>‡</sup>Raman characterization and part of the RSMS experiments were carried out by D. Christofilos and J. Arvanitidis.

## III-2 Absorption spectroscopy of individual nanotubes

Spatial modulation spectroscopy technique (SMS) was initially developed by Arbouet et al. in 2004 to measure the absolute absorption cross-section of single gold nanoparticles [121]. The method presents two primary advantages: (i) it allows direct access to the absolute absorption cross-section of nano-objects, (ii) measurements at the single-object level do not suffer from ensemble averaging effects. Since then, SMS has been used for the characterization of metallic nano-particles, nano-dimers and nano-rods [122,123]. In this work, SMS is adapted to the direct measurement of the absolute absorption cross-section of individual carbon nanotubes deposited on transparent substrates or freely suspended across trenches. Moreover, a variant of the method named reflective spatial modulation spectroscopy (RSMS) has been developed in order to perform absorption spectroscopy of nanotubes supported on opaque substrates.

### III-2.1 Spatial modulation spectroscopy

The absorption cross-section  $C_{\text{abs}}$  of single-wall carbon nanotubes ranges from 1 to  $3 \times 10^{-17} \text{ cm}^2$  per carbon atom, corresponding to values smaller than  $1 \text{ nm}^2/\text{nm}$  (Tab. II.1). The relative transmission  $\Delta T/T$  measures the absorbance of the object in the beam spot, i.e. the ratio of the absorption cross-section of the object to the beam spot size  $D_s$ . Assuming that a  $1 \mu\text{m}$  segment of an individual CNT is illuminated, a beam spot size of  $1 \mu\text{m}^2$ , the absorbance of the CNT yields  $10^{-3}$  or 0.1%. In other words, the relative change in the transmission signal  $\Delta T/T$  introduced by the presence of a single CNT in a laser beam is of the order of  $10^{-3}$ , and this signal is going down to few  $10^{-5}$  far from the absorption peaks. The magnitude of  $C_{\text{abs}}$  and  $\Delta T/T$  in CNT is comparable to the measurement of Arbouet et al. for single gold nanoparticles [121]. Therefore, it is a good choice to use spatial modulation spectroscopy (SMS) to access to the absolute absorption cross-section of individual carbon nanotubes.

#### III-2.1.a Principle

Considering an individual carbon nanotube either deposited on a transparent substrate or freely-suspended across a slit (samples FS-1, FS-2, Q-3), the principle of the SMS method is sketched in Fig. III.7. The CNT sample is placed between two high numerical aperture 100X objectives arranged in a confocal manner. An incident laser beam of incident power  $P_i$  is tightly focus on the CNT using this system. Due to the presence of the nano-object at position  $(x_0, y_0)$ , the transmitted field is the sum of the incident electrical field  $\mathbf{E}_i$  and the scattered one by the object  $\mathbf{E}_s$ . More precisely, the extinction cross-section  $C_{\text{ext}}$ , defined as the sum of the absorption  $C_{\text{abs}}$  and scattering  $C_{\text{sca}}$  cross-sections, depends only on the scattering amplitude in the forward direction (cf. optical



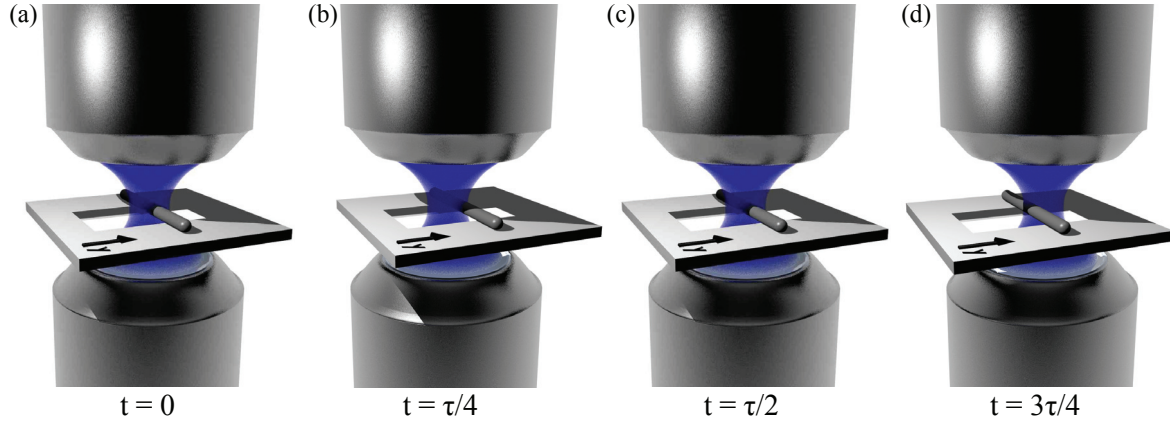


**Figure III.7:** Principle of spatial modulation spectroscopy. An incident laser beam is tightly focus on the nanotube sample using a 100X high numerical aperture objective ( $NA = 0.7$  – top objective). Outcoming light is collected by a second 100X objective ( $NA = 0.8$  – bottom), and directed towards the detection photodiode. From (a) to (d), sketch of the spatial modulation of the CNT sample. The sample position is modulated along the  $y$ -axis direction, at frequency  $f$  (associated period  $\tau$ ) and amplitude  $\delta y$ , with respect the center of the fixed laser focal spot.

theorem in [124]). The transmitted power is:<sup>c</sup>

$$P_T = P_i - C_{\text{abs}} I_i(x_0, y_0), \quad (\text{III.1})$$

where  $I(x, y)$  is the incident light beam intensity profile in the focal plane. The light intensity is measured using a conventional silicon photo-diode (PD). With such system detection of relative transmission smaller than  $10^{-2}$  should be impossible due mainly to the intrinsic noise of the laser source and lack of sensitivity of the PD. To overcome this issue, the position of the sample is periodically modulated at high frequency ( $f = 1.5$  kHz and associated period  $\tau = 1/f$ ), with amplitude  $\delta y$  of the order of the spot size. In the following, the spatial modulation, realized by means of a linear piezo actuator, takes place along the  $y$ -direction with:

$$\delta y(t) = \delta y \sin(2\pi f t). \quad (\text{III.2})$$

This operation implies a periodic change of the transmitted signal:

$$P_T(t) = P_i - C_{\text{abs}} I_i(x_0, y_0 + \delta y \sin(2\pi f t)), \quad (\text{III.3})$$

where  $P_T(t + \tau) = P_T(t)$ . Therefore, transmission change is proportional to both the extinction cross-section and the difference of intensity when the CNT is centered (at

<sup>c</sup>In this equation, the scattering energy is neglected with respect to the second term on the right-hand side. This approximation assumes that scattering is sufficiently small in the detection solid angle (cf. Bohren et Huffman for details).

$t = 0 \bmod(1/f)$  giving  $I_i(x_0, y_0)$  and shifted with respect to its initial position (at  $t \neq 0 \bmod(1/f)$ ) with  $I_i(x_0, y_0 + \delta y \sin(2\pi ft))$ :

$$\Delta P_T = P_T(t) - P_i \approx -C_{\text{abs}}[I_i(x_0, y_0 + \delta y \sin(2\pi ft)) - I_i(x_0, y_0)]. \quad (\text{III.4})$$

It is illustrated in Fig. III.7 over one spatial modulation period  $t \in [0, \tau = 1/f]$ : at  $t = 0$  the object located at the center of the beam spot absorbs  $C_{\text{abs}}I_i(x_0, y_0)$ , at times  $t > 0$  the object is at position  $(x_0, y_0 + \delta y \sin(2\pi ft))$  and absorbs a power  $C_{\text{abs}}I_i(x_0, y_0 + \delta y \sin(2\pi ft))$ . Using a **synchronous detection** system, the relative change in the transmission signal imputed to the presence of the CNT is directly measurable. A quantitative description of the component  $P_T$ , at the modulation frequency, provides the absolute value of the extinction cross-section.

### III-2.1.b Absolute absorption cross-section in carbon nanotubes

In the case of few-wall carbon nanotubes, the scattering cross-section is two orders of magnitude smaller than the absorption cross-section, thus in the framework of this thesis  $C_{\text{ext}}$  is approximated by  $C_{\text{abs}}$  [14]. The amplitude of the relative transmission change,  $\Delta T/T \approx \Delta P_T/P_T$  is set by the CNT absorption cross-section and its orientation with respect to the direction of spatial modulation. Considering sufficiently *small modulation amplitude*, and for small absorption cross-section such that  $\Delta P_T \ll P_T$ , the following relation holds to the second order  $\delta y^2$  (from (III.3)):

$$P_T(t) \approx P_i - C_{\text{abs}} I_i(x_0, y_0) - C_{\text{abs}} \left. \frac{\partial I_i}{\partial y} \right|_{x_0, y_0} \delta y \sin(2\pi ft) - \frac{1}{2} C_{\text{abs}} \left. \frac{\partial^2 I_i}{\partial^2 y} \right|_{x_0, y_0} \delta y^2 \left[ \frac{1 - \cos(4\pi ft)}{2} \right]. \quad (\text{III.5})$$

The signal is composed of two oscillating terms at frequency  $f$  and  $2f$ , which are directly accessible using the synchronous detection. In our experiment the intensity in the focal plane is approached by a **Gaussian profile** as shown in Fig. III.8.a (this point is addressed in the next section). Hence, the fundamental component of the transmitted power presents two peaks with opposite signs symmetric with respect to the center of the laser spot, and zero signal is observed at the spot center (Fig. III.8.c). The second harmonic component shows maximum signal at the center of the focal point and two attenuated satellite peaks of opposite sign (Fig. III.8.c). In experiments, detection at  $2f$  is preferred as the position of the object is superimposed with the main maximum of  $\Delta T/T$ .

The transmission change detected by the system corresponds to the Fourier component

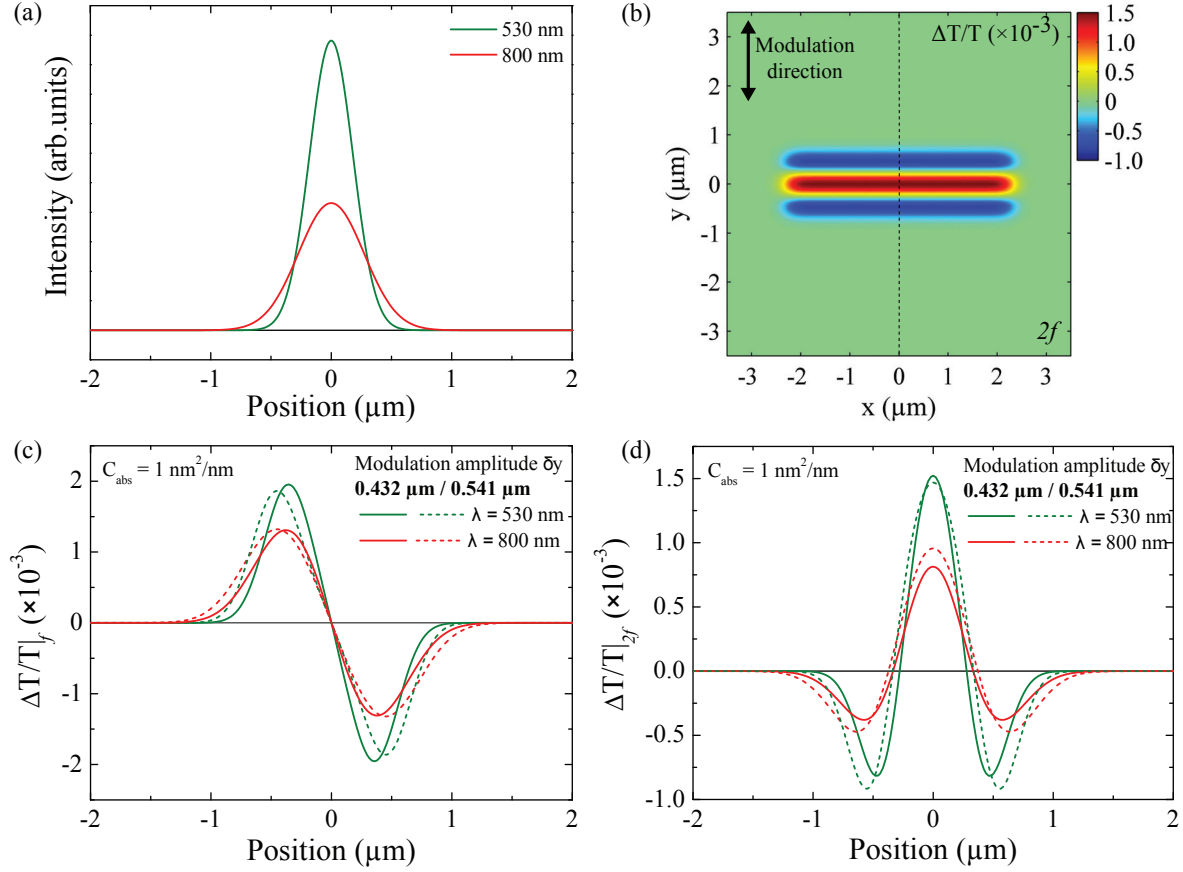


**Figure III.8:** Computed relative transmission  $\Delta T/T$  signal for two excitation wavelengths and two modulation amplitudes. (a) Normalized Gaussian profile modeling the intensity of the laser beam in the focal plane for two wavelength. (b) Computed SMS image of a 4  $\mu\text{m}$  long nanotube oriented perpendicular to the modulation direction – synchronous detection at the second harmonic. (c,d) Relative transmission profiles along the modulation direction (dashed line in (b)) computed at  $f$  and  $2f$  for the two vibration amplitudes adopted in the experiments regarding the laser wavelength.

of  $\Delta T/T$  at the modulation frequency:

$$\Delta T|_f = C_{\text{abs}} \frac{2}{\tau} \int_{-\tau/2}^{\tau/2} I_i(x_0, y_0 + \delta y \sin(2\pi ft)) \cos(2\pi ft) dt, \quad (\text{III.6a})$$

$$\Delta T|_{2f} = C_{\text{abs}} \frac{2}{\tau} \int_{-\tau/2}^{\tau/2} I_i(x_0, y_0 + \delta y \sin(2\pi ft)) \sin(4\pi ft) dt. \quad (\text{III.6b})$$

The relative transmission  $\Delta T/T$  is derived by including the normalisation factor which is, in our experiments,  $T = 2/\pi$  – it corresponds to the Fourier component of a rectangular-function signal with normalized amplitude. In the case of CNTs,  $\Delta T/T$  also depends on nanotube's orientation with respect to the direction of spatial modulation  $\theta_{\text{CNT}}$ , as well as on its illuminated length  $L_{\text{ill}}$  (cf. Fig. III.9.a). In other words, the CNTs absorption cross-section is weighted by the light intensity profile, thus

$$C_{\text{abs}}[L] = \int_{L_{\text{ill}}} C_{\text{abs}}[L^2] I_i(x, y) ds, \quad (\text{III.7})$$

where  $s$  is the curvilinear abscissa along the nanotube. The term on the left-hand side, which is in length unit, corresponds to the absorption cross-section per unit length  $C_{\text{abs,L}} - C_{\text{abs,L}}$  is the only relevant parameter for nanotubes with length  $L$  larger than  $L_{\text{ill}}$ . In the following of this thesis, we conveniently use  $C_{\text{abs}}$  instead of the  $C_{\text{abs,L}}$ . Finally, the relative transmission of an individual CNT is related to its absorption cross-section per unit length through the relation

$$\left. \frac{\Delta T}{T} \right|_f = C_{\text{abs}} \frac{\pi}{\tau} \int_{L_{\text{ill}}} \int_{-\tau/2}^{\tau/2} I_i(x_0, y_0 + \delta y \sin(2\pi ft)) \sin(2\pi ft) dt ds, \quad (\text{III.8a})$$

$$\left. \frac{\Delta T}{T} \right|_{2f} = C_{\text{abs}} \frac{\pi}{\tau} \int_{L_{\text{ill}}} \int_{-\tau/2}^{\tau/2} I_i(x_0, y_0 + \delta y \sin(2\pi ft)) \sin(2\pi ft) dt ds, \quad (\text{III.8b})$$

where the inverse of the terms of proportionality on the right-hand side are defined as  $K_f$  and  $K_{2f}$ , respectively; such that  $C_{\text{abs}} = K_f \Delta T/T|_f$  and  $C_{\text{abs}} = K_{2f} \Delta T/T|_{2f}$ . The present procedure is valid for nanotubes of length bigger than the spot size, i.e. the illuminated segment of the tube  $L_{\text{ill}}$  is exactly the laser spot size, otherwise corrections should be applied to the spot profile. From the relative transmission  $\Delta T/T$  detected at  $f$  or  $2f$ , the quantitative measurement of the absolute absorption cross-section of an individual CNT requires the knowledge of:

- i. the intensity profile  $I(x, y)$  which is assumed to be Gaussian (experimentally verified in Sec. III-2.1.d),

- ii. the characteristics of the spatial modulation (frequency  $f$  and amplitude  $\delta y$ , controlled experimentally),
- iii. and the nanotube's orientation  $\theta_{\text{CNT}}$  and its illuminated length  $L_{\text{ill}}$  (cf. Fig. III.9.a, directly observable during sample rastering).

To illustrate the influence of the different parameters listed above, the relative transmission of a single cylinder of diameter much smaller than its length, with  $C_{\text{abs}} = 1 \text{ nm}^2/\text{nm}$ , is computed for: **(A)** different vibration amplitudes/spot sizes (Fig. III.8), **(B)** various nanotube's orientations (Fig. III.9).<sup>d</sup>

**(A)** The main axis of the elongated nano-object is oriented perpendicular to the modulation direction ( $\theta_{\text{CNT}} = 90^\circ$ ). While rastering the surface and detecting the second harmonic component of the transmission, the tube shows up as a three-line signal with central maximum superimposed with the object (Fig. III.8.b). Fundamental and second harmonic  $\Delta T/T$  profiles along the modulation direction, for two wavelengths and two vibration amplitudes, are plotted in Figs. III.8.c,d. For fixed wavelength, the signal intensity depends on the vibration amplitude, thus  $\delta y$  can be adapted experimentally to increase the signal-to-noise ratio. Practically,  $\delta y$  is set to  $0.432 \text{ } \mu\text{m}$  while studying carbon nanotubes with blue and visible laser light ( $\leq 700 \text{ nm}$ ), whereas a value of  $0.541 \text{ } \mu\text{m}$  is adopted in near-IR spectral range ( $\geq 700 \text{ nm}$ ). The optimum value of vibration amplitude is about the FWHM of the beam in the focal plane:  $\delta y^{\text{Optimum}} = 1.08 D_s$  (see Sec. III-2.1.d).

**(B)** Fig. III.9 shows computed SMS imaging of the cylinder for different orientation with respect to the modulation direction. For synchronous detection at both  $f$  and  $2f$ , the optimal configuration is achieved for orientation of the tube perpendicular to the vibration direction ( $\theta_{\text{CNT}} = 90^\circ$ ), in which case  $\Delta T/T$  is homogeneous along the cylinder. In the opposite situation ( $\theta_{\text{CNT}} = 0^\circ$ ), only the two ends of the object show a significant signal. Continuous change of the signal occurs for orientation angles in between these two situations ( $\theta_{\text{CNT}} = 30^\circ$  and  $\theta_{\text{CNT}} = 60^\circ$ ).

To summarize, SMS technique associates spatial modulation of the sample position and synchronous detection system. The second harmonic component of the relative transmission signal is related to the absolute absorption cross-section of carbon nanotubes via the relation (III.8). The orientation of the CNTs with respect to the vibration direction is crucial to achieve optimal signal-to-noise ratio, as well as the vibration amplitude and the laser spot size. All these parameters are characterized for our setup in the two forthcoming paragraphs, using either nanotubes or metallic nanoparticles for which  $C_{\text{abs}}$  is well defined.

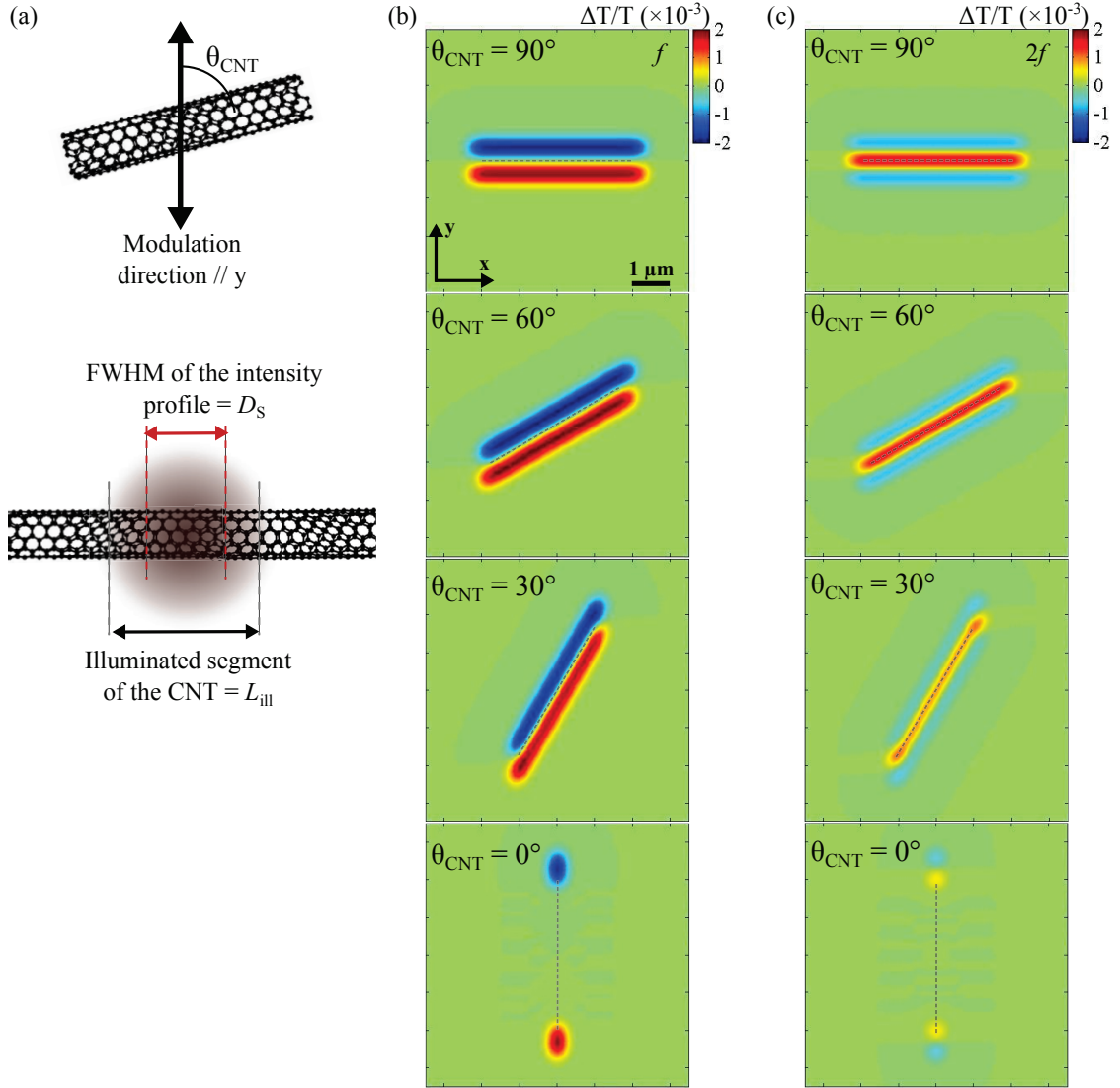


**Figure III.9:** Computed SMS response for different CNT orientation. (a) Definition of: the angle between the direction of spatial modulation and the nanotube main axis  $\theta_{\text{CNT}}$ , the FWHM of the Gaussian intensity profile in the focal plane  $D_S$ , and the length of the nanotube illuminated  $L_{\text{ill}}$ . (b,c) Relative transmission signal computed for different orientation of the nanotube. The modulation amplitude is  $\delta y = 432 \text{ nm}$  and  $D_S = 424 \text{ nm}$ .

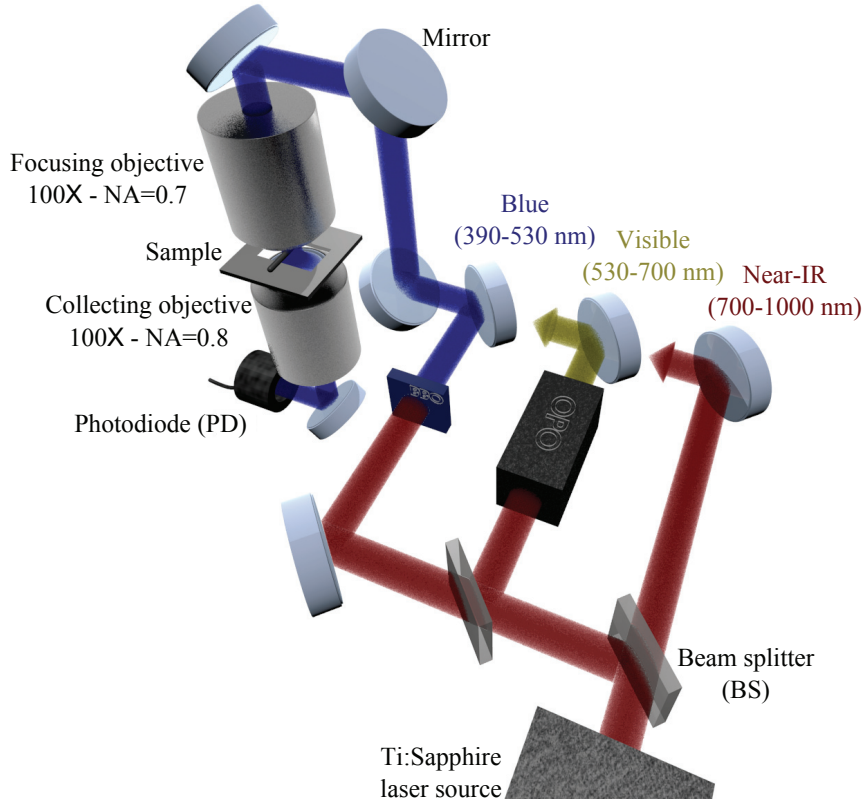


**Figure III.10:** Spatial modulation spectroscopy experimental setup. The three tunable laser lines, giving access to pulsed-laser light with wavelength between 390 and 1080 nm, are represented: the Ti:Sapphire source (near-IR), the optical parametric amplifier (visible), the BBO crystal (second harmonic generation – blue and near-UV). The laser beam is focused on the sample by means of a high numerical aperture 100X objective. The outgoing light is collected with a similar objective and detected using a photodiode (PD).

### III–2.1.c Experimental setup

In this section, I describe the setup developed for the study of the optical properties of individual carbon nanotubes (Fig. III.10). The setup is composed of three ensembles: **(A)** the laser sources operating over a broadband of wavelength (390 nm to 1080 nm), **(B)** the optical elements that engineer the laser beam, **(C)** the system of focus/modulation/detection introduced in Sec. III–2.1.a.

**(A)** The Ti:Sapphire tunable laser source delivers pulsed-laser light in the near-IR between 700 and 1080 nm (red beam on the right hand side). The laser mode is the fundamental  $TEM_{00}$  described by Gaussian beam optics. Blue and near-UV light, from 390 to 540 nm, is obtained by means of second harmonic generation taking place in

<sup>d</sup>The parameters of the model are chosen in order to represent situations close to experiment: spot size  $D_S = 0.8\lambda$ , spatial modulation amplitude  $\delta y = 0.432\mu\text{m}$  and  $0.541\mu\text{m}$ , individual carbon nanotubes with absorption cross-section close to  $1\text{ nm}^2/\text{nm}$ .



a BBO thin crystal excited with the Ti:sapphire source (left hand side – beam line red/blue). Visible part of the spectrum, between 500 and 700 nm, is accessible upon pumping of an optical parametric oscillator with 820 nm laser pulses (middle laser line red/yellow). Beam splitters (transparent grey squares) distribute the Ti:Sapphire laser beam to the elements composing the setup. Movable mirrors select the beam impinging on the sample.

(B) Between the light sources and the entrance of the focusing objective, the laser beam is dilated and collimated using combinations of lenses such that the entrance pupil of the focusing objective is over-illuminated. The beam linear polarization is controlled using the association of a quarter-wave plate and a linear polarizer. Optical attenuators are inserted in the laser path such that the laser power impinging on the sample is kept below 1  $\mu$ W.

(C) The laser beam is tightly focus on the CNT using a high numerical 100X objective with high numerical aperture  $NA = 0.7$ . The collection of the light is performed by a second 100X objective with  $NA = 0.8$ . With the view to detecting individual CNTs with the highest possible contrast, the input aperture of the focusing objective is over-illuminated so that the laser beam is focused close to the diffraction limit on the object. Thus, considering nearly plane waves impinging on the objective's aperture, the beam intensity profile at the focal point observes an Airy pattern which is approximated by a Gaussian profile. In this situation, the full-width at half maximum (FWHM) of the beam at the diffraction limit is defined as:

$$D_S^{\text{th}} = \frac{0.515 \lambda}{NA}, \quad (\text{III.9})$$

thus  $D_S^{\text{th}} = 0.74 \lambda$  for the focusing objective. Although the input aperture of the focusing objective is over-illuminated, we cannot obtained perfect plane waves experimentally, thus  $D_S$  is measured at  $0.80 \lambda$  (see Sec. III-2.1.d). Transmitted light is detected using a silicon photodiode, and the synchronous detection is realized with a lock-in amplifier (LIA). The numerator in the relative transmission term  $\Delta T/T$  is measured with a digital multimeter. The sample is mounted on a piezo actuator and a three-axis stage. The latter allows rastering of the surface and optimisation of the focus. The former is directly controlled by the internal oscillator of the lock-in amplifier which delivers a sinusoidal signal at frequency 1.5 kHz with effective amplitude voltage  $V_{\text{LIA}}$ . The choice of the frequency is a trade-off between the mechanical capabilities of the actuator and the signal-to-noise ratio.

### III-2.1.d Calibration of the experimental parameters

The properties of the spatial modulation and the laser beam in the focal plane are characterized experimentally by studying the absorption of a single metallic nanoparticle.<sup>e</sup> Its size needs to be much smaller than the beam spot, and its absorption cross-section should stay smaller than few  $\mu\text{m}^2$  (corresponding to  $\Delta T/T$  smaller than  $10^{-2}$ ). A SMS

<sup>e</sup>The same calibration procedure is possible using CNTs, but the plasmonic absorption of gold nanoparticles is much easier to understand.



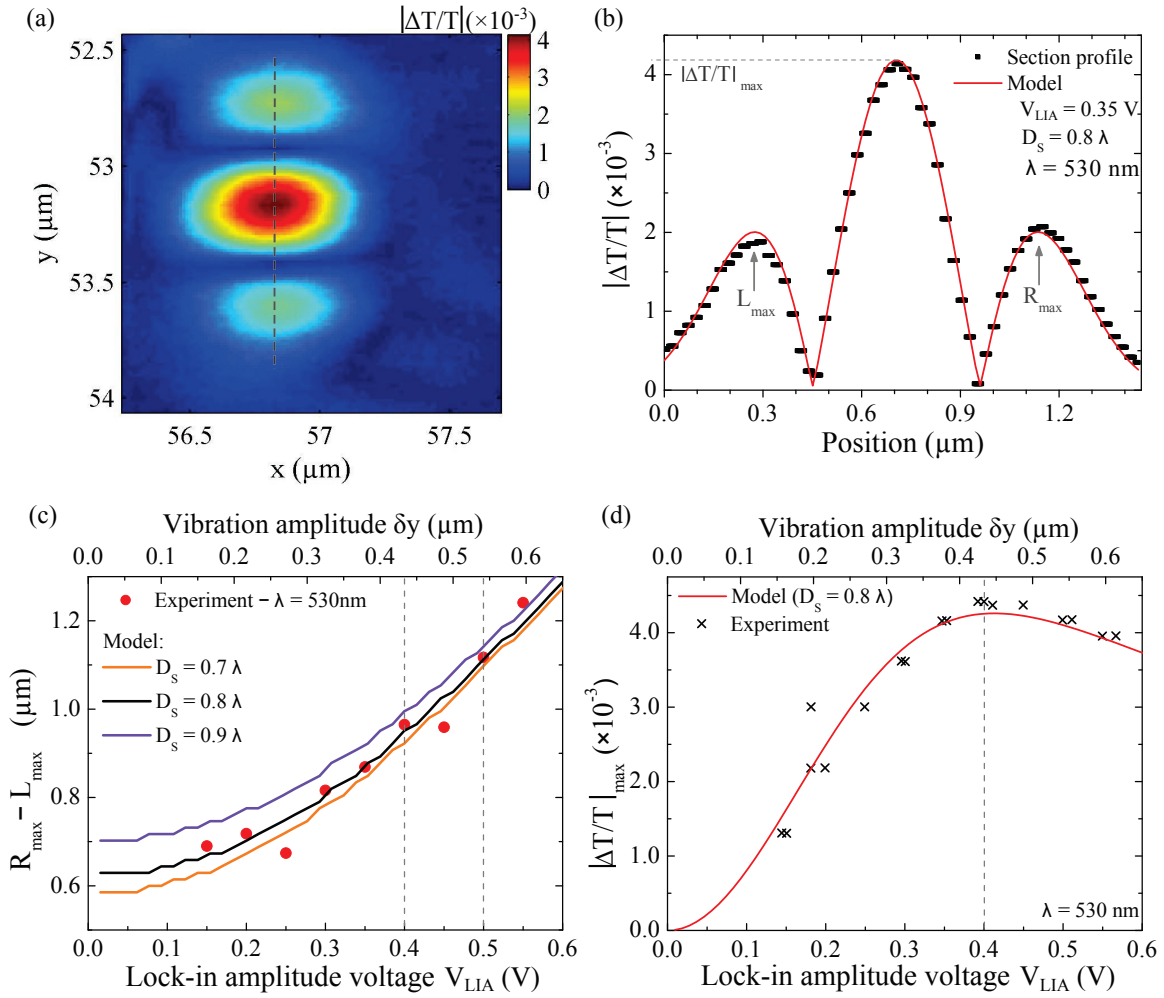


**Figure III.11:** Calibration: laser beam size and spatial modulation amplitude. (a) SMS imaging at  $2f$  of a single gold nanoparticle (laser wavelength 530 nm). The input signal of the piezo actuator is set to  $f = 1.5 \text{ kHz}$  and  $V_{\text{LIA}} = 0.35 \text{ V}$ . (b) Relative transmission profile in the modulation direction (dashed line in (a)). Data points are fitted with the model using vibration amplitude  $\delta y = 0.38 \mu\text{m}$  and spot size  $D_s = 424 \text{ nm}$ . (c) Distance between the adjacent peaks (shown in (b)) versus both actuator input voltage and corresponding modulation amplitude. Measurements are best adjusted while including a beam size  $D_s = 0.8 \lambda$  in the model. (d) Optimisation of the relative transmission signal at  $2f$  with respect to the vibration amplitude – laser wavelength set to 530 nm.

image of a gold nanoparticle detected at  $2f$  is shown in Fig. III.11.a; the piezo actuator input voltage and frequency are 0.35 V and 1.5 kHz, respectively. In the direction of spatial modulation (parallel to  $y$ -axis) the relative transmission profile presents a maximum intensity  $|\Delta T/T|_{\max}$  of  $4.2 \times 10^{-3}$  (Fig. III.11.b). The two adjacent peaks have amplitude around  $2 \times 10^{-3}$ , they are separated by a distance  $|R_{\max} - L_{\max}|$  of  $0.9 \mu\text{m}$ . These two quantities,  $|\Delta T/T|_{\max}$  and  $|R_{\max} - L_{\max}|$ , are measured versus the controllable actuator input voltage  $V_{\text{LIA}}$  (Figs. III.11.c,d). These two graphs are the corner stones of the calibration process, in fact they provide experimental values for the parameters necessary to relate the relative transmission and the absolute absorption cross-section. In Fig. III.11.c, the data points are best fitted with the model including:<sup>f</sup>

- a Gaussian laser intensity profile in the focal plane with  $D_S = 0.8 \lambda$ ,
- an amplitude of spatial modulation  $\delta y = 1.08 V_{\text{LIA}} [\mu\text{m}]$ .

Furthermore, Fig. III.11.d shows that best signal-to-noise ratio is achieved for modulation amplitude  $\delta y = 432 \text{ nm}$  for excitation wavelength  $\lambda = 530 \text{ nm}$ . In the following, the amplitude of the vibration is set to:  $432 \text{ nm}$  ( $V_{\text{LIA}} = 0.4 \text{ V}$ ) for blue and visible light ( $\leq 700 \text{ nm}$ ),  $541 \text{ nm}$  ( $V_{\text{LIA}} = 0.5 \text{ V}$ ) in the near-IR ( $\geq 700 \text{ nm}$ ).

### III-2.1.e Absorption spectroscopy of individual carbon nanotubes

#### SMS applied to nanotubes

In the previous paragraph, the parameters of the SMS technique have been characterized experimentally using a single nanoparticle. Herein, the SMS technique is applied to an individual free-standing carbon nanotube (FS-2 CNT 1). Its SMS image is shown in Fig. III.12.a, where the laser wavelength and the vibration amplitude are set to  $\lambda = 745 \text{ nm}$  and  $\delta y = 0.541 \mu\text{m}$ , respectively. Another important parameter to consider in the case of a CNT is the incident light polarization direction: it needs to be parallel to the nanotube main axis to achieve maximum absorption (see Sec. II-1.1).<sup>g</sup> As expected from the computed SMS signal (see Sec. III-2.1.b), the tube shows up as three parallel lines, with maximum amplitude superimposed with the real nanotube location (Fig. III.12.b). Surface mapping allows to determine the orientation angle between the nanotube and the modulation direction:  $\theta_{\text{CNT}} = 20^\circ$ . Relative transmission profile normal to the CNT axis is well adjusted with the cylinder model using the calibrated spot size  $D_S = 0.8 \lambda$  and vibration amplitude (Fig. III.12.c). Using (III.8), the absorption cross-section of this nanotube is about  $C_{\text{abs}} = 0.6 \text{ nm}$ . Integrating these parameters into the cylinder model, computed SMS image shows very good agreement with the experiment (Fig. III.12.b). Besides, it is important to point out that ‘dust’ nanoparticles and/or impurities adsorbed onto the CNT surface appear in the SMS image as localized intense three-spot pattern (red on Fig. III.12.a).<sup>h</sup> As a consequence, the position on the nanotubes at

<sup>f</sup>The nanoparticle is modelled by a point object, and the relation between  $\Delta T/T$  and  $C_{\text{ext}}$  is expressed in Sec. III.6.

<sup>g</sup>This point is addressed experimentally in Chaps. IV.

<sup>h</sup>Optical response of these dust particles is clearly visible due the high sensitivity of the SMS technique. In practice, these particles are easily missed in Raman spectroscopy.

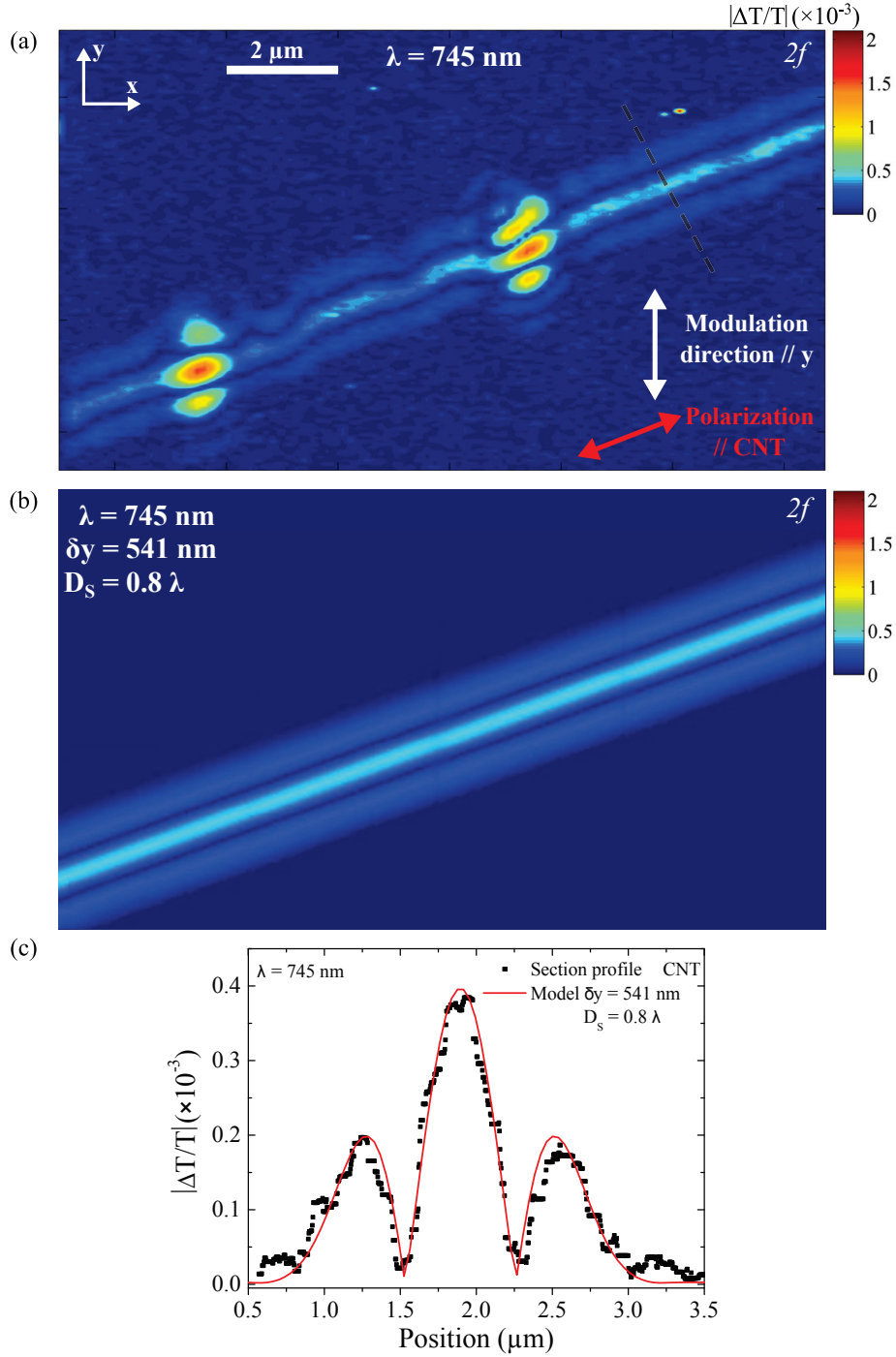


**Figure III.12:** Absorption-based imaging of an individual freely suspended SWNT. (a) SMS image at  $2f$  with  $f = 1.5 \text{ kHz}$ ,  $\delta y = 0.541 \mu\text{m}$ , and  $\lambda = 745 \text{ nm}$ . (b) Computed SMS image of a cylinder with the experimental parameters of (a). (c) Relative transmission profile along the dashed line shown in (a). The carbon nanotube shows up as three parallel lines with maximum superimposed with its real position. Intense red spots are assigned to ‘dust’ particles and/or impurities adsorbed on the tube. (see text for details)

which the absorption measurements are performed is carefully chosen in order to avoid any disturbing signals from these particles. A typical ‘clean’ region is shown on the top right hand side of the nanotube in Fig. III.12.a, where the absorption seems quiet homogeneous along the CNT.

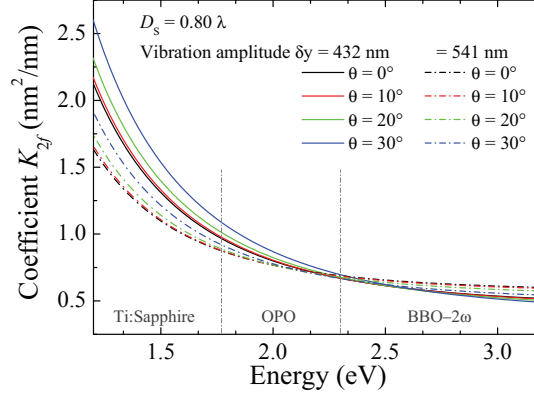


**Figure III.13:** Relation between relative transmission and absorption cross-section in carbon nanotubes given by (III.8) through the relation of proportionality  $C_{\text{abs}} = K_{2f} \Delta T/T$  ( $\text{nm}^2/\text{nm}$ ). Parameters for the modulation amplitude and spot size are those usually adopted during the experiments. For blue/visible and near-IR laser light, the vibration amplitude is set to  $0.432 \mu\text{m}$  and  $0.541 \mu\text{m}$ , respectively.

### Measurement methods

In carbon nanotubes, the relative transmission at  $2f$  is directly proportional to the absolute value of the absorption cross-section through the relation  $C_{\text{abs}} = K_{2f} \Delta T/T$  (with unit  $\text{nm}^2/\text{nm}$ ), and  $K_{2f}$  is given by (III.8). The coefficient of proportionality  $K_{2f}$  is plotted in Fig. III.13 for the typical experimental parameters that are utilized throughout this thesis. In practice, we always follow the same procedure for characterizing the optical and structural properties of a carbon nanotube:

- i. the CNT is located and preliminary characterized using either atomic force microscopy or Raman spectroscopy.
- ii. The CNT is imaged and located with SMS – the orientation angle of the CNT with respect to the modulation direction is observed at this stage.
- iii. At fixed wavelength, we study the light-polarization dependency of  $C_{\text{abs}}$ .
- iv. For incident light polarized parallel to the CNT, its absorption spectrum is measured.
- v. Depending on the results, we usually choose to further study the light-polarization dependence of  $C_{\text{abs}}$  at other wavelengths. Raman spectroscopy is also performed for many additional excitation wavelengths to confirm the structure of the nanotube.

(in fact, the absorption spectrum of a CNT provide precious information regarding the laser excitation that should be used for Raman scattering studies).

- vi. When possible, the procedure is repeated for the same nanotube placed in a different environment.

Points i. and ii. are prior (preliminary) to the absorption spectroscopy measurements and should be described in this chapter, whereas the other points are presented and analyzed in the two following chapters. In the previous section (Sec. III-1), we have already introduced AFM, TEM, and SEM characterization of the samples. In this part and the next one (Sec. III-2.2.a), we present (R)SMS imaging of some of the nanotubes studied in this thesis.

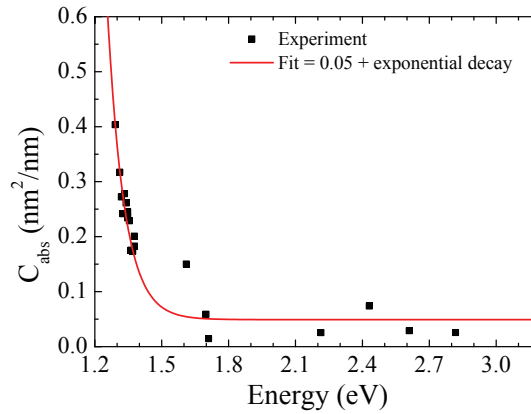


**Figure III.14:** Experimental determination of the wavelength dependent sensitivity limit for free-standing carbon nanotubes. This quantity is the absorption cross-section measured in empty space (far from any object). The value is between 0.04 and 0.05 nm<sup>2</sup>/nm above 1.3 eV ( $\lambda \leq 900$  nm), and increases greatly in the IR. This phenomenon is less pronounced for nanotubes supported on substrates as larger incident power is used.

### Limitations

In order to avoid laser damaging of carbon nanotubes, the incident laser power is kept well below  $\sim 1 \mu\text{W}$  (corresponding to average intensity  $I_0 \sim 1 \text{ kW/cm}^2$ ). In photodiodes the signal-to-noise ratio decreases with decreasing incident photon flux.<sup>i</sup> Fig. III.14 shows the spectrum the ‘background’ absorption, measured in empty space far from any object (also called noise or sensitivity limit). The sensitivity limit exhibits an average value  $\sim 0.05 \text{ nm}^2/\text{nm}$  in the spectral range  $\sim 1.35 - 3.2 \text{ eV}$  (or  $390 - 900 \text{ nm}$ ). However, significant increase of the noise limit is observed in the infra-red ( $\lambda < 900 \text{ nm}$  or  $E > 1.35 \text{ eV}$ ) which is still not clearly understood yet. The beam spot size, which is

<sup>i</sup>Noise in photodetectors is discussed in [125].

bigger in the infra-red, might explain the reduction of the SNR in relation with the incident photon flux. Although it does affect  $C_{\text{abs}}$  for parallel polarization, the sensitivity limit will restrict the absorption features that we can resolve for incident light normally polarized to the CNTs. Whenever the measured signal corresponds to the sensitivity limit,  $C_{\text{abs}}$  will be set to zero in order to not mislead the reader.

The second error on the measurements arises from the laser beam focusing at the diffraction limit with high numerical aperture objectives (see (III.9)). Assuming a linear polarization parallel to  $x$  before the objective ( $z$  perpendicular to the sample surface) and an homogeneous illumination of the objective input aperture, at the focal point part of the beam power  $P_t$  is transferred to the other two polarizations. More precisely, few percents of  $P_t$  leaks to the  $y$ -polarization and around 10% goes to the  $z$ -polarization [126, 127].<sup>j</sup> This effect could also be different for tubes deposited on layered substrates [114].

### III-2.1.f SMS imaging of carbon nanotubes

Figs. III.4.a,b,c and Figs. III.5.b,c,d show SMS images of individualized free-standing nanotubes that are studied in this thesis (as labeled directly on the images). As mentioned, imaging provides information on the tubes orientation with respect to the spatial modulation direction which is vertical ( $// y$ ). It also allows to locate clean regions of the nanotubes where its absorption is homogeneous, i. e. not disturbed by dust/impurities adsorbed onto the CNTs surface (see Fig. III.4.a and Figs. III.5.c). The polarization is set parallel to the CNTs to obtain maximum contrast. Depending on the laser excitation wavelength and on the nanotubes  $C_{\text{abs}}$ , they appear more or less brighter on the images (compare for instance CNT 2 (SWNT) and the bundle on Fig. III.4.a).

## III-2.2 Reflective spatial modulation spectroscopy

In the previous section, SMS technique is applied to the investigation of the absorption properties of CNTs either freely suspended or deposited on transparent substrates. However, technological applications, e. g. in optoelectronic and NEMS systems, require the fabrication of devices with CNTs mainly supported on opaque substrates [7, 128]. In electronics widely used substrates are made of degenerated silicon bulk with a thin  $\text{SiO}_2$  layer showing a thickness between 100 and 500 nm. Here, we propose to investigate the absorption properties of carbon nanotubes deposited on such opaque substrates by means of reflective spatial modulation spectroscopy (RSMS).

### III-2.2.a Principle and theoretical background

The principle of the RSMS technique is identical to SMS except that focusing and collection of light are performed with the same objective. In the setup (Fig. III.10), a

<sup>j</sup>At the time I was writing this thesis, I had not implemented yet the exact calculation as described in [127].



semi-transparent mirror is placed in the beam path before the objective such that the light reflected on the sample is directed onto the photodiode.

In the presence of a nanoparticle at point  $(x_0, y_0)$  in the focal plane, the reflected field is the sum of the one reflected by the substrate and the one scattered by the object [124]. This point is detailed later. Assuming that the particle is much smaller than the focal spot size  $D_S$ , plus a small surface reflectivity  $R$ , the power impinging onto the PD is

$$P_R(t) \approx RP_i - C_{\text{abs}}\sqrt{R}I_i(x_0, y_0 + \delta y \sin(2\pi ft)), \quad (\text{III.10})$$

where the notations are identical to (III.3). In the case of layered substrates, as the silicon substrates studied in this thesis, this expression has to be generalized to take into account Fabry-Pérot effects, i.e. the amplitude and phase of the effective EM-field directly above the substrate surface). A simple form of the correction to (III.11) is derived for real reflection coefficient  $r$ , i.e. valid for wavelengths close to the Fabry-Pérot extrema. In this case,  $\sqrt{R}$  in the second term on the right-hand side is replaced by  $\sqrt{R}\sqrt{I_{\text{surf}}}$ , where  $I_{\text{surf}}$  represents the intensity enhancement factor at the surface due to Fabry-Pérot effects. More precisely, the relative reflection signal is

$$\frac{P_R - RP_i}{RP_i} \equiv \frac{\Delta R}{R} \approx -\frac{C_{\text{abs}}}{A_{\text{slab}}} [I_i(x_0, y_0 + \delta y \sin(2\pi ft)) - I_i(x_0, y_0)], \quad (\text{III.11})$$

where  $A_{\text{slab}} = \sqrt{R/I_{\text{surf}}}$  includes the correction due to the presence of the substrate. Fig. III.18 shows the wavelength dependence of these parameters for silicon substrates with  $\text{SiO}_2$  layers of two different thicknesses. The method to obtain the absorption cross-section of CNTs supported on substrates is identical to the one presented in Sec. III-2.1. The relation between  $C_{\text{abs}}$  and  $\Delta R/R$  is obtained by simply including the correction coefficient in (III.8):

$$C_{\text{abs}} = A_{\text{slab}}K_{2f}\Delta R/R. \quad (\text{III.12})$$

A more advanced formulation of the relation between absorption cross-section and relative reflection is derived within the Mie theory framework following the method described in ref. [124] (cf. Chap.3, pp.57).<sup>k</sup> In the present problem, we consider absorption and scattering by a single arbitrary particle, with specified size, shape and optical properties, that is deposited on a substrate with reflection coefficient  $r$  in air. The object is illuminated with a linearly polarized monochromatic wave  $\mathbf{E}_i(\mathbf{r}, t)$ , with direction of propagation perpendicular to the substrate surface. For sake of simplicity, the discussion is limited to plane harmonic waves – this description is not as rigid as it seems, in fact an arbitrary field can be decomposed into its Fourier components which are plane waves.<sup>l</sup> Analytical solution to the problem is possible if the particle is embedded in a homogeneous medium. To approach this situation, the present problem is modelled according to Fig. III.16 where the following hypothesis are included:

<sup>k</sup>The same treatment is exactly addressed by Bohren and Huffman for the situation of an arbitrary particle embedded in a transparent medium, which corresponds to the SMS configuration.

<sup>l</sup>One should consider paraxial beam in a more general description because the light is focused with high numerical aperture objectives.

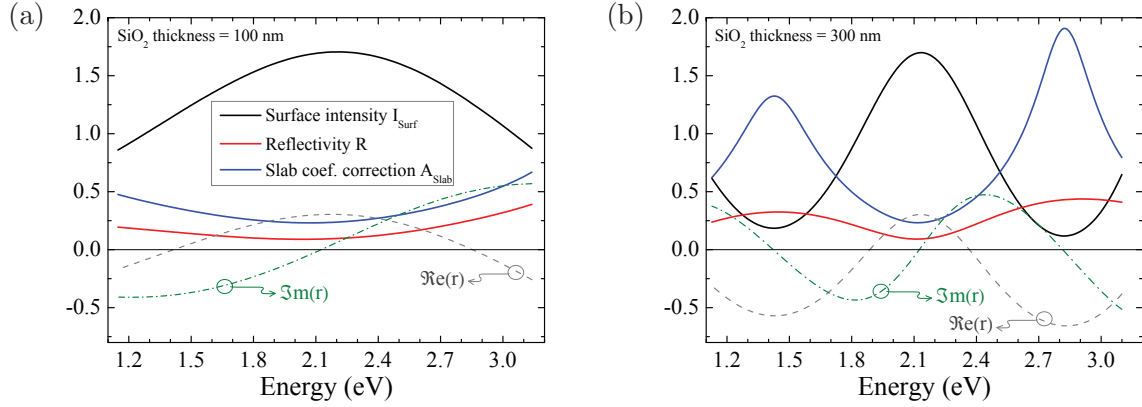


**Figure III.15:** Slab correction to the absorption cross-section for Si/SiO<sub>2</sub> substrates. The silicon dioxide layer thickness is 100 nm in (a) and 300 nm in (b). Real and imaginary part of the reflection coefficient  $r$  are also shown on the graph. (see text for details)

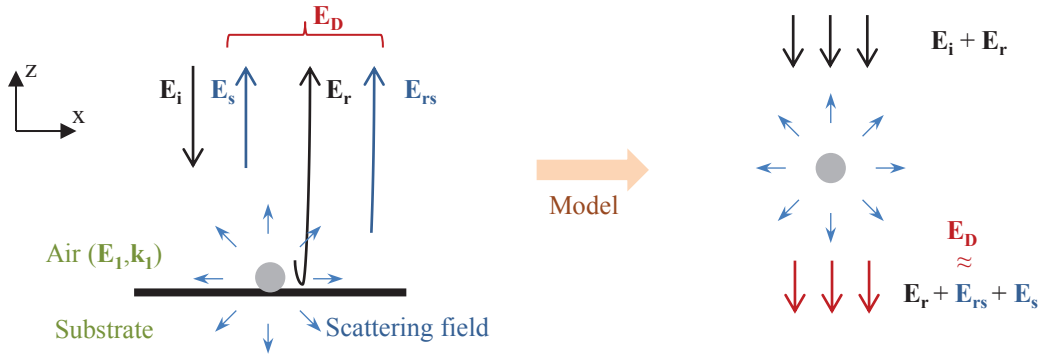


**Figure III.16:** Model Mie theory: absorption and scattering by a small arbitrary object lying on a substrate. (left) Schematic representation of the problem:  $\mathbf{E}_i$  incident field,  $\mathbf{E}_r$  direct reflection of the incident field on the substrate,  $\mathbf{E}_s$  scattering field from  $\mathbf{E}_i$ ,  $\mathbf{E}_{sr}$  scattering field from  $\mathbf{E}_r$ ,  $\mathbf{E}_D$  sum of the field propagating towards the photodiode. In the model, the object is embedded in a homogeneous medium (air) and is excited by the effective field  $\mathbf{E}_i + \mathbf{E}_r$ . Multiple scattering is neglected, and reflections of the scattering fields on the surface are neglected, hence the electromagnetic field detected is the sum of the reflected field and the scattering fields propagating in the backward direction.



- the scattering field originates from the effective field directly above the surface of the substrate, i. e.  $\mathbf{E}_s \propto \mathbf{E}_i$  and  $\mathbf{E}_{rs} \propto +\mathbf{E}_r$ .
- The scattering fields propagating in the forward direction reflected and on the surface are neglected – this approximation holds for low reflectivity material surfaces.
- The discussion is limited to first-order scattering processes.

In this model, the object is embedded in a homogeneous non-absorbing medium (air in this case) and illuminated with the equivalent field  $\mathbf{E}_i + \mathbf{E}_r$  propagating effectively in the forward direction. The EM-field impinging on the detector, which is virtually placed in the forward direction, is the sum of: the reflected field  $\mathbf{E}_r$ , the total first-order scattering field  $\mathbf{E}_s + \mathbf{E}_{rs}$  (Fig. III.16). Bohren and Huffman showed that, in the far-field limit, the field scattered by an arbitrary particle is a linear function of the incident field. This relation, for  $\mathbf{E}_i$  and the corresponding scattering field  $\mathbf{E}_s$ , is expressed in spherical coordinate system  $(\rho, \phi, \theta)$  as

$$\begin{pmatrix} \mathbf{E}_{//s} \\ \mathbf{E}_{\perp s} \end{pmatrix} = \frac{e^{ik_1\rho}}{-ik_1\rho} \begin{pmatrix} S_2 & S_3 \\ S_4 & S_1 \end{pmatrix} \begin{pmatrix} \mathbf{E}_{//i} \\ \mathbf{E}_{\perp i} \end{pmatrix}, \quad (\text{III.13})$$

where the subscribe ‘//’ and ‘ $\perp$ ’ designate the EM fields parallel and perpendicular to the scattering plane, respectively (see Fig. III.17.a for the notations). The matrix of elements  $S_i$  ( $i = 1, 2, 3, 4$ ) is called amplitude scattering matrix. In the case of carbon nanotubes, which are modeled as nanowires or hollow cylinders, the scattering field is better expressed in cylindrical coordinates  $(\rho, \phi, z)$ , for normal excitation, by the linear relation:<sup>m</sup>

$$\begin{pmatrix} \mathbf{E}_{//s} \\ \mathbf{E}_{\perp s} \end{pmatrix} = \sqrt{\frac{2}{\pi k_1 \rho}} e^{i(k_1 \rho + \frac{3\pi}{4})} \begin{pmatrix} T_1 & T_4 \\ T_3 & T_2 \end{pmatrix} \begin{pmatrix} \mathbf{E}_{//i} \\ \mathbf{E}_{\perp i} \end{pmatrix}. \quad (\text{III.14})$$

Scattering and absorption of nanowires and hollow cylinders are discussed in details in Appx. B. Complete resolution of the problem demonstrates that the wave front of the scattering field in CNTs is a cone (Fig. III.17.c). The cone’s aperture depends on the direction of propagation of the incident light with respect to the tube main axis, defined as  $\theta_{\text{exc}}$ . This pattern was observed experimentally by Joh et al. using Rayleigh scattering (Fig. III.17.d).

All the elements are now defined to derive the linear relation between the power impinging on the photodiode  $P_i$  and the extinction cross-section of the object  $C_{\text{ext}}$ . I recall at this point that the detector is placed in the forward direction aligned with direction of the incident beam ( $\phi = 180^\circ$  in cylindrical coordinates /  $\phi = 180^\circ$  and  $\theta = 90^\circ$  in spherical coordinates). This configuration of the detection is important for the calculation/measurement of the absolute absorption cross-section, in fact the **optical theorem** says that the extinction depends only on the scattering amplitude in

---

<sup>m</sup>For the notations in cylindrical coordinates refer to Fig. III.17.b.

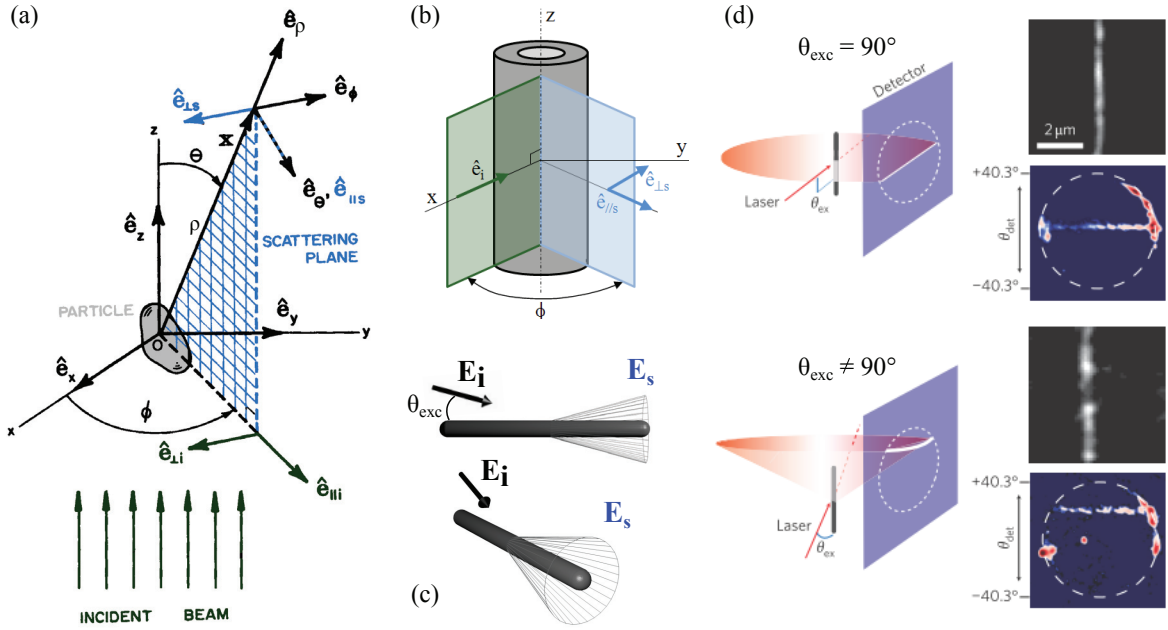


**Figure III.17:** Scattering behaviour for nanotubes. (a) Notations adopted for the resolution of the Mie scattering model for arbitrary particles (adapted from [124]). (d) Notations for hollow cylinders (cylindrical coordinates). (c) Wave front of light scattering by a cylinder modelling CNTs for excitation angle  $\theta_{exc}$ . (d) Experimental observation of the scattering pattern of an individual carbon nanotube [14]. Spatial Rayleigh images (upper inset) and radiation patterns from Fraunhofer imaging (lower inset) for normal incidence ( $\theta_{exc} = 90^\circ$ ) and for  $\theta_{exc} \neq 90^\circ$ .

the forward direction. Therefore, for linearly polarized light, the power on the detector is

$$P_R = |r|^2 P_i + I_{surf} P_s - C_{ext} I_i (\text{Re}(r) + |r|^2 + \text{Im}(r) \tan(\varphi_s)), \quad (\text{III.15})$$

where  $\varphi_s$  is the complex phase of the sum of the diagonal elements in the amplitude scattering matrix, i.e.  $\varphi_s = \text{Im}(S_1 + S_2)/\text{Re}(S_1 + S_2)$  or  $\varphi_s = \text{Im}(T_1 + T_2)/\text{Re}(T_1 + T_2)$ . The first term on the right-hand side is the power of the incident light that is reflected on the substrate and enters the detector. The second one is the power of the scattering field that is collected in the solid angle of the collection objective – for  $\text{NA} = 0.8$  the solid angle is about  $\pi/2$ . This term is negligible with respect to the third one since  $C_{abs} \gg C_{sca}$  ( $C_{ext} \approx C_{abs}$ ), which holds for few-wall carbon nanotubes and small bundles. The third term contains the extinction cross-section of the object pondered by the correction due to the presence of the substrate. Finally, the theoretical relative reflection signal is

$$\frac{\Delta R}{R} = -C_{abs} I_i A_{slab}^{th} = -C_{abs} I_i \left[ 1 + \frac{\text{Re}(r)}{R} + \frac{\text{Im}(r)}{R} \tan(\varphi_s) \right], \quad (\text{III.16})$$

where  $R = |r|^2$ . This relation has the same form as the one obtain for CNTs on transparent substrates, expect for the second and third terms in the brackets that add

the correction from the substrate. The calculated correction term  $A_{\text{slab}}^{\text{th}}$  contains the quantity  $\varphi_s$  which is not accessible experimentally, in fact only  $C_{\text{ext}} = \text{Re}(S_1 + S_2)$  (or  $C_{\text{ext}} = \text{Re}(T_1 + T_2)$ ) is directly measurable with (R)SMS). For the silicon substrates with 100 and 300 nm thick  $\text{SiO}_2$  layer, Fig. III.18 compares the correction coefficient  $A_{\text{slab}}^{\text{th}}$  for  $\text{Im}(r) = 0$  (plain lines) and  $A_{\text{slab}}$  (dash/dotted lines) that is used in practice via (III.12). They show good agreement in the regions where  $\text{Im}(r)$  is close to zero (cf. Fig. III.15). This analysis tells us the spectral regions in which the absolute value of the absorption cross-section can be measured, i.e. where the third term in (III.16) is negligible. Especially, in the case of the substrate with 100 nm thick  $\text{SiO}_2$  layer, a broadband range from 1.8 to 2.2 eV is accessible for the measurements – the error is kept below 15%.

At this point, we have all the ingredients to measure the absolute absorption cross-section of individual carbon nanotubes on opaque substrates. Results for CNTs deposited on Si/ $\text{SiO}_2$  substrates are presented in Chap. IV, and also in [12].

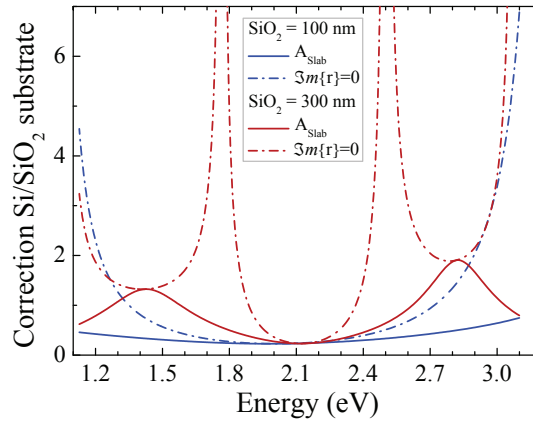


**Figure III.18:** Approximation slab correction to the absorption cross-section for silicon substrates with  $\text{SiO}_2$  layer thickness 100 and 300 nm. These correction coefficients are inserted in relation (III.12) for the relation between absorption cross-section and relative reflection.  $A_{\text{slab}}$  is the approximated correction that is used in experiments (plain lines). Dash/dotted lines that draws the correction calculated from (III.16) assuming a real reflection coefficient.

### III–2.2.b Imaging of carbon nanotubes on opaque substrates

In this section, RSMS technique is utilized for the imaging of individualized carbon nanotubes on opaque substrates. Results are compared to more classical surface imaging techniques that are atomic force microscopy (AFM) and scanning electron microscopy (SEM). In fact, RSMS and SMS methods can be easily combined with other characterization methods more commonly used in condensed matter such as: Raman spectroscopy, luminescence, AFM, SEM, and transmission electron microscopy (TEM). As a consequence, the **same** carbon nanotube can be studied with different techniques.

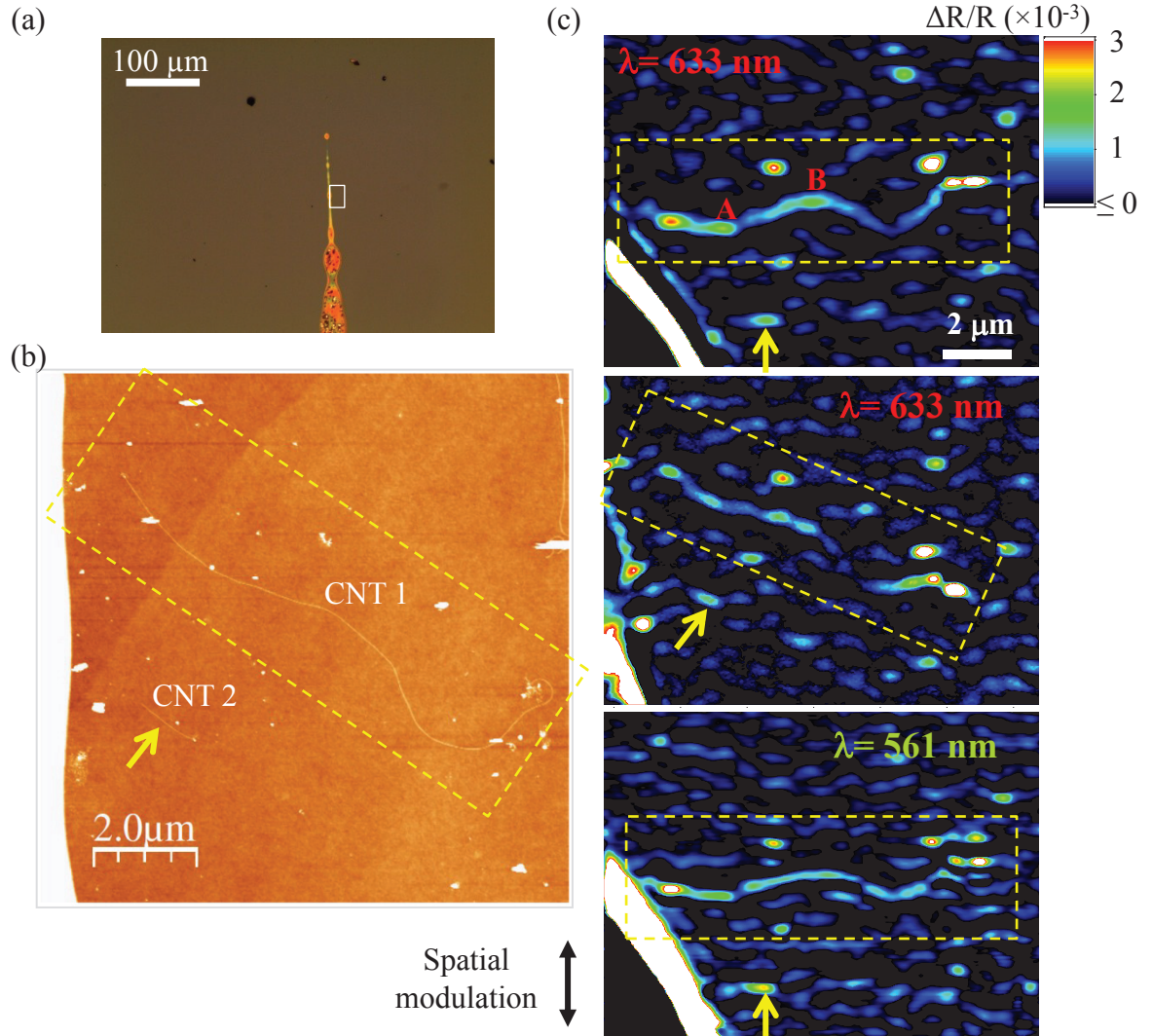


**Figure III.19:** Absorption imaging of individual CNTs on opaque Si/SiO<sub>2</sub> substrate. Markers on the surface (a) allowed us to locate the same isolated nanotubes with AFM (b) and RSMS (c). Absorption-base imaging of the same region for different wavelengths and different sample orientation with respect to the modulation direction shows that RSMS response depend on these parameters.

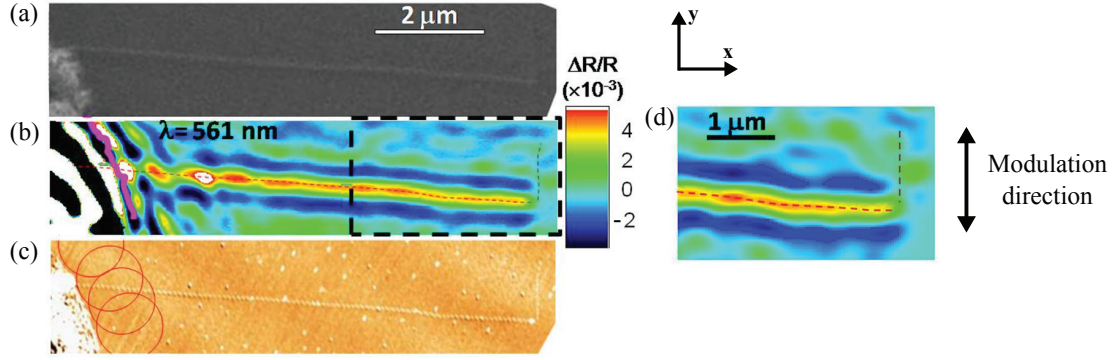


**Figure III.20:** Comparison of RSMS imaging with other visualization techniques on opaque substrate. (a) SEM, (b) RSMS (with  $\lambda = 561$  nm,  $D_S = 400$  nm,  $\delta y = 270$  nm along  $y$ , and  $x$ -polarized light), and (d) AFM images of a CNT close to a lithographically produced contact. The nanotube appears shorter in RSMS than in AFM or SEM micrographs because of the large contribution of the contact to the optical signal, due to the smaller optical resolution consequence of the spot size and sample modulation (circles on the AFM image indicate approximately the zone where the contact influences the RSMS signal; its edge is superimposed on the RSMS image of the nanotube, thick purple line). The RSMS image is in very good agreement with numerical simulations (d) performed on the area depicted by the dashed rectangle in (b). The small vertical nanotube and background particles visible in the AFM image are also taken into account in the simulation.

In Fig. III.19, the same sample area is imaged with AFM and RSMS at two laser wavelengths (561 nm and 633 nm), showing two individual carbon nanotubes (cf. supporting informations of Christofilos et al. for their Raman signature [12]). Top and middle images in Fig. III.19.c have been acquired with the 633 nm laser line, but with two different sample orientations ( $\theta_{\text{CNT}} = 90^\circ$  and  $\theta_{\text{CNT}} = 45^\circ$ ) with respect to the spatial modulation direction, which is vertical. The RSMS signal measured for the long nanotube CNT 1 is weaker in the case of  $\theta_{\text{CNT}} = 45^\circ$ , in agreement with the previous discussion with regard to the signal dependence on the orientation angle (see Fig. III.9). The image recorded with the wavelength of 561 nm shows sharper features, due to the fact that beam focusing is tighter for shorter wavelengths. AFM  $10 \times 10 \mu\text{m}^2$  image has been carried out in more than 3 hours, while less than 15 min were required to obtain each  $12 \times 12 \mu\text{m}^2$  RSMS image with a step of 170 nm. This example attests that RSMS and SMS are high-contrast absorption-based imaging techniques with relatively fast acquisition times. The adaptability of the technique is further demonstrated in Fig. III.20, where a single CNT attached to a lithography produced gold contact is imaged with SEM (a), RSMS (b), and AFM (c). Extremely good agreement is shown between the three techniques. The tip of the CNT, which is observed parallel to the modulation direction with AFM and MEB, is absent on the RSMS image that is again in agreement with the discussion in Fig. III.9. Non-homogeneous RSMS signal on the sample surface is explained by the presence of dust particles, as well as disturbed Fabry-Pérot effects due to the roughness

of the contact surface between Si and SiO<sub>2</sub>.

To test our results, we investigated the **absorption of mono- and bi-layer graphene** flakes on Si/SiO<sub>2</sub> substrates. The absorption of graphene is rather simple and provides a good base for testing the RSMS technique. Results are fully described and analyzed in Appx. C and show good agreement with the corrections  $A_{\text{slab}}$  and  $A_{\text{slab}}^{\text{th}}$  in the regions of  $\text{Im}(r) \rightarrow 0$ .





# Absorption spectroscopy of single-wall carbon nanotubes

# IV

---

*In this section, the full characterization of the absorption response of individual single-wall carbon nanotubes is measured using spatial modulation spectroscopy and its alternative configuration in reflection. As demonstrated in the previous chapter, this technique provides direct access to the absolute absorption cross-section  $C_{\text{abs}}$  of individual CNT. Thus, in comparison to previous measurements of  $C_{\text{abs}}$  reported in the literature, our gain is twofold. First, we do not suffer from averaging effects from ensemble measurements. Second, the direct access to  $C_{\text{abs}}$ , offered by our technique do not require any hypothesis concerning the nanotubes properties. Consequently, for the first time, absorption cross-sections of SWNTs placed in different environments are directly comparable. Besides the advantages listed above, broadband polarized absorption provides access to new aspects of light-matter interactions in carbon nanotubes. Energy transition shifting, absorption peak broadening, and polarization anisotropy are all investigated in details for SWNTs subject to various environments: freely suspended, supported on a substrate, and in bundle.*

## IV–1 Free-standing SWNTs

The direct access to the close-to-intrinsic absorption characteristics of carbon nanotubes is possible when the environment that can influence the tubes properties is removed, i. e. for freely suspended CNTs. In this part, we focus on the study of the free-standing single-wall carbon nanotubes of samples FS-1 and FS-2 (see Sec. III–1.2).

### IV–1.1 Broadband absorption cross-section

The absorption spectra of individual free-standing semiconducting single-wall carbon nanotubes are shown in Fig. IV.1.a,b and Fig. IV.3.a,b. In both cases, the filled and empty symbols are the data collected with SMS technique for incident laser light polarized, respectively, parallel and perpendicular to the nanotubes. The raw measurements are directly related to values of absorption cross-section using the method described in Sec. III–2.1. Sharp absorption peaks and a constant non-resonant absorption are the main features observed in all spectra for parallel polarization. The former are character-



istics of exciton energy transitions  $S_{ii}$  and confirms that absorption of semiconducting CNTs is ruled by Wannier excitons.

### Characteristics quantities of the absorption

Here we define quantities that characterize the absorption of carbon nanotubes. For parallel polarization, energy transitions  $S_{ii}$  show up as narrow Lorentzian-like peaks of amplitude  $C_{\text{abs},S_{pp}}^{\text{exc}}$  (or exciton absorption cross-section) and full-width at half maximum  $\gamma_{S_{ii}}$ . The amplitude at the maximum of each peak  $S_{ii}$ , including the non-resonant absorption  $C_{\text{abs}}^{\text{nr}}$ , is noted  $C_{\text{abs},S_{ii}}^{\text{peak}}$ . A relevant quantity is the oscillator strength  $f_C$  of an exciton resonance that is directly proportional to the integrated area of its absorption peak. The latter is derived from  $C_{\text{abs},S_{ii}}^{\text{exc}}$  and  $\gamma_{S_{ii}}$ . Using a fitting procedure that will be detailed in the following paragraphs, all these data are collected and organized in tables, e. g. see Tab. IV.1.

Carbon nanotubes spectra exhibit a polarization dependent absorption between light polarized parallel  $C_{\text{abs}}^{\parallel}$  or orthogonal  $C_{\text{abs}}^{\perp}$  to the nanotube axis. The polarization dependent data are fitted by  $C_{\text{abs}}^{\parallel} \cos^2 \theta_{\text{pol}} + C_{\text{abs}}^{\perp} \sin^2 \theta_{\text{pol}}$ ,  $\theta_{\text{pol}} = 0$  being the direction parallel to the nanotube axis in the following.  $\theta_{\text{pol}}$  measured the angle between the polarization direction and the nanotube axis.

## IV–1.2 Semiconducting SWNTs of family type I

### IV–1.2.a Structure assignment

Fig. IV.1 shows the absorption and Raman spectra of two SC-SWNT of family type I. Chirality-assignment  $(n,m)$  of each tube is obtained using both the positions  $E_{ii}$  of the exciton energy transitions and the frequency of the RBM. More precisely, the diameter of the nanotubes is derived from  $\omega_{\text{RBM}}$  using the relation  $\omega_{\text{RBM}}[\text{cm}^{-1}] = 204/d[nm] + 27$  [105], and the resonances  $E_{ii}$  determine the chirality using the Kataura plot. Details about structure assignment for the free-standing SWNT can be found in Appx. A.

The absorption spectrum of CNT 1 (sample FS-2) is shown in Fig. IV.1.a. The resonances  $S_{ii}$  are located at 1.66, 2.21 and 2.61 eV. Moreover, we notice a significant constant out-of-resonance absorption of about  $0.14 \text{ nm}^2/\text{nm}$ ; this point will be addressed later in more details. Raman spectra measured for few laser excitations close to the absorption resonances present identical radial breathing mode at  $128.5 \text{ cm}^{-1}$  which corresponds to a nanotube diameter of  $2.01 \text{ nm}$  (Fig. IV.1.e). From the diameter and the three energy transitions, we infer that this nanotube is a (22,6) semiconducting SWNT (the other less probable possibility is (23,4)), the resonances are identified as  $S_{33}$ ,  $S_{44}$  and  $S_{55}$ . Profiles of the G-band region present LO and TO optical phonon modes at  $1591 \text{ cm}^{-1}$  and  $1576 \text{ cm}^{-1}$ , respectively. The frequency difference between these modes and their FWHM ( $5 \text{ cm}^{-1}$  for both modes) confirms the semiconducting and individual characters of the nanotube [19].

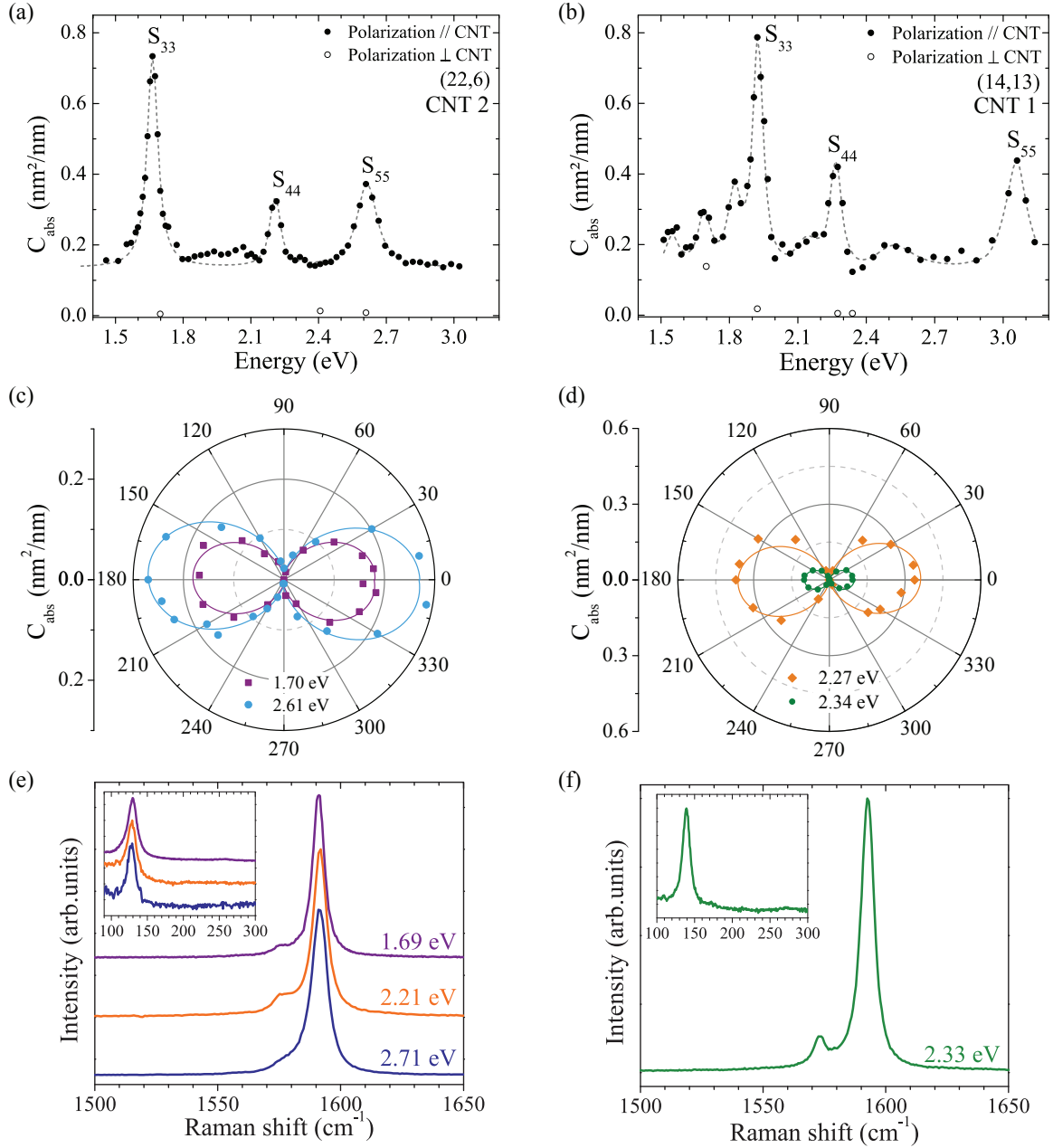


**Figure IV.1:** Absorption and Raman spectroscopy of individual free-standing type I semiconducting SWNTs. Results are presented for the (22,6) (CNT 1, left panels) and (14,13) (CNT 2, right panels) semiconducting SWNTs. (a,b) Absolute absorption cross-section spectrum for incident light parallel (full dots) and perpendicular (open dots) to the nanotube. The dashed line is the result of the fit detailed in the main text. (c,d) Light-polarization-dependent absorption cross-section for two laser excitation energies. The experimental data (symbols) are fitted using  $C_{\text{abs}}^{\parallel} \cos^2 \theta_{\text{pol}} + C_{\text{abs}}^{\perp} \sin^2 \theta_{\text{pol}}$  function (line),  $\theta_{\text{pol}} = 0$  being the direction parallel to the nanotube. (e,f) Raman spectra showing the tangential modes and radial breathing mode (inset) measured with three different excitation energies labeled on the figure close to absorption peaks.

The absorption spectrum of the free-standing CNT 2 (sample FS-2) is shown in Fig. IV.1.b. For incident light polarized parallel to the nanotube axis, exciton resonances are recognized at 1.93, 2.27 and 3.06 eV. Resonant Raman spectroscopy yields a RBM at  $139 \text{ cm}^{-1}$  corresponding to a diameter of 1.82 nm, as well as G-modes compatible with an individual semiconducting SWNT (Fig. IV.1.b). Correlation of the positions of the three main absorption peaks for parallel polarization with the diameter identifies this carbon nanotube as an individual (14,13) semiconducting SWNT of family type I. Absorption peaks at 1.93, 2.27 and 3.06 eV are assigned to the energy transitions  $S_{33}$ ,  $S_{44}$ , and  $S_{55}$ , respectively.

#### IV–1.2.b Exciton, phonon-assisted and non-resonant absorption

At this point, carbon nanotubes (22,6) and (14,13) have been identified using the positions of their exciton resonances and their diameter obtained with resonant Raman spectroscopy. Here, we detail the procedure adopted to fit the absorption spectra and thus extract the quantities:  $C_{\text{abs},S_{ii}}^{\text{exc}}$ ,  $\gamma_{S_{ii}}$ ,  $C_{\text{abs}}^{\text{nr}}$ , and  $C_{\text{abs},S_{ii}}^{\text{peak}}$ .

##### Semiconducting (22,6) SWNT

The optical transitions are fitted with Voigt profiles after subtracting the constant  $C_{\text{abs}}^{\text{nr}} = 0.14 \text{ nm}^2/\text{nm}$ . The Lorentzian function fits the exciton peak, while the Gaussian intensity profile accounts for the broadening due to the laser linewidth, with a FWHM  $\approx 14, 18$  and  $24 \text{ meV}$  for the near IR (700-1000 nm), visible (530-700 nm) and blue (390-530 nm) part of the spectra, respectively). Outcome of the fitting procedure for the (22,6) SWNT, which includes both a uniform non resonant absorption and the exciton peaks, is plotted on Fig. IV.1.a (dashed grey curve). The spectral features between 1.8 and 2.1 eV are not well reproduced, which implies that they do not arise from the same light-matter interaction processes as the exciton resonances  $S_{ii}$ ; this point is discussed later. The extracted amplitudes  $C_{\text{abs},S_{ii}}^{\text{exc}}$  and spectral widths  $\gamma_{S_{ii}}$  of the three excitonic resonances are reported in Tab. IV.1 (second row). The exciton peak linewidths tend to increase for highest energy transitions, varying from  $\approx 50 \text{ meV}$  for the  $S_{33}$  and  $S_{44}$  resonances to  $\approx 100 \text{ meV}$  for the  $S_{55}$ . The peak amplitude of excitonic absorption also depends on the energy transitions, decreasing from  $C_{\text{abs},S_{33}}^{\text{exc}} = 0.6 \text{ nm}^2/\text{nm}$  (corresponding to  $2.5 \times 10^{-17} \text{ cm}^2/\text{C atom}$ ) to  $C_{\text{abs},S_{44}}^{\text{exc}} = 0.2 \text{ nm}^2/\text{nm}$ , and then slightly increasing for the highest energy transition  $S_{55}$ . These direct absorption measurements provide experimental evidence for a non-constant optical oscillator strength of the different excitonic resonances, as well as a exciton dependent surface conductivity  $\sigma_S$ .<sup>a</sup>

##### Semiconducting (14,13) SWNT

Following the same procedure, exciton resonances  $S_{33}$ ,  $S_{44}$ , and  $S_{55}$  yield amplitude and linewidth that are similar to those of the (22,6) SWNT, i.e. a larger absorption cross-section for  $S_{33}$  and a broadening of energy transition  $S_{55}$  in comparison to others (see first row in Tab. IV.1). The non-resonant absorption yields  $0.12 \text{ nm}^2/\text{nm}$ . The

---

<sup>a</sup>These two points are discussed in details later

observation of similar characteristics for the two nanotubes is compatible with the fact that (22,6) and (14,13) SWNTs have comparable diameters and belong to the same semiconducting family (type I as  $\text{mod}(n-m, 3) = +1$ ). The absorption profile resulting from the fitting process is plotted in Fig. IV.2.b (red line). The exciton peaks and the non-resonant absorption are well reproduced by the profile, whereas few absorption side-features cannot be accounted for exciton transitions and require particular attention.

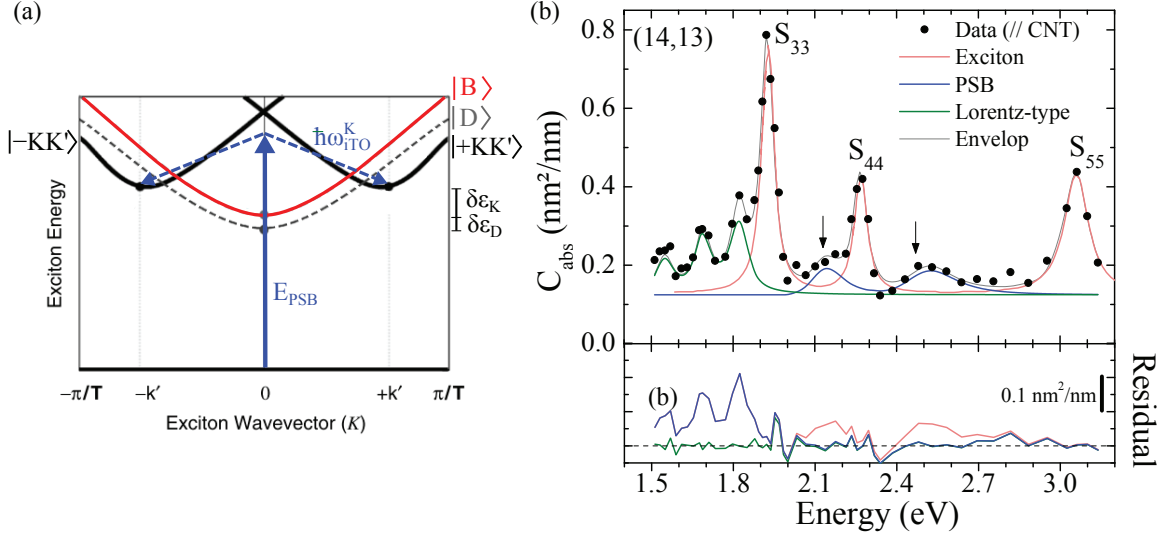


**Figure IV.2:** Principle of phonon-assisted absorption and fitting procedure of absorption spectra. (a) Sketch of the phonon-assisted absorption which give rise to the phonon side bands in the absorption spectra. During this two-particle process, a phonon of energy  $E_{\text{PSB}}$  is absorbed while a phonon of energy  $\hbar\omega_{\text{ITO}}^K$  and momentum  $\pm k'$  is created in the nanotube (see also Fig. II.8). (b) Detailed fitting procedure of the (14,13) SWNT absorption spectrum.

### Absorption side-features

The two broad absorption features that appear about 200 meV above the exciton transitions  $S_{33}$  and  $S_{44}$  are attributed to phonon-assisted optical transitions (indicated by black arrows in Fig. IV.2.b), or so called phonon side-bands (PSBs). As demonstrated in Sec. II-2.2.b, photon momentum imposes that light can couple with only two of the four singlet states and only the  $|B\rangle$  state is bright for the lower Rydberg state (Fig. II.8). The two K-momentum dark states  $|\pm KK'\rangle$ , resulting from the mixing of one electron and one hole from two different valleys ( $K$  and  $K'$ ), cannot couple directly to light. However, an indirect absorption process involving both a photon and an optical phonon allows the creation of an exciton in one of the dark state  $|\pm KK'\rangle$ . This excitonic absorption process is allowed under the conditions of both total momentum and total energy conservation, and yields maximum probability for transitions between the exciton ground state and the band edge of  $|\pm KK'\rangle$ . The phenomena of phonon-assisted absorption were first addressed theoretically by Perebeinos et al. in 2005 [129]. This work was followed by

many experimental studies that aimed at understanding this process by: photoluminescence [83, 130–135], photothermal heterodyne detection [9], and Rayleigh scattering [10]. Torrens et al. established that PSBs arise from the coupling between K-momentum dark exciton states ( $\pm |KK'\rangle$ ), and near-zone edge  $TO$  optical phonon modes  $K_{iTO}$  [132]. This process is sketched in Fig. IV.2.a: one photon of energy  $E_{\text{PSB}}$  is absorbed close to the center of the Brillouin zone, and one phonon is created with momentum  $\pm k'$  and energy  $\hbar\omega_{iTO}$ . The process involving the creation of both a exciton and a phonon is less inquired to take place as its probability is proportional to the number of phonons  $n_{\text{phonon}}$ , whereas the former process shows probability  $\propto 1 + n_{\text{phonon}}$ .<sup>b</sup> Although the splitting  $\delta_K$  between band edges of  $|B\rangle$  and  $\pm |KK'\rangle$  is supposed to scale as  $\sim 6/d^2$  in meV ( $d$  in nm) [135], for  $S_{33}$  and  $S_{44}$  transitions in free-standing SWNTs Berciaud et al. measured  $\delta_K \sim 35$  meV [10]. Then, the two PSBs, located at 2.21 eV and 2.52 eV, are associated to mixed-states of K-momentum dark excitons with in-plane near zone edge  $TO$  phonon modes (momentum  $k'_{iTO}$  and energy  $\sim 160$  meV). These features were fitted using the absorption model detailed in references [129] and [132, 135] including a broadening of about 50 meV. More precisely, the absorption profile of a single exciton peak  $E_{ii}$  including its PSBs is expressed as [129]:

$$I_{\text{abs}, E_{ii}}(E) \sim \delta(E - E_{ii}) + \frac{A_{iTO}\delta(\delta_K - E)}{(\delta_K + \hbar\omega_{iTO}^K)^2} \quad (\text{IV.1})$$

where the first and second terms account for the main exciton resonance (approximated by a delta function here) and the phonon-assisted absorption ( $A_{iTO}$  is the exciton-phonon coupling), respectively. As demonstrated by Perebeinos et al. this profile is described by the function

$$I_{\text{abs}, E_{ii}}(E) \sim \frac{A_{iTO}\delta(E_{ii} + \delta_K + \hbar\omega_{iTO}^K - E)}{(E - E_{ii})^2 + (A_{iTO}\delta(E_{ii} + \delta_K + \hbar\omega_{iTO}^K - E))^2}. \quad (\text{IV.2})$$

Then, an analytic expression for the PSB profile can be obtained by approximating the delta distribution by a Lorentzian function that reproduce the asymmetric lineshape of the PSB (see blue curve in Fig. IV.2.b).<sup>c</sup>

The three side peaks present below  $S_{33}$  are equally spaced ( $\sim 130$  meV) starting from the K-momentum dark exciton level (Fig. IV.2.b). To our knowledge, such peaks have never been observed in absorption experiments, whereas similar features arise from phonon-assisted emission in PL experiments [132]. Although their signature in the absorption spectrum resembles to bound exciton complexes (BECs) observed in semiconductors, it is unlikely that impurities and/or defects would create such equally-spaced peaks [42]. This is supported by the negligible D-band observed in the Raman spectrum (more than three order of magnitude smaller than the G-band). However, the energy spacing could match the energy of in-plane near zone edge transverse acoustic phonon modes  $K_{iTA}$ , which suggests phonon-assisted absorption below the bright exciton [98].

<sup>b</sup>Phonon side-bands are also observed in photoluminescence where both a photon and a phonon are emitted.

<sup>c</sup>After testing different functions to fit our data, this approximation gives the best result.

On the other hand, the peak around 1.68 eV presents a less pronounced polarization anisotropy, i.e. its absorption for perpendicular light excitation is significant. In this case, this peak could be interpreted as a cross-polarized transition  $S_{ij}$ . Finally, the mechanisms leading to these absorption side features are still unclear, nevertheless they can be fitted fairly well with three Lorentzian functions (see green curve in Fig. IV.2.b).

The grey line in Fig. IV.2.b is the result of the fit for the (14,13) SWNT absorption spectrum while including all the spectral features listed above. The low values of the residual over the whole spectrum demonstrates that we asset all features of the spectrum.

### Interpretation absorption features

To summarize, the fitting procedure describe above is applied to all absorption spectra in this thesis. Starting from the data, the excitonic transitions are addressed first before including possible phonon-side bands using the profile described in (IV.2). Eventually side features are not reproducible using the different profiles described before, in this case this part of the spectrum is not included in the fit. For example, the side peaks showing up around 1.9 eV and 2.05 eV in the absorption of the (22,6) SWNT (IV.1 ) cannot be fitted with PSB profile. It seems that the PSB of  $S_{33}$  resonance arises around 1.86 eV but it is mingled with other more complicated features between 1.9 and 2.05 eV (for this reason we chose not to fit this part of the spectrum). The comparison of the absorption spectra of the free-standing (14,13) and (22,6) SWNTs, showing strong PSBs in the first nanotube and weak side features in the other one, suggests that the coupling strength between K-momentum dark exciton and near zone edge optical phonon depends on the nanotubes chirality (chiral angle 12 for (22,6) and 29 for (14,13)). This behavior has already been proposed in refs. [78,135].

Another possible explanation for the assignment of absorption side-features has been proposed very recently by Verdenhalven and Malić in their theoretical investigation of the absorption for  $S_{11}$  and  $S_{22}$  [74]. They showed that the total oscillator strength is not always carried by the fundamental exciton  $|1u\rangle$  only but absorption is possible to the excited exciton states (e.g.  $|2u\rangle$ ) closer to the continuum. The latter features could fall in the same energy range as the PSBs but we could expect different profile. Moreover, the existence of these excited exciton states for high-order transitions is doubtful since they are expected to have smaller Coulomb interactions. Further experimental and theoretical study are required to confirm the nature of the absorption side-features with precision, e.g. temperature-dependent absorption might provide a way to discriminate phonon-assisted absorption and direct absorption to excited exciton states.

### IV-1.2.c Measurements uncertainties

Rigorously, all sources of noise should be included to evaluate total uncertainty on the measurements, including: the laser beam shaping and stability, the mechanical stability, the photodiode response, the lock-in amplifier response, and the environmental changes in the lab room. The evaluation of the uncertainty is obviously a tedious work and is not addressed in this thesis. As a rule of thumb, the uncertainties on these absolute absorption measurements are of the order of 10%, which reflects the maximum dispersion



of the values measured at different times. To the very extreme case, the uncertainties on these absolute absorption measurements are  $\pm 0.025$  nm, corresponding to  $\pm 0.1 \times 10^{-17}$  cm<sup>2</sup>/C atom for SWNTs diameters close to 2 nm.

### IV–1.3 Semiconducting SWNTs of family type II

Family behaviors have been observed in the optical properties of carbon nanotubes, i. e. semiconducting SWNTs of type I and type II respond differently to light excitation. To gain insights on this point, we measured the absorption of two type II semiconducting SWNTs (Figs. IV.3.a,b). The analysis of the Raman spectra in Figs. IV.3.e,f yield diameters of 2.24 nm ( $\omega_{\text{RBM}} = 118$  cm<sup>-1</sup>) and 2.49 nm ( $\omega_{\text{RBM}} = 109$  cm<sup>-1</sup>) for the two nanotubes, respectively. The two tubes show strong LO phonon modes close to 1592 cm<sup>-1</sup>, and weak TO phonon modes slightly shifted to lower frequencies as in good agreement with the diameter dependence of  $\omega_{\text{TO}}$  [19]. The absorption and Raman spectra clearly demonstrate the individual and single walled character of these two semiconducting nanotubes.

Considering both the absorption peaks positions in Fig. IV.3.a,b and the diameters, the 2.24 nm (CNT 3) and 2.49 nm (CNT 4) nanotubes are assigned to semiconducting SWNTs of family II (precise chirality assignment is discussed in Appx. A and yields the most probable chirality (24,7) and (31,2) for CNT 3 and CNT 4, respectively). In this region of diameter, CNTs of different chirality show close lying energy transition  $E_{ii}$  for each  $i$ . For this reason, the nanotubes can be possibly assigned to different chiralities (the assignment does not change the interpretation of the results as long as the nanotubes nature and family type (I or II for semiconducting tubes) are determined). Then, the exciton transitions in these two tubes are identified as  $S_{33}$ ,  $S_{44}$ ,  $S_{55}$ , and  $S_{66}$ , as depicted in Fig. IV.3.a,b. The characteristics of their excitonic resonances are listed in Tab. IV.1 (4<sup>th</sup> and 5<sup>th</sup> rows). Interestingly, strong phonon-side bands are observed at 1.99 eV and 2.81 eV in CNT 3, i. e. 200 meV and 190 meV above the  $S_{44}$  and  $S_{66}$  resonances, respectively. The other nanotube also shows strong PSBs at 1.96 eV and 2.84 eV, respectively, 170 meV and 180 meV above the  $S_{44}$  and  $S_{66}$  transitions.

PSB features composing the absorption spectra of the SWNTs can be compared between the four nanotubes presented. Vora et al. reported a significant dependence of the PSB amplitude with the nanotubes chirality (family behavior and chiral angle) [135]. Our data for the four selected SWNTs seem to confirm this tendency.

### IV–1.4 Interpretation and oscillator strength

#### Peak absorption cross-section

The peak absorption cross-sections of the SWNTs are reported in Fig. IV.4.a.  $C_{\text{abs},S_{ii}}^{\text{peak}}$  are measured in the range  $1 - 5 \times 10^{-17}$  cm<sup>2</sup>/C atom with strong variations between the transitions  $S_{ii}$  and the nanotubes. These values are in agreement with those reported in the literature for similar tubes [14,107]. Family behavior is observed through the ratio  $C_{\text{abs},S_{33}}^{\text{peak}}/C_{\text{abs},S_{44}}^{\text{peak}}$  which yields  $\sim 2$  and  $\sim 0.9$  for type I and II SC-SWNTs, respectively. [110,136].

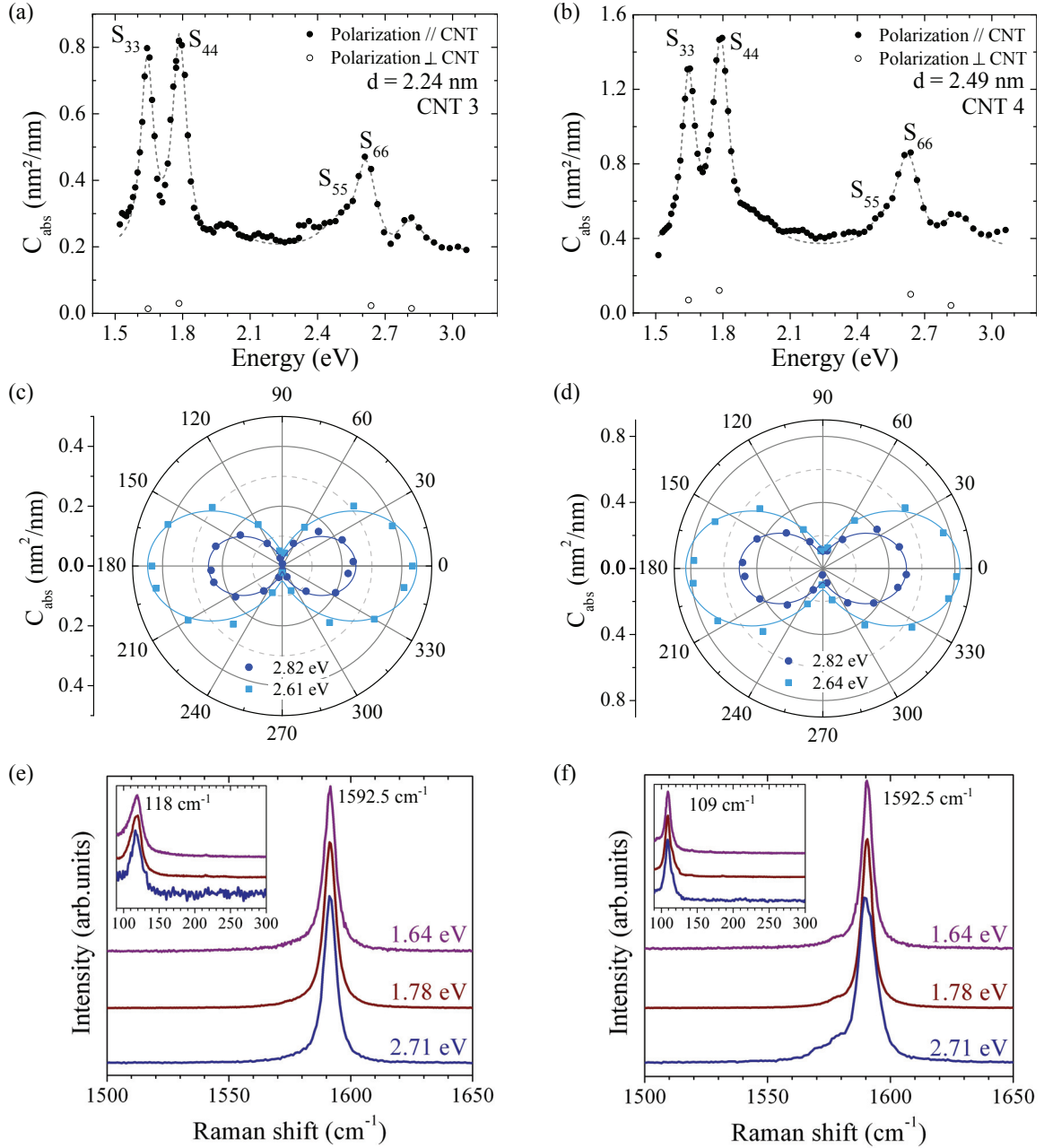


**Figure IV.3:** Absorption and Raman spectroscopy of individual free-standing type II semiconducting SWNTs. Results are presented for the  $d = 2.24$  nm (CNT 3, left panels) and the  $d = 2.49$  nm (CNT 4, right panels) semiconducting SWNTs. (a,b) Absolute absorption cross-section spectrum for incident light parallel (full dots) and perpendicular (open dots) to the nanotube. The dashed line is the result of the fit detailed in the main text. (c,d) Light-polarization-dependent absorption cross-section for two laser excitation energies. The experimental data (symbols) are fitted using  $C_{\text{abs}}^{\parallel} \cos^2 \theta_{\text{pol}} + C_{\text{abs}}^{\perp} \sin^2 \theta_{\text{pol}}$  function (line),  $\theta_{\text{pol}} = 0$  being the direction parallel to the nanotube. (e,f) Raman spectra showing the tangential modes and radial breathing mode (inset) measured with three different excitation energies labeled on the figure close to absorption peaks.



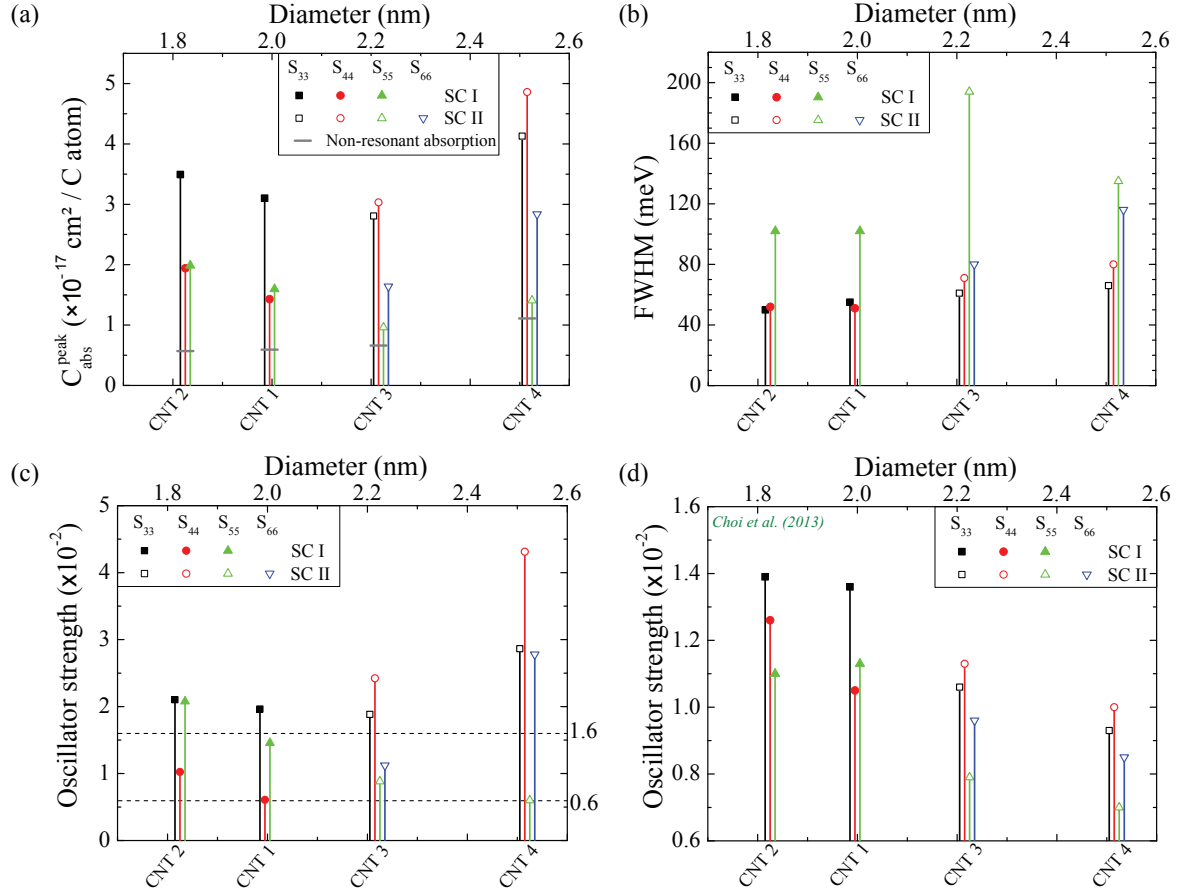


**Figure IV.4:** Absorption properties of individual free-standing single-wall carbon nanotubes. Quantitative absorption measurements for parallel polarization are plotted versus nanotube diameters. The SWNT chiral indices and angles are indicated on the figure. (a) Absolute absorption cross-section at the energy transitions. (b) Full-width at half maximum of the exciton transitions. (c) Experimental oscillator strength per C-atom  $f_C$  obtained from (IV.3) and values in Tab. IV.1. (d) Theoretical  $f_C^{\text{th}}$  computed from (II.21) and ref. [96].

SWNT	Assignment	Energy transition	$E_{ii}$ (eV)	$C_{\text{abs}}$ (nm <sup>2</sup> /nm)	$C_{\text{abs}}$ (10 <sup>-17</sup> cm <sup>2</sup> /C atom)		$\gamma_{S_{ii}}$ (meV)
					$C_{\text{abs},S_{ii}}^{\text{exc}}$	$C_{\text{abs},S_{ii}}^{\text{peak}}$	
$d = 1.83$ nm $\theta_c = 29^\circ$ CNT 2	SC type I (14,13)	$S_{33}$	1.93	0.64	2.9	3.5	50
		$S_{44}$	2.27	0.3	1.4	1.9	52
		$S_{55}$	3.06	0.31	1.4	2	102
$d = 2$ nm $\theta_c \leq 12^\circ$ CNT 1	SC type I (22,6) (23,4)	$S_{33}$	1.66	0.6	2.5	3.1	55
		$S_{44}$	2.21	0.2	0.8	1.4	51
		$S_{55}$	2.61	0.24	1	1.6	102
$d = 2.22$ nm $\theta_c \leq 12^\circ$ CNT 3	SC type II (24,7)	$S_{33}$	1.64	0.57	2.1	2.8	61
		$S_{44}$	1.79	0.63	2.4	3	71
		$S_{55}$	2.5	0.08	0.3	1	194
		$S_{66}$	2.62	0.26	1	1.6	80
$d = 2.52$ nm $\theta_c \leq 10^\circ$ CNT 4	SC type II (30,4) (31,2)	$S_{33}$	1.65	0.91	3	4.1	66
		$S_{44}$	1.79	1.13	3.7	4.9	80
		$S_{55}$	2.5	0.09	0.3	1.5	135
		$S_{66}$	2.63	0.52	1.7	2.8	116

**Table IV.1:** Absorption characteristics of individual single-wall carbon nanotubes. After subtracting a constant non-resonant contribution, peaks of the absorption spectra plotted in Figs. IV.1 and IV.3 are fitted using Voigt profiles with fixed Gaussian linewidth accounting for the laser lineshape. The extracted widths  $\gamma_{S_{ii}}$  correspond to the full-width at half maximum of the Lorentzian functions describing the excitonic resonances. Note:  $C_{\text{abs},S_{ii}}^{\text{peak}} = C_{\text{abs},S_{ii}}^{\text{exc}} + C_{\text{abs}}^{\text{nr}}$ .

### Exciton linewidth

Fig. IV.4.b presents the evolution of the exciton FWHM with both diameter and energy transition  $S_{ii}$ .  $\gamma_{S_{33}}$  and  $\gamma_{S_{44}}$  have values in the range 45 – 80 meV, whereas higher-order resonances yield FWHM greater than 100 meV. Although the nanotubes belong to different families and have various chiral angles,  $\gamma_{S_{ii}}$  shows an increasing trend with diameter suggesting a decrease of the overall exciton lifetime.

Rayleigh scattering shows broader exciton peaks [10, 137], and PL excitation experiments reported linewidths below  $\sim 30$  meV for the  $S_{11}$  and  $S_{22}$  resonances [15, 65]. Previous work reported a broadening of the energy transitions in photothermal absorption with respect to PLE, that is attributed to the presence of non-luminescent traps [9].

### Oscillator strength

Exciton peaks are characterized by their FWHM  $\gamma_{S_{ii}}$  and their amplitude (see Tab. IV.1). Although the laser linewidth is accounted in the fit procedure, the peak amplitude is hardly comparable from one laser to another. Therefore, a quantity of choice which characterize the excitonic absorption of nanotubes is the **oscillator strength per carbon atom**. The latter is directly proportional to the area of the exciton peak and is expressed as (without units) [106]:

$$f_C = \frac{4\varepsilon_0 cm_e}{\hbar e^2} \int C_{\text{abs}}^{\text{exc}}(E) dE, \quad (\text{IV.3})$$

where the constant leading the integral gives  $9.11 \cdot 10^{15} \text{ cm}^2 \cdot \text{eV}^{-1}$ , and  $C_{\text{abs}}$  is in units of  $\text{cm}^2/\text{C atom}$ .<sup>d</sup> The oscillator strength  $f$  is proportional to the probability to find an electron and a hole at the same position, and  $f_C$  can be interpreted as the mean number of electron-hole pair in each C-atom that are promoted to excited states through one photon excitation.  $f$  is related to the exciton lifetime and its spatial expansion. For example, a typical value of  $f_C$  in SWNTs is 0.01 which means that one electron results from the excitation of one hundred C-atom. Combining oscillator strength and the radiative exciton lifetime provide an estimate of the exciton size (see [106] for the method applied to (6,5) SWNTs). The exciton lifetime was estimated to be of the order of tens of picoseconds for high-order energy transitions (this value differs from those obtain in small nanotubes for  $S_{11}$  and  $S_{22}$ ) [14, 67, 94]. In the following we concentrate on the analysis of the oscillator strength per C-atom uniquely.

Fig. IV.4.c sketches the  $f_c$  values for the four free-standing SWNTs.  $f_C$  ranges from 0.005 to 0.025 for the three smaller nanotubes, and values up to 0.043 are observed for the larger tube. These values are in good agreement with results for  $S_{11}$  and  $S_{22}$  in small diameter tubes excited with unpolarized light [106]. Strong variations of the oscillator strength per C-atom are observed from one energy transition to the other for a given nanotubes, as well as between CNTs. Clear difference is observed between type I SC-SWNTs and type II SNWTs. The former show weaker oscillator strength for the  $S_{44}$ , whereas the situation is reversed in the latter. This trend is in good agreement with recent theoretical study that yield the analytic formula (II.21) for  $f_C$  in semiconducting nanotubes [96]. The computed values are reported in Fig. IV.4.d and show an overall decrease of  $f_C$  with increasing diameters. Experimentally, the oscillator strength exhibit an overall increase with  $d$ , which is in good agreement with theoretical studies on  $S_{11}$  and  $S_{22}$  [74, 110]. Exciton lifetime that is inversely proportional to the oscillator strength shows overall decrease for energy transitions  $S_{33}$ ,  $S_{44}$ , and  $S_{66}$ , whereas it increases for  $S_{55}$ . This point should be addressed carefully without either the knowledge of exciton size or direct measurement of the exciton lifetime.

## IV–1.5 Optical conductivity

From a general point of view, the absorption cross-section of a nano-object is related to the imaginary part of its polarisability (or, equivalently, to the real part of its optical conductivity) and is possibly affected by local field effects [124]. For an elongated nanotube of diameter  $d$  and length  $L$ , with  $d \ll \lambda \ll L$ , in a homogeneous medium of refractive index  $n_m$ , the local field is actually identical to the incident electric field when light is polarized parallel to the nanotube axis. In this configuration, the absorption cross section per unit length,  $C_{\text{abs,L}}$ , computed in the quasi-static approximation then simply writes:

$$C_{\text{abs,L}}(\omega) = \frac{\pi d Z_0}{n_m} \text{Re}(\sigma_s(\omega)), \quad (\text{IV.4})$$

---

<sup>d</sup>This relation is derived from the Thomas-Raiche-Kuhn sum rule stating that the sum of all oscillator strengths  $f$  from one sub-band to all other states is equals to the atomic number  $Z$ .

where  $Z_0 = 1/\varepsilon_0 c_0$  is the impedance of the medium and  $\sigma_s$  the real part of the nanotube sheet conductivity. The absorption cross section per carbon atom is then given by:

$$C_{\text{abs}}(\omega) = \frac{a_C^2}{d} C_{\text{abs,L}}(\omega), \quad (\text{IV.5})$$

where  $a_C$  is the radius of the equivalent surface occupied by a carbon atom in the crystalline lattice ( $a_C = a_0^2 \sin(\pi/3)/2\pi \text{ nm}^2 = 8.36 \cdot 10^{-3} \text{ nm}^2$ ). Using this simple model, the absolute absorption spectra of SWNTs measured here yield access to their optical conductivity  $\sigma_s(\omega)$  at the excitonic transitions or out of resonance.

The three smallest semiconducting SWNTs investigated in this work with diameter  $d$  in the 1.8-2.2 nm range, show a non-resonant absorption cross-section  $C_{\text{abs}}^{\text{nr}} = (0.6 \pm 0.1) \times 10^{-17} \text{ cm}^2/\text{C atom}$  (Tab. IV.1). This  $C_{\text{abs}}^{\text{nr}}$  value is almost independent of the family of the nanotube (type I or II) and not affected by the presence of a substrate, suggesting it reflects an intrinsic properties of SWNT (at least for small SWNTs, only the largest diameter nanotube with  $d = 2.5 \text{ nm}$  showing a larger non-resonant absorption. However in this CNT the orthogonally polarized absorption is also larger than the one measured for smaller tubes, Fig. IV.3b). Using this  $C_{\text{abs}}^{\text{nr}}$  value and the previous expression with  $n_m = 1$  for free-standing SWNT, a non-resonant optical conductance is derived:  $\sigma_s^{\text{nr}} = (6 \pm 1) \times 10^{-5} \Omega^{-1}$  (Fig. IV.5). This value is comparable to the frequency independent ‘ideal’ sheet conductivity of graphene which has been addressed theoretically and measured recently in the infra-red:  $\sigma_g = G_0\pi/2$  where  $G_0$  is the quantum of conductance [138–140]. The non-resonant absorption measured in SWNTs is thus possibly a consequence of their conductivity and of identical physical origin as the absorbance of graphene, i.e. directly related to the fine structure constant.

However, recent measurement of the graphene optical conductivity in the visible and UV spectral range yields deviation from the constant  $\sigma_g$  obtained in the near-IR (and from tight-binding calculations in the single-particle model) [141]. Precisely, graphene optical absorption arising from inter-band transitions presents a broad and asymmetric absorption peak near the saddle-point singularity at the M-point in the graphene dispersion (around 4.62 eV in pristine graphene, and is expected to depend on doping). This feature is explained by including many-body interactions showing an exciton resonance at an energy below the saddle-point singularity coupled with the existing continuum of electronic states [141]. Although UV absorption features from similar origin have been predicted in carbon nanotubes [142], their contribution to the visible absorption vanishes due to the discreet DOS resulting from zone-folding. Therefore, only frequency independent sheet conductivity should be considered in this case as stated before. On the other hand, the continuum of the lower energy resonances  $S_{ii}$  ( $i < 2$ ) is expected to contribute to the non-resonant absorption at higher energy through creation of free electron-hole carriers.

To summarize, we have proposed two physical origins for the non-resonant absorption, one identical to the absorbance of graphene (see discussion above) and the other due to exciton continuum in CNTs. Nevertheless, further investigations will help to clarify the

origin of  $C_{\text{abs}}^{\text{nr}}$  which seems to scale with nanotube diameter [109].

Similarly, the absorption cross-sections per unit length measured for the excitonic transitions can be expressed in terms of optical conductance. For the investigated SWNT, they are found to be a few units of quantum conductance  $G_0$ , varying in the  $4G_0$  to  $9G_0$  range for the  $S_{33}$  and  $S_{44}$  transitions (see also Tab. IV.1). This range is compatible with the results of recent Rayleigh scattering experiments [14, 143]. However, much larger systematic dependence of  $\sigma_S(\omega)$  (or of the absorption cross-section) on the excitonic transitions, and thus of the associated oscillator strength  $f_C$ , is demonstrated by our absorption measurements (Fig. IV.4).

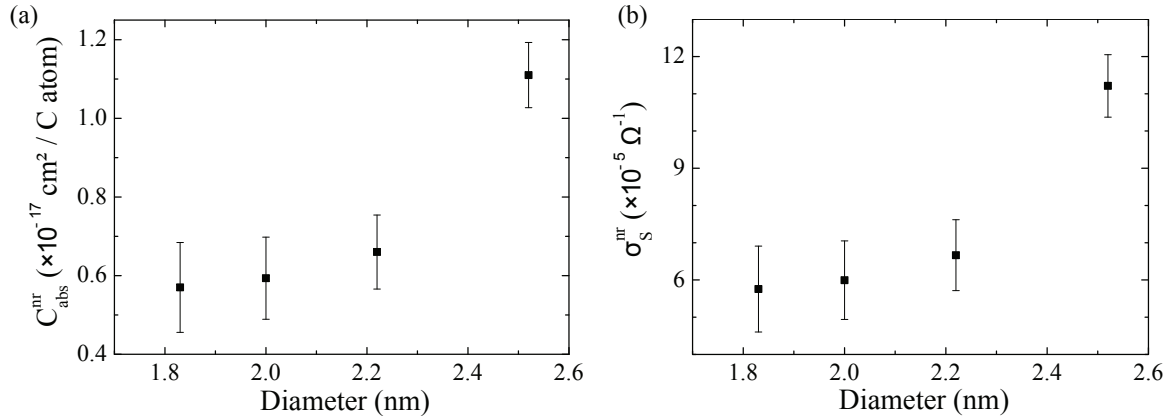


**Figure IV.5:** Non-resonant absorption and conductivity measured in individual free-standing SC-SWNTs.

## IV–2 Single-wall carbon nanotube bundles

Broadband absolute absorption of free-standing nanotubes have been discussed. Freely suspended individual SWNTs are appealing candidates for the investigation of CNT intrinsic electronic properties. Moreover, this experimental configuration resemble the situations addressed in most theoretical studies. The main drawback of such sample concerns the difficulties to control the structure of the synthesized nanotubes: chirality, number of walls, bundling, ... For practical applications, many groups have made a lot of progress towards the control of nanotubes growths supported on specific substrates and/or embedded into different media. Although a large amount of studies deal with the optical properties of these carbon nanotubes, quantitative analysis of the results is often challenging in the presence of environmental effects.

In this section, we analyse the optical response of semiconducting SWNTs interacting with metallic nanotubes. In other words, bundles composed of one semiconducting SWNT and metallic SWNT(s) are characterized by means of absorption and Raman spectroscopy. Preliminary analysis of the influence of the tube-tube interactions on the absorption response is proposed in the last paragraph.

## IV-2.1 Absorption and Raman spectroscopy

Optical properties of free-standing bundles composed of two or three SWNTs are investigated by means of absorption and Raman spectroscopy. Two selected nanotube bundles are selected from sample FS-2:

- bundle B1 with absorption and Raman spectra in left panels of Fig. IV.6,
- bundle B2 with absorption and Raman spectra in right panels of Fig. IV.6.

This is interesting to notice that absorption spectra of bundles still show sharp excitonic peaks (the absorption main features are well fitted with Lorentzian-like profile whereas they cannot be reproduced with band-to-band transition model) and non-resonant absorption background. Resonant Raman spectroscopy is performed close to the different absorption resonances allowing the diameter identification of each nanotube composing the bundle. In the following, the results are described for each sample independently, and a general interpretation is proposed thereafter.

### Identification bundle B1

The absorption spectrum of B1 show absorption peaks at energy values 1.71, 1.90, 2.00, 2.20 and 2.71 eV (Fig. IV.6.a). Depending on the laser excitation, Raman spectra present LO and TO phonon modes characteristic of either semiconducting (Fig. IV.6.b) or metallic (Fig. IV.6.c) nanotubes.<sup>e</sup> The semiconducting part of the bundle shows a sharp  $G^+$  peak (LO phonon) and  $G^-$  mode (TO phonon) at  $1592\text{ cm}^{-1}$  and  $1573\text{ cm}^{-1}$  respectively. A weak mode shows up around  $1579\text{--}1580\text{ cm}^{-1}$  which is sometimes observed in substrate-supported nanotubes or in bundles, its origin is still not clear though. For the three excitation energy, the same single RBM at  $123\text{ cm}^{-1}$  is observed, yielding a diameter  $d_{SC} = 2.12\text{ nm}$  [105]. Raman spectra show a response typical of a metallic tube for the absorption doubled-peak around 2.0 eV and is associated with a RBM frequency at  $191\text{ cm}^{-1}$  (corresponding diameter  $d_M = 1.24\text{ nm}$ ).

Chirality assignment is possible using the diameters ( $d_{SC}$  and  $d_M$ ) and the positions of the absorption peaks. Using the same procedure as for free-standing SWNTs, we derive the composition of the bundle with possible chirality assignment:

- (20,10) type I semiconducting SWNT with  $d_{SC} = 2.11\text{ nm}$ ,<sup>f</sup>
- (12,6) metallic SWNT with  $d_M = 1.24\text{ nm}$ .

<sup>e</sup>Detailed analysis of Raman spectra in carbon nanotubes is beyond the scope of this thesis and the discussion should be kept short on this point. Further details can be found in the following reference list (not exhaustive): [18, 19, 33, 89, 98, 99, 105, 144–146].

<sup>f</sup>We give here the most probable chirality which do not exclude few other possible choices. It is important to notice the nature of the tube: type I.

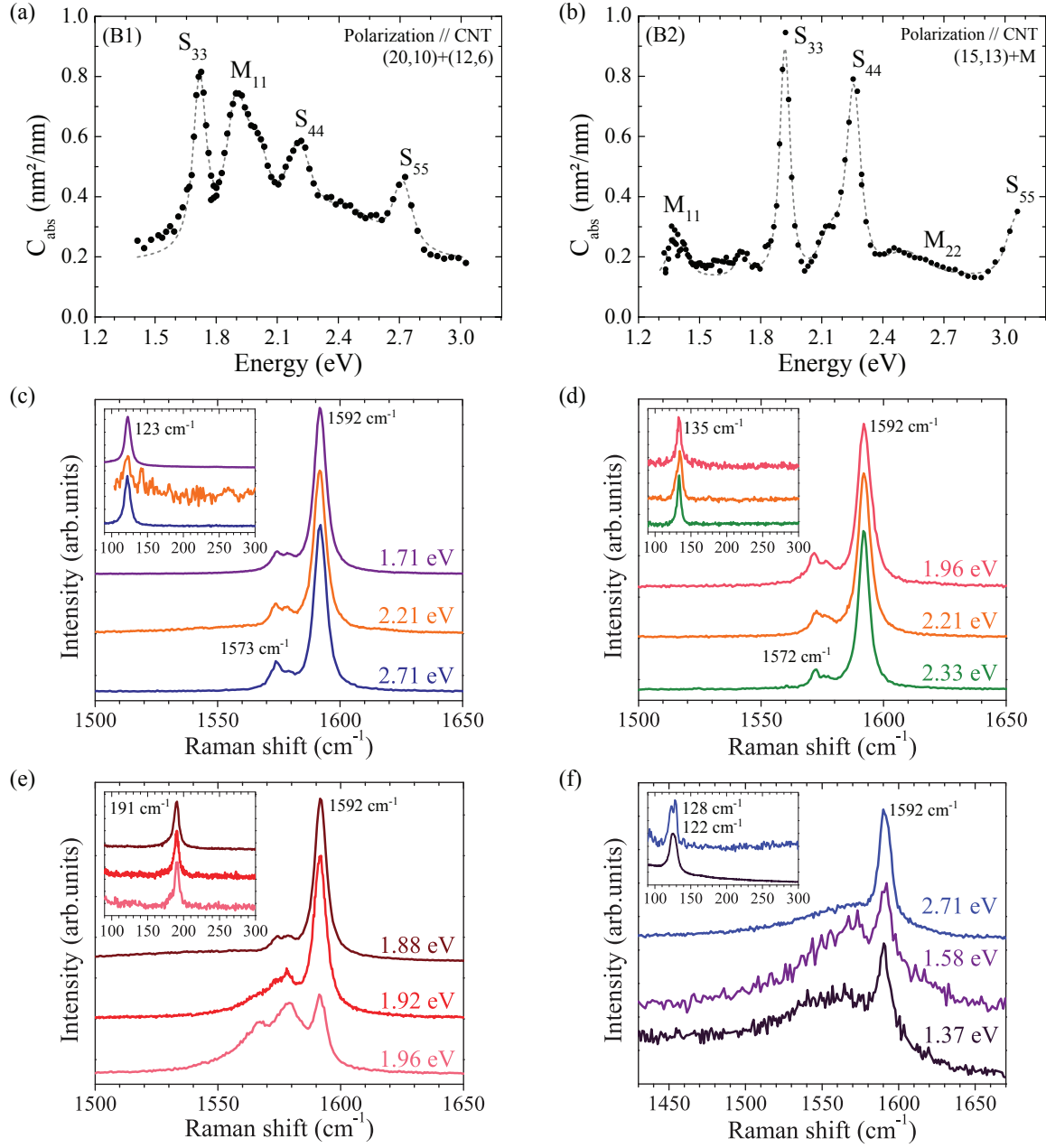


**Figure IV.6:** Absorption and Raman spectroscopy of two free-standing bundles of SWNTs. Results are presented for the B1 (left panels) and B2 (right panels) bundles, each composed of both semiconducting and metallic SWNTs. (a,b) Absolute absorption cross-section spectrum for incident light parallel. The dashed line is the result of the fit detailed in the main text. (d-f) Raman spectra showing the tangential modes and radial breathing mode (inset) measured with three different excitation energies labelled on the figure close to absorption peaks (see text for details).



### Identification bundle B2

Absorption peaks at positions 1.37, 1.42, 1.92, 2.26, 3.06 eV are observed on the absorption spectrum of B2 (Fig. IV.6.b). Raman spectra at different excitation energy show either semiconducting (Fig. IV.6.d) or metallic (Fig. IV.6.f) typical behavior. B2 is composed of:

- one type II semiconducting SWNT with  $d_{SC} = 1.89$  nm (RBM at  $135$   $\text{cm}^{-1}$ ) identified as (15,13).
- two metallic SWNTs with  $d_M = 2.01$  nm and  $2.14$  nm (RBM at  $128.5$   $\text{cm}^{-1}$  and  $122$   $\text{cm}^{-1}$ , respectively).

### Raman LO and TO phonon modes

As labeled on the absorption spectrum (Fig. IV.6.a,b), peaks have been associated with the nanotubes energy transitions based on both the Kataura plot and their diameters. Before presenting into details the fitting of the absorption data, we further discuss the G-phonon modes region of the Raman spectra (Fig. IV.6.c-f). We recall the difference between semiconducting nanotubes which present two ‘thin’ phonon modes  $G^+$  (LO phonons) and  $G^-$  (TO phonon), whereas metallic CNTs are characterized by a thin  $G^+$  mode (TO phonon) and broad  $G^-$  mode (LO phonon).<sup>g</sup>  $G^+$  peak is measured at  $1592$   $\text{cm}^{-1}$  for all Raman spectra. For semiconducting SWNTs, clear  $G^-$  feature is identified around  $1572$   $\text{cm}^{-1}$  in both samples (the two nanotubes present comparable diameter). Another mode is present around  $1580$   $\text{cm}^{-1}$  that is usually present for tubes on substrate, and could be attributed here to the interaction between nanotubes (this mode is absent for individual free-standing SWNTs).

In the case of metallic tubes, broad  $G^-$  phonon appear at about  $1570$   $\text{cm}^{-1}$  and its intensity depend on the excitation energy based on resonant conditions. For example, for excitation  $1.88$  eV in B1, we observed both RBM from the metallic tube and G-modes from the semiconducting nanotube (Fig. IV.6.e). However, both RBM and G-phonon modes are characteristic of the metallic CNT at  $1.96$  eV. This behavior is explained by the Stokes Raman scattering process which consists in the absorption of a photon whose energy is incremented by the energy of the probed phonon (either RBM or G-phonon modes in nanotubes). For example, for laser excitation  $1.88$  eV, G-phonon modes associated with the semiconducting tube are excited ( $\sim 200$  meV above  $S_{33}$ ), and in the meantime the RBM of the metallic tube is observed as the laser excitation is resonant with  $M_{11}$ .

In summary, combination of absorption and Raman spectroscopy allow full identification and characterization of each absorption peak. Following a similar procedure we were able to determine the composition of bundles composed of more than five nanotubes. Still, in these type of samples excitonic absorption features are observed on top of a non-resonant absorption which is greatly enhanced.

<sup>g</sup>The situation is different for zig-zag and armchair nanotubes which are characterized by a single peak [18].



### Absorption features in bundles

Absorption spectra were fitted using the method described in Sec. IV–1.2.b: Voigt profiles for the energy transition peaks, possible phonon side-bands, and constant non-resonant absorption. We underline that Lorentzian-like profiles proved to be the best candidates for the fitting of the absorption peaks even in the case of metallic nanotubes, in fact band-to-band transition model fails to reproduce the spectra.

Results of the fits are plotted on the spectra (gray dashed lines in Fig. IV.6.a,b) and the exciton peak characteristics are reported in Tab. IV.2. First, we observe a splitting of the metallic absorption peaks  $M_{11}$  (into  $M_{ii(-)}$  and  $M_{ii(+)}$ ) explained by trigonal warping effect [20, 62]. In the absorption spectrum of B2, the experimental data between 1.5 and 1.7 eV are not well reproduced using Lorentzian profiles, moreover no excitonic transition is expected in this spectral range. This additional ‘non-resonant’ absorption is explained by the presence of pronounced free carrier absorption as a consequence of weak exciton binding energy in metallic nanotubes accompanied by a transfer of the oscillator strength to the continuum of states [73, 95].<sup>h</sup> This behavior is a strong indication that the  $M_{11}$  transitions keep their excitonic nature despite the strong free-carriers screening effects present in metallic materials. From the fitting result in B2 (Fig. IV.6.b) we extract an exciton binding energy of about 50 meV, consistent with previous observation [95]. In B1 (Fig. IV.6.a), identification of this behavior proved to be more difficult, nevertheless a important non-excitonic absorption is observed close to the  $M_{11}$  resonances, and more particularly the range 2.4-2.6 eV cannot be adjusted with either excitonic or band-to-band model (PSB and/or excited exciton states of  $S_{44}$  can also be present in this spectral region). Theoretical support will provide additional insights in these phenomena.

The metallic nanotubes in B2 are expected to have transitions  $M_{22(-)}$  and  $M_{22(+)}$  in the region between 2.4 and 2.6 eV as demonstrated by the Raman response for laser excitation 2.71 eV (Fig. IV.6.f) and the Kataura plot [16, 44]. However, this spectral range is subject to different absorption phenomena as possible PSB and/or excited exciton states from  $S_{44}$  mix with the four  $M_{22}$ . Hence, it was hardly possible to separate these contributions in the absorption signal. Doorn et al. showed that, in this diameter range, optical response of  $M_{22}$  is roughly one order of magnitude smaller than signal from  $M_{11}$  [62]. Given the relatively small amplitude of the  $M_{11}$  energy transitions, we can assume the  $M_{22}$  to be strongly damped in comparison to the amplitude of the PSB.<sup>i</sup> As a consequence, the feature around 2.45-2.5 eV was addressed using the PSB profile introduced in Sec. IV–1.2.b. This interpretation is confirmed by the observation of a strong PSB associated with the resonance  $S_{33}$  at about 2.1 eV (approximately 200 meV above the main resonance). These PSBs are hardly distinguishable in B1 (absent or mixed up with the strong non-resonant absorption), where the semiconducting SWNT

<sup>h</sup>Malić et al. estimated binding energies smaller than 100 meV for  $M_{11}$  and  $M_{22}$  for nanotube diameters bigger than 1 nm. [73]

<sup>i</sup>The semiconducting SWNT in B2 is identified as (15,14), thus its absorption response is close to the one measured for the (14,13) SWNT which present strong PSB around 2.5 eV (see Fig. IV.1.b).

is assigned to (20,10). These observations are consistent with the results in individual free-standing (22,6) and (14,13) SWNTs, and supports the possible dependence of the PSB amplitude with nanotube chiral angle. Besides, the side-peaks appearing at 1.7 eV in B2 (below the main exciton  $S_{33}$  of (15,13)) resemble the features observed in (14,13). No clear PSB is observed above the metallic energy transitions. They are expected to be twenty times weaker than the main exciton peak and damped in the continuum [10].

Bundle SWNT	Probable assignment	Energy transi- tion	$E_{pp}$ (eV)	$C_{abs}$ (nm <sup>2</sup> /nm)	$C_{abs}$ (10 <sup>-17</sup> cm <sup>2</sup> /C atom)		$\gamma_{pp}$ (meV)
					$C_{abs}^{exc}$	$C_{abs}^{peak}$	
$d = 2.11$ nm $\theta_c = 19^\circ$	SC type I (20,10)	$S_{33}$	1.71	0.57	2.3	2.7	70
		$S_{44}$	2.2	0.32	1.3	1.7	159
		$S_{55}$	2.71	0.24	1	1.4	94
$d = 1.24$ nm $\theta_c = 19^\circ$	Metallic (12,6)	$M_{11(-)}$	1.9	0.45	3	4.1	118
		$M_{11(+)}$	2	0.27	1.8	2.9	132
$d = 1.90$ nm $\theta_c = 28^\circ$	SC type II (15,13)	$S_{33}$	1.92	0.82	3.6	3.8	48
		$S_{44}$	2.26	0.65	2.9	3.0	71
		$S_{55}$	3.06	0.23	1	1.2	86
$d = 2.01$ nm $d = 2.14$ nm	Metallic $\times 2$	$M_{11}$	1.37	0.12	0.5	1	58
		$M_{11}$	1.42	0.09	0.4	0.9	65

**Table IV.2:** Absorption characteristics of free-standing bundles of single-wall carbon nanotubes. Top and bottom bunch of rows present the exciton characteristics of the bundles B1 and B2, respectively. The corresponding absorption spectra are shown in Fig. IV.6.a,b, as well as the results of the fits (dashed grey lines).

## IV-2.2 Interpretation of absorption in bundles

The properties ( $C_{abs}$ , FWHM, oscillator strength) of the excitonic energy transitions are listed in Tab. IV.2 (top for B1, bottom for B2). We also assigned in the table the most probable chirality for each SWNT based on results from absorption and Raman spectroscopy. The properties of the semiconducting SWNTs, (15,13) in B1 and (20,10) in B2, are plotted in Fig. IV.7 along with the results obtained for individual nanotubes. Values of  $C_{abs,S_{ii}}^{peak}$ ,  $\gamma_{S_{ii}}$ , and  $C_{abs}^{nr}$  are comparable to the measurements on individual free-standing SWNTs (Sec. IV-1). However, some differences should be underlined due to bundling effects and the presence of metallic nanotubes. More particularly, for  $S_{ii}$  resonances close to  $M_{11}$  in B1 and  $M_{22}$  in B2 we observe few changes either in their amplitude or linedwidth. These changes are directly observable on the oscillator strength (Fig. IV.7.c) that show enhanced values for  $S_{44}$  transitions in comparison to adjacent individual tubes and to theoretical trend (Fig. IV.7.d). The metallic nanotubes influence is clearly visible for the  $S_{44}$  exciton peak of the (20,10) CNT (in bundle B1) which is about two times larger than expected. However, energy transitions  $S_{33}$  (below the metallic resonance) and  $S_{55}$  (far from the metallic resonance) appear not to be much affected by the presence of the metallic CNT. These differences are more difficult to observe in B2.

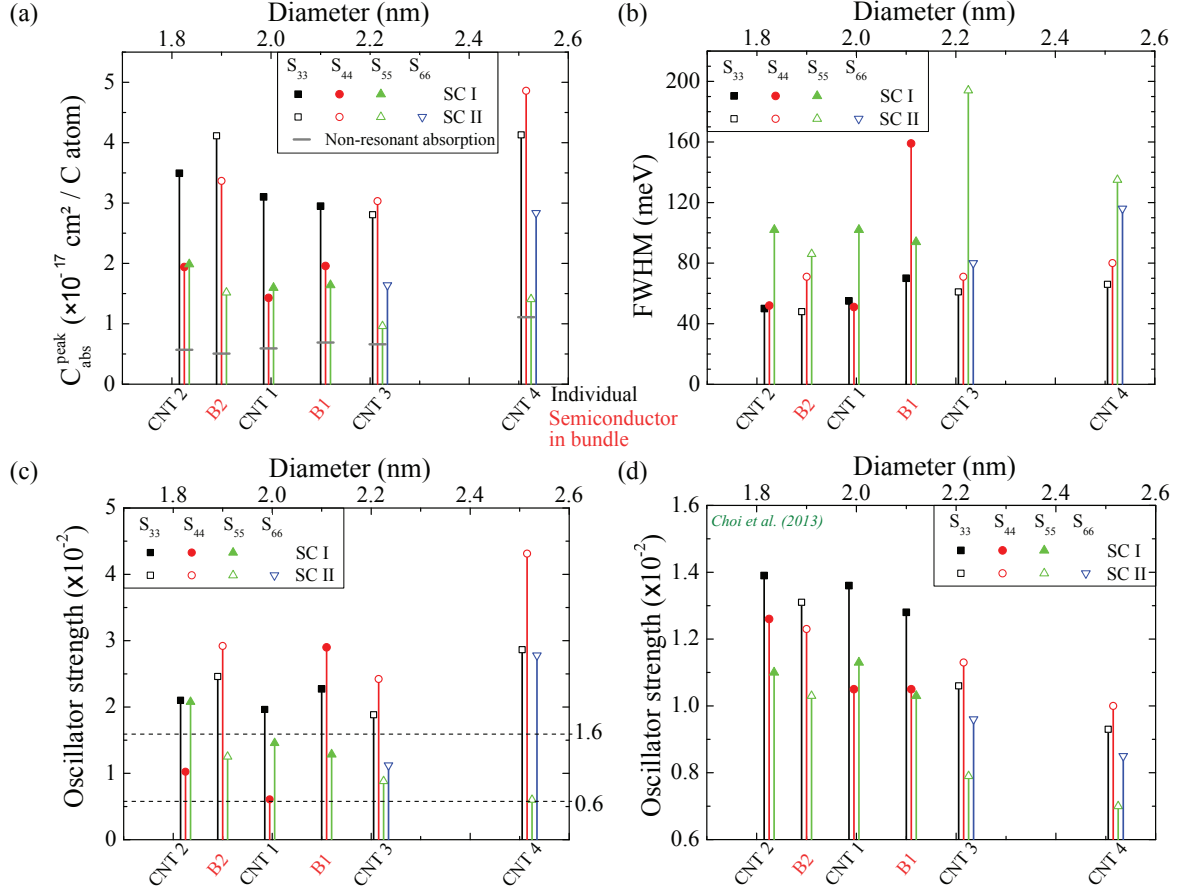


**Figure IV.7:** Absorption properties of semiconducting SWNTs included in free-standing bundles. Quantitative absorption measurements for parallel polarization are plotted versus nanotube diameters for semiconducting nanotubes in bundles B1 (20,10) and B2 (15,13). Results for individual free-standing SWNTs are also reported on the graphs for comparison (see also Fig. IV.4). (a) Absolute absorption cross-section at the energy transitions. (b) Full-width at half maximum of the exciton transitions. (c) Experimental oscillator strength per C-atom  $f_C$  obtained from (IV.3) and values in Tab. IV.2. (d) Theoretical  $f_C^{\text{th}}$  computed from (II.21) and ref. [96].

Fig. IV.7.a shows that values of non-resonant absorption are similar to those observed in individual nanotubes (horizontal thick grey lines). This would suggest that non-resonant absorption is mainly a consequence of the continuum of states above the main exciton peaks. In fact, it is stronger close to high-order transitions in the observed semi-conducting nanotubes ( $S_{33}$ ,  $S_{44}$ ,...). However, the non-resonant absorption from the metallic tubes could show different effect for different diameters (Fig. IV.1.a,b), further measurements on individual metallic SWNTs would help to clarify this point.

In B1, metallic peaks  $M_{11(-)}$  and  $M_{11(+)}$  are separated by 100 meV (energy positions are 1.9 and 2.0 eV, respectively) and a lower value of absorption cross-section is observed for  $M_{11(+)}$ . Linewidths of these resonances are in good agreement with Raman studies reported on ensemble of metallic CNTs by Doorn et al. [62]. Additionally, Raman excitation profiles (not shown here) measured for the energy transitions  $S_{33}$  and  $M_{11(-)}$  yield, respectively, 1.72 eV and 1.87 eV for the peak positions as well as 58 meV and 90 meV for their FWHM. Positions of the resonances agree with the absorption spectrum, while the linewidths measured with Raman are slightly smaller.<sup>j</sup>

In B2, metallic resonances  $M_{11(-)}$  and  $M_{11(+)}$  are 50 meV one from the other, and have both smaller amplitudes and narrower linewidths as compared to the small diameter metallic tube observed in B1. Our observations are in good agreement with the study of Doorn et al. on metallic nanotubes [62,149]. The results reported in this work also confirm the small absorption cross-section of  $M_{22}$  in comparison to  $M_{11}$ .

## IV-3 Substrate interactions

In the last section, we observed that tube-tube interactions can influence the photo-physics of CNTs. To gain insights in these effects, we propose to test these effects in others environments, i.e. individual and bundles are placed on opaque/transparent substrates. As our optical approach permits to investigate single nanotubes either suspended or on an opaque substrate (using either SMS or R-SMS), it offers the unique possibility of measuring quantitative modifications of the optical response of CNTs in these two situations.

### IV-3.1 Absorption spectroscopy of SWNT on Si/SiO<sub>2</sub> substrate: first measurement

The first direct measurement of the absolute absorption cross-section reported in the literature have been performed on the SWNT presented in Fig. III.2 (sample Si-4) using RSMS technique (details can be found in ref. [12]) . Here, extended view of the main results are presented.

<sup>j</sup>This can be accounted for various effect reported recently in the litterature such as non-Condon effects (intensities arising from resonance with incident and scattered photons are different) and quantum interferences (between close-lying energy transitions) [147,148]

### Sample characterization

Structure identification of the CNT was derived from the combination of three techniques: AFM, Raman spectroscopy, absorption. AFM measured an apparent diameter of  $1.6 \pm 0.1$  nm (Fig. III.2.b), where the error is estimated from the dispersion on several measurement along the CNT.

Raman spectroscopy performed at different laser line excitation shows tangential mode  $G^+$  at  $1595 \text{ cm}^{-1}$  (the up-shift of the LO phonon compared to the standard value  $\sim 1592 \text{ cm}^{-1}$  suggests strong doping effects from the substrate) and RBM at  $148 \text{ cm}^{-1}$  (Fig. IV.8.b). The latter is observed only for excitation energy 1.96 eV but not for 1.83 eV and 2.21 eV. From the Raman results, two conclusions can be drawn:

- the RBM frequency is inversely proportional to the nanotube diameter  $d$ , which, in our system, can be estimated using the expression established for vertically aligned SWNTs synthesized by CVD on a quartz substrate  $\omega_{RBM} = 217.8/d + 15.7$  (with  $d$  in nanometers). Then, the measured RBM frequency yields  $d \approx 1.65$  nm for the investigated CNT, in agreement with the value range of 1.5-1.7 nm estimated by AFM.
- Observation of radial-breathing mode requires that the CNT is excited at one of its absorption resonance. Hence, one energy transition is present close to 1.96 eV, whereas not resonances are present at 1.83 eV and 2.21 eV.

The linewidth of the RBM mode ( $6 \text{ cm}^{-1}$ ) suggest the individual character of this nanotube. However, to further support this hypothesis, absorption spectrum is measured in the ranges 2.3-3.1 eV (Fig. IV.8.a) and 1.55-1.75 eV. Only one absorption peak is observed at 2.76 eV with abnormally strong  $C_{\text{abs}}$  (Tab. IV.3 - row (18,5)). This is attributed to the important variation of the Fabry-Pérot response in the blue part of the spectrum (Fig. III.15.b), and possible experimental errors. From the Kataura plot, reporting the energy transitions 1.96 eV and 2.76 eV, as well as the diameter 1.65 nm, we can presume the present nanotube is an individual semiconducting SWNT with most probable chirality (18,5) [44]. The resonances at 1.96 eV and 2.76 eV are identified as  $S_{33}$  and  $S_{44}$ , respectively.

### Absolute absorption cross-section

The first direct measurement of the absorption cross-section was performed in the region around 2.1 eV where the Fabry-Pérot effects are attenuated providing a more confident measurement (see Sec. III-2.2 for details). Close to the  $S_{33}$  resonance, for light polarized along the nanotube's axis ( $E_{\text{exc}} = 1.96 \text{ eV}$ ),  $C_{\text{abs}}$  yields  $0.35 \text{ nm}^2/\text{nm}$  (corresponding to  $1.8 \times 10^{-17} \text{ cm}^2/\text{C atom}$ ). The values obtained for the out-of-resonance conditions ( $E_{\text{exc}} = 2.21 \text{ eV}$ ) are about five times smaller but not negligible:  $0.07 \text{ nm}^2/\text{nm}$  or  $0.6 \times 10^{-17} \text{ cm}^2/\text{C atom}$ . These values of absolute absorption cross-sections, obtained with a direct measurement method, are in good agreement with those reported in the literature (Tab. II.1).

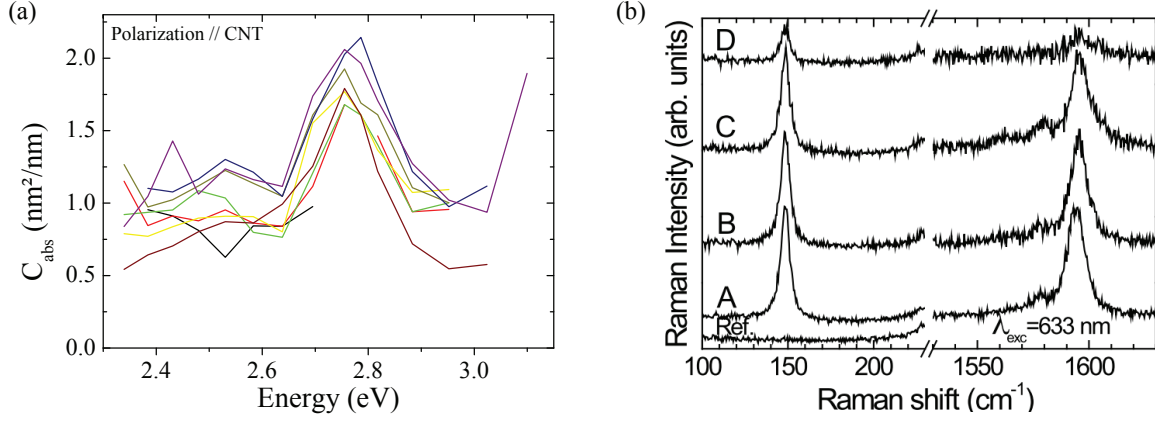


**Figure IV.8:** (a) Absorption and (b) Raman scattering of the (18,5) SWNT supported on Si/SiO<sub>2</sub> substrate (Si-4 sample) incident beam polarized parallel to the nanotube.

### Polarization response

The polarization dependence of  $C_{\text{abs}}$  is also determined close to  $S_{33}$  (Fig. IV.9). The contrast factor, defined as the ratio of  $C_{\text{abs}}$  between parallel and perpendicular polarization response, is about 2.3:1. Similar polarization anisotropy has been obtained for different CNTs at wavelengths in and out of resonance with one of their electronic transitions (with a mean contrast of about 2:1). Our direct measurement is in very good agreement with the polarization absorption anisotropy determined indirectly in recent photo-induced current experiments in individual CNTs [55,56]. Conversely, Rayleigh and Raman scattering studies show much larger contrast associated with a stronger antenna effect [49, 98] emphasizing the different nature of the involved light-matter interaction mechanisms.

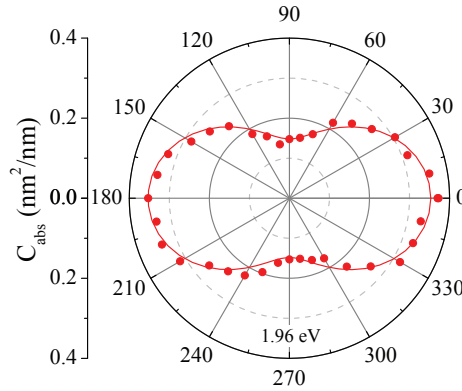


**Figure IV.9:** Polarization-dependent absorption of the (18,5) SWNT on Si/SiO<sub>2</sub> substrate (Si-4 sample) for laser excitation close to  $S_{33}$  (1.96 eV). The experimental data (symbols) are fitted using  $C_{\text{abs}}^{\parallel} \cos^2 \theta_{\text{pol}} + C_{\text{abs}}^{\perp} \sin^2 \theta_{\text{pol}}$  function (line),  $\theta_{\text{pol}} = 0$  being the direction parallel to the nanotube.



### IV–3.2 Comparison of the absorption response between free-standing and substrate-supported SWNT

As our optical approach permits to investigate single nanotubes either suspended or on an opaque substrate (using either SMS or RSMS), it offers the unique possibility of measuring quantitative modifications of the optical response of the same SWNT in these two environments.

#### IV–3.2.a Absorption spectroscopy

The absorption spectrum measured by RSMS on the SiO<sub>2</sub>/Si supported part of the (14,13) SWNT (SI-SWNT) show large modifications as compared to that measured by SMS on its free-standing part (FS-SWNT), Fig. IV.10.a and Fig. IV.1.b, respectively. The latter is studied in details in Sec. IV–1.2.b. For light polarized parallel to the tube axis, the three excitonic peaks  $S_{33}$ ,  $S_{44}$  and  $S_{55}$  are still visible but are red-shifted and considerably broadened, and their relative peak amplitude modified, as compared to the FS-SWNT case. These effects can be quantified by fitting the measured SI-SWNT spectrum using the method described in Sec. IV–1.2.b (Fig. IV.10.a dashed line), yielding a red shift of 60 meV and a five times broadening of the  $S_{33}$  and  $S_{44}$  resonances (1st row in Tab. IV.3 to be compared with 1st row in Tab. IV.1). The  $S_{55}$  transition is less altered, as it is red-shifted by 20 meV and its linewidth increasing by less than a factor of three (in SI-SWNT the  $S_{33}$ ,  $S_{44}$  and  $S_{55}$  exhibiting similar width). For sake of clarity, excitonic absorption responses (+ non-resonant absorption) of (14,13) in the two situations are both plotted on the same graph (Fig. IV.10.b).

Different re-normalization of the peak absorption amplitude is not explained by a simple dipolar model or Mie theory. The SI-SWNT is embedded in an effective material (substrate+water layer) with dielectric constant  $\epsilon_m$ . Sample FS-1 has a 100 nm thick Si/SiO<sub>2</sub> layer, then  $C_{\text{abs}}$  is measured relatively accurately in the range 1.8-2.2 eV (see Sec. III–2.2). Hence, amplitudes of  $S_{33}$  and  $S_{44}$  could be considered as absolute, and the change in the ratio  $S_{33}/S_{44}$  imputed to the environment interactions are still not explained.

Interestingly, the absorption cross-section measured here on a (14,13) semiconducting SWNT is in very good agreement with the first RSMS measurement performed for few wavelengths on the chirality-identified (18,5) type I SWNT, of diameter  $d=1.65$  nm and grown by CVD on 300 nm silica on silicon substrate (Sec. IV–3.1 and [12]). In particular, the reported out-of-resonance absorption,  $C_{\text{abs}}^{\text{nr}} = 0.6 \times 10^{-17} \text{ cm}^2/\text{C atom}$ , is very close to that measured here, and the  $S_{33}$  excitonic absorption per carbon atom of the (18,5) SWNT ( $C_{\text{abs},S_{33}}^{\text{exc}} = 1.2 \times 10^{-17} \text{ cm}^2/\text{C atom}$ , after subtraction of  $C_{\text{abs}}^{\text{nr}}$ ) consistent with that obtained here on the (14, 13) SI-SWNT for the same transition ( $C_{\text{abs},S_{33}}^{\text{exc}} = 1 \times 10^{-17} \text{ cm}^2/\text{C atom}$ ).

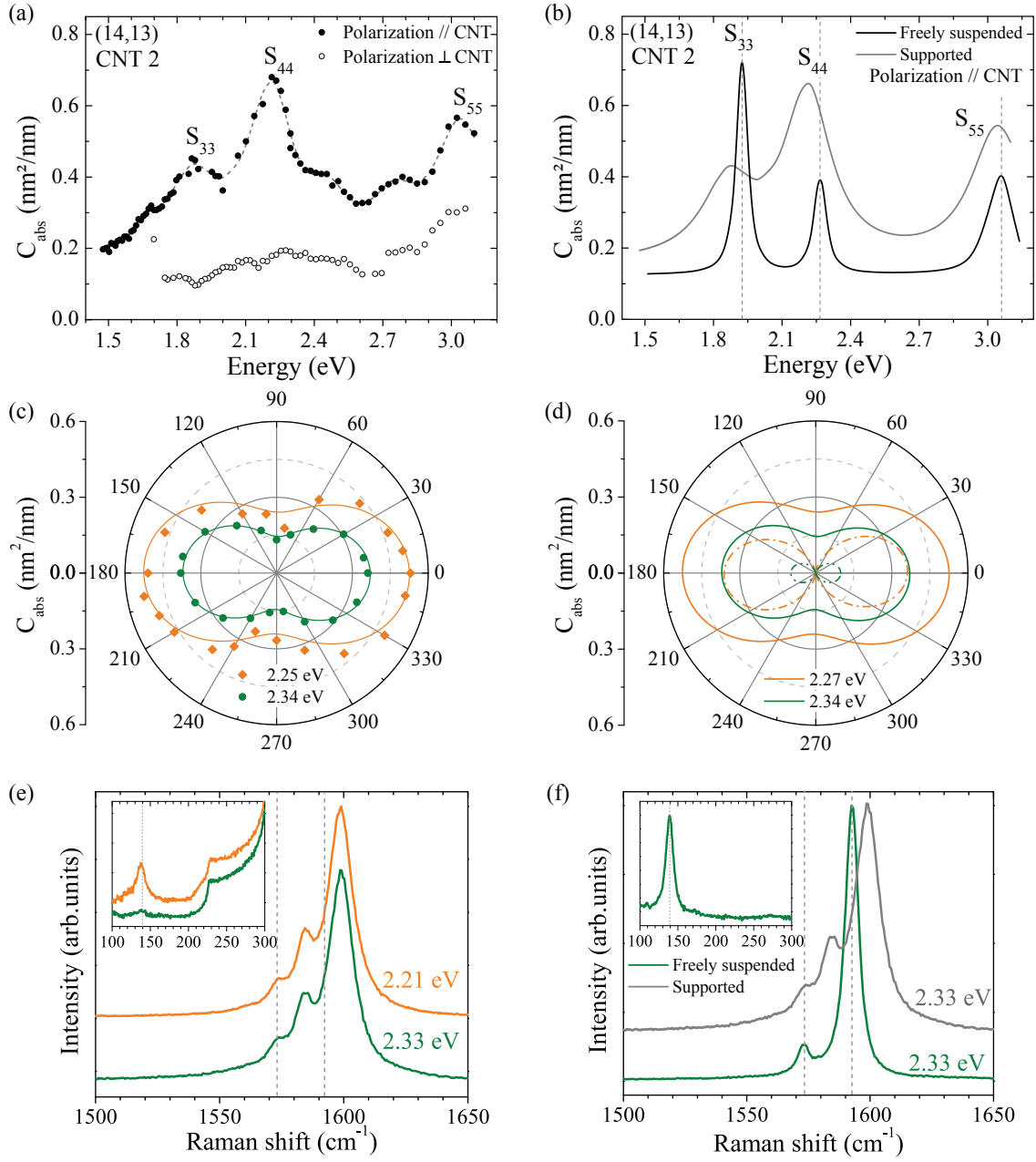


**Figure IV.10:** Absorption of (14,13) SWNT supported on Si/SiO<sub>2</sub> substrate (left panels) and comparison with the freely suspended optical properties of the same nanotube (right panels). (a,b) Broadband absorption spectra. (c,d) Light-polarization-dependent absorption cross-sections (dashed curves stand for the free-standing segment response). The experimental data (symbols) are fitted using the  $C_{\text{abs}}^{\parallel} \cos^2 \theta_{\text{pol}} + C_{\text{abs}}^{\perp} \sin^2 \theta_{\text{pol}}$  function (line),  $\theta_{\text{pol}} = 0$  being the direction parallel to the nanotube. (e,f) Raman spectra (with excitation energies labeled on the figure).



### IV–3.2.b Polarization-dependent absorption

An additional striking feature is the large reduction of light polarization effect. Significant absorption is still observed for the supported section of the tube for light polarized perpendicularly to the tube axis (see open dots in Fig. IV.10.a), with, however, only weak remaining structures (except in the  $S_{55}$  spectral region subject to uncertainty on the amplitude). While the absorption is almost fully polarized in the free-standing region, the SI-SWNT spectra exhibit a photon energy dependent contrast factor between light polarized parallel or orthogonal to the nanotube axis ranging from 2:1 to 4:1 (Figs. IV.10.c,d). This wavelength dependence suggests different coupling of the excitonic states with the substrate and, possibly, activation of dark states. More generally, weakening of the polarization dependence can be ascribed to softening of the antenna effect for deposited carbon nanotubes, associated to weakening of the depolarization field inside the tube [12, 55, 56]. As a consequence, cross-polarized energy transitions, i. e.  $E_{ij}$  with  $i \neq j$ , show increasing absorption, but features are not clearly resolved (it might be the consequence of the presence of the substrate).

### IV–3.2.c Raman scattering

The impact of the substrate has been confirmed by Raman measurements. While no significant change is observed for the RBM frequency and width ( $\omega_{\text{RBM}} = 139$  and  $138 \text{ cm}^{-1}$ , with a FWHM of 11 and  $13 \text{ cm}^{-1}$  for the FS-SWNT and SI-SWNT, respectively), both the LO and TO modes of the G-band are up-shifted and broadened in the SI-SWNT, with apparition of additional peaks associated to modes of other symmetries (Figs. IV.10.e,f). The upshift of the LO phonon from  $1592.5$  to  $1599 \text{ cm}^{-1}$  suggests relatively strong p-doping of the SI-SWNT, but could also results from other effects, e. g. substrate-induced radial stress, as described below.

### IV–3.2.d Substrate effects on the absorption response of SWNTs

To summarize, absorption and Raman signals show the following differences between FS-SWNT and SI-SWNT photo-physics:

- redshift and broadening of all energy transitions  $S_{33}$ ,  $S_{44}$ , and  $S_{55}$ , as well as changes in the  $C_{\text{abs}}$  ratio  $S_{33}/S_{44}$ ,
- weakening of the depolarization field and increase of the perpendicular polarization absorption,
- blueshift of the tangential modes (no significant influence on the RBM), as well as the apparition of two new phonon modes in the G-band.

It emphasizes the influence of the environment on the light-matter interaction mechanisms involved in each situation.

SWNT	Assignment	Energy transition	$E_{pp}$ (eV)	$C_{abs}$ ( $\text{nm}^2/\text{nm}$ )	$C_{abs}$ ( $10^{-17} \text{ cm}^2/\text{C atom}$ )		$\gamma_{pp}$ (meV)
					$C_{abs}^{exc}$	$C_{abs}^{peak}$	
$d = 1.83 \text{ nm}$ $\theta_c = 29^\circ$ <b>Si/SiO<sub>2</sub> substrate</b>	SC type I (14,13) CNT 2	$S_{33}$	1.87	0.22	1	1.7	273
		$S_{44}$	2.21	0.48	2.2	2.9	244
		$S_{55}$	3.04	0.39	1.8	2.5	272
$d = 1.65 \text{ nm}$ $\theta_c = 12^\circ$ <b>Si/SiO<sub>2</sub> substrate</b>	SC type I (18,5)	$S_{33}$	1.96	0.24	1.2	1.8	–
		$S_{44}$	2.76	0.89	4.5	9.4	150
		$S_{55}$	3.09(*)				
$d_{AFM} = 1.9 \pm 0.1 \text{ nm}$ <b>Quartz ST-cut</b> Q3 - CNT 3 Bundle	SC type II $d \approx 1.7 - 1.9 \text{ nm}$	$S_{33}$	1.89	0.14	0.6	1.4	64
		$S_{44}$	2.09	0.12	0.5	1.3	171
	Metallic $d \approx 1.7 - 1.9 \text{ nm}$	$M_{11(-)}$	1.37	0.10	0.5	1.3	81
		$M_{11(+)}$	1.43	0.05	0.2	1.1	104
		$M_{22(-)}$	2.55	0.10	0.5	1.3	167
		$M_{22(+)}$	2.72	0.09	0.4	1.3	100
$d_{AFM} = 2.2 \pm 0.1 \text{ nm}$ <b>Quartz ST-cut</b> Q3 - CNT 2 Bundle	SC type I	$S_{22}$	1.51	0.20	1.34	2.34	122
	$d \approx 1.1 - 1.4 \text{ nm}$	$S_{33}$	2.52	0.18	1.2	2.2	169
	SC type II	$S_{33}$	1.86	0.11	0.47	1.11	235
	$d \approx 1.8 - 2.1 \text{ nm}$	$S_{44}$	2.05	0.16	0.69	1.23	150

**Table IV.3:** Absorption characteristics of carbon nanotubes deposited on either Si/SiO<sub>2</sub> or quartz substrates. After subtracting a constant non-resonant contribution, peaks of the absorption spectra plotted in Figs. IV.8, IV.10 and IV.13 are fitted using Voigt profiles with fixed Gaussian linewidth accounting for the laser lineshape. The extracted widths  $\gamma_{S_{ii}}$  correspond to the full-width at half maximum of the Lorentzian functions describing the excitonic resonances.

### Exciton broadening

Broadening of the excitonic transition linewidth results from the decrease of the exciton lifetime. This phenomenon have been observed experimentally for matrix-embedded SWNTs [59,82,83,92,97], as well as for substrate-supported nanotubes [113,114,150,151]. Few possible mechanisms can explain a decrease of exciton lifetime (sketch in Fig. IV.11):

- i. the relatively small separation between the bright  $|B\rangle$  and dark  $|D\rangle$  states would suggest that they are equally populated at room temperature (assuming efficient coupling between the two states, they can reach a thermal equilibrium). However, several papers use the three-level model depicted in Fig. IV.11.a to explain bi-exponential PL decay and ponder environmental effects (they provide an extrinsic fast non-radiative relaxation process that tend to suppress the long-time decay pathway accounted to  $|D\rangle$ ) [82,83].
- ii. An enhanced multi-phonon decay of localized excitons trapped in defects which are induced by potential fluctuation of the tube local environment (Fig. IV.11.b, adapted from [152]).
- iii. A phonon-assisted indirect exciton ionization due to the presence of free-carriers which are able to create a phonon and an intra-band electron-hole pair (Fig. IV.11.c).
- iv. Auger-type inter-band scattering in p-doped carbon nanotubes, where an electron is the valence and conduction bands are both scattered to a higher energy sub-

band (above the Fermi level which is in the valence band) and to a lower energy sub-band, respectively.

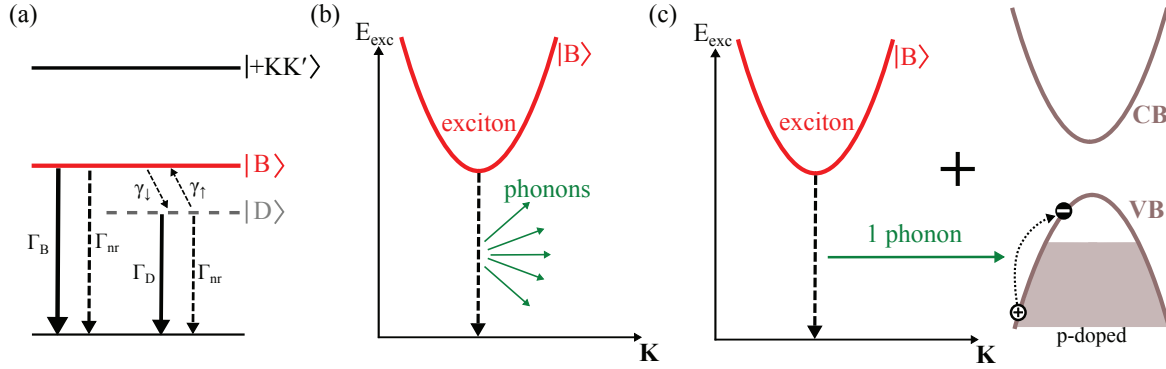


**Figure IV.11:** Sketch of exciton non-radiative decay mechanisms/pathways.

Steiner et al. investigated the difference between the freely suspended and supported segments of a single SWNT by means of Raman spectroscopy [114]. In particular, they observe a broadening of the  $S_{33}$  resonance by only a factor  $\sim 1.5$  for the supported nanotube on the same type of substrate ( $S_{33}$  is five times broader in our case). They attribute this phenomenon to exciton localization in the supported nanotube due to potential fluctuations introduced by the environment, explained by chemical interactions (p-doping from a thin water layer surrounding the nanotube [153]) and/or stress-induced strain due to substrate roughness [30, 31, 154]. It suggests that exciton decay pathways (2) and (3) are enhanced.

### Raman scattering

Consistent with our results, Steiner et al. observed the apparition of two new features in the tangential mode region, i.e. the appearance of new phonon modes, that they attribute to a relaxing of the selection rules for the supported nanotube. This interpretation would also partially explain the increasing of cross-polarization absorption. Symmetry breaking results from van-der-Waals interactions with the substrate resulting in radial deformation of relatively large nanotubes deposited on surfaces [30, 31, 36, 154]. Such radial deformation has been shown experimentally in many works to be able to induce Raman upshifts of the G-band (see for instance review [27]) and red-shifts of energy transitions  $S_{ii}$  [28, 29, 32]. Nevertheless, direct conclusions cannot be driven as most of those experiments are done in hydrostatic or quasi-hydrostatic conditions whereas the surface induced radial deformations are to be related to a unidirectional constraint. Besides, Soares et al. proposed a slight increase of the carbon-carbon bonds close to a surface, then the stiffening of the LO phonon mode would indicate that effective radial strain does not affect significantly the nanotube optical properties [154]. On the other hand, blue-shift of the LO phonon mode has been explained by high charge transfer p-doping [155] which occurs through interactions with both the silanol dangling bonds at the  $\text{SiO}_2$  surface [154] and the water layer [153, 156, 157].

### Energy transitions redshift

The last and most studies environmental effect is the red-shift of the absorption resonances which can be explained by three different phenomena:

- dielectric screening of the carriers interactions inside the nanotube [66, 70, 83, 86, 97, 113, 114, 151, 158–161],
- substrate stress-induced strain [162–164],
- doping due to chemical interactions [155, 157, 165],

The role and importance of these phenomena are discussed more extensively below. In good agreement with our observations, Steiner et al. measured a red-shift of  $55 \pm 10$  meV for the energy transition  $S_{33}$  which they explained by both exciton localization at defect sites and dielectric scaling of the free exciton binding energy [114]. Photoluminescence experiments and theoretical calculations, completed with SWNT embedded in different media, yield red-shifts of about 40 meV for  $S_{11}$  and below 30 meV for  $S_{22}$  [158, 159]. According to these results, dielectric screening (with possible chemical doping) seems to be the main phenomenon responsible for the red-shifts and broadening of the exciton resonances observed in the supported SWNT. They are accompanied by exciton localization at the substrate surface due to potential fluctuations which support broadening and red-shift of the exciton peaks.

In the many-body picture, dielectric screening tends to decrease both the electron-electron interactions  $E_{e-e}$  and exciton binding energy  $E_b$ . These two effects shift the resonance to opposite ways and scales with the background dielectric constant  $\epsilon_m$  as:  $E_{e-e}/\epsilon_m$  and  $E_b/\epsilon_m^\alpha$ . Although early theoretical works [67, 78] expected a value  $\alpha = 1.4$ , recent Raman experiments [86, 161] carried out on nanotubes embedded in different homogeneous environment yield  $\alpha = 1.2$ . Assuming  $E_b \approx 300$  meV and  $E_{e-e} \approx 650$  meV for  $S_{33}$  and  $S_{44}$  [85], along with effective  $\epsilon_m$  in the range between 1.77 (water) and 2.37 (amorphous silicon dioxide), the overall red-shift is evaluated to take values greater than 160 meV (Fig. IV.12), overestimating our data by a factor of  $\sim 3$ . To match the observed 50 meV red-shifts, an external dielectric constant around 1.2 should be considered in this simple scaling model. The parameter  $\alpha$  have been estimated and measured for  $S_{11}$  and  $S_{22}$ , and verified by several photoluminescence and Raman studies. However, the different nature of excitonic transitions  $S_{33}$  and  $S_{44}$  (see Sec. II-2.2.c) also suggest the revision of the scaling law in the presence of a dielectric environment. Another method to explore includes dielectric screening directly in the Ohno potential before calculations of the energy transitions in the many-body picture [70].

On top of the dielectric screening effects, substrate stress-induced strain and chemical doping might play a role in the energy shifts of the resonances, as shown already for spectral broadening and Raman scattering. Since all resonances observe a red-shift, uniaxial strain applied by the substrate along the tube is discriminated [162, 164].<sup>k</sup> On

<sup>k</sup>Uniaxial strain shift adjacent energy transitions in opposite directions.

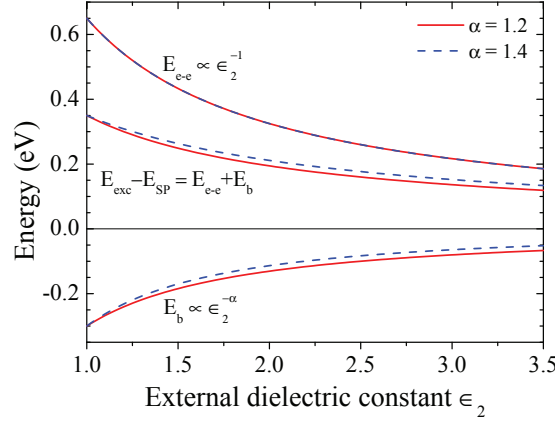


**Figure IV.12:** Scaling of exciton energy with the dielectric environment for the  $S_{33}$  (or  $S_{44}$ ) transition in a 2 nm semiconducting nanotube. The binding energy and self energy scales with the environment dielectric constant  $\epsilon_m$ . The scaling parameter is analyzed in [66] ( $\alpha = 1.4$ ) and in [161] ( $\alpha = 1.2$ ).

the opposite, radial deformation induced by tube-substrate Van-der-Waals forces is in agreement with our data [28, 29, 32]. We nevertheless concede that even if doping could participate to the modification of the G-band position, it is unlikely that the homogeneous red-shift of the different high-order resonances is related to such effect (unless very high doping).

### IV–3.3 SWNTs on quartz substrate

To get further insights in the environmental effects on the absorption properties of SWNTs, we study the optical response of carbon nanotubes deposited on quartz substrate (sample Q3). Among the three nanotubes investigated, one bundle of two SWNTs (CNT 3) has been identified after analysis of combined results from AFM, Raman scattering, and absorption spectroscopy. On the other hand, identification of the nature of CNT 2 is still unclear based on the absorption spectrum: this tube is either a bundle of two semiconducting SWNTs or a DWNT. The latter hypothesis is not clear in the Raman spectrum (only one laser excitation), nevertheless our CVD growth is more likely to synthesized DWNT. Not to mislead the reader, we assume in this chapter that both CNT 2 and CNT 3 are bundles of two SWNTs.

#### IV–3.3.a AFM and Raman spectroscopy

AFM yield an effective diameter  $d$  of  $1.9 \pm 0.1$  nm and  $2.2 \pm 0.1$  for CNT 3 and CNT 2, respectively (Fig. III.3). The G-band profile of each tube (Figs. IV.13.e,f), obtained for laser excitation 1.96 eV, is composed of two narrow components (Lorentzian functions) at 1592 (resp. 1592) and 1582 (resp. 1580)  $\text{cm}^{-1}$  for CNT 3 (resp. CNT 2), respectively. Linewidths of all tangential phonon modes are in the range 8-10  $\text{cm}^{-1}$ . Such profile is

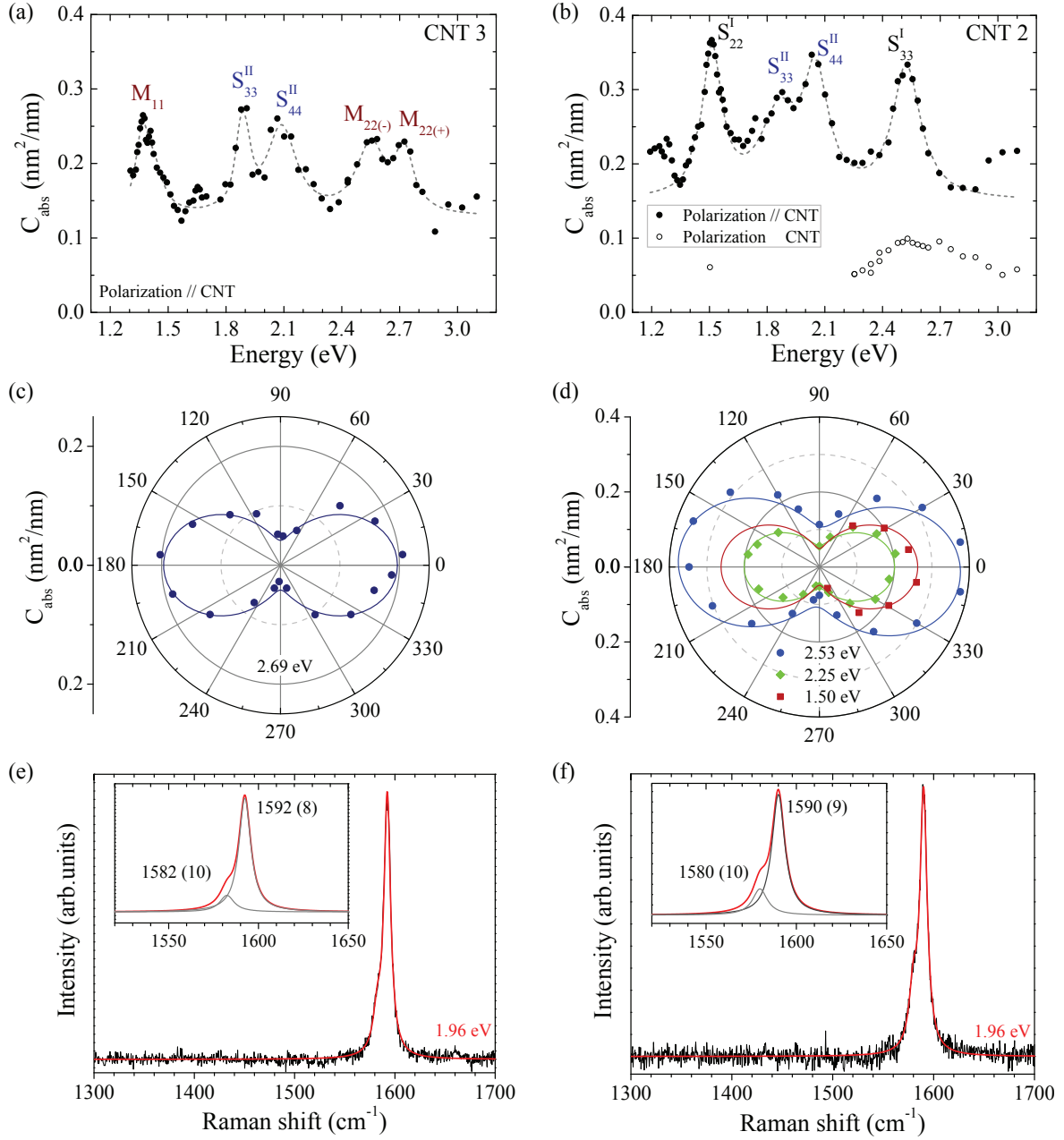


**Figure IV.13:** Absorption and Raman scattering of the quartz-supported carbon nanotubes (sample Q-3, left panels CNT 3 & right panels CNT 2). (a,b) Absolute absorption cross-section spectrum for incident light parallel (full dots) and perpendicular (open dots) to the nanotube. The dashed line is the result of the fit detailed in the main text. (c,d) Light-polarization-dependent absorption cross-section for different laser excitation energies. The experimental data (symbols) are fitted using  $C_{\text{abs}}^{\parallel} \cos^2 \theta_{\text{pol}} + C_{\text{abs}}^{\perp} \sin^2 \theta_{\text{pol}}$  function (line),  $\theta_{\text{pol}} = 0$  being the direction parallel to the nanotube. (e,f) Raman spectra showing the tangential modes for excitation energy 1.96 eV, experimental data (black curve) and fitting profile (red curve) detailed in the insets. Labels indicate the frequency of the phonon modes and their linewidths (in between brackets).



characteristic of (individual) chiral SWNT with relatively large diameter ( $\gtrsim 2.5$  nm) [18, 19, 145, 146]. Despite that laser excitation is close to an absorption resonance, no RBM has been observed in both samples, due to experimental limitation of our setup. However, it indicated that this transitions in the absorption spectrum should be attributed to a chiral semiconducting tube.

### IV–3.3.b Absorption spectroscopy

#### Absorption spectra

Figs. IV.13.a,b show the absorption spectra of the CNTs for parallel polarization. In agreement with our previous observation, the spectra are composed of absorption peaks on top of a constant non-resonant absorption background. The fitting procedure described in Sec. IV–1.2.b yield a fairly good agreement with our data (dashed lines in Fig. IV.13.a,b, and outcomes in Tab. IV.3, 3rd & 4th rows).

It confirms that optical absorption energy transitions keep their excitonic nature for nanotubes deposited on ST-cut quartz (the peak are fitted with Lorentzian-like profiles). Energy transitions are reported on the Kataura plot of V. Popov including excitonic corrections. AFM and Raman results provide hypotheses for structure identification of the tubes: (a) the maximum diameter, and (b) the resonance around 2.0 eV is associated with semiconducting chiral SWNTs. Using these constraints, we conclude that the sample CNT 3 is composed of two SWNTs, one semiconducting of family type II and the other metallic. Both yield diameters in the range 1.7-1.9 nm, and their transitions are labeled accordingly in Fig. IV.13.a. Similarly, two semiconducting SWNTs, one of each family type, compose CNT 2. The type I and type II semiconducting SWNTs are compatible with diameters in the range 1.1-1.4 nm and 1.8-2.1 nm, respectively. Precise identification of nanotubes chirality is impossible due to substrate-induced energy shift(s) of the resonances which cannot be pondered in our experiment. Based on the results of Sores et al. who estimated a red-shift of  $\sim 100$  eV for SWNTs on quartz [154], most probable diameter is about the center of the diameter ranges proposed (we underline that the knowledge of the nature and family of the sample are the only relevant information for most of the discussion within this thesis).

Although the absorption spectra presents the same absorption features as for free-standing CNTs and nanotubes deposited on silicon substrate, a striking difference is observed in the values of  $C_{\text{abs}}$  for the exciton peaks (column  $C_{\text{abs}}^{\text{exc}}$  and  $C_{\text{abs}}^{\text{peak}}$  in Tab. IV.3 and Tab. IV.1). On the one hand, the non-resonant absorption ( $C_{\text{abs}}^{\text{nr}} = 0.13\text{nm}^2/\text{nm}$  and  $C_{\text{abs}}^{\text{nr}} = 0.15\text{nm}^2/\text{nm}$  for CNT 3 and CNT 2, respectively) is in good agreement with the values measured for the other types of sample, it underlies the intrinsic nature of  $C_{\text{abs}}^{\text{nr}}$  as discussed in Sec. IV–1.5. On the other hand, the amplitude of the exciton peaks in each SWNT observe only small variation of absorption cross-section from one energy transition to the others. This behavior contrasts with the important variations of  $C_{\text{abs}}^{\text{exc}}$  for free-standing tubes and CNTs deposited on Si/SiO<sub>2</sub> substrates (see previous sections). Interestingly, recent Rayleigh scattering study carried out on the same type of sample yield similar results [14], thus suggesting enhanced tube-substrate interactions

in this type of sample.

### Polarization dependent absorption

Figs. IV.13.c,d present the light polarization-dependent absorption for different laser excitation in samples CNT 2 and CNT 3. Antenna-effect characteristic  $C_{\text{abs}}^{\parallel} \cos^2 \theta_{\text{pol}} + C_{\text{abs}}^{\perp} \sin^2 \theta_{\text{pol}}$  response is observed for all measurements. Nevertheless, significant absorption is observed for incident light polarized perpendicular to the nanotubes, in good agreement with the results observed for CNTs deposited on silicon substrates. These measurements confirm that substrate-deposited carbon nanotubes show weaker antenna effects, i. e. the depolarization field does not suppress completely cross-polarized absorption, in comparison to free-standing tubes.

## IV-4 General comments on the absorption of SWNT

Throughout this chapter, we addressed the absolute absorption cross-section of single-wall carbon nanotubes placed in different environments: freely suspended, supported on substrates, and in small bundles. The influence of the nanotubes environments reflects on the main characteristics of the excitonic resonances: their peak absorption cross-sections  $C_{\text{abs},E_{ii}}^{\text{peak}}$ , their linewidths  $\gamma_{E_{ii}}$ , and their oscillator strength per carbon atom  $f_C$ . For all tubes, the values of  $C_{\text{abs},E_{ii}}^{\text{peak}}$  are in good agreement with those reported in the literature for tubes of similar diameter [14], and for smaller nanotubes [22, 106, 107].

In free-standing individual SWNTs, we observe important variations of all characteristic quantities from one energy transition to the others and measure the first family behavior of the absolute absorption, i. e. a difference between type I and type II semiconducting SWNTs. Evolution of  $C_{\text{abs}}$  with respect to CNT diameter and/or chiral angle is not clear with the limited number of nanotubes investigated.


Bundling and substrate influence the characteristic of the excitonic resonances. In bundles,  $S_{ii}$  resonances close to energy transitions of a metallic tube  $M_{ii}$  seems to observe a broadening. Electrodynamics interactions tend to increase electron-hole distance [66, 70], thus demonstrating that dielectric screening is not the exclusive mechanism involved in inter-tube interaction. The latter is rather dominated by exciton tunneling processes [166].

Important variations of exciton parameters for substrate-supported SC-SWNTs are explained by environment interactions via three phenomena: dielectric screening, stress-induced strain, and chemical doping. The significant broadening of the  $S_{ii}$ , concomitant with a decrease of the exciton lifetime, is correlated to the apparition of new relaxation pathways and exciton localization due to surface potential fluctuations.





# Absorption spectroscopy of double-wall carbon nanotubes



*In this chapter, we discuss the absorption and Raman spectroscopy of individual double-wall carbon nanotubes freely suspended or interacting with an environment (substrate and others nanotubes). Although SWNTs have been the object of many studies in the past two decades, only few research works have investigated the photo-physics of DWNTs. Very few studies were carried out at the single-nanotube level, nevertheless this approach could provide new insights in the optical properties of this class of nanotubes. At first, the DWNTs are identified with Raman spectroscopy which provides a good estimate of the nanotubes' structural characteristics. Secondly, the absorption of several individual free-standing DWNTs is discussed. Finally, the evolution of the tubes absorption properties is investigated regarding two different environments, i. e. in the presence of a metallic SWNT and supported on a substrate. The combination of absorption and Raman spectroscopy techniques proposes a new all-optical approach to address the photo-physics of DWNTs.*

## V-1 State-of-the-art

Double-wall carbon nanotubes present intriguing optical and electronic properties. As they share the one-dimensional character of SWNTs, in a first approach their properties are understood from those of SWNTs. Nevertheless, DWNTs are ideal candidates to gain insight in fundamental questions related to interwall coupling, energy or charge transfer processes between walls, and environmental effects. In fact, their unique two-wall coaxial structure offers several advantages for both fundamental and applied studies, e. g. the inner nanotube is isolated/protected from the environment, and the interwall interactions probe changes of the outer tube characteristics (functionalization, self-assembling, ...). DWNTs are serious candidates for applications in sensing and optoelectronics, under the conditions that certain of their properties (photoluminescence, electrical transport), in some cases superior to SWNTs and MWNTs, are confirmed.

### Raman spectroscopy

Identification of the structure of DWNTs is required to address their physical properties. Raman spectroscopy is a powerful technique for non-invasive characterization of

individual DWNT, i.e. it probes the nature (semiconducting or metallic) and the diameter of both the inner nanotube (diameter  $d_{\text{in}}$  and chiral index  $(n,m)$ ) and the outer tube ( $d_{\text{out}},(n',m')$ ). Although TEM offers access to the chiral indices of each tube, either by electron diffraction or high-resolution imaging, this type of instrument is not always available or not adapted to certain samples. Moreover, exposure to the electron beam might damage nanotubes. Our samples have been characterized with Raman spectroscopy prior to the absorption measurements. This point is detailed in the next sections.

Raman spectrum of a SWNT shows mainly tangential phonon modes (or  $G^+$  and  $G^-$  phonon modes in chiral nanotubes) and one radial breathing mode related to the tube's diameter ( $\omega_{\text{RBM}} = 204/d + 27$  for our samples).<sup>a</sup> In the case of a DWNT, similar features are observed for each of the two coaxial tubes, i.e. four G-phonon modes (assuming the inner and outer nanotubes are both chiral tubes) and two breathing-like modes (BLM). The phonon modes do not correspond to the behavior of two isolated SWNTs. In fact their frequencies and amplitudes are modified due to either quantum-mechanical coupling between the inner and outer tubes or phonon interferences [148,167]. The coupling between the inner and outer walls is mainly evidenced by the shift of the breathing-like phonon modes (BLM) to higher frequencies in comparison to the RBM observed for each corresponding isolated tube. More precisely, this phenomenon described by a model of two coupled oscillators leads to a counterphase BLM ( $\omega_{\text{out}}$  at high frequency) and an in-phase BLM ( $\omega_{\text{in}}$  at low frequency) corresponding to, respectively, counterphase and in-phase expansion/compression of the inner and outer tubes cross-sections (as illustrated in Fig. V.1.a). BLM frequencies depend on the inner and outer walls diameters as well as on the interwall distance  $\Delta d/2$ . Popov and Henrard calculated the diameter dependence of  $\omega_{\text{out}}$  and  $\omega_{\text{in}}$  assuming a fixed interwall distance of 0.335 nm (interlayer distance in graphite) and considering van der Waals interaction between the inner and outer tubes [168]. Fig. V.1.a presents these results in two situations depending on the RBM *vs.* diameter relations of the inner and outer nanotubes when considered as isolated.<sup>b</sup> In fact, these two relations (one for the inner SWNT  $\omega_{\text{RBM,in}}$  and one for the outer SWNT  $\omega_{\text{RBM,out}}$ ) set the fundamental frequencies of the two oscillators in the model. Environment-free SWNTs, i.e. the inner tube in DWNT, observe the relation  $\omega_{\text{RBM,in}} = 228/d$  while the expression of the outer tube RBM frequency is either set to  $\omega_{\text{RBM,out}} = 228/d$  (black) or  $\omega_{\text{RBM,out}} = 204/d + 27$  (olive). Within the framework of this thesis, and based on our observation for SWNTs, our data are compared to the BLM calculated with  $\omega_{\text{RBM,out}} = 204/d + 27$  (olive symbols and lines in Fig. V.1.a). The same figure illustrates the upshift of the BLM in comparison to the RBM measured for isolated nanotubes (dashed lines).

We recall that the RBM of an isolated SWNT is observed only for resonant excitation

---

<sup>a</sup>The study of the 2D band, corresponding to inter-valley phonon modes, is beyond the scope of this thesis.

<sup>b</sup>We gracefully thank V. Popov and M. Paillet for providing the calculated data and useful discussions.

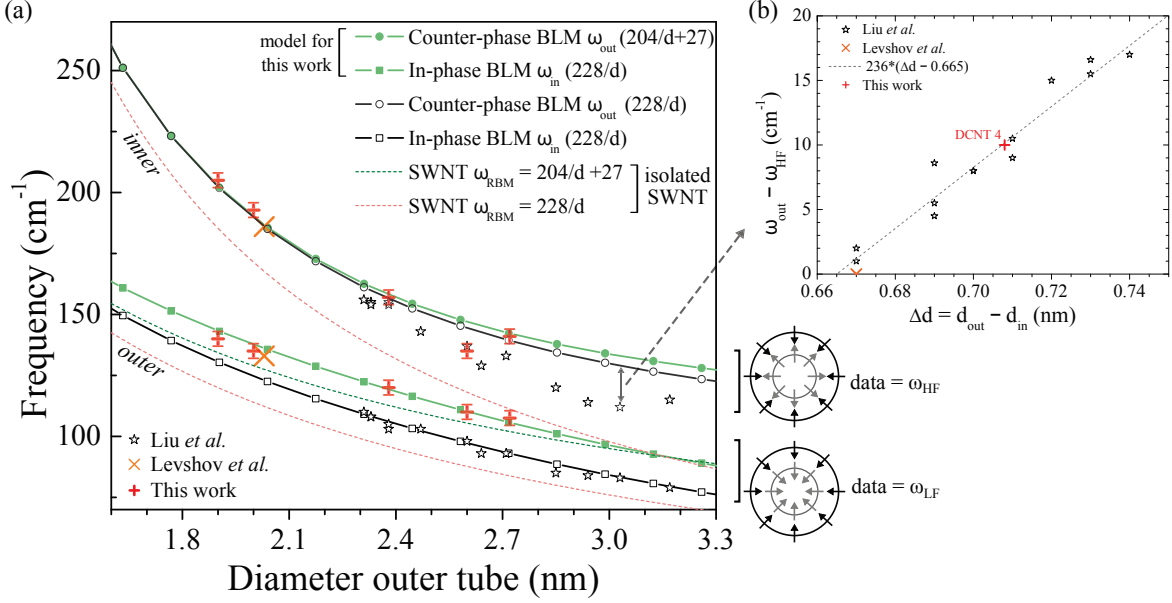


**Figure V.1:** Diameter identification of double-wall carbon nanotubes from resonant Raman spectroscopy. (a) Breathing-like modes *vs.* outer wall diameter: (black & olive) calculated data for fixed interwall separation 0.335 nm ([116,168] and private communication with M. Paillet), (symbols) experimental data. The low and high frequency modes correspond to in-phase and counter-phase breathing modes of the inner and outer tubes. Dashed lines illustrate the relation between radial breathing modes and diameter in isolated SWNTs (see text for more details). (b) Deviations of the high-frequency BLM from the results of the coupled oscillator model (for example the grey double arrow) are explained by changes in the interwall distance. Only DCNT 4 shows an interwall separation different from 0.335 nm (red cross).

(RRS – resonant Raman spectroscopy), i. e. when the laser excitation line is close to one of the absorption energy transitions of the tube. As a direct consequence of the interwall coupling, resonant excitation of one nanotube (inner or outer wall) reveals the two BLM in the Raman spectrum. The mechanical coupling has been reported for individual bundles [104] and first evidence in DWNTs by Levshov et al. [116]. Recently, a quantum-mechanical model also explained the Raman intensity ratio of the two BLM ( $I_{out}/I_{in}$ ) [167]. Briefly, by including the relative phase factor and the Frank-Condon effects (the excited state has a displaced potential energy surface compared with that of the ground state), the authors addressed quantum interferences between BLM modes that explained changes in  $I_{out}/I_{in}$  for different laser excitation. Duque et al. reported the observation of quantum interference between G-phonon modes associated to two optical energy transitions [148], this discussion is beyond the scope of this thesis though.

Data from refs. [116,167], obtained from Raman spectroscopy of individual structure-assigned free-standing DWNTs, are reported in Fig. V.1.a. The BLM of the (12,8)@(16,14) DWNT measured by Levshov et al. (on a sample similar to FS-1 and FS-2) match the

calculated data for interwall distance 0.335 nm. On the other hand, deviations of counterphase BLM ( $\omega_{\text{HF}}$ ) measured by Liu et al. with respect to the calculation of Popov and Henrard ( $\omega_{\text{out}}$ ) are accounted by changes in the interwall distance. The difference  $\omega_{\text{out}} - \omega_{\text{HF}}$  is plotted in Fig. V.1.b as a function of the diameter difference between inner and outer nanotubes. It shows a clear correlation between  $\Delta d$  and the frequency deviations of the measured counterphase BLM data from the calculated ones. This observation demonstrates the interwall distance is not constant for all DWNTs. Hence, this parameter should also be taken into account to identify the structure of the nanotube from Raman spectroscopy.

### Photoluminescence and absorption

Optical properties of DWNTs depend on interwall interactions which are function of: the interwall distance, and the characteristics (nature, diameter, chirality) of the inner and outer walls. The ability of DWNTs to exhibit photoluminescence have been the object of long debates in the past 10 years. In fact, PL is efficiently quenched in SWNT bundles due to the many non-radiative relaxation pathways and energy/charge transfers between tubes [166]. Similar phenomena could be reasonably expected in DWNTs as interwall coupling is encouraged by the large contact area between inner and outer walls (in SWNT bundles only a small portion of a tube wall interacts with its neighbors). The answer is still unclear as some studies reported observation of PL from the inner tubes [169–171], while others on different DWNTs do not. Yang et al. suggested that photoluminescence properties depend on diameter and chirality [172], but eluding the question of environmental effects on the PL quantum yield [169]. Furthermore, PL intensity modifications was ascribed to exciton transfer from the inner wall to the outer one whose bandgap is smaller [171]. Suppression of PL was explained by the strong quenching of exciton states by metallic outer tubes. The photoluminescence intensity is likely to depend on relative strength of interwall transfer and radiative recombination of excitons. Still micro-PL study of individual DWNTs placed in different environments would help to answer this question.

Photoluminescence excitation and absorption on small-diameter DWNTs ensemble measured redshifts as small as few meV of the energy transitions of both the inner ( $E_{ii}^{\text{in}}$ ) and outer ( $E_{ii}^{\text{out}}$ ) nanotubes [170, 171, 173]. A theoretical study reported energy shifts almost one order of magnitude larger originating from dielectric screening effects and exciton binding energy re-normalization [174]. However, exciton-exciton interactions were not included in this study, and overlapping of energy transitions from the inner and outer walls could possibly modify the overall absorption properties of DWNTs. Tomio et al. examined the influence of screening effects, which are a consequence of interwall Coulomb interactions, on excitons and optical spectra of DWNTs [174]. They report changes in the excitation energy, exciton binding energy, and oscillator strength with respect to SWNTs as they studied the three systems: SC@SC, SC@M, M@SC, with different ratio  $d_{\text{out}}/d_{\text{in}}$ . To summarize, their results show that lower energy exciton states  $|B\rangle$  redshifts by few tens of meV whereas stronger shifts are observed for the

excited exciton states ( $n_B \geq 2$ ) and the continuum band edges. The two latter effects are enhanced in metallic tubes. In all cases, the exciton binding energy of  $|B\rangle$  is reduced by  $\sim 100$  meV, whereas the oscillator strength decreases by less than  $\sim 5\%$ . Finally, significant increase of the continuum absorption is observed, as well as a decrease of the energy gap between  $|B\rangle$  and continuum band-edge. These phenomena are even more pronounced for metallic resonances.

### Field-effect transistor

Field-effect transistor (FET) devices based on the electrical transport properties of DWNTs develop attractive properties for environment sensing at the nanoscale level. The inner tube FET response probes changes of the outer tube environment and geometry. For example, after functionalization of the outer wall with specific receptors, the inner tube FET response is sensitive to the external concentration of target entities [175]. Pressure-induced modifications of the outer tube cross-section can be utilized as high-sensitive pressure sensor [26]. Other applications can be imagined, as well as combination with the DWNTs optical properties (absorption and PL).

## V-2 Raman spectroscopy

In this section, the structural characteristics of five individual free-standing DWNTs are obtained from Raman scattering experiments. More precisely, from the analysis of their breathing-like modes and tangential modes we derived the diameter and nature of both their inner and outer walls (see details in Sec. V-1).

Raman spectroscopy experiments on these samples (suspended on FS-1 and FS-2) have been carried out by Matthieu Paillet and Huy-Nam Tran at the Laboratoire Charles Coulomb in the University of Montpellier. Their work covers the investigation of BLM and tangential modes (also the 2D phonon modes) for many different laser excitation wavelengths. These results are complementary to absorption spectroscopy for assessing the optical properties of DWNTs. Although we sometimes refer to the results obtained from Raman spectroscopy, only part of them are presented in this thesis. In fact, detailed discussion of Raman spectroscopy is beyond the scope of this work and will only lengthen the discussion; we rather concentrate on the interpretation of few selected Raman spectra serving our purposes.

### V-2.1 Breathing-like modes

After examination of the Raman spectra, five DWNTs were identified: DCNT 1 to DCNT 5. Their inner and outer wall diameters have been derived from the BLM frequencies, as discussed in Sec. V-1. In practice, the outer tube diameter  $d_{\text{out}}$  of a DWNT is obtained by comparing the high-frequency ( $\omega_{\text{HF}}$ ) and low-frequency ( $\omega_{\text{LF}}$ ) BLM frequencies (red symbols in Fig. V.1.a) with the calculated data of Popov and Henrard [168]

(olive in the same graph).<sup>c</sup> Additional correction to the interwall distance (in Popov model  $\Delta d = 0.335$  nm) can be estimated from Fig. V.1.b. Our results are summarized in Tab. V.1:  $d_{\text{out}}$  ranges from 1.90 to 2.72 nm and  $d_{\text{in}}$  falls in the interval 1.23-2.05 nm. Only DCNT 4 presents an interwall separation different from 0.335 nm, yielding a value of 0.354 nm which accounts for the difference between the measured  $\omega_{\text{HF}}$  and the calculation counter-phase mode  $\omega_{\text{out}}$  ( $\omega_{\text{HF}} - \omega_{\text{out}} = 10 \text{ cm}^{-1}$  for DCNT 4).

Sample	$\omega_{\text{LF}}$ ( $\text{cm}^{-1}$ )	$\omega_{\text{HF}}$ ( $\text{cm}^{-1}$ )	$d_{\text{out}}$ (nm)	Interval* $d_{\text{out}}$ (nm)	$\Delta d$ (nm)	$d_{\text{in}}$ (nm)	Type
DCNT 1	135	193	2.00	/	0.67	1.32	SC@SC
DCNT 2	107.5	141	2.72	[2.68; 2.75]	0.67	2.05	SC@SC
DCNT 3	140	205	1.90	/	0.67	1.23	SC@M
DCNT 4	110	135	2.60	[2.53; 2.67]	0.708	1.892	M@SC
DCNT 5	120	157	2.38	[2.35; 2.44]	0.67	1.71	M@SC

**Table V.1:** Breathing-like modes data and diameters of double-wall carbon nanotubes. (\*)The diameter interval is estimated from the uncertainty on the BLM frequency estimated at  $\pm 3 \text{ cm}^{-1}$ . All these data are plotted in Fig. V.1 (red).

## V-2.2 Tangential modes

Although analysis of BLM provides inner and outer walls diameters, the nature of each wall (semiconducting SC or metallic M) can be determined from the tangential modes. More generally, only the examination of tangential modes and BLM for different laser excitation, and combined with the absorption spectra, allows the identification of individual DWNTs.

### DCNT 1

Fig. V.2.a shows the Raman spectra of DCNT 1 for two laser excitation energies: 1.59 eV and 1.88 eV. Both present two BLM and four tangential modes which characteristics are listed in the table included in Fig. V.2.a. Moreover, based on the values of diameters ( $d_{\text{out}} = 2.00$  nm,  $d_{\text{in}} = 1.32$  nm) and the Kataura plot, this sample nanotube necessarily contains a DWNT (this point is even more obvious after examination of the absorption spectrum). The G-band profile is composed of four phonon modes: two  $G^+$  modes at  $\sim 1592 \text{ cm}^{-1}$  and  $\sim 1586 \text{ cm}^{-1}$ , two  $G^-$  modes at  $1557 \text{ cm}^{-1}$  and  $1577 \text{ cm}^{-1}$ . Their linewidths are about  $5 \text{ cm}^{-1}$ , and their amplitudes depend on the excitation energy. These observations are characteristic of chiral semiconducting nanotubes, thus DCNT 1 is assigned to a SC@SC double-wall carbon nanotube.

### DCNT 2

For laser excitation 1.48 eV, Raman spectra of DCNT 2 present two BLM and a single sharp tangential mode at  $1587 \text{ cm}^{-1}$  with a weak shoulder at about  $1575 \text{ cm}^{-1}$  (Figs. V.3.a,b). Assuming a SWNT, this G-band profile agrees with a close-to zig-zag

<sup>c</sup>The uncertainty on the BLM frequencies is estimated at  $3 \text{ cm}^{-1}$ , which includes the instrumental errors as well as the uncertainty on the coupled oscillator model.



semiconducting nanotube. However, interpretations of this type of profile is more complex in this sample as we also observe quantum interferences between tangential modes (not shown). At 2.21 eV, the G-band profile is composed of three phonon modes located at 1570, 1575, and 1590  $\text{cm}^{-1}$  (their linewidths are smaller than 5  $\text{cm}^{-1}$ ) characteristic of chiral semiconducting CNTs. In this case, the phonon mode at 107.5  $\text{cm}^{-1}$  is almost completely smeared out. From these observations, if we assume a bundle of two SWNTs, both will be semiconducting and present diameters 1.79  $\text{cm}^{-1}$  and 2.53  $\text{cm}^{-1}$ . The Kataura plot infer that no energy transition is available at 1.48 eV, which dismiss this hypothesis. In fact, the Raman intensity ratio of the two BLM can vary significantly as a function of the excitation wavelength. This phenomenon is a consequence of quantum interferences between breathing-like phonon modes in DWNTs [167]. After examination of Raman excitation and diffusion profiles of all phonon modes (not presented in this thesis) [147, 148, 167], a good agreement between theory and our measurements is reached and DCNT 2 is identified as an individual DWNT with both walls of semiconducting nature (one of family type I and the other of family type II).

### DCNT 3

Figs. V.4.a,b present the Raman spectra of DCNT 3 for four laser excitation energies (1.48, 1.53, 1.58, and 1.65 eV) chosen such that they probe different absorption transitions (see also Fig. V.4.c for the absorption spectrum and related comments in the next section). For all excitation energies, two breathing-like phonon modes are measured at 140  $\text{cm}^{-1}$  and 205  $\text{cm}^{-1}$ , while relatively important changes of the tangential modes profiles are observed. Excitation 1.48, 1.53, and 1.65 eV all exhibit two  $G^+$  phonon modes at 1585 and 1596  $\text{cm}^{-1}$  (with linewidths 4 and 6  $\text{cm}^{-1}$ , respectively) as well as a  $G^-$  mode at 1555  $\text{cm}^{-1}$  (FWHM  $\sim 4 \text{ cm}^{-1}$ ). On the other hand, the remaining Raman spectrum presents a broad  $G^-$  phonon mode (asymmetric profile with linewidth broader than 80  $\text{cm}^{-1}$ ) in addition to the two  $G^+$  phonons. These observations demonstrate that this sample is composed of a chiral semiconducting tube and a chiral metallic nanotube. In addition to the absorption results, Raman spectroscopy probes an energy transition from each tube and measures two BLM phonon modes in all cases, which lead to the conclusion that this nanotube is a SC@M double-wall carbon nanotube.

### DCNT 4

The Raman spectrum of DCNT 4 (Fig. V.5.a), for laser excitation 2.33 eV, is composed of two BLM (109 and 135  $\text{cm}^{-1}$ ) and two tangential modes at 1586 and 1592  $\text{cm}^{-1}$  (with associated linewidth 6 and 5  $\text{cm}^{-1}$ , respectively). Assuming SWNTs, this observation suggests the presence of two chiral SC nanotubes with diameters 1.89 and 2.49 nm. Absorption energy transitions corresponding to such SC-SWNTs are in fact resonant with the excitation 2.33 eV (see Kataura plot, e. g. in Fig. V.5.d). However, the absorption spectrum (Fig. V.5.c) shows two resonances at 1.44 and 1.51 eV (labelled R2 and R3), one is assigned to the  $S_{33}$  of the larger nanotube whereas, recalling the Kataura plot, the other one is incompatible with our hypothesis. After combined examination of the absorption and Raman spectra, we conclude that this nanotube is an individual DWNT

with metallic inner wall and semiconducting outer wall (M@SC). Complementary Raman scattering measurements on the substrate-supported segment of DCNT 4 confirmed this conclusion.

### **DCNT 5**

Raman scattering signal of DCNT 5 was measured with more than twenty different laser energies and at two different positions of the freely suspended segment of the sample (on the left-hand side and in the middle, respectively, points ‘FD’ and ‘FB’, as shown in the SMS image of DCNT 5, Fig. V.6.b). Here, we present selected Raman spectra corresponding to the excitation energies 1.49, 1.51, and 1.53 eV (Fig. V.6.a), acquired at point FB of the nanotube. All spectra measure three peaks (120, 145, and  $157\text{ cm}^{-1}$ ) in the breathing-modes region and at least four tangential modes: two sharp peaks at 1590 and  $1593\text{ cm}^{-1}$  (FWHM  $\sim 4\text{ cm}^{-1}$ ) assigned to  $G^+$  modes, a small-amplitude feature at  $1578\text{ cm}^{-1}$  characteristic of a chiral semiconducting tube, and a broad non-symmetric feature below  $1575\text{ cm}^{-1}$  which testifies the presence of at least one chiral metallic nanotube. From the combined examination of the Raman and absorption spectra, as well as comparison with the Kataura plot, we conclude that DCNT 5 is composed of a DWNT (M@SC) and a metallic SWNT. SMS imaging of the sample (Fig. V.6.b) shows that DCNT 5 splits into two nanotubes on the left-hand side of the trench. Raman and absorption spectroscopy at point FD proves that this branch is the individual DWNT, and logically the other one (dashed line) is the M-SWNT.

## **V–3 Absorption spectroscopy of free-standing DWNT**

In the previous section, both inner and outer walls characteristics of DWNTs, i. e. their diameters and nature, have been identified with Raman spectroscopy. Absorption spectra of these nanotubes also provided important information for the structure assignment. In this part, we discuss the absorption spectra of the individual free-standing DWNTs DCNT 1 to DCNT 3 (Tab. V.1). The absorption of nanotubes DCNT 4 and DCNT 5 are also studied in the presence of other environments (substrate, metallic SWNT) and will be discussed in the next section. Following the analysis procedure described for SWNTs, we examine the absorption features of the DWNTs that we then compare to those of SWNTs.

### **V–3.1 Double-wall nanotube of type SC@SC**

As Sec. IV–1 presents a detailed analysis of the absorption of individual semiconducting SWNTs, we first investigate the absorption response of SC@SC double-wall nanotubes. In fact, in the presence of metallic tubes, interpretation of the absorption signal is possibly more complicated, e. g. see Sec. IV–2.

### V-3.1.a DCNT 1

#### Absorption spectrum and structure identification

For incident light polarized along the nanotube, the measured spectrum of the absorption cross-section per unit length,  $C_{\text{abs}}(E)$ , of DCNT 1 is plotted in Fig. V.2.b. Five peak features are observed at 1.59, 1.90, 2.20, 2.42, and 2.80 eV with absorption cross-section 0.50, 0.12, 0.31, 0.35, and 0.13 nm<sup>2</sup>/nm, respectively, overlapping a non-resonant absorption background of 0.23 nm<sup>2</sup>/nm (maximum deviations on these absolute absorption measurements are  $\pm 0.025$  nm<sup>2</sup>/nm).

For further structure identification, the position of these absorption features and the diameters ( $d_{\text{in}} = 1.32$  nm,  $d_{\text{out}} = 2.00$  nm) are reported on the Kataura plot (Fig. V.2.c). Using the method described in Appx. A (see also refs. [18, 44, 89]), a rigid shift of the theoretical optical transitions calculated for SWNTs was applied to best match the peak features (shifts of +0.30 eV and +0.41 eV were applied to the calculated optical transitions with  $p < 4$  and  $p \geq 4$ , respectively).<sup>d,e</sup> The instrumental uncertainty on the peaks positions was estimated to be 2 nm, and reported with error bars on the Kataura plot. From Fig. V.2.c, and assuming small shifts of the  $E_{ii}$  resonances in DWNTs with respect to SWNTs [170, 171, 174], features at 1.90, 2.20, and 2.80 eV are assigned to the resonances, respectively,  $S_{33}^{\text{out}}$ ,  $S_{44}^{\text{out}}$ , and  $S_{55}^{\text{out}}$ , of the semiconducting outer nanotube. Likewise, absorption peaks at 1.59 and 2.42 eV correspond to the semiconducting inner tube transitions  $S_{22}^{\text{in}}$  and  $S_{33}^{\text{in}}$ , respectively. The absorption peaks in Fig. V.2.b are labeled accordingly to these observations.

Thanks to the absorption and Raman measurements, both the inner and outer nanotubes are assigned to chiral semiconducting tubes of type I. Moreover, we infer that the inner (resp. outer) wall exhibit a small (resp. large) chiral angle. In the case of DCNT 1, constraints on the interwall distance and positions of the energy transitions restrain our choice to a single chirality assignment: (14,4)@(15,14). Although high-order transitions ( $p \geq 4$ ) are in good agreement with theory, measured  $S_{22}^{\text{in}}$  (absorption) and  $S_{22}^{\text{out}}$  (at 1.25 eV, obtained from resonant Raman spectroscopy) are both blue-shifted by more than 100 meV in comparison to the calculated energy transitions [16, 18, 44]. This result somehow differs from the small redshifts measured by photoluminescence on small DWNTs [170, 171] and theoretical calculations [174]. On the other hand, our measurements for high-order transitions are in good agreement with the results reported in the literature.

#### Characteristics of the excitonic energy transitions

The properties of the absorption transitions were obtained by fitting the measured ab-

<sup>d</sup> $p = 1, 2, 4, 5, 7, \dots$  corresponds to  $S_{11}, S_{22}, S_{33}, S_{44}, S_{55}, \dots$ ; and  $p = 3, 6, \dots$  stands for  $M_{11}, M_{22}, \dots$  (see Sec. II-1.1)

<sup>e</sup>In refs [18, 44, 89], in order to include excitonic effects to calculated energy transitions, rigid shifts +0.32 eV and 0.43 eV are applied to transitions with  $p < 4$  and  $p \geq 4$ , respectively. This difference of rigid shift between low-order and high-order energy transitions (0.11 eV) is kept constant in our analysis.

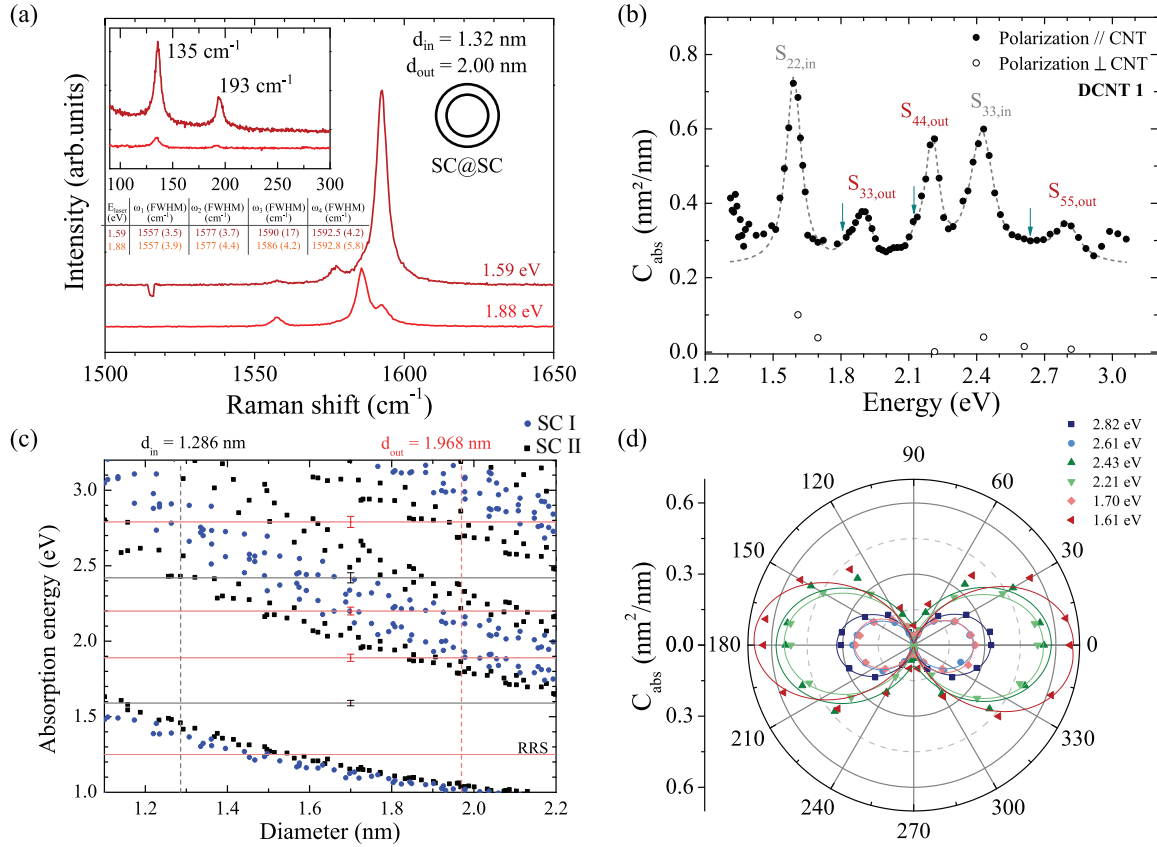


**Figure V.2:** Absorption and Raman spectroscopy of the free-standing double-wall nanotube DCNT 1 identified as (type-I SC)@(type-I SC). (a) Raman spectra showing the tangential phonon modes and BLM (inset graph) measured with two different lasers. (inset table) characteristics of the tangential modes. (b) Absolute absorption cross-section spectrum for incident light polarized parallel (full dots) and perpendicular (open dots) to the nanotube. The dashed line is the result of the fit detailed in the text. (c) Structure assignment with the Kataura plot: comparison between measured absorption energies (red and gray lines) and theoretical optical transition energies (black squares and blue dots, type I and type II semiconducting nanotubes, respectively) as a function of nanotube diameter. Left scale corresponds to the energy in the experimental absorption spectrum. Theoretical optical transitions are obtained by shifting the calculated data of ref. [44]: +0.30 and +0.41 eV for transitions with  $p < 4$  and  $p \geq 4$ , respectively. For the sake of clarity, the metallic tubes have been removed from the plot. Vertical dashed lines show the diameters of the inner (grey) and outer (red) walls. (RRS) Energy transition obtained from resonant Raman scattering. (d) Light-polarization-dependent absorption cross-section for different laser excitation energies. The experimental data (symbols) are fitted using  $C_{\text{abs}}^{\parallel} \cos^2 \theta_{\text{pol}} + C_{\text{abs}}^{\perp} \sin^2 \theta_{\text{pol}}$  functions (lines),  $\theta_{\text{pol}} = 0$  being the direction parallel to the nanotube axis.

sorption spectrum. As detailed for SWNTs, the process involves fitting of the peaks with Voigt functions including fixed Gaussian FWHM, which accounts for the laser linewidth, on top of a constant non-resonant absorption ( $C_{\text{abs}}^{\text{nr}}$ ). Tab. V.2 records the characteristics of the exciton peaks, i. e. their absorption cross-section  $C_{\text{abs},E_{ii}}^{\text{exc}}$  (in  $\text{nm}^2/\text{nm}$ ), FWHM  $\gamma_{E_{ii}}$  (in meV), and area (in  $\text{nm.eV}$ ). As in SWNTs, absorption side-features are observed at 1.84, 2.13, and  $\sim 2.62$  eV (indicated by cyan arrows in Fig. V.2.b). The two former are well fitted with Lorentzian-like functions, whereas the later presents an asymmetric lineshape (it is adjusted with asymmetric phonon-side band profile, see Sec. IV-1.2.b for details). The feature at 2.62 eV, located  $\sim 200$  meV above  $S_{33}^{\text{in}}$ , can possibly correspond to the PSB of  $S_{33}^{\text{in}}$ . The other two features, red-shifted by about 50 meV with respect to their respective nearest outer tube resonances (likewise, they are blue-shifted by about 240 meV from  $S_{22}^{\text{in}}$  and  $S_{33}^{\text{out}}$ ), are hardly explained by phonon-assisted absorption. They might correspond to excited exciton states [72,74], yet Tomio et al. estimated an energy separation of 50-100 meV between the lower-energy bright exciton  $|B\rangle$  (or  $E_{ii}$ ) and the first excited exciton. Another possible explanation involves interwall coupling resulting in the activation of new excitons states, still this hypothesis requires further theoretical investigations.

DCNT 1 SC@SC	$E_{ii}$ (eV)	$C_{\text{abs}}^{\text{exc}}$ ( $\text{nm}^2/\text{nm}$ )	$\gamma_{E_{ii}}$ (meV)	Area ( $\times 10^{-2}$ $\text{nm.eV}$ )	$C_{\text{abs}}$ ( $\times 10^{-17}$ $\text{cm}^2/\text{C-atom}$ )			Oscillator strength ( $\times 10^{-2}$ per C-atom)	
					$C_{\text{abs},\text{SW}}^{\text{exc}}$	$C_{\text{abs},\text{NT}}^{\text{exc}}$	$C_{\text{abs},\text{NT}}^{\text{peak}}$	$f_{\text{C},\text{SW}}$	$f_{\text{C},\text{NT}}$
$S_{22}^{\text{in}}$	1.59	0.50	77	6.0	3.20	1.26	1.85	3.6	1.4
$S_{33}^{\text{out}}$	1.90	0.12	76	1.4	0.51	0.30	0.79	0.6	0.3
$S_{44}^{\text{out}}$	2.20	0.31	67	3.3	1.32	0.78	1.37	1.3	0.8
$S_{33}^{\text{in}}$	2.42	0.35	123	6.8	2.30	0.88	1.47	4.0	1.6
$S_{55}^{\text{out}}$	2.80	0.13	102	2.1	0.55	0.33	0.92	0.8	0.5

**Table V.2:** Absorption characteristics of DCNT 1 (DWNT of type SC@SC).

**DEFINITIONS:** as for SWNTs, absorption cross-sections are either directly expressed in surface area per unit length ( $\text{nm}^2/\text{nm}$ ) or in unit of surface area per carbon atom ( $\text{cm}^2/\text{C atom}$ ). The relation between the two considers the number of atoms per unit length.<sup>f</sup> For each excitonic energy transition in a DWNT, we define its excitonic ( $C_{\text{abs},\text{NT}}^{\text{exc}}$ ) and peak ( $C_{\text{abs},\text{NT}}^{\text{peak}}$ ) absorption cross-sections, as well as its oscillator strength ( $f_{\text{C},\text{NT}}$ ), with respect to the total number of C-atom per unit length of the DWNT (including atoms from the inner and outer walls). Furthermore, the energy transition can often be associated with a resonance of the inner or outer nanotube, hence, in this case, we define both the excitonic absorption cross-section ( $C_{\text{abs},\text{SW}}^{\text{exc}}$ ) and oscillator strength ( $f_{\text{C},\text{SW}}$ ) with respect to the number of atoms in one of the walls.

The outer tube yields exciton linewidth  $\gamma_{S_{33}^{\text{out}}}$  and  $\gamma_{S_{44}^{\text{out}}}$  thirty percent larger than our observations for free-standing SWNTs of similar diameter (see CNT 1 and CNT 2 in Fig. IV.4 and Tab. IV.1, and also Fig. V.8.b).  $\gamma_{S_{33}^{\text{in}}}$  is two times broader in comparison to

<sup>f</sup>In DWNTs the number of atoms per unit length, for 2 nm outer nanotubes, is about 1.5 times larger than in SWNTs.

both the outer nanotube and isolated SWNTs. These observations indicate faster decay of the excitons via new relaxation pathways possibly initiated by local potential fluctuations arising from dielectric screening and interwall coupling [82, 114]. The values of absorption cross-sections tend to be attenuated for certain energy transitions in comparison to SWNTs. The outer wall presents values of  $C_{\text{abs,SW}}^{\text{exc}}(S_{33}^{\text{out}})$  and  $C_{\text{abs,SW}}^{\text{exc}}(S_{55}^{\text{out}})$  more than three times smaller than in the SWNT CNT 1. The DWNT oscillator strength per C-atom ( $f_{\text{C,NT}}$ ) tends to yield smaller values in comparison to isolated SWNTs of similar diameters (Fig. V.8.c).  $f_{\text{C,NT}}$  associated with transitions from the inner nanotube are in average two times bigger than those assigned to the outer wall. On the other hand, under the assumption that the inner and outer tubes interact only via electromagnetic potentials, i. e. an exciton peak can be associated with one of the two walls,  $f_{\text{C,SW}}$  yields values comparable but still smaller than those observed in SWNTs (compare the values of column  $f_{\text{C,SW}}$  in Tab. V.2 and oscillator strengths of SWNTs in Fig. IV.4).

### Polarization-dependent absorption

At last, we analyze the polarization-dependent absorption cross-section signal for different laser excitation energies (Fig. V.2.d). The ratio  $C_{\text{abs}}^{\parallel}/C_{\text{abs}}^{\perp}$  is bigger than six in all cases inferring strong antenna effects also in DWNTs. Negligible absorption is generally measured for perpendicular polarization except for excitation at the energy of the inner tube resonances (1.61 eV and 2.43 eV) as shown in Fig. V.2.b (open symbols). This observation suggests weaker depolarization field in the inner wall as compared to the outer wall. This phenomenon could again find its origin in the dielectric screening effects and interwall coupling [57, 176].

### V-3.1.b DCNT 2

In this part, we study the absorption of DCNT 2 which is, as DCNT 1, a double-wall carbon nanotube composed of two semiconducting tubes. On the other hand, its outer and inner diameters ( $d_{\text{out}} = 2.72$  nm and  $d_{\text{in}} = 2.05$  nm, respectively) are larger than in the previous sample DCNT 1.

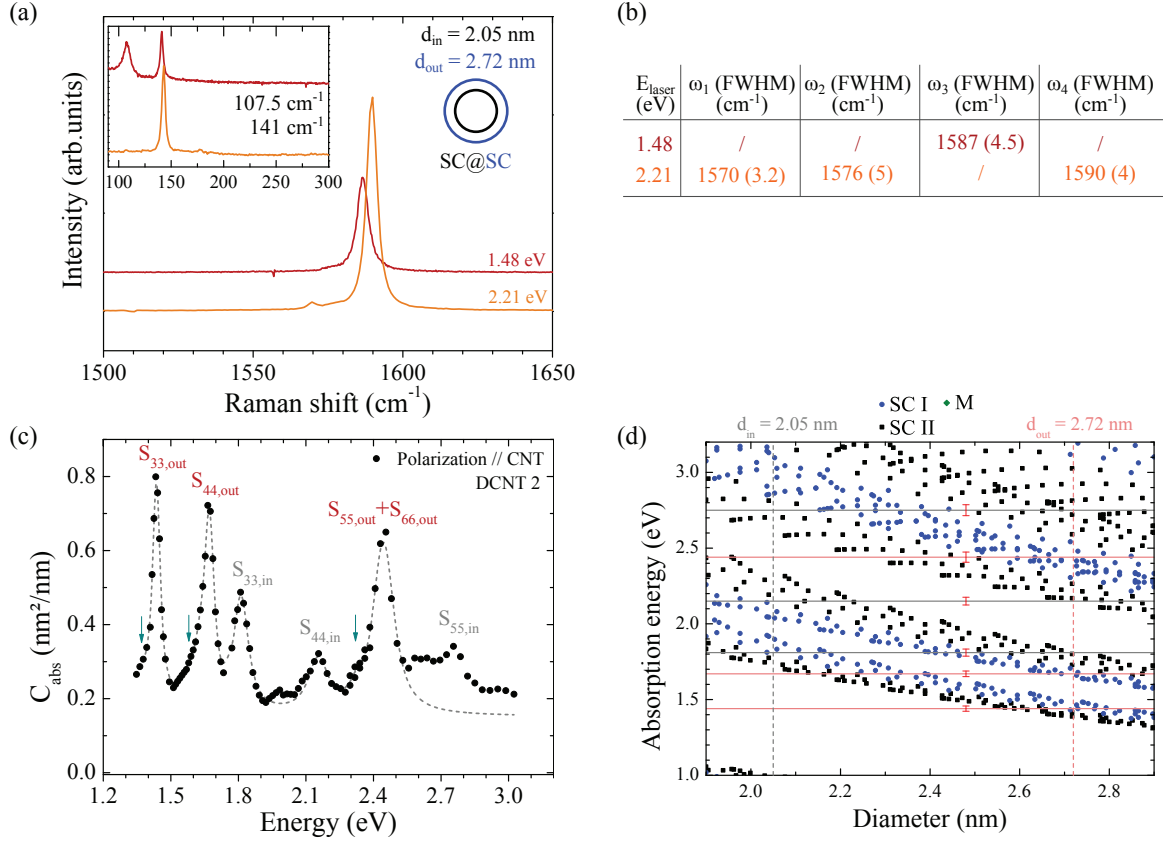
### Absorption spectrum and structure identification

Fig. V.3.c presents the spectrum of the absorption cross-section per unit length of DCNT 2 for incident light polarized parallel along the nanotube. On top of a constant non-resonant absorption ( $C_{\text{abs}}^{\text{nr}} \approx 0.15 \text{ nm}^2/\text{nm}$ ), six absorption peaks are observed at 1.44, 1.67, 1.81, 2.15, 2.44, and 2.75 eV associated with absorption cross-section 0.62, 0.51, 0.31, 0.15, 0.49, and 0.24  $\text{nm}^2/\text{nm}$ . They are reported on the Kataura plot in Fig. V.3.d (horizontal red lines), along with the diameters measured with Raman spectroscopy (vertical red and grey lines standing for the outer and inner tubes, respectively).<sup>g</sup> After interrelating absorption and Raman results, we conclude that the inner (resp. outer) tube is semiconducting of family type I (resp. type II). On the one hand, resonances at 1.44, 1.67, and 2.44 eV are associated with  $S_{33}^{\text{in}}$ ,  $S_{44}^{\text{in}}$ , and a mix  $S_{55}^{\text{in}} + S_{66}^{\text{in}}$ , respectively.

---

<sup>g</sup>The calculated optical transitions are obtained here from ref. [16].





**Figure V.3:** Absorption and Raman spectroscopy of the individual free-standing double-wall nanotube DCNT 2 identified as (type-I SC)@(type-II SC). (a) Raman spectra showing the tangential phonon modes and BLM (inset graph) measured for two laser excitation energies. (b) Characteristics of the tangential modes. (c) Absolute absorption cross-section spectrum for incident light polarized parallel to the nanotube. The dashed line is the result of the fit detailed in the text. (d) Structure assignment with the Kataura plot: comparison between measured absorption energies (horizontal red and gray lines) and theoretical optical transitions from ref. [16] (black squares and blue dots, type I and type II semiconducting nanotubes, respectively) as a function of nanotube diameter. For the sake of clarity, the metallic tubes have been removed from the plot. Vertical dashed lines show the diameters of the inner (gray) and outer (red) walls.



On the other hand, peaks at 1.81, 2.15, and 2.75 eV correspond to  $S_{33}^{\text{out}}$ ,  $S_{44}^{\text{out}}$ , and  $S_{55}^{\text{out}}$ , respectively. Although exact chirality identification is complicated, the results indicate that both inner and outer nanotubes exhibit large chiral angles.

### Characteristics of the excitonic energy transitions

The characteristics of the exciton resonances (Tab. V.3) were obtained by fitting the measured absorption spectrum. We followed the same procedure as introduced for DCNT 1. The result of the fit, plotted in Fig. V.3.c (dashed grey curve), captures the main absorption features, but fails to reproduce data around 1.9-2.0 eV and above 2.6 eV. As indicated by blue arrows, we included Lorentzian-like functions at 1.37, 1.58, 1.63, and 2.32 eV in order to obtain good agreement of the main absorption peaks with Voigt profiles. Absorption features around  $S_{55}^{\text{in}}$  are clearly not well reproduced with only Voigt and PSB profiles. As in DCNT 1, some of these side absorption peaks are lying directly ( $\sim 40 - 100$  meV) below the main excitonic transitions of the outer nanotube. Few interpretation to these absorption features have been proposed: phonon-assisted absorption, excited exciton transitions, and activation of absorption states due to inter-wall coupling. Further temperature and polarization dependent investigations as well as lineshape analysis would help to determine the origin of all these features [15, 72].

DCNT 2 SC@SC	$E_{ij}$ (eV)	$C_{abs}^{\text{exc}}$ (nm <sup>2</sup> /nm)	$\gamma_{E_{ij}}$ (meV)	Area ( $\times 10^{-2}$ nm.eV)	$C_{abs}$ ( $\times 10^{-17}$ cm <sup>2</sup> /C-atom)			Oscillator strength ( $\times 10^{-2}$ per C-atom)	
					$C_{abs,SW}^{\text{exc}}$	$C_{abs,NT}^{\text{exc}}$	$C_{abs,NT}^{\text{peak}}$	$f_{C,SW}$	$f_{C,NT}$
$S_{33}^{\text{out}}$	1.44	0.62	35	3.4	1.91	1.09	1.68	0.95	0.54
$S_{44}^{\text{out}}$	1.67	0.51	43	3.4	1.57	0.89	1.48	0.96	0.55
$S_{33}^{\text{in}}$	1.81	0.31	70	3.4	1.26	0.54	1.13	1.30	0.54
$S_{44}^{\text{in}}$	2.15	0.15	97	2.3	0.61	0.26	0.85	0.84	0.36
$S_{55}^{\text{out}} + S_{66}^{\text{out}}$	2.44	0.49	97	7.5	1.51	0.86	1.45	2.09	1.19
$S_{55}^{\text{in}}$	2.75	0.24	/	/	/	0.62	1.21	/	/

**Table V.3:** Absorption characteristics of DCNT 2 (DWNT of type SC@SC).

Similar to the results for DCNT 1, in DCNT 2, the inner tube exciton peaks ( $S_{33}^{\text{in}}$  and  $S_{44}^{\text{in}}$ ) are two times broader than those of the outer tube (Tab. V.3). Moreover, the linewidths of resonances  $S_{33}^{\text{out}}$  and  $S_{55}^{\text{out}}$  are smaller than our observations for isolated SWNTs. Absorption cross-sections ( $C_{abs,NT}^{\text{exc}}$ ,  $C_{abs,NT}^{\text{peak}}$ , and  $C_{abs,SW}^{\text{exc}}$ ) present smaller values in comparison to SWNTs but comparable to our measurements for DCNT 1 (Fig. V.8.a). Likewise, the DWNT oscillator strengths per C-atom stays about 0.4-0.6 (the peak at 2.44 eV which might contain two excitons is discriminated here) which is two to three times smaller than in the case of SWNTs (Fig. V.8.c).

It is also interesting to compare the exciton properties of the inner tube ( $d_{\text{in}} = 2.05$  nm) to those of the outer wall in DCNT 1 (they exhibit similar diameters, are both semiconducting tubes of family type I, and possess large chiral angles). Excitons characteristics of  $S_{33}$  and  $S_{44}$  in DCNT 2 are comparable with those of excitons  $S_{44}$  and  $S_{33}$  in DCNT 1, respectively. Precisely, oscillator strengths of  $S_{33}$  and  $S_{44}$  yield 0.54 and 0.36 in DCNT 2, while we measure values 0.3 and 0.8 in DCNT 1. In other words, the

absorption strength is redistributed among excitons when going from the inner tube in DCNT 2 to the outer one in DCNT 1.

Finally, we notice an overall decrease of exciton oscillator strength in DCNT 2 as compared to DCNT 1 (compare column  $f_{C,NT}$  in Tab. V.3 and Tab. V.2, and see Fig. V.8.c). This observation is in good agreement with the simple scaling law  $f_C \sim d^{-1}$  introduced in Sec. II-2.2.c, whereas this simple relation is not verified for the freely suspended SWNTs studied in Sec. IV-1.

### V-3.2 Double-wall nanotube of type SC@M

After investigating absorption of two DWNTs composed exclusively of semiconducting tubes, we examine the absorption response of DCNT 3 identified as a SC@M double-wall carbon nanotube. Raman spectroscopy yields diameters 1.90 nm and 1.23 nm for the outer and inner walls, respectively. DCNT 3 is directly comparable to DCNT 1 in terms of size whereas the metallic nature of the outer wall is expected to impact differently on the optical properties of DCNT 3 [174, 176].

#### Absorption spectrum and structure identification

The spectrum of the absorption cross-section of DCNT 3 is plotted in Fig. V.4.c for polarization along the nanotube. The main absorption features, obtained from the fitting of the spectrum, are observed at 1.36 (R1), 1.46 (R2), 1.52 (R3),  $\sim 1.65$  (R4), 2.60 (R5), 2.77 (R6), and 2.88 (R7) eV with associated absorption cross-sections 0.63, 0.69, 0.22, 0.11, 0.21, 0.14, and 0.24 nm<sup>2</sup>/nm, respectively. A non-resonant absorption of 0.11 nm<sup>2</sup>/nm was included in the fitting process. It is important to notice that the optical absorption transitions associated with the metallic wall keep their excitonic nature as they best fit with Lorentzian profiles [95, 174] (the same results is obtained for M@SC double-wall carbon nanotubes as shown in the next section). Absorption and Raman scattering results are combined to tentatively identify the nanotubes composing DCNT 3. Positions of the absorption features and diameters are reported on the Kataura plot in Fig. V.4.e (horizontal red lines and vertical dashed lines, respectively). Rigid shift of the calculated optical transitions from ref. [44] (+0.34 and +0.43 eV for transitions with  $p < 4$  and  $p \geq 4$ , respectively) allows to match all the absorption features but R4 with exciton resonances from either a chiral semiconducting tube (inner tube with  $d_{in} = 1.23$  nm) or a chiral metallic nanotube (outer tube with  $d_{out} = 1.9$  nm). These results agree with the evolution of the tangential phonon modes profile between the four laser excitation energies (Fig. V.4.a and Sec. V-2.2).

R1 and R2 correspond to the metallic resonances  $M_{11(-)}^{out}$  and  $M_{11(+)}^{out}$  while R3 is identified as  $S_{33}^{in}$ . The three high-energy absorption features (R5, R6, R7) contain the energy transitions  $M_{22(-)}^{out}$ ,  $M_{22(+)}^{out}$ , and  $S_{44}^{in}$ . As they lie close from one another, it is difficult to provide a definitive assignment. Nevertheless, linewidths of R5 and R7 (192 and 292 meV, respectively), as well as their relative amplitudes with respect to  $M_{11(-)}^{out}$  and  $M_{11(+)}^{out}$ , suggest that these features correspond to  $M_{22(-)}^{out}$  and  $M_{22(+)}^{out}$ , following the observations of Doorn et al. [62]. Hence, R6 is probably the  $S_{44}$  resonance of the inner tube. Again,

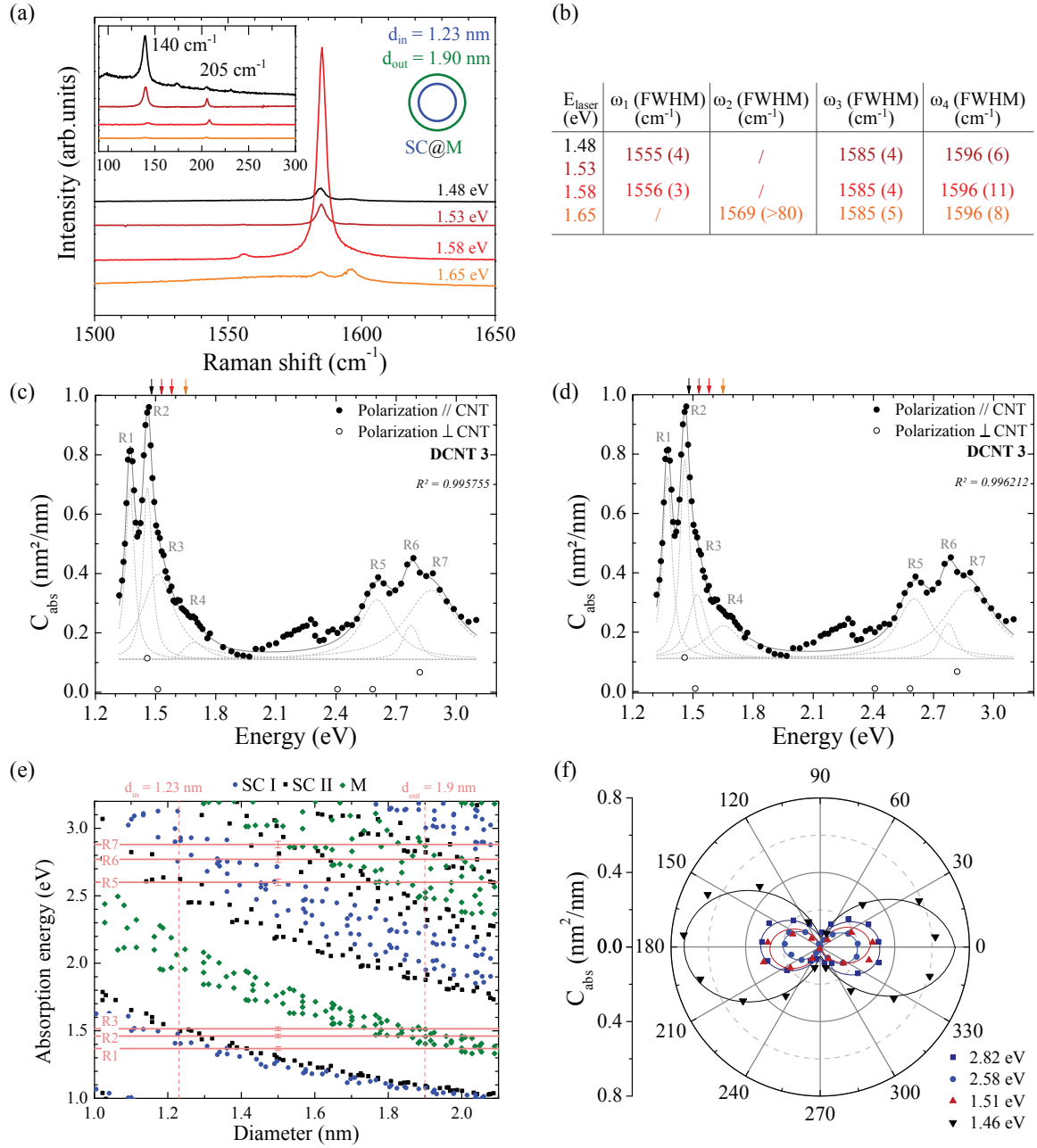


**Figure V.4:** Absorption and Raman spectroscopy of the individual free-standing double-wall nanotube DCNT 3 identified as SC@M. (a) Raman spectra showing the tangential phonon modes and BLM (inset graph) measured for different laser excitations. (b) Characteristics of the tangential modes. (c,d) Absolute absorption cross-section spectrum for incident light polarized along the nanotube. The dashed lines are the results of the fits detailed in the text. (continued on next page 135)

**Figure V.4:** (continuation) Absorption and Raman spectroscopy of the double-wall nanotube DCNT 3. (e) Structure assignment with the Kataura plot: comparison between measured absorption energies (horizontal red lines) and theoretical optical transition energies as a function of nanotube diameter. Left scale corresponds to the energy in the experimental absorption spectrum. Theoretical optical transitions are obtained by shifting the calculated data of ref. [44]: +0.32 and +0.43 eV for transitions with  $p < 4$  and  $p \geq 4$ , respectively. Vertical dashed lines show the diameters of the inner and outer walls. (f) Light-polarization-dependent absorption cross-section for different laser excitation energies. The experimental data (symbols) are fitted using  $C_{\text{abs}}^{\parallel} \cos^2 \theta_{\text{pol}} + C_{\text{abs}}^{\perp} \sin^2 \theta_{\text{pol}}$  functions (lines),  $\theta_{\text{pol}} = 0$  being the direction parallel to the nanotube.

all this analysis supposes that each exciton resonance can be associated exclusively with one of the two tubes composing the DWNT, i.e. it considers only interwall screening effects [174]. When excitonic transitions of inner and outer walls overlap, it is likely that quantum coupling and mixing of exciton states will modify the excitonic dispersion in DWNTs [166]. Further theoretical investigations addressing this point might explain the complex lineshapes of the absorption features.

### Characteristics of the excitonic energy transitions

The characteristics of the absorption features are recorded in Tab. V.4, where R4 was adjusted with either an asymmetric phonon-side band profile (Fig. V.4.c) or a Lorentzian-like function (Fig. V.4.d). The coefficient of determination ( $R^2$ ) yields 0.9958 in the former case and 0.9962 in the latter one. Data points in the range 2.1-2.3 eV were excluded from the fitting process as it is not totally clear yet if the jump of  $C_{\text{abs}}$  around 2.2-2.3 eV is due to absorption side features or/and possible instrumental artefact.<sup>h</sup> The choice of R4 profile impacts on the properties of resonances R1 to R3. Bigger (resp. smaller) values of oscillator strength  $f_{\text{C,NT}}$  were measured for R1 and R2 (resp. R3) when R4 was fitted with a Voigt profile (Fig. V.4.d) than in the situation where R4 was fitted with a phonon-assisted absorption profile Fig. V.4.c. In the former case,  $\gamma_{S_{33}^{\text{in}}}$  (104 meV) is compatible with the results obtained for SC@SC DWNTs, whereas in the latter case, we observe a broadening of  $S_{33}^{\text{in}}$  ( $\gamma_{S_{33}^{\text{in}}} = 191$  meV) that might be explained by stronger carrier screening due to the presence of the metallic outer wall. Furthermore, influence of the continuum of states associated with the metallic tube energy transitions, i.e. blue-shifted by few tens of meV with respect to the  $M_{ii}^{\text{out}}$  in SWNTs [95], is still unclear in DWNTs.

The bundle B2 (cf. Sec. IV-2) is composed of a semiconducting SWNT ( $d = 1.90$  nm) and two metallic SWNTs of diameters  $\sim 2.0 - 2.1$  nm. Then, the absorption properties of these M-SWNTs are directly comparable to those of the outer wall of DCNT 3.

<sup>h</sup>Mismatch of  $C_{\text{abs}}$  can sometimes occur at the extremities of the spectral regions accessible with different laser sources – the border between the OPO and BBO spectral ranges is precisely at about 2.35 eV. Further verification is required to address this point.

DCNT 3 SC@M	$E_{ii}$ (eV)	$C_{abs}^{exc}$ (nm <sup>2</sup> /nm)	$\gamma_{E_{ii}}$ (meV)	Area ( $\times 10^{-2}$ nm.eV)	$C_{abs}$ ( $\times 10^{-17}$ cm <sup>2</sup> /C-atom)			Oscillator strength ( $\times 10^{-2}$ per C-atom)	
					$C_{abs,SW}^{exc}$	$C_{abs,NT}^{exc}$	$C_{abs,NT}^{peak}$	$f_{C,SW}$	$f_{C,NT}$
R4 peak fitted with Voigt profile									
R1 ( $M_{11(-)}^{out}$ )	1.37	0.63	55	5.4	2.77	1.7	2.0	2.2	1.3
R2 ( $M_{11(+)}^{out}$ )	1.46	0.69	56	6.1	3.04	1.8	2.1	2.4	1.5
R3 ( $S_{33}^{in}$ )	1.52	0.22	104	3.6	1.5	0.6	0.9	2.2	0.9
R4	1.65	0.11	211	3.6	/	0.3	0.6	/	0.9
R4 peak fitted with phonon side band profile									
R1 ( $M_{11(-)}^{out}$ )	1.37	0.59	47	4.4	2.6	1.6	1.9	1.7	1.1
R2 ( $M_{11(+)}^{out}$ )	1.46	0.60	48	4.5	2.65	1.6	1.9	1.8	1.1
R3 ( $S_{33}^{in}$ )	1.51	0.29	191	8.7	2.0	0.8	1.05	5.3	2.1
R4	PSB @1.69	0.06	/	/	/	0.16	0.45	/	/
R5	2.60	0.21	192	6.3	0.9	0.56	0.85	2.5	1.5
R6	2.77	0.14	68	1.5	0.95	0.4	0.7	0.6	0.4
R7	2.88	0.24	292	11	1.05	0.64	0.93	4.4	2.7

**Table V.4:** Absorption characteristics of DCNT 3 (DWNT of type SC@M).

Although similar linewidths are observed in both samples, the absorption cross-sections of the exciton resonances, and to greater extent their oscillator strengths, are enhanced in the metallic nanotube included in the DWNT (a factor of about six is observed for  $M_{11}$ ). Both samples experience the presence of a semiconducting nanotube but our results prove that interwall coupling is of different nature in DWNTs.

The absorption cross-section, linewidth, and oscillator strength of  $S_{33}^{in}$ , for the two fitting hypotheses, are comparable to those observed for the semiconductor inner tube in DCNT 1 (Fig. V.8). Interestingly,  $C_{abs,NT}^{exc}$  and the FWHM of the resonances  $M_{11}^{out}$  are comparable to those of external semiconducting walls. Conversely,  $f_{C,NT}$  of the excitonic transitions of the outer metallic nanotube are almost two times larger than in the outer walls of the other DWNTs. To summarize, in DCNT 3 (SC@M), the oscillator strengths per C-atom of the excitonic transitions of both inner and outer walls yield values in the range  $\sim 1 - 2$  somehow closer to the results obtained for isolated SWNTs and generally larger than in the other DWNTs (Fig. V.8.c).

### Polarization-dependent absorption

Finally, Fig. V.4.f shows the polarization-dependent absorption cross-section signal for few laser excitation energies. As for DCNT 1, strong depolarization effects are observed in DCNT 3. For incident light polarized perpendicular to the nanotube, noticeable absorption is observed only for excitation energies 1.46 eV and 2.82 eV (see open symbols in Fig. V.4.c).

## V-3.3 Double-wall nanotube of type M@SC

After presenting the properties of SC@SC and SC@M double-wall nanotube, it is logical to investigate the absorption characteristics of M@SC nanotubes. These results are presented and discussed in the next section.

## V-4 Environment effects on double-wall nanotubes absorption properties

In the last section, we discussed the absorption properties of individual freely suspended DWNTs. As shown for SWNTs (Chap. IV), the environment of the nanotubes has impacts on their optical response (absorption and Raman scattering in this work). Therefore, in this section, we study the environment dependence of the absorption characteristics of two individual double-wall carbon nanotubes (DCNT 4 and DCNT 5). At first, their structures and absorption properties are investigated while they are isolated and freely suspended. Then, their absorption responses are examined either at their extremities which are substrate-supported (Si/SiO<sub>2</sub> substrate FS-1) or in the presence of a metallic SWNT.

### V-4.1 Substrate effects on the absorption response of a DWNT

Fig. V.5.b shows SMS and RSMS images of the freely suspended (FS-DCNT 4) and substrate-supported segments (SI-DCNT 4) of the double-wall carbon nanotube DCNT 4 (sample FS-1).

#### V-4.1.a Freely suspended

Fig. V.5.c presents the spectrum of the absorption cross-section of the freely suspended segment of DCNT 4, for incident light polarized along the nanotube. Seven absorption peaks are observed at positions 1.44 (R2), 1.51 (R3), 1.77 (R5), 2.27 (R6), 2.42 (R7), 2.74 (R8), and 2.99 (R9), associated with absorption cross-section 0.64, 0.52, 0.48, 0.25, 0.34, 0.15, and 0.18 nm<sup>2</sup>/nm, on top of a constant non-resonant absorption background (0.3 nm<sup>2</sup>/nm). In Sec. V-2.2 (paragraph DCNT 4), the inner (resp. outer) wall has been identified as a chiral metallic (resp. semiconducting of family type I) nanotube with diameter 2.60 nm (resp. 1.89(2) nm). The positions of the absorption peak were reported on the Kataura plot (Fig. V.5.d), where a rigid shift was applied to the calculated optical transitions to best match the data (+0.26 eV and +0.35 eV for transitions with  $p < 4$  and  $p \geq 4$ , respectively). According to the diameters and the absorption peaks energies, the features R2, R3, R5, R6, and R7 can be assigned to the resonances  $S_{33}^{\text{out}}$ ,  $M_{11(+)}^{\text{in}}$ ,  $S_{44}^{\text{out}}$ ,  $S_{55}^{\text{out}}$ , and  $M_{22(-)}^{\text{in}}$ , respectively. The absorption features R8 and R9 are difficult to associate with one or the other wall but are presumably composed of resonances  $S_{66}^{\text{out}}$ ,  $M_{22(+)}^{\text{in}}$  and  $S_{77}^{\text{out}}$ .

The measured spectrum was fitted using the same procedure as described for the other DWNTs (the result is plotted in Fig. V.5.c). In contrast to previous samples (SC@SC and SC@M), only a few absorption side-features are observed apart from the main peaks. Differences between the data and the fitting results are possibly explained by phonon-assisted absorption and/or excited-exciton states, e. g. absorption of the continuum of states associated with  $M_{11(+)}^{\text{in}}$  (R3) around 1.6 eV.



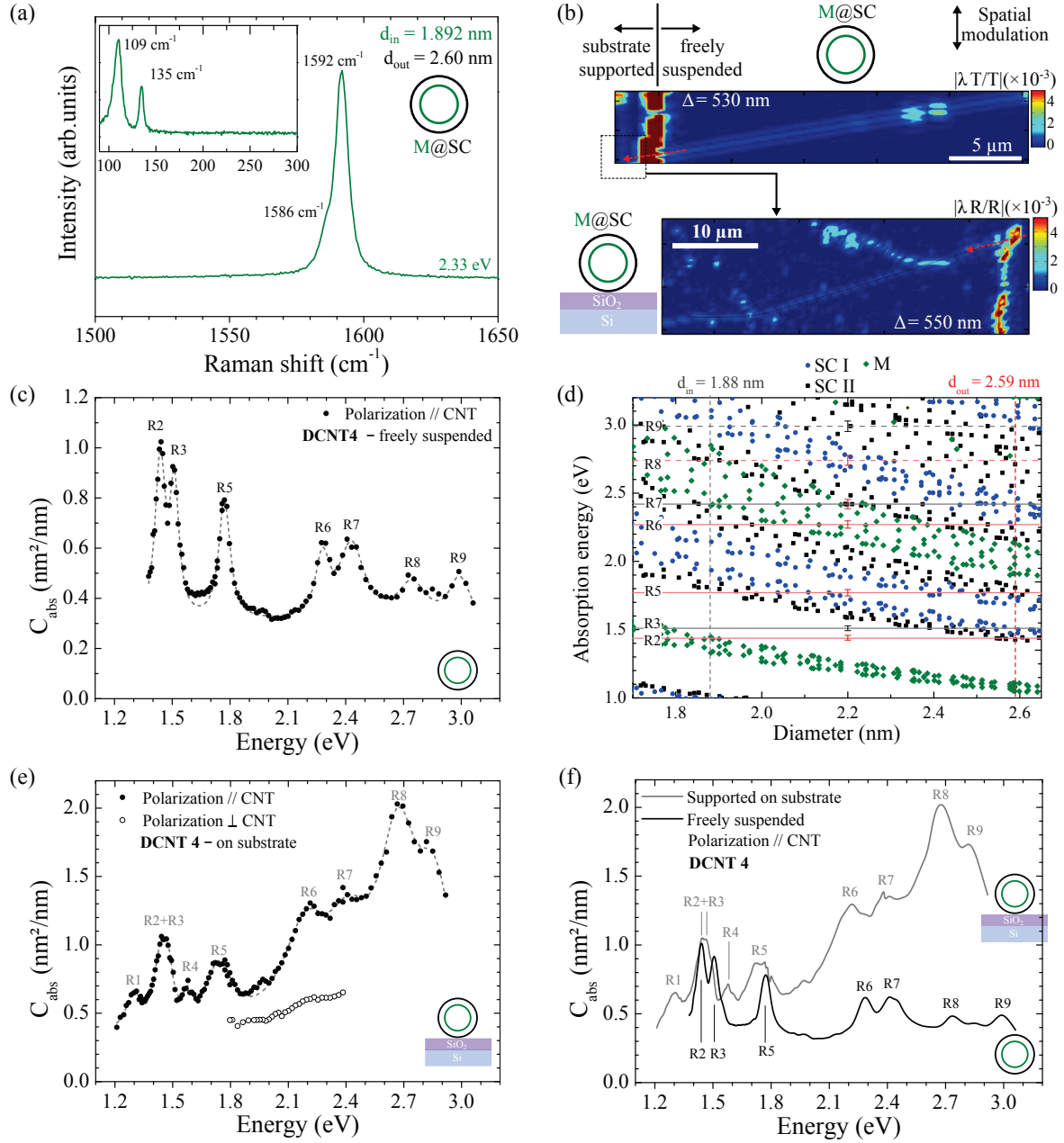


**Figure V.5:** Environment dependent absorption of the individual double-wall nanotube DCNT 4 identified as M@SC. (a) Raman spectra showing the tangential phonon modes and BLM (inset graph). (b) SMS and RSMS imaging of freely suspended and substrate-supported segments, respectively. Spatial modulation direction is vertical, and incident light is polarized along the nanotube. (c) Absolute absorption cross-section spectrum of the freely suspended segment for incident light polarization along the nanotube. The dashed line is the result of the fit detailed in the text. (continued on next page 139)



**Figure V.5:** (continuation) Environment dependent absorption of the double-wall nanotube DCNT 4. (d) Structure assignment with the Kataura plot: comparison between measured absorption energies (horizontal red and gray lines) and theoretical optical transition energies as a function of nanotube diameter. Left scale corresponds to the energy in the experimental absorption spectrum. Theoretical optical transitions are obtained by shifting the calculated data of ref. [44]: +0.26 and +0.35 eV for transitions with  $p < 4$  and  $p \geq 4$ , respectively. Vertical dashed lines show the diameters of the inner (grey) and outer (red) walls. (e) Absorption cross-section spectrum of the substrate-supported segment for incident light parallel (black dots) and perpendicular (open symbols) to the nanotube. (f) Comparison of the absorption spectra presented in (c) and (e).

Characteristics of the excitonic transitions (Tab. V.5) are comparable to our previous observations (see Fig. V.8 for comparison with SC@SC and SC@M nanotubes). The inner metallic tube, which is similar to the metallic outer wall of DCNT 3, shows analogous linewidths increase between  $M_{11}^{\text{in}}$  and  $M_{22}^{\text{in}}$ , as well as comparable values  $f_{\text{C,SW}}$ . However, from the point of view of the DWNT, the excitons of its inner metallic tube carries less of the overall oscillator strength ( $f_{\text{C,NT}} = 0.7 \& 1.35$ ) as compared to the metallic outer nanotube of DCNT 3 ( $f_{\text{C,NT}} \sim 1.3 \& 1.5$ ).

DCNT 4 M@SC	$E_{ii}$ (eV)	$C_{abs}^{\text{exc}}$ (nm <sup>2</sup> /nm)	$\gamma_{E_{ii}}$ (meV)	Area ( $\times 10^{-2}$ nm.eV)	$C_{abs}$ ( $\times 10^{-17}$ cm <sup>2</sup> /C-atom)			Oscillator strength ( $\times 10^{-2}$ per C-atom)	
					$C_{abs,SW}^{\text{exc}}$	$C_{abs,NT}^{\text{exc}}$	$C_{abs,NT}^{\text{peak}}$	$f_{\text{C,SW}}$	$f_{\text{C,NT}}$
<b>R2</b> ( $S_{33}^{\text{out}}$ )	1.44	0.64	59	5.9	2.06	1.2	1.75	1.7	1.0
<b>R3</b> ( $M_{11}^{\text{in}}$ )	1.51	0.52	50	4.1	2.3	1.0	1.55	1.6	0.7
<b>R5</b> ( $S_{44}^{\text{out}}$ )	1.77	0.48	65	4.9	1.55	0.9	1.45	1.4	0.8
<b>R6</b> ( $S_{55}^{\text{out}}$ )	2.27	0.25	69	2.7	0.8	0.5	1.05	0.8	0.45
<b>R7</b> ( $M_{22}^{\text{in}}$ )	2.42	0.34	149	8.0	1.5	0.6	1.15	3.2	1.35
<b>R8</b>	2.74	0.15	163	3.8	/	0.28	0.80	/	0.65
<b>R9</b>	2.99	0.18	105	3.0	/	0.35	0.95	/	0.5

**Table V.5:** Absorption characteristics of the freely suspended part of DCNT 4 (DWNT of type M@SC).

The linewidths of the energy transitions  $S_{33}$  and  $S_{44}$  of the semiconducting (of family type I) outer wall are larger than those observed for the semiconducting (of type II) outer tube of DCNT 2, but similar to isolated SWNTs (Fig. V.8.b). Likewise, comparing the semiconducting outer nanotube in DCNT 4 and DCNT 2, larger oscillator strengths  $f_{\text{C,NT}}$  are observed in the former.  $f_{\text{C,NT}}(S_{33})$  and  $f_{\text{C,NT}}(S_{44})$  yield 1.0 and 0.8 in DCNT 4 but they drop to 0.54 and 0.55 in DCNT 2. These results reveal the impact of the nature of the inner tube on the absorption properties of the outer one.

#### V-4.1.b Substrate supported

##### Results

Fig. V.5.e presents the optical absorption spectra of the supported segment of DCNT

4, for incident light polarized parallel (black dots) and perpendicular (open symbols) to the nanotube. The spectrum for parallel polarization is compared to the absorption response of the free-standing segment (Fig. V.5.f). We observe similar absorption features in the two but with significant modifications of the peaks energy positions, linewidths, and amplitudes. Overall, the absorption cross-section is enhanced in the supported segment.<sup>i</sup> To quantify these changes, the measured absorption spectrum of SI-DCNT 4 was fitted using the procedure described before (grey dashed curve in Fig. V.5.e). The main difficulty consisted in choosing the appropriate non-resonant absorption background, on top of which we can accurately reproduce the shapes of the main features with Voigt profiles. According to our results for SWNTs (Sec. IV–3), we set the constant non-resonant absorption to the same value as the one measured for FS-DCNT 4, i. e.  $C_{\text{abs}}^{\text{nr}} = 0.3 \text{ nm}^2/\text{nm}$ . Furthermore, identification of the absorption peaks in the IR region is troublesome as both R1 and R4, also yielding the two BLM of DCNT 4 under resonant Raman excitation, are not observed in FS-DCNT 4. Likewise, the profile of the resonance around 1.45-1.5 eV was assumed to be composed of two Voigt functions as it gives a better results than a single Voigt profile.

Fig. V.5.f and Tab. V.6 present the identifications of the energy transitions, as well as their positions and their peak absorption cross-section, for both the FS-DCNT 4 and the SI-DCNT 4. Energy transitions are more or less red-shifted in the supported segment as compared to FS-DCNT 4. In fact,  $\Delta E_{ii}$  ranges from almost no shift for the lower-order resonances to about  $-100 \text{ meV}$  for higher-order transitions. Interestingly, the redshift amplitude and the oscillator strength per C-atom in FS-DCNT 4 ( $f_{\text{C,NT}}$  in Tab. V.5) observe opposite evolution with respect to resonance order, i. e. small redshifts take place for the energy transitions with large  $f_{\text{C,NT}}$  and vice versa.

DCNT 4 M@SC	FS-DCNT 4 freely suspended		SI-DCNT 4 substrate-supported		
	$E_{ii}$ (eV)	$C_{\text{abs,NT}}^{\text{peak}}$ ( $\times 10^{-17} \text{ cm}^2/\text{C-atom}$ )	$E_{ii}$ (eV)	$C_{\text{abs,NT}}^{\text{peak}}$ ( $\times 10^{-17} \text{ cm}^2/\text{C-atom}$ )	$\Delta E_{ii}$ (meV)
<b>R1</b>	/	/	1.30	1.2	/
<b>R2</b> ( $S_{33}^{\text{out}}$ )	1.44	1.75	1.44	1.6	0
<b>R3</b> ( $M_{11}^{\text{in}}$ )	1.51	1.55	1.48	1.0	-30
<b>R4</b>	/	/	1.58	0.9	/
<b>R5</b> ( $S_{44}^{\text{out}}$ )	1.77	1.45	1.74	1.4	-30
<b>R6</b> ( $S_{55}^{\text{out}}$ )	2.27	1.05	2.19	1.8	-80
<b>R7</b> ( $M_{22}^{\text{in}}$ )	2.42	1.15	2.41	1.6	-10
<b>R8</b>	2.74	0.80	2.67	3.0	-70
<b>R9</b>	2.99	0.95	2.86	2.2	-140

**Table V.6:** Comparison of the absorption characteristics of freely-suspended and substrate-supported segments of DCNT 4.

In SI-DCNT 4, higher-energy transitions ( $E > 2 \text{ eV}$ ) present linewidths larger than  $200 \text{ meV}$ , i. e. they are about two times broader than in the FS-DCNT 4. Likewise, R5 is almost three times broader in SI-DCNT 4 ( $\gamma_{R5} = 167 \text{ meV}$ ) than in FS-DCNT 4

<sup>i</sup>As shown in Sec. III–2.2 the interval of confidence for  $C_{\text{abs}}$  is 1.8-2.2 eV for silicon substrate coated with a 100 nm  $\text{SiO}_2$  layer.

( $\gamma_{R5} = 65$  meV) On the other hand, R2 and R3 linewidths yield comparable values in the supported ( $\gamma_{R2} = 45$  meV and  $\gamma_{R3} = 84$  meV) and freely suspended ( $\gamma_{R2} = 59$  meV and  $\gamma_{R3} = 50$  meV) segments.

### Discussion

To summarize, the optical absorption properties of excitonic transitions of DCNT 4 undergo significant modifications when the ‘environment free’ nanotube (freely suspended segment) is deposited on the silicon substrate. As discussed for a SWNT (Sec. IV-3.2), they are affected by several environment-induced effects: charge-carrier dielectric screening, stress-induced strain, chemical doping, and their direct consequences that are exciton localization and activation of new energy transitions. Assuming a realistic chemical doping, it is not expected to influence metallic and high-order semiconducting resonances [153,175]. Due to the interwall interactions (of van-der-Waals type) in DWNTs, effects of radial deformation induced by tube-substrate Van-der-Waals forces are relatively attenuated compared to SWNTs [30,177]. Therefore, it is likely that dielectric screening could play an important role in the substrate-induced modifications of the DWNT optical properties.

## V-4.2 Bundling effects on the absorption response of a DWNT

In this part, DCNT 5, a DWNT with inner metallic wall ( $d_{in} = 1.71$  nm) and outer semiconducting wall ( $d_{out} = 2.38$  nm), is studied by means of absorption spectroscopy at three different positions along the tube: FD, FB, and SS. From combined examination of optical spectra (Raman Fig. V.6.a and absorption (Fig. V.6.c spectra) and (R)SMS imaging (Fig. V.6.b), we established that FD, FB, and SS correspond to DCNT 5 freely-suspended, DCNT 5 interacting with a metallic SWNT (still freely suspended), and DCNT 5 supported on the substrate FS-1, respectively.

### V-4.2.a Results

#### FD-DCNT 5

FD-DCNT 5 absorption spectrum, measured for incident light polarized along the nanotube, shows main absorption features at 1.53 (R1), 1.91 (R2), 2.38 (R3), 2.64 (R4), and 2.93 (R5) eV with absorption cross-sections 1.2, 0.26, 0.20, 0.16, and 0.33 nm<sup>2</sup>/nm, on top of a constant non-resonant background  $C_{abs}^{nr} = 0.14$  nm<sup>2</sup>/nm (Fig. V.6.c, red triangles). After reporting these results on the Kataura plot (Fig. V.6.f), and applying a rigid shift to the calculated optical transitions, we matched the transitions labeled R1 to R5 with resonances of the inner and outer walls. R2 and R3 are associated with  $S_{44}^{out}$  and  $S_{55}^{out}$ , respectively. R4 corresponds probably to  $M_{22(-)}^{in}$ , while R5 is composed of  $M_{22(+)}^{in}$  or/and  $S_{66}^{out}$  resonances. These absorption features were fitted with Voigt functions on top of the constant non-resonant background, and including Lorentzian-type side peaks at 1.85 and 2.01 eV (the characteristics of the energy transitions are listed in Tab. V.7, DWNT rows). Besides, the profile of R1 is composed of two Voigt functions (L1 and L2)

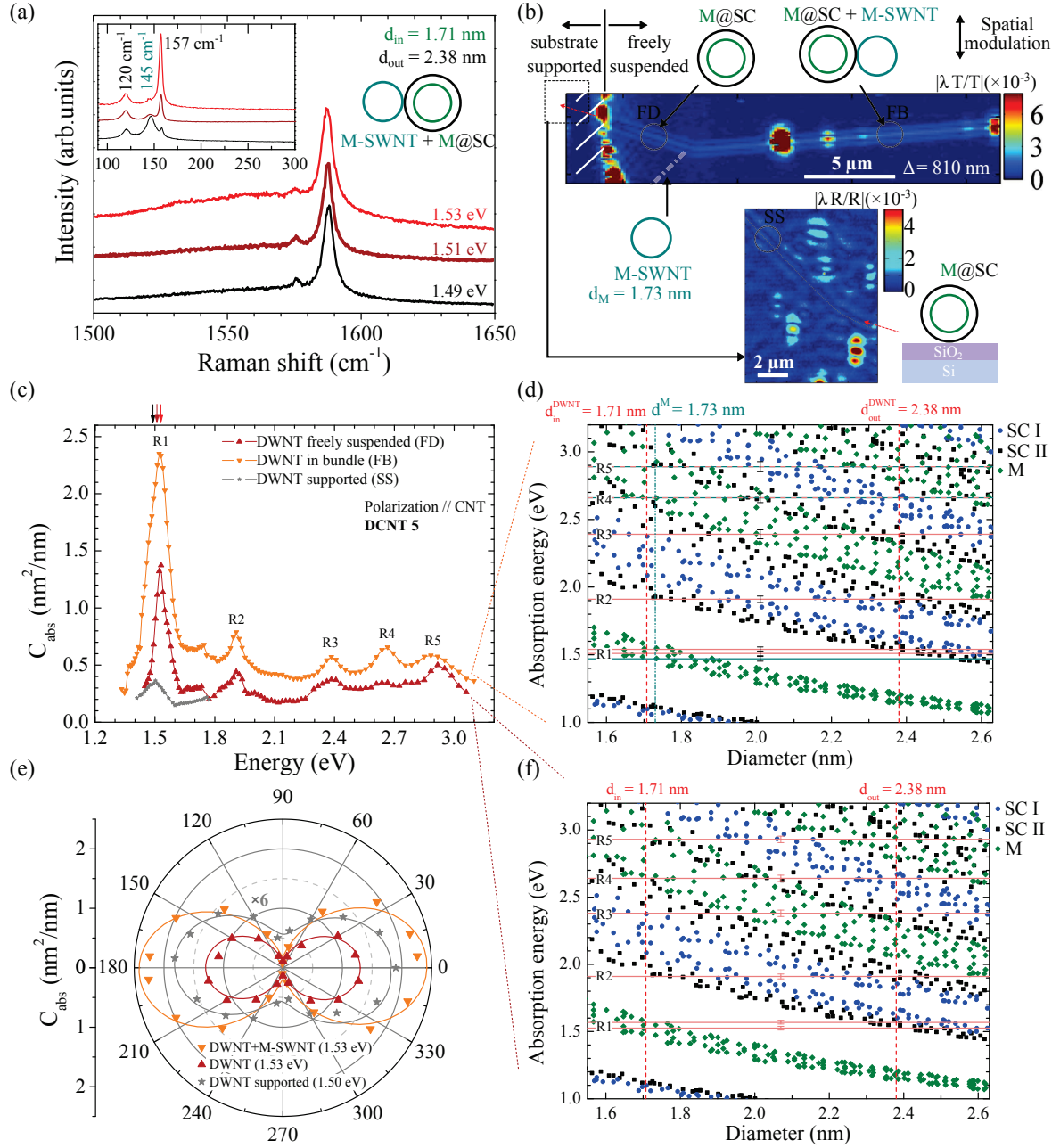


**Figure V.6:** Environment dependent absorption of the double-wall nanotube DCNT 5 identified as M@SC. (a) Raman spectra showing the tangential phonon modes and breathing modes (inset graph) of the segment DWNT+M-SWNT (measured at position FB). (b) SMS and RSMS imaging of freely suspended and substrate-supported segments, respectively. Spatial modulation direction is vertical, and incident light is polarized along the nanotube sample. (c) Absorption cross-section spectra of different segments of the same DWNT: the freely suspended DWNT (red triangles), the free-standing bundle DWNT+M-SWNT (orange upside-down triangles), the substrate-supported DWNT (grey stars). (continued on next page 143)

**Figure V.6:** (continuation) Environment dependent absorption of the double-wall nanotube DCNT 5. (d,f) Structure assignment with the Kataura plot: comparison between measured absorption energies (horizontal lines) and theoretical optical transition energies as a function of nanotube diameter. Left scale corresponds to the energy in the experimental absorption spectrum. Theoretical optical transitions are obtained by shifting the calculated data of ref. [44]: +0.29 and +0.38 eV for transitions with  $p < 4$  and  $p \geq 4$ , respectively. Vertical dashed lines show the diameters of the inner (grey) and outer (red) walls of the DWNT. The cyan lines are correspond to the features of the metallic SWNT. (e) Light-polarization-dependent absorption cross-section at the energy transition R1 for three environment. The experimental data (symbols) are fitted using  $C_{\text{abs}}^{\parallel} \cos^2 \theta_{\text{pol}} + C_{\text{abs}}^{\perp} \sin^2 \theta_{\text{pol}}$  functions (lines),  $\theta_{\text{pol}} = 0$  being the direction parallel to the nanotube.

corresponding to  $M_{11(-)}^{\text{in}}$  and  $S_{33}^{\text{out}}$  (Fig. V.7.c). Based on the examination of the optical transitions of the metallic tubes close to  $d_{\text{in}}$  in the Kataura plot, the energy position of  $M_{11(+)}^{\text{in}}$  can be estimated in between 30 and 100 meV above  $M_{11(-)}^{\text{in}}$ . Thus, either  $M_{11(+)}^{\text{in}}$  is included in R1 and its contribution is very weak, or it is on the right-hand side of R1 ( $\sim 1.65$  eV) mixed with some other side features (either excited exciton states or the continuum of  $M_{11}^{\text{in}}$ ). In all cases, taking into account  $M_{11(+)}^{\text{in}}$  in order to reproduce the peak R1 did not improve significantly the quality of the fit.

DCNT 5 M@SC		$E_{ii}$ (eV)	$C_{\text{abs}}^{\text{exc}}$ (nm <sup>2</sup> /nm)	$\gamma_{E_{ii}}$ (meV)	Area ( $\times 10^{-2}$ nm.eV)	$C_{\text{abs}}$ ( $\times 10^{-17}$ cm <sup>2</sup> /C-atom)			Oscillator strength ( $\times 10^{-2}$ per C-atom)	
						$C_{\text{abs},\text{SW}}^{\text{exc}}$	$C_{\text{abs},\text{NT}}^{\text{exc}}$	$C_{\text{abs},\text{NT}}^{\text{peak}}$	$f_{\text{C,SW}}$	$f_{\text{C,NT}}$
DWNT	R1	1.525	1.12	53	9.3	/	2.3	2.6	/	1.7
	L1+L2	1.57	0.32	54	2.7	/	0.65	1.04	/	0.5
	R2	1.91	0.26	63	2.6	/	0.53	0.82	/	0.5
	R3	2.38	0.20	152 ?	4.8 ?	/	0.41	0.70	/	0.9 ?
	R4	2.64	0.16	274 ?	6.9 ?	/	0.33	0.62	/	1.3 ?
	R5	2.93	0.33	186 ?	9.6 ?	/	0.67	1.06	/	1.8 ?
R1 profile fitted with three Voigt functions										
DWNT + M-SWNT	(L3)	1.47	0.59	52	4.8	2.85	0.84	1.2	2.1	0.63
	(L4)	1.51	0.67	68	7.2	/	0.96	1.3	/	0.94
	(L5)	1.54	1.48	96	22.3	/	2.13	2.5	/	2.92
	R1 profile fitted with four Voigt functions									
	(L6)	1.47	0.61	54	5.2	2.95	0.88	1.25	2.3	0.68
	(L7)	1.53	0.29	54	2.5	1.40	0.42	0.79	1.1	0.32
	(L7)	1.51	0.54	63	5.3	/	0.78	1.15	/	0.70
	(L8)	1.54	1.38	97	2.1	/	1.98	2.35	/	2.75
	R2	1.91	0.33	76	3.9	/	0.47	0.95	/	0.52
	R3	2.39	0.19	77	2.3	/	0.27	0.74	/	0.30
	R4	2.66	0.27	122	5.2	/	0.39	0.86	/	0.68
	R5	2.89	0.23	175	6.3	/	0.33	0.80	/	0.83

**Table V.7:** Absorption characteristics of DCNT 5 (M@SC).

Although energy transitions R1 and R2 present characteristics comparable to our previous results, higher-energy absorption features (R3, R4, and R5) exhibit very broad

peaks that we normally observe only for substrate-supported tubes (these values can be compared with those obtained for DCNT 4 which is also a M@SC double-wall nanotube).

### FB-DCNT 5

We proceed to the same type of analysis of the absorption spectrum of FB-DCNT 5

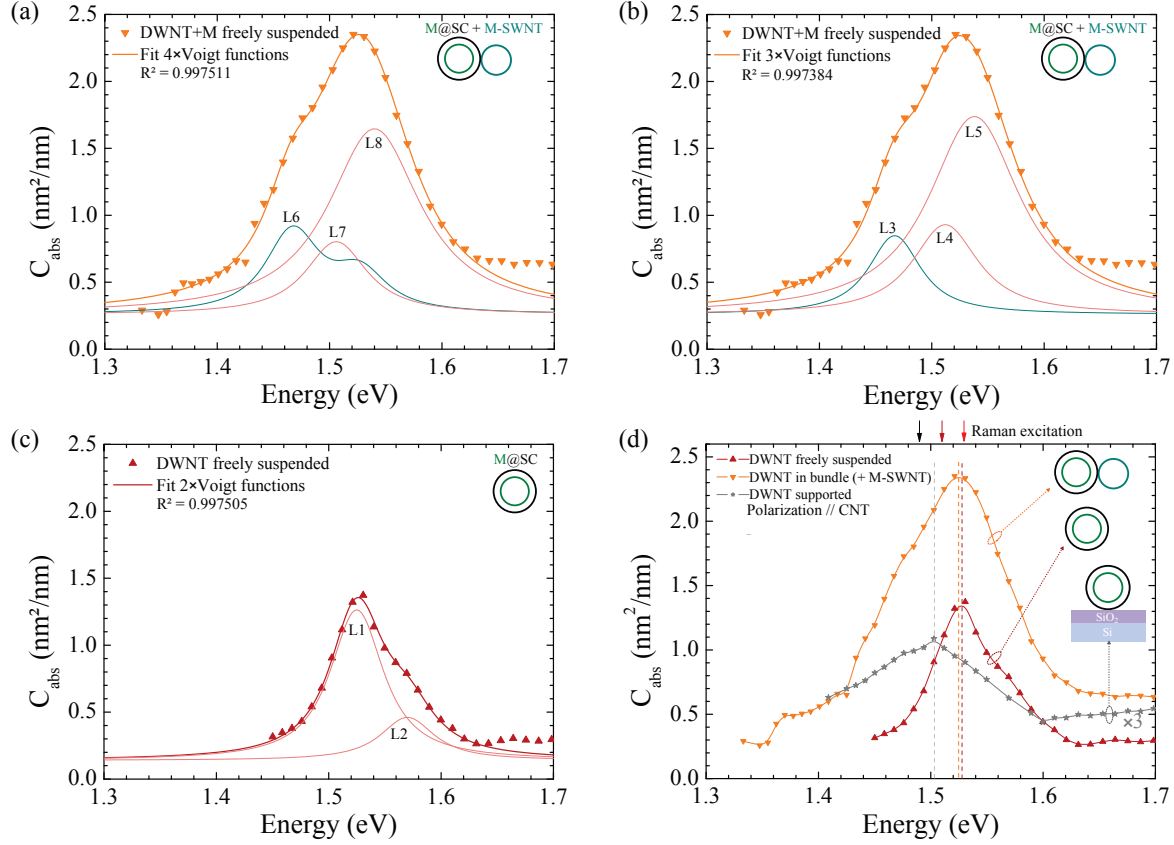


**Figure V.7:** Absorption fitting of overlapping excitonic transition in different environments. Comparison of the outcomes of the fitting procedure for the absorption peak R1 in FS-DCNT 5 (c) and FB-DCNT 5 (a,b). (d) Absorption cross-section spectra of different segments of DCNT 5 close to the absorption feature R1.

(Fig. V.6.c, orange upside-down triangles). The absorption response shows features similar to FD-DCNT 5 but an enhanced absorption cross-section by a factor of at least 1.5. The energy positions of the main absorption features and their characteristics are listed in Tab. V.7 (rows DWNT+M-SWNT) where we included a non-resonant absorption  $C_{\text{abs}}^{\text{nr}} = 0.25 \text{ nm}^2/\text{nm}$ . To account for the  $M_{11}$  resonance of the M-SWNT and reproduce the new shape of R1, at least one additional Voigt function had to be included in the fit of R1. From Raman excitation profiles (not shown) and the Kataura plot in Fig. V.6.d, we infer the M-SWNT resonances ( $M_{11(-)}$  and  $M_{11(+)}$ ) observe an energy splitting of 60 meV, have an amplitude ratio  $\sim 0.5$ , and both exhibit a linewidth of about 55 meV.<sup>j</sup>

<sup>j</sup>This is in good agreement with the extended work on metallic SWNTs reported in ref. [62].



Fig. V.7.a presents the result of the fit of R1 including these hypotheses. Hence, R1 is composed of the double-peak function L6 (two Voigt functions) reproducing  $M_{11(-)}$  and  $M_{11(+)}$  from the M-SWNT, and the DWNT energy transitions (based on Raman excitation profiles,  $S_{33}^{\text{out}}$  and  $M_{11(-)}^{\text{in}}$  are correspond to L7 and L8, respectively). When R1 was fitted with only three Voigt functions, i.e. neglecting  $M_{11(+)}$ , the characteristics of the excitons were slightly modified but the quality of the fit was rather identical (Fig. V.7.b and Tab. V.7).

### Polarization-dependent absorption

Fig. V.6.e compares the polarization-dependent absorption at the maximum of the energy transition R1 between FD-DCNT 5, FB-DCNT 5, and SS-DCNT 5.  $C_{\text{abs}}^{\parallel}/C_{\text{abs}}^{\perp}$  is unchanged between FD-DCNT 5 ( $\sim 12$ ) and FB-DCNT 5 ( $\sim 10$ ), whereas it decreases to  $\sim 3$  for the substrate-supported segment of the DWNT. This observation confirms the results obtained for SWNTs: the presence of a metallic SWNT close to an isolated DWNT or SWNT does not alter significantly its polarization-dependent antenna effects. Only substrates can significantly attenuate the strength of the depolarization field of isolated nanotubes and thus modify their polarization response [12, 55, 56] (see also discussion in Sec. IV-3).

### V-4.2.b Discussion

Absorption spectra of FD-DCNT 5, FB-DCNT 5, and SS-DCNT 5 show significant environment-induced modifications of their energy transitions (Figs. V.6.c and V.7.d). In particular, we observe energy shifts and absorption renormalization of the excitonic transitions (Tab. V.8). However, the measured changes of the DWNT absorption properties, due to interactions with either the M-SWNT or the silicon substrate, do not present systematic patterns.

DCNT 5 M@SC	FD-DCNT 5 free-standing DWNT		DWNT+M-SWNT FB-DCNT 5 freely suspended			SS-DCNT 5 DWNT substrate-supported		
	$E_{ii}$ (eV)	$C_{\text{abs},NT}^{\text{peak}}$ ( $\times 10^{-17}$ cm <sup>2</sup> / C-atom)	$E_{ii}$ (eV)	$C_{\text{abs},NT}^{\text{peak}}$ ( $\times 10^{-17}$ cm <sup>2</sup> / C-atom)	$\Delta E_{ii}$ (meV)	$E_{ii}$ (eV)	$C_{\text{abs},NT}^{\text{peak}}$ ( $\times 10^{-17}$ cm <sup>2</sup> / C-atom)	$\Delta E_{ii}$ (meV)
<b>R1</b>	1.53	2.74	1.525	3.36	-5	1.50	0.74	-30
<b>R2</b>	1.91	1.04	1.91	0.33	0	/	/	/
<b>R3</b>	2.38	0.82	2.39	0.19	+10	/	/	/
<b>R4</b>	2.64	0.70	2.66	0.27	+20	/	/	/
<b>R5</b>	2.93	0.62	2.89	0.23	-40	/	/	/

**Table V.8:** Comparison of the absorption characteristics of DCNT 5 (M@SC) in different environments.

Our attempts to fit the absorption main feature R1 were based on the assumption that overlapping energy transitions both are independent and keep their excitonic nature. As mentioned previously, more advanced theory should directly consider mixed excitonic states in DWNTs as it has been already proposed for bundled SWNTs [166]. This model would help to gain insights in interwall interactions in DWNTs and understand the differences with systems of interacting SWNTs.



## V–5 Discussion on the absorption of DWNTs

### V–5.1 Excitonic energy transitions

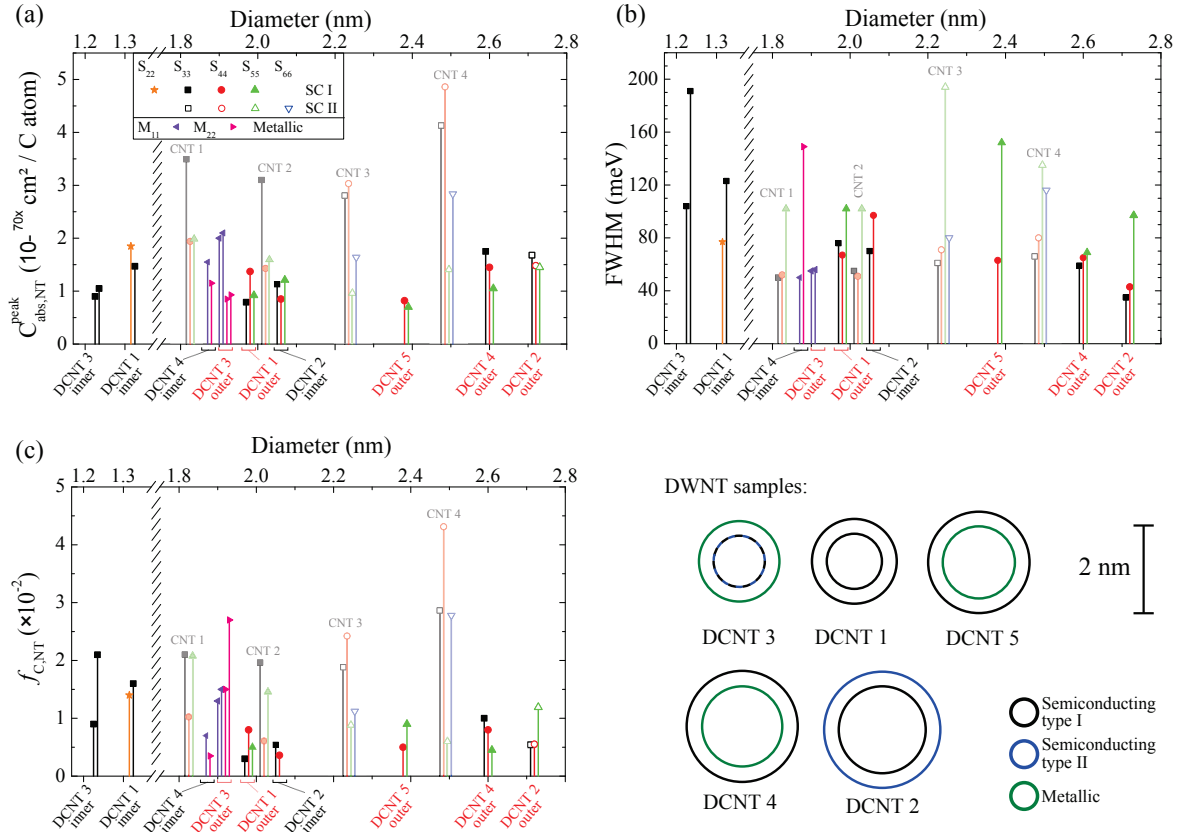


**Figure V.8:** Absorption properties of individual free-standing double-wall carbon nanotubes. The characteristics of the excitonic energy transitions in the studied DWNTs (DCNT 1 to DCNT 5) are plotted versus inner and outer nanotubes diameters: (a) peak absorption cross-section, (b) linewidth, and (c) oscillator strength. Energy transitions associated with either the inner or outer wall of each sample are labeled under the graphs – black and red labels stand for inner and outer walls, respectively. Dim symbols and lines recall the absorption characteristics of individual free-standing DWNTs.

Absorption spectra of individual free-standing double-wall carbon nanotubes are composed of excitonic energy transitions on top of a constant non-resonant absorption background. Their optical absorption properties resemble those of SWNTs expect for newly arising absorption side-features that need to be further examined in future works. Fig. V.8 summarize the exciton characteristics in DWNTs and provide a comparison with those of semiconducting SWNTs (dim symbols and lines). Overall, their peak absorption cross-sections are of the same magnitude or slightly smaller than values measured in SWNTs (Fig. V.8.a), precisely  $C_{\text{abs,NT}}^{\text{peak}} \lesssim 2 \times 10^{-17} \text{ cm}^2 / \text{C atom}$  in DWNTs.

Both classes of nanotubes present comparable exciton broadening (Fig. V.8.b), yet some modulations occur in DWNTs depending on the diameter, nature, and position (inner or outer wall) of the nanotubes. The oscillator strength per C-atom of excitons in DWNTs,  $f_{C,NT}$ , are generally smaller than in isolated SWNTs (Fig. V.8.c). This is partly explained by the larger number of carbon atoms par unit length in DWNTs. Expressing the oscillator strength per C-atom with respect to each wall,  $f_{C,SW}$ , might offer a more rigorous way to compare resonances in DWNTs and SWNTs (for individual SWNTs  $f_{C,NT} = f_{C,SW}$ ) but the issue of interwall mixed excitonic states in DWNTs needs to be addressed beforehand.

## V-5.2 Non-resonant absorption

The optical sheet conductivity  $\sigma_S(\omega)$  of DWNTs can be derived from  $C_{abs}$  based on the same models as proposed for SWNTs (Sec. IV-1.5 and Appx. B). In particular, the non-resonant absorption yields values of sheet conductivity  $\sigma_S^{nr}$  in the range  $\sim 3-6 \times 10^{-5} \Omega^{-1}$  (Fig. V.9), i.e. comparable to the results obtained for SWNTs. Unlike in SWNTs,  $\sigma_S^{nr}$  fluctuates from one DWNT to another without systematic dependence on their nature (SC@SC, M@SC, and SC@M) or diameter. On average,  $\sigma_S^{nr}$  is lower in DWNTs than in SWNTs, meaning that the effective sheet conductivity ‘carried’ by each wall in a DWNT is smaller than in SWNTs.

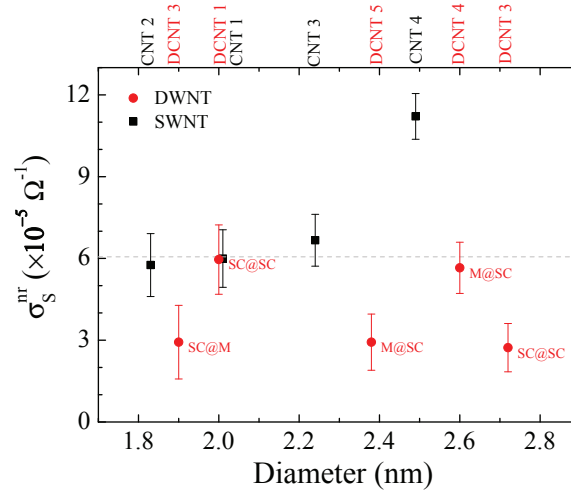


**Figure V.9:** Non-resonant absorption and conductivity in individual free-standing DWNTs. Values measured for SWNTs are recalled for comparison. The horizontal dashed line shows the ideal frequency independent graphene sheet conductivity.



# **Part 3**

## **Electrical transport**



# Electronic transport in individual carbon nanotube bundles under pressure

## VI

*In this chapter, we report electrical transport measurements of individualized carbon nanotubes under extreme conditions, where the behavior of nanotube-based field-effect transistors, in the classical and Coulomb blockade regime, under gas-pressure was investigated. We were able to characterize the nanotube devices using micro-Raman spectroscopy and/or atomic force microscopy, which is always challenging in high-pressure experiments.*

### VI–1 Carbon nanotubes under pressure

Mechanical stress modifies the tubes interaction with their environment, but also their intrinsic properties. The evolution of CNTs' cross-section under hydrostatic pressure was investigated both experimentally [177,178] and theoretically. [163,179–182]. For carbon nanotubes, three regions of pressure are expected, the boundaries of which depend on the nanotubes structural characteristics such as their diameter and number of walls. Pressure points separating these regions are usually called ovalization pressure ( $P_{\text{oval}}$ ) and collapse pressure ( $P_{\text{col}}$ ). From ambient pressure to  $P_{\text{oval}}$ , the nanotube cross-section decreases homothetically with pressure. Above this point, ovalization of the cross-section becomes more and more pronounced as pressure increases. This process stops at the collapse pressure where the tube cross-section adopts a peanut shape [178]. Up to now, it has not been possible to observe the influence of these structural changes on the intrinsic electronic properties of carbon nanotubes and calculations provide contradictory results.

Previous works conducted on a CNT-based field-effect transistor (CNT-FET) with nanotubes lying on gold contacts concluded on the importance to minimize Schottky barriers at the tube-electrode contacts [26]. For this reason, in this thesis we have prepared CNT-FET devices with source-drain palladium electrodes evaporated onto the tubes [183]. This configuration provides additional insights in the strain-induced evolution of the electronic properties of carbon nanotubes.

## VI–2 Experimental details

### VI–2.1 Sample preparation

Carbon nanotubes were produced by laser ablation (Rice University) and deposited on commercial silicon substrates with a thermally grown silicon dioxide layer of 300 nm. At first, they were localized with respect to pre-patterned gold electrodes using scanning electron microscopy in low current configuration to avoid surface contamination. Standard lift-off process and e-beam lithography were performed to contact CNTs between palladium electrodes of 50 nm high. Both conducting epoxy and gold wires were used to contact a selected CNT-FET on the sample holder, with two contacts on the source and drain electrodes (bias voltage  $V_{SD}$ ). One additional connection to the degenerated silicon substrate served as back gate (voltage  $V_G$ ). Electronic transport measurements were carried out with a classical DC-measurement setup (Fig. VI.1).

### VI–2.2 Characterization of the device at ambient pressure

In Figs. VI.1.a-c, the contacted nanotube here studied is observed by scanning electron microscopy and atomic force microscopy. The latter yields an apparent diameter of  $2.4 \pm 0.2$  nm. The length  $L$  of the CNT between the two electrodes is about 700 nm. Additional insights in the nature of the CNT sample were obtained by means of Raman spectroscopy. The experiment was performed at ambient conditions using a commercial Aramis Raman system with two laser sources: 633 nm (HeNe) and 473 nm (Cobalt). Fig. VI.1.e shows the Raman spectra for the two excitation wavelengths with incident light polarized along the main axis of the tube. For the 473 nm excitation, the G-band profile is composed of two narrow components at  $1593\text{ cm}^{-1}$  ( $G^+$ ) and  $1561\text{ cm}^{-1}$  ( $G^-$ ), with associated full-width at half maximum (FWHM) of 8 and  $9\text{ cm}^{-1}$ , respectively. It is characteristic of a chiral semiconducting single-wall carbon nanotube (SWNT) with diameter in the range 1-2 nm [19, 145]. A radial breathing mode (RBM) is observed at  $210\text{ cm}^{-1}$  from which a diameter of  $1.11 \pm 0.02$  nm is derived [105]. For laser excitation 633 nm, G-phonon modes are much broader and the  $G^-$  mode is down-shifted to  $1554\text{ cm}^{-1}$ . A RBM, presenting a slight asymmetric profile, is observed at  $203\text{ cm}^{-1}$ . These features of the tangential modes and RBM are characteristic of a metallic SWNT of diameter  $1.16 \pm 0.02$  nm [44, 144]. To summarize, based on the Raman spectra, our CNT-transistor is composed of a small bundle of a semiconducting and a metallic SWNT with both diameters in the range 1.1-1.2 nm. The diameter measured with AFM, as well as the FWHM of the different phonon modes, indicate that a limited number of other tubes are possibly present in the bundle.

The  $\sim 90\text{ k}\Omega$  resistance of the CNT-FET (both in air and inside the pressure chamber) is typical of the low contact resistance obtained for CNTs buried into palladium contact electrodes. As discussed in the introduction, it confirms a reduction of the Schottky barriers in comparison to CNT-FET devices with nanotubes lying onto the contact electrodes [25, 26]. The electronic transport properties of the CNT-FET were obtained



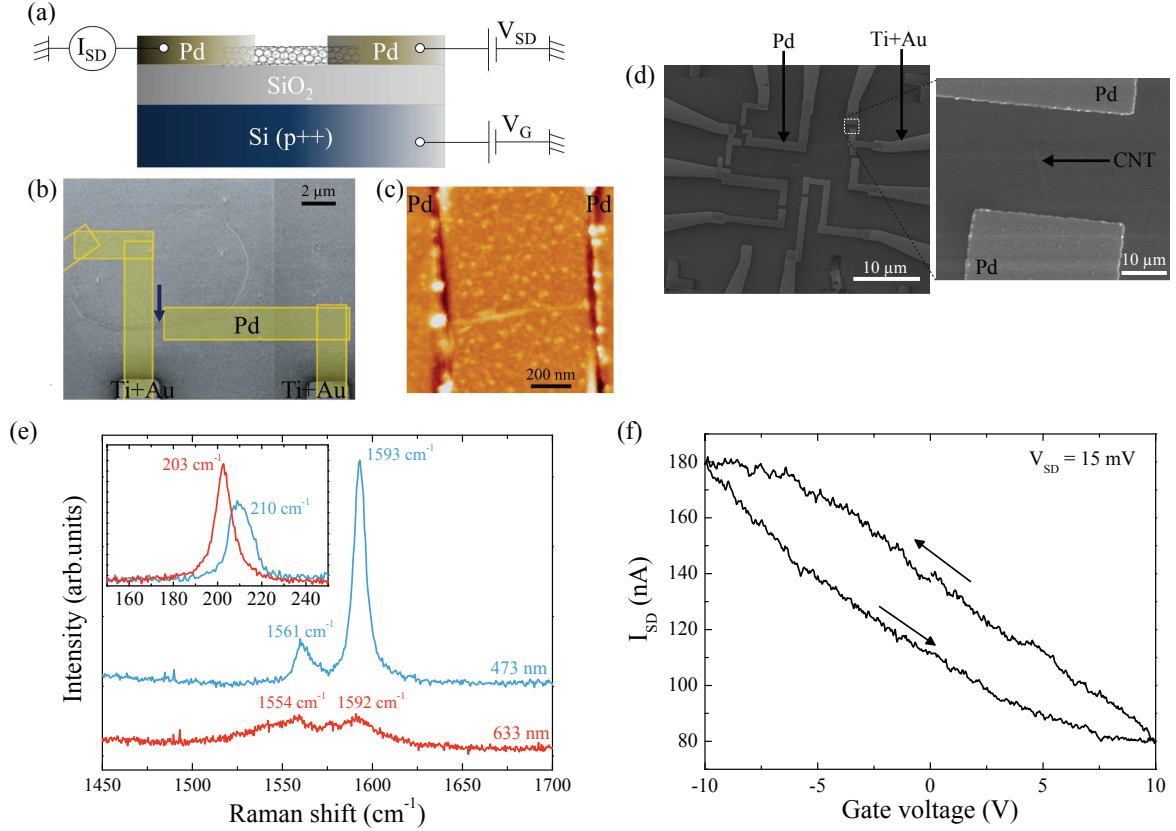


**Figure VI.1:** CNT-based field effect transistor (FET) including two palladium electrodes connecting the CNT for source-drain current measurements ( $I_{SD}$ ) as well as a back gate voltage control ( $V_G$ ). (a) Sketch of the device. (b) Scanning electron microscopy image of the substrate surface showing the studied individual CNT before being contacted by the as drawn electrodes. (c) Atomic force microscopy image of the region indicated by the blue arrow in (b), the diameter measured is  $2.4 \pm 0.2$  nm. (d) SEM images of the sample showing multiple CNT-FET, and (right) zoom in the region of a contacted nanotube. (e,f) Characterization of the field effect transistor under ambient conditions in air. (e) Raman spectra in the G-phonon region measured for excitation wavelengths 473 nm (blue line) and 633 nm (red line). (inset) Radial breathing modes observed at  $210 \text{ cm}^{-1}$  and  $203 \text{ cm}^{-1}$  for excitations 472 nm and 633 nm, respectively. (f) Transistor response showing p-doping in air, and hysteresis arising from charge traps below the nanotube.

by analyzing its  $I_{SD}$ - $V_G$  curve, i.e., measuring the current flowing through the CNT ( $I_{SD}$ ) while sweeping the gate voltage between  $-10 \text{ V}$  and  $+10 \text{ V}$  at fixed source-drain voltage  $V_{SD} = 15 \text{ mV}$ . In air, under ambient conditions, the response was typical of a p-type field effect transistor with non-zero OFF-state at  $V_G > 10 \text{ V}$  (Fig. VI.1.f); where the OFF-state is defined as the range of gate voltage in which the current response of the transistor is minimum. The p-type behavior is not intrinsic to nanotubes but rather induced by doping in air [153]. The observed hysteresis arises from the screening of the gate-induced

electric field by free charges in the nanotube vicinity (mainly located in potential traps on the silicon surface) [184–187]. Gate voltage sweeping produces a reorganization of these charges, which explains the hysteresis observed in the  $I_{SD}$ - $V_G$  curves. The current in the OFF-state is about 80 nA, and confirms the presence of at least one metallic nanotube in our device. In conclusion, the CNT-FET is formed of a bundle composed of at least a metallic and a semiconducting CNT with diameters between 1.1 and 1.2 nm. The CNT-FET is p-doped in air under ambient conditions, as confirmed by both the  $I_{SD}$ - $V_G$  characteristic and the slight upshift of the G-phonon modes. Ovalization and collapse pressures for 1.15 nm nanotubes have been predicted theoretically at minimum pressures of 20 kbar [180, 181] and 30–40 kbar [163, 179], respectively. Experimentally no data are available for such small diameter tubes.

### VI–2.3 High pressure measurements

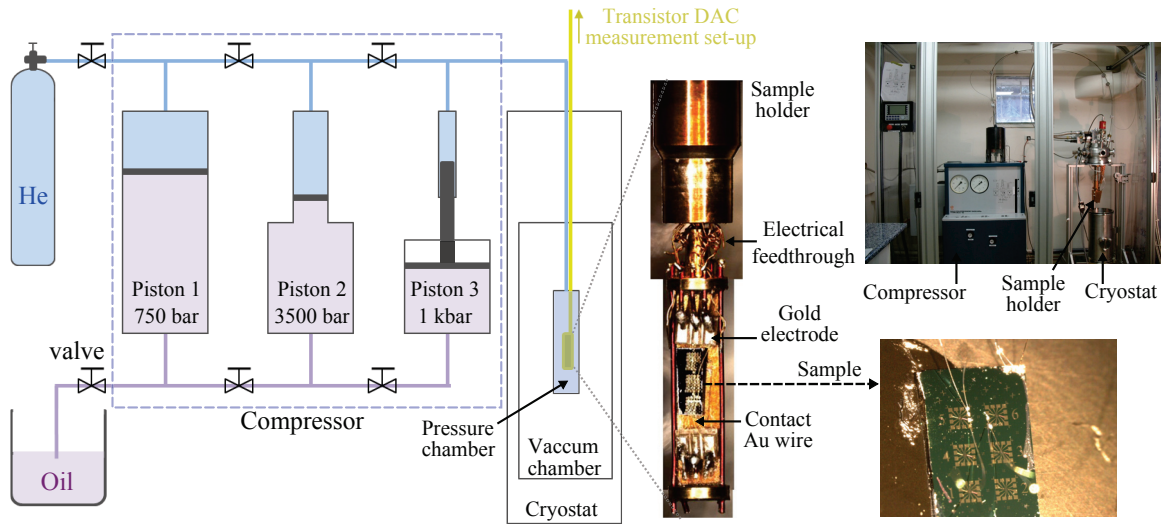


**Figure VI.2:** Electrical transport measurements at high pressure. (left panel & top/right picture) Gas compressor and cryostat providing extreme conditions of pressure (up to 10 kbar) and temperature (down to  $\sim 10$  K). The pressure of helium (blue) in the pressure chamber is increased via consecutively raising the pistons 1, 2 and 3 (the maximum gas pressure achievable with each piston stage is given on the scheme). Manganine gauges probe the pressure applied to the sample. (middle images) The sample is mounted on the sample holder sealed inside the pressure chamber. Electrical feed-through provide external access to the in-situ electrical response of field-effect transistor devices. (bottom/right picture) Microscope view of the sample surface.

The high-pressure experimental system is described in detail in ref [188] and sketched in Fig. VI.2. It includes both a gas compressor and a cryostat. The nanotube device is isolated in a chamber filled with helium gas standing pressures up to 10 kbar, thermally

coupled to the cryostat operating at temperatures below 10 K. Here we present preliminary measurements carried out on an isolated CNT bundle exposed to pressures up to 9 kbar under ambient temperature. Besides, we performed the first electronic transport measurements on individualized CNTs subjected to high pressures (4.5 kbar) and low temperatures ( $\leq 10$  K).

The device was sealed inside the high pressure chamber at 20 bar in helium gas. Comparing the  $I_{SD}$ - $V_G$  curves in air (Fig. VI.1.f) and in helium (Fig. VI.3, 20 kbar), the CNT-FET response changes from p-type to ambipolar (both n- and p-conduction) with non-zero OFF-state current during the operation. The ambipolar characteristic is observed as long as the CNT-FET is kept under helium environment. Precisely at 20 kbar, n-conductivity dominates and the neutrality point is closer to zero gate voltage. This transformation is accompanied with a shift of the minimum of the  $I_{SD}$ - $V_G$  curve (defined as  $V_{G,min}$ ) to lower gate voltage values (close to  $V_G = 0$ ) in comparison to the results in air. These changes involve a long relaxation process (of the order of 10 hours) to stabilize the CNT-FET response (not shown here). Few possible mechanisms can explain this change in the transistor characteristics. Most probably changes of the nanotube's environment are predominant, as for example desorption of water molecules from the CNT's surface [153]. However, due to the applied hydrostatic pressure (20 bar), an evolution of the adhesion-state of the CNT on a rough surface coupled with substrate-CNT charge transfer mechanisms cannot be totally excluded, as discussed later.

After this operation, pressure was increased up to a maximum value of 9 kbar with measurements every 500 bar in average during both pressure increase and release. Low temperature measurements were performed by cooling down the device to about 10 K at 4.5 kbar after pressure release. Unfortunately, the signal was lost in the last downstroke process at about 4 kbar due to failure of one of the contacts.

## VI-3 Results

The pressure evolution of the  $I_{SD}$ - $V_G$  measurements are presented in Fig. VI.3 (curves at different pressures were shifted vertically for sake of clarity). For each pressure, several remarkable points of the  $I_{SD}$ - $V_G$  response probe the pressure evolution of the CNT-FET. All these probe parameters are detailed in the following.

The two current minima  $V_{G,min}$  of the CNT-FET response (indicated by black squares and red circles in Fig. VI.3) provides information on the pressure dependence of both the gate voltage hysteresis and the resistance of the metallic nanotube ( $R_{min}$ ) [26]. The latter is reported in Fig. VI.4. It shows three pressure regimes. At low pressures, no noticeable evolution of the resistance is observed. Around 2 kbar, the resistance starts to increase with a slope of  $55 \text{ k}\Omega.\text{kbar}^{-1}$  or  $14 \text{ \%.kbar}^{-1}$  respective to the resistance in the low pressure regime. Above 6 kbar, a more pronounced increase of the metallic nanotube resistance versus pressure is observed ( $105 \text{ k}\Omega.\text{kbar}^{-1}$ ).

Each curve shows a typical hysteresis response of the CNT-FET while sweeping up

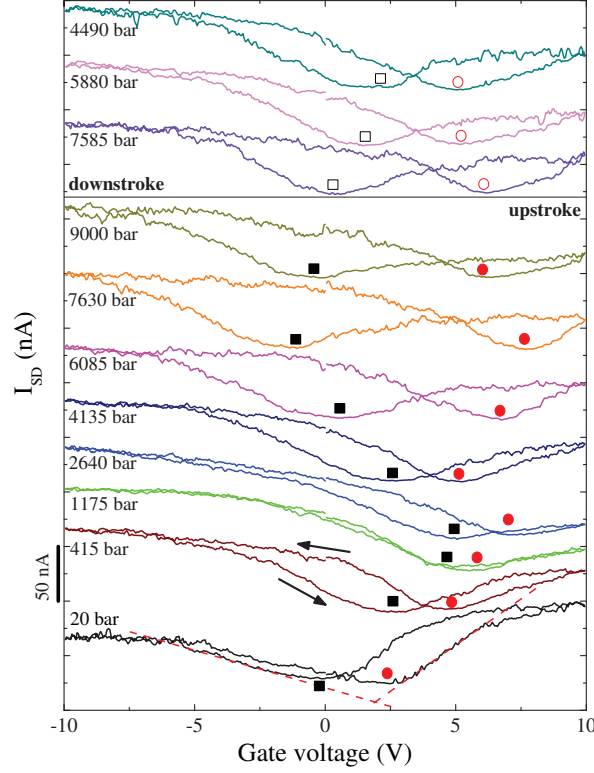


**Figure VI.3:** Pressure evolution of the CNT transistor characteristics. Each  $I_{SD}$ - $V_G$  curve is current-shifted for clarity. The black arrows indicate the direction in which the gate voltage is swept. Black squares and red dots locate the position of the current minima for gate voltage up-sweep  $V_{G,min}^i$  and down-sweep  $V_{G,min}^d$ . Red dashed lines: example of linear fits performed to extract the electron and hole mobilities.

or down the gate voltage. Probing and comparing the response between these two situations provide information on the CNT environment. Fig. VI.5 presents the pressure dependence of the gate voltage in the OFF-state at  $V_{G,min}$  (extracted from Fig. VI.3). Also in Fig. VI.5, the gate voltage hysteresis is defined as  $\Delta V_{G,min} = V_{G,min}^d - V_{G,min}^i$ , where  $V_{G,min}^i$  ( $V_{G,min}^d$ ) is the position of the minimum of current  $I_{SD}$  while up-sweeping (down-sweeping) the gate voltage. At pressures below 2 kbar, we observe important shifts of the OFF-state positions to higher values. In the meantime, the gate voltage hysteresis decreases slightly, involving small changes of charges trapped in the vicinity of the tube. More precisely, in the case of oxidized silicon substrates, pressure might reverse the equilibrium of the hydroxylation reaction (cf. Caillier [26] for details). Above 2 kbar,  $V_{G,min}^i$  decreases monotonically from +6 V down to -1 V corresponding to a n-doping of the CNT-FET. Between 2 and 4 kbar,  $V_{G,min}^d$  decreases monotonically parallel to  $V_{G,min}^i$ , whereas it tends to stay roughly constant at around 6 V for pressures above 4 kbar. Meanwhile, the gate voltage hysteresis constantly increases with pressure starting from 2 kbar: from 1 V at 2 kbar to 7 V at 9 kbar (Fig. VI.5). This observation implies changes in

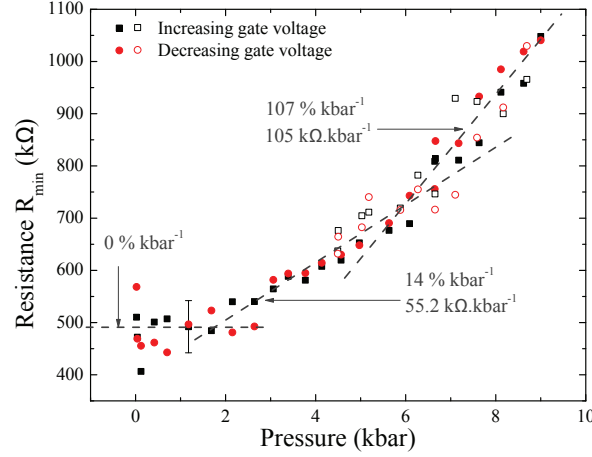


**Figure VI.4:** Analysis of the metallic CNT resistance behavior under pressure, extracted from the OFF-state transistor characteristics in Fig. VI.3. Filled and open symbols account for pressure increase and decrease, respectively. Dashed lines are linear fits in three pressure regions.

the nanotube environment, possibly by charge trapping on the silicon substrate, adsorbed species directly on the CNT, modification of the adhesion-state of the CNT on the rough substrate surface, or tube-tube interactions. Further investigations would be required to clarify the exact origin of our observations. We notice again the reversibility of the results.

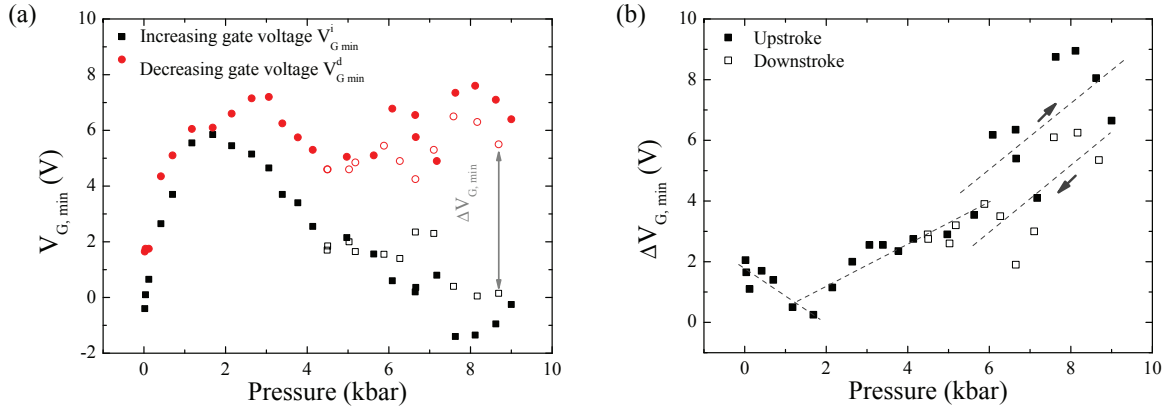


**Figure VI.5:** Evolution of the gate voltage hysteresis under pressure. (a) Gate voltage of the OFF-state in Fig. VI.3. Filled and open symbols refer to pressure increase and decrease, respectively. (b) Hysteresis amplitude  $\Delta V_{G,\min} = V_{G,\min}^d - V_{G,\min}^i$ .

Besides the metallic component and environment effects, the pressure evolution of the semiconducting response of the CNT-FET is probed by: electron and hole effective mobilities, and the ON-state currents. Fig. VI.6 presents the pressure evolution of the

electron and hole effective mobilities ( $\mu_e$  and  $\mu_h$ ). Mobility values are extracted from the linear fits as shown in Fig. VI.3 and the formula  $\mu_{e,h} = l^2(\partial I_{SD}/\partial V_G)/CV_{SD}$ , where the capacitance  $C$  is about  $10^{-17}$  F [189]. Below 1-2 kbar, we observed important evolution of the effective mobility of electrons and holes with pressure (Fig. VI.6). Within this pressure range, the CNT-FET switches from n-type prevailing with  $\mu_e \simeq 700 \text{ cm}^2.(\text{Vs})^{-1}$  and  $\mu_h \simeq 150 \text{ cm}^2.(\text{Vs})^{-1}$ , to p-type dominant with  $\mu_e \simeq 150 \text{ cm}^2.(\text{Vs})^{-1}$  and  $\mu_h \simeq 400 \text{ cm}^2.(\text{Vs})^{-1}$ . Above 2 kbar, hole effective mobility stays constant around  $400 \text{ cm}^2.(\text{Vs})^{-1}$ , yet electron effective mobility shows intermediate behavior between 1 and 4 kbar before stabilizing around  $250 \text{ cm}^2.(\text{Vs})^{-1}$  at higher pressure. Therefore, results presented in Fig. VI.6 show that pressure modifies significantly both electron and hole conduction under 2 kbar, while at higher pressures only electron mobility is affected between 1 and 4 kbar.

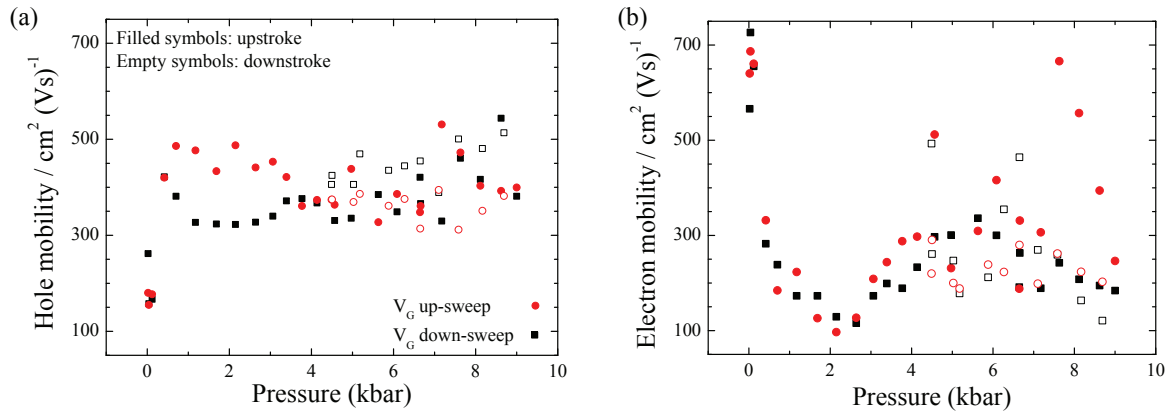


**Figure VI.6:** Pressure dependence of the the electron and hole effective mobilities in the FET device. Mobilities are extracted from linear fitting of the  $I$ - $V_G$  curves as shown in Fig. VI.3.

The pressure evolution of the semiconducting CNT is investigated by means of another method. It consists in following the pressure evolution of the currents at the ON-states. Here, the p-conductivity and n-conductivity ON-states are reached close to gate voltages  $-10$  V and  $+10$  V, respectively. To be accurate and study only the semiconducting contribution to the CNT-FET response, we need to remove the signal associated with the metallic component of the CNT-FET. These results are depicted in Fig. VI.7, along with the difference of current in the n-branch ON-state and p-branch ON-state  $\Delta I_{SD}^{ON}$  (inset). Similar analysis method was employed elsewhere to investigate modifications of the Schottky barriers under pressure at the contacts between semiconducting CNTs and metallic electrodes [26, 190]. The graphs in Fig. VI.7 show the presence of three pressure states. A high pressure regime (above 4 kbar) where both source-drain currents decrease steadily with identical slopes of  $-2.1 \text{ nA.kbar}^{-1}$ . Below 1-2 kbar, considerable variations of  $I_{SD}(V_G = -10\text{V})$  and  $I_{SD}(V_G = +10\text{V})$  are observed. The former rises significantly from 20 to 70 nA, while the latter drops from 70 to 10 nA. Then, the CNT-FET



device undergoes change from n-type dominant conduction to a more pronounced p-type behavior at low pressure ( $< 1\text{-}2$  kbar), which is clearly visible in the  $\Delta I_{SD}^{ON}$  graph. The intermediate pressure range ( $\sim 1$  to 4 kbar) presents stronger variations of the n-channel transistor characteristic, which is in agreement with the changes observed in the electron mobility.

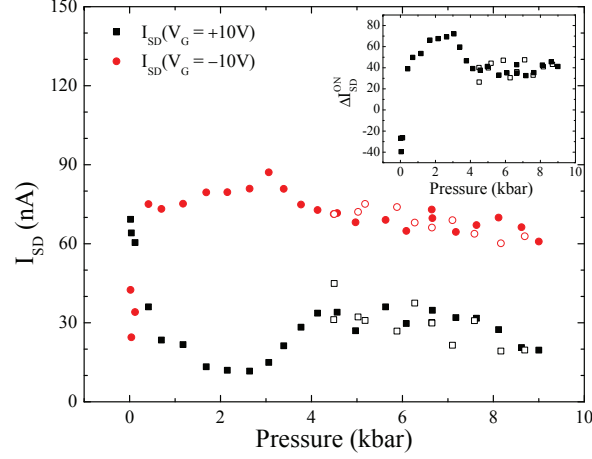


**Figure VI.7:** Analysis of the p and n branches of the transistor characteristics under pressure via the evolution of currents at  $+10$  and  $-10$  V. (inset) Difference between  $I_{SD}(V_G = -10V)$  and  $I_{SD}(V_G = +10V)$ . Filled and open symbols represent measurements during upstroke and downstroke, respectively.

## VI-4 Discussion

From the results, three regimes have been identified in the pressure evolution of the CNT-FET (at ambient temperature): (1) a low pressure phase ( $P \lesssim 2$  kbar), (2) an intermediate pressure region between  $\sim 2$  kbar and 4–6 kbar, (3) a high pressure regime ( $P \gtrsim 4$  kbar). The analysis of the CNT-FET response is conducted according to the parameters of the  $I_{SD}$ - $V_G$  curves introduced in the previous section. In other words, the observed pressure evolution of the CNT-FET can be associated with different elements of the system: metallic or semiconducting CNTs, CNT-electrode contacts, environment.

The resistance of the metallic component of the CNT-FET clearly shows the three pressure regimes. As stated, theoretical works reported tube ovalization at a pressure of few tens of kbar in 1.1 nm environment-free SWNT, i.e., well above the pressure range accessible here. However, symmetry losses and van der Waals forces (interaction with the substrate and/or other nanotubes) have been found to facilitate radial cross-section changes in CNT [30,36,191]. Consequently, contact-interactions with the substrate tend to initiate the ovalization process at lower pressures, or at least to create ovalization spots along the CNT due to the roughness of the substrate surface. Such tube cross-section modifications can be responsible for changes in the electrical resistance through



at least two different mechanisms: i) by an intrinsic modification of the tube electronic characteristics [192], or ii) through a modification of the barriers at the CNT-electrode contacts [25]. This last process could occur at a higher pressure than the first one as cross-section ovalization is likely to initially take place far from the CNT-electrode contacts and propagates towards the electrodes in which the nanotube is anchored, as ovalization should be delayed at the contact zone due to supporting effect of the contact. The two step changes observed in Fig. VI.4 could then find their origin in such considerations or/and the contribution of two different metallic tubes to the observed signal. Previous study of metallic nanotubes deposited directly onto gold electrodes observed a single pressure-evolution regime, in fact the CNT-FET device is dominated by the tube-electrode contact resistance [25, 26]. Moreover, in such system, the overall resistance of the device monotonically decreases with pressure at  $-1.6 \text{ \% kbar}^{-1}$ . Hence, in our case, the observation of three distinct regimes in the metallic resistance pressure-evolution suggests that not only the CNT-electrode contact resistance is probed. Further experiments are required to determine the origin of the two-regime resistance increase: either pure intrinsic evolution of the metallic tube properties under pressure, CNT-electrode contacts, CNT-substrate interactions, interactions between the CNTs of the bundle, or a mixture of all. The reversibility of the results proves that no permanent degradation occurs either in the CNT or at the tube-electrode contacts.

The evolution of the semiconducting component of the CNT-FET under pressure observes also three pressure regimes (Figs. VI.5, VI.6, VI.7), corresponding to different responses of the semiconducting CNT. These modifications are well explained by environment-induced nanotube p-doping at low pressure and n-doping above 2 kbar, possibly due to increasing interaction with the silanol groups at the  $\text{SiO}_2$  surface, and variation of the equilibrium state of the oxygen/water redox couple [153]. At low pressure ( $< 1\text{-}2 \text{ kbar}$ ), an important increase of the p-type conductivity of the transistor device is observed, as well as an up-shift of  $V_{G,\min}^i$  and  $V_{G,\min}^d$ . At high pressure ( $> 4 \text{ kbar}$ ), steady electron and hole effective mobilities suggest that pressure does not influence the intrinsic conduction properties of the semiconducting component of the bundle, whereas the strong increase of the hysteresis  $\Delta V_G$  is consistent with changes in the nanotube electrostatic environment. The pressure range from 1 to 4 kbar is intermediate between the high and low pressure behaviours, showing that the nanotube's environment and its interaction with the CNT-FET is strongly pressure dependent. On the one hand, modifications in nanotube-substrate adhesion state accompanied by substrate-CNT charge transfers explain well the important changes observed at low pressure. On the other hand, high pressure behaviour is apparently dominated by the evolution of the nanotube's environment: charge trapping/released on the silicon substrate, adsorption/desorption of species directly on the CNT, changes in the equilibrium of the redox water/oxygen reaction.

## VI-5 Coulomb blockade under pressure

In this section, we present preliminary measurements of the response of CNT-based field-effect transistors in the Coulomb blockade regime at high pressure. At first, the CNT-FET studied above at ambient temperature is cooled down to about 11 K while the surrounding pressure is maintained at 4.5 kbar. The resulting differential conductance as a function of both the source-drain and the gate voltages demonstrates the presence of Coulomb blockade at high pressure (Fig. VI.8.a). The Coulomb diagram shows non-periodic peaks with no conduction at  $V_{SD} = 0$  V, which is characteristic of a diffusive regime involving several potential barriers along the nanotube besides the CNT-electrode contact barriers.

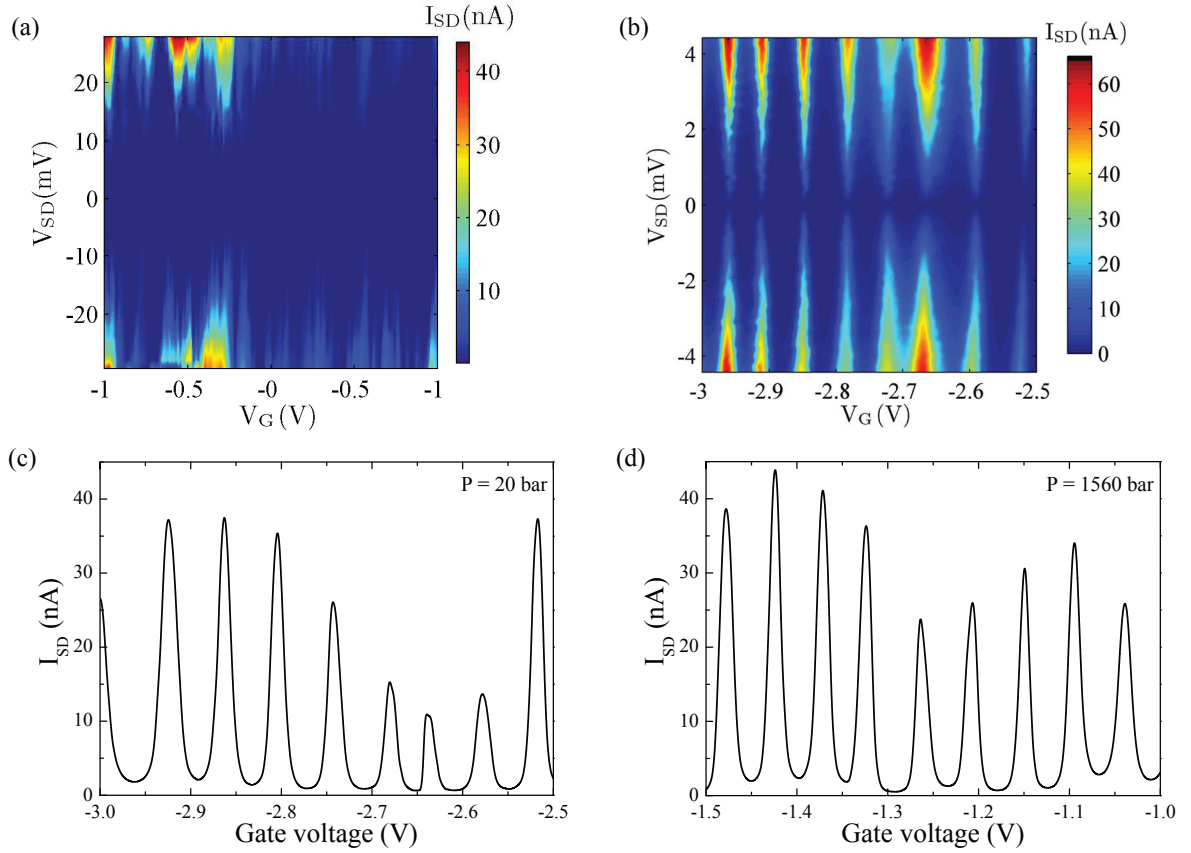


**Figure VI.8:** Observation of Coulomb blockade in individual carbon nanotubes bundles at low and high pressure. (a) CNT-FET in the Coulomb blockade regime at high pressure (4.5 kbar). Color map of the current  $I_{SD}$  as a function of the source-drain voltage  $V_{SD}$  and gate voltage  $V_G$ . (b-d) Different CNT-FET in the Coulomb blockade regime at 20 and 1560 bar. (b) Color map of the current  $I_{SD}$  as a function of the source-drain voltage  $V_{SD}$  and gate voltage  $V_G$ , showing clear Coulomb diamonds at 20 bar. (c,d)  $I_{SD}$ - $V_G$  curve showing periodic current peaks for  $V_{SD} = 3$  mV. In this range of gate voltage, the periods at 20 bar and 1560 bar are  $57 \pm 6$  mV and  $55 \pm 4$  mV, respectively.

To gain insights in the pressure evolution of the CNT-FET response in the Coulomb regime, we investigated another similar device composed of a small bundle of semiconducting and metallic nanotubes. In this case, Coulomb blockade at low (20 bar) and high (1560 bar) pressures has been observed (Figs. VI.8.b-d). The low pressure Coulomb diagram shows clear diamond-like conductance from which we extract: the charging energy  $E_C = 6$  meV, the total capacitance of the device  $C_\Sigma = 13$  aF, the gate capacitance  $C_G = 2.6$  aF [193].  $C_G$  is approximated by the capacitance between a finite wire, with the characteristics of the CNT (diameter  $d$  and effective length  $l_{eff}$ ), embedded in a medium of dielectric constant  $\varepsilon_m$ , and a conducting plate (the back gate) placed at a distance  $b$ . Thus, an expression of the effective length of the nanotube is given by  $l_{eff} = C_G \ln(4b/d) / 2\pi\varepsilon_0\varepsilon_m$ , where the  $b$  is the silicon dioxide layer thickness of 300 nm, the environment dielectric constant is set to the one of  $\text{SiO}_2$  (3.6), and the diameter of the nanotube is about 1 nm. We find an effective length of 90 nm which is five times smaller than the real length of the nanotube, thus demonstrating that our nanotube bundle is subdivided by potential barriers along its length already at 20 bar. These portions are assimilated to quantum dots with different charging energy that activate at different gate voltages. In Figs. VI.8.b-d, we compare the transistor response  $I_{SD}$ - $V_G$  at  $V_{SD} = 3$  mV at pressures 20 and 1560 bar, in the Coulomb blockade regime, for selected range of gate voltage in which a single quantum dot is probed (the other dots are activated). No noticeable pressure-induced modification is observed on the conduction peak period, yielding  $57 \pm 6$  mV and  $55 \pm 4$  mV at 20 bar and 1560 bar, respectively. Then, in this case, a pressure increase from 20 and 1560 bar does not significantly modify the nanotube intrinsic properties. It suggests that the stress-induced changes observed at ambient temperature in the previous CNT-FET are mainly due to modifications of the interactions between the nanotube and its environment, at least in the low pressure regime ( $\gtrsim 2$  kbar).

# Conclusion

---

## Absorption spectroscopy

Optical studies of carbon nanotubes, in particular based on single nanotube spectroscopy, are still in their infancy. The knowledge of many fundamental properties, e.g. the absorption cross-section and the characteristics of excitons for a wide range of nanotubes, is still partial and much experimental work is required to fully understand them.

In this thesis, spatial modulation spectroscopy techniques and its reflective counterpart (namely reflective spatial modulation spectroscopy) have been developed for optical detection and absorption characterization of an individual CNT either embedded in a transparent medium or deposited on an opaque substrate. Based on synchronous detection of the modulated part of the transmitted or reflected light in a spatial-modulation setup, these methods grant direct access to the absolute absorption cross-section of CNTs in different environments. They also permit non-invasive high-contrast optical imaging of single nano-objects as demonstrated for free-standing CNTs and nanotubes on silicon. Furthermore, the flexibility, low technical requirements and ease of integration of these techniques make them easily implementable and in-situ combinable with structural (AFM) or spectroscopic (Raman) investigations on the same nano-object on any (transparent or opaque) substrate.

Our most significant results have been the quantitative determination of the absorption cross-section spectra of individual structure-identified carbon nanotubes (see figure p. 164). From this study, conclusions have been drawn regarding the dependencies of CNTs absorption characteristics, i.e. mainly their excitonic transitions and non-resonant absorption background, on the type of nanotube (number of walls, nature, diameter, or chirality) and environment. In freely suspended semiconducting SWNTs, we have demonstrated a systematic trend of the oscillator strength with an oscillatory kind of behavior for adjacent excitonic lines, having opposite variations in type I and II semiconducting SWNTs. Such considerations have proven to be more difficult to address in the case of DWNTs as any general tendency of the exciton characteristics is hardly observable. However, considering the exciton characteristics weighted by the number of carbon atoms, larger effective values of absorption cross-section and oscillator strength are observed in SWNTs than in DWNTs, implying that light is more efficiently absorbed by the carbon atoms in SWNTs. Our measurements have demonstrated that absorption of DWNTs is only partially described by our knowledge of exciton characteristics in isolated SWNTs and including interwall dielectric screening. We have proposed, as is

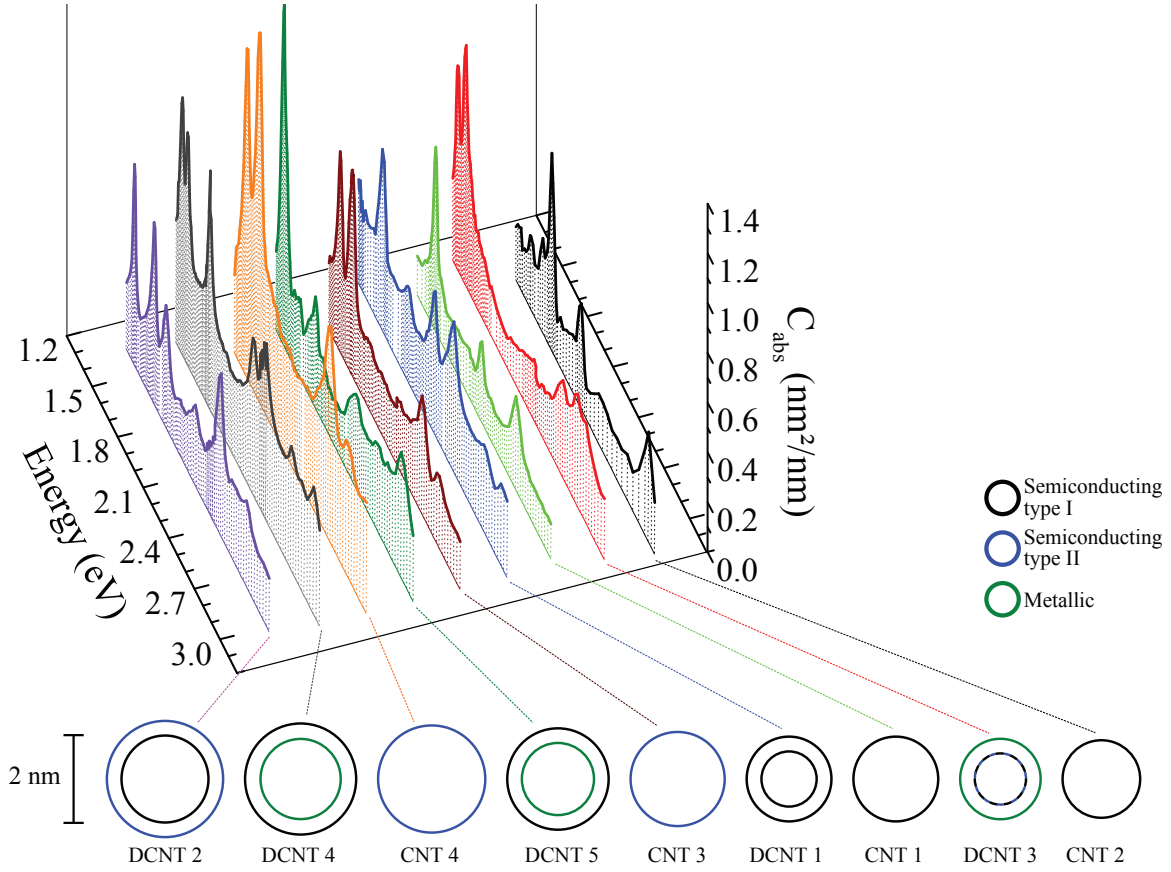


**Figure:** Spectra of the absolute absorption cross-section of all the individual free-standing single- and double-wall carbon nanotubes investigated in this dissertation.

also suggested in reports for SWNT bundles, that interwall quantum coupling alters the exciton state characteristics and should be examined in future theory.

Comparison of the absorption spectrum measured for the same individual nanotube (SWNT or DWNT) free-standing or deposited on a Si/SiO<sub>2</sub> substrate directly shows that CNT interaction with a substrate induces a large broadening of the excitonic transitions concomitant with a shift of their frequency, and an increase of their oscillator strength associated with a strong depolarization effect. Some of these changes have been ascribed to dielectric screening of many-body effects, possibly accompanied by substrate stress-induced strain and chemical doping. Furthermore, substrate and environment interactions trigger exciton localization effects and new exciton decay pathways, as well as new energy transitions. In the same ways, the comparison of the spectrum obtained for the same freely suspended DWNT isolated or put in a bundle (with a metallic SWNT) shows changes of the exciton characteristics (energy, linewidth, and oscillator strength). Conversely, excitonic characteristics are not systematically altered when a single semiconducting SWNT is included in a bundle with metallic SWNTs. These modifications of the absorption properties of nanotubes in bundles might be the consequence of inter-

wall or inter-tube interactions via dielectric screening effects and/or quantum coupling of exciton states from different tubes.

Some of our efforts have been focused on the study of the dependence of CNTs absorption cross-section on excitation light polarization. In free-standing nanotubes (SWNT or DWNT), either individual or included in a bundle, strong depolarization effects are observed resulting in almost complete attenuation of the absorption measured for incident light polarized perpendicular to the nanotubes. On the contrary, in substrate-supported CNTs a significant absorption cross-section is still observed for polarization perpendicular to the tubes. For deposited carbon nanotubes, weakening of the polarization dependence can be ascribed to softening of the antenna effect which is correlated to weakening of the depolarization field therefore allowing crossed-polarized energy transitions to take place.

Finally, a significant non-resonant absorption background is observed in all investigated nanotubes, either free-standing or supported, with amplitude comparable to the ideal graphene absorbance. Although this non-resonant background shows smooth diameter dependence in individual SWNTs, significant fluctuations have been measured in DWNTs. Despite this, the contribution of the continuum of the metallic energy transitions to the non-resonant absorption needs to be clarified in future work.

### **Electrical transport under pressure**

This thesis also reports on the investigation of electrical transport properties of carbon nanotube based field-effect transistors under extreme conditions of pressure and temperature.

Interpretation of the results is complex as pressure can possibly have many effects on the field-effect transistors. Overall, two pressure regimes are observed: a low pressure one (below 1-2 kbar) showing mostly changes of nanotube interaction with its environment, and a high pressure regime ( $> 4$  kbar) where the device response is influenced by various phenomena including environmental effects, modification of nanotube/electrode contact barriers, and/or evolution of the intrinsic cross-section of the nanotubes.

At last, preliminary measurements of field-effect transistors in the Coulomb blockade regime have been reported for carbon-nanotube-based field-effect transistor devices subject to high hydrostatic pressure of 4.5 and 1.6 kbar. Despite our difficulties to draw a clear conclusion on the effect of pressure on the dielectric properties of nanotube transistor devices, low temperature measurements ( $< 10$  K) have provided the first experimental evidence of Coulomb blockade at high pressure and the conservation of the ballistic behavior of charge carriers in nanotubes under important stress-induced strain.

### **Outlook**

The quantitative results reported in this dissertation for the absorption properties are of particular relevance for investigation and modeling of the intrinsic electronic properties of carbon nanotubes either free-standing or supported (a situation relevant for practical applications). Furthermore, the experimental approach developed in this work opens many possibilities for investigating other types of individual nanotubes or the impact of

nanotube interaction in bundles.

In future work, a systematic study of nanotubes of different types might help to assess more precisely the dependencies of the exciton characteristics on the structure of CNTs (diameter, chiral angle, nature, number of walls) and excitonic transition. As mentioned in the text, investigation of the temperature dependence of the absorption properties of the freely suspended CNTs is likely to give more insight in the characteristics of both the main exciton states and the absorption side features (phonon-assisted absorption, excited exciton states, . . . ). Likewise, continuous tuning of the environment, e. g. via hydrostatic pressure or humidity control, will provide precious information on the evolution of nanotubes absorption properties regarding the ‘strength’ of the nanotube-environment interactions or nanotube-nanotube interactions. For example, a metrological study of both isolated DWNTs and bundles of SWNTs by means of absorption and Raman spectroscopy will ideally shed light on the inter-wall coupling processes.

Concerning electrical transport measurements, it is of great importance to extend our work to well characterized individual carbon nanotubes integrated in various field-effect transistor devices. A straightforward proposition would consist of performing this study on freely suspended individual nanotubes in order to reduce interactions with the environment. After electrical current cleaning, pressure evolution of the electronic transport in CNTs would depend primarily on their intrinsic properties and contact barriers. An alternative approach where the design of the sample transistor device is adapted for both electrical transport measurements and optical spectroscopy will grant access to the pressure dependence of the nanotubes opto-electronic properties.



# **Part 4**

## **Appendix**



# Structure assignment of SWNT A

---

*In the following, we detail the procedure providing possible assignment of the four semi-conducting SWNTs presented in Sec. V-3. As mentioned in the text, pseudo-experimental Kataura plot for high-order energy transitions (at least  $S_{33}$  and  $S_{44}$  have been measured experimentally) are reported in refs. [16, 18, 44] (see also Sec. II-2.2.c). Thus, energy transitions  $S_{33}$  and  $S_{44}$  can be treated with relative confidence, still  $S_{55}$  and  $S_{66}$  should be considered more carefully.*

## Description of the procedure

Structure assignment of each nanotube follows the different steps listed here:

- i. The diameter is set from the radial breathing mode (RBM) frequency  $\omega_{\text{RBM}}$  (the relation between the two is detailed in the main text:  $\omega_{\text{RBM}} = 204/d + 27$  with  $\omega_{\text{RBM}}$  and diameter  $d$  in  $[\text{cm}^{-1}]$  and  $[\text{nm}]$ , respectively).
- ii. The energy positions of the peaks in the absorption spectra are reported on the Kataura plot proposed by V. Popov in ref. [44].
- iii. The peak and chirality assignment is possible after rigid shift of the calculated resonances in the Kataura plot. This procedure is justified in ref. [18].

In Tab. A.1, the experimental data of the free-standing SWNTs are reported for sake of clarity: Uncertainties on both the diameters and the peaks positions are included:

- i. *Raman spectroscopy*:  $\omega_{\text{RBM}}$  is measured with an uncertainty of  $1 \text{ cm}^{-1}$  corresponding to an uncertainty on the diameter of  $0.02 \text{ nm}$  for the two smaller nanotubes

	$\omega_{\text{RBM}}$ ( $\text{cm}^{-1}$ )	Diameter (nm)	$S_{33}$ (eV)	$S_{44}$ (eV)	$S_{55}$ (eV)	$S_{66}$ (eV)	Absorption spectrum	Raman spectrum
<b>CNT 1</b>	128.5	2.01	1.66	2.21	2.61		Fig. IV.1.a	Fig. IV.1.c
<b>CNT 2</b>	139	1.82	1.93	2.27	3.06		Fig. IV.1.a	Fig. IV.1.d
<b>CNT 3</b>	118	2.24	1.64	1.79	2.50	2.62	Fig. IV.3.a	Fig. IV.3.c
<b>CNT 4</b>	109	2.49	1.65	1.79	2.50	2.63	Fig. IV.3.b	Fig. IV.3.d

**Table A.1:** Experimental data for free-standing SWNTs.

and 0.03 nm for the two others (marked as vertical dashed lines in the following graphs). In order to take into account other error sources such as the uncertainty on the RBM *vs.* diameter relationship, we consider hereafter an uncertainty of 3  $\text{cm}^{-1}$  on  $\omega_{\text{RBM}}$ .

- ii. *Absorption spectroscopy*: uncertainty is set by the spectral linewidths of the different laser sources and the precision of the feedback spectrometer. The laser linewidths are discussed in the main text. The overall uncertainty coming from the spectrometer is about 2 nm. Then, the maximum uncertainty on the absorption peak positions is: 20, 30, and 50 meV in the near IR (700-1000 nm), visible (530-700 nm), and blue (390-530 nm) part of the spectra, respectively. They are sketched with red horizontal bands in the following Kataura plots.

### Assignment CNT 1 (Fig. A.1)

The G-band profile of this tube is composed of 2 narrow components meaning that it is a chiral semiconducting SWNT. Its diameter deduced from  $\omega_{\text{RBM}}$  ( $128.5 \pm 3 \text{ cm}^{-1}$ ) is  $d = 2.01 \pm 0.06 \text{ nm}$ , i.e. nanotubes with diameters in the range 1.95-2.07 nm are considered as potential candidates (see Fig. A.1). Three peaks are observed in the absorption spectrum (Fig. IV.1.a, main text). Possible candidates can be discriminated with respect to the energy difference between the two low energy transitions ( $0.54 \pm 0.045 \text{ eV}$ ). Using this criteria, only two possibilities are found: (23,4) or (22,6) with diameters of 1.977 nm and 2 nm, respectively. Both tubes are **type I** chiral semiconducting tubes. A very good agreement within measurements error bars is found for the  $S_{33}$ ,  $S_{44}$ , and  $S_{55}$  of the (23,4) (resp. (22,6)) nanotube by applying a rigid energy shift to the calculated energies [44] of 0.3 eV (resp. 0.31 eV). Since the (22,6) diameter is closer from the one deduced from  $\omega_{\text{RBM}}$ , this assignment is the most probable one.

### Assignment CNT 2 (Fig. A.2)

The G-band profile of CNT 2 is also composed of 2 narrow components meaning that it is a chiral semiconducting SWNT. The diameter  $d = 1.82 \pm 0.05 \text{ nm}$  is derived from  $\omega_{\text{RBM}}$  ( $139 \pm 3 \text{ cm}^{-1}$ ), i.e. potential candidates in the range 1.77-1.87 nm need to be taken into consideration (Fig. A.2). The absorption spectrum shows three energy transitions. Following the method applied for CNT 1, the energy difference between the two lower energy peaks ( $0.34 \pm 0.05 \text{ eV}$ ) limits the number of possible candidate to the only one tube (14,13) with diameter 1.833 nm. The latter is semiconducting and belongs to **type I** family. After rigid shift of the calculated resonances [44] of 0.36 eV,  $S_{33}$  and  $S_{44}$  yield very good agreement with the Kataura plot within error bars.  $S_{55}$  is slightly blue-shifted in comparison to the calculated energy transition, but the latter value cannot be verified due to the lack of experimental data for  $S_{55}$  and higher-order energy transitions.

### Assignment CNT 3 (Fig. A.3)

The G-band profile of this tube is composed of two narrow components where the low frequency phonon mode ( $G^-$ ) is weak and close to the high energy one ( $G^+$  mode). It means that CNT 3 is a chiral semiconducting SWNT. The RBM frequency  $\omega_{\text{RBM}}$

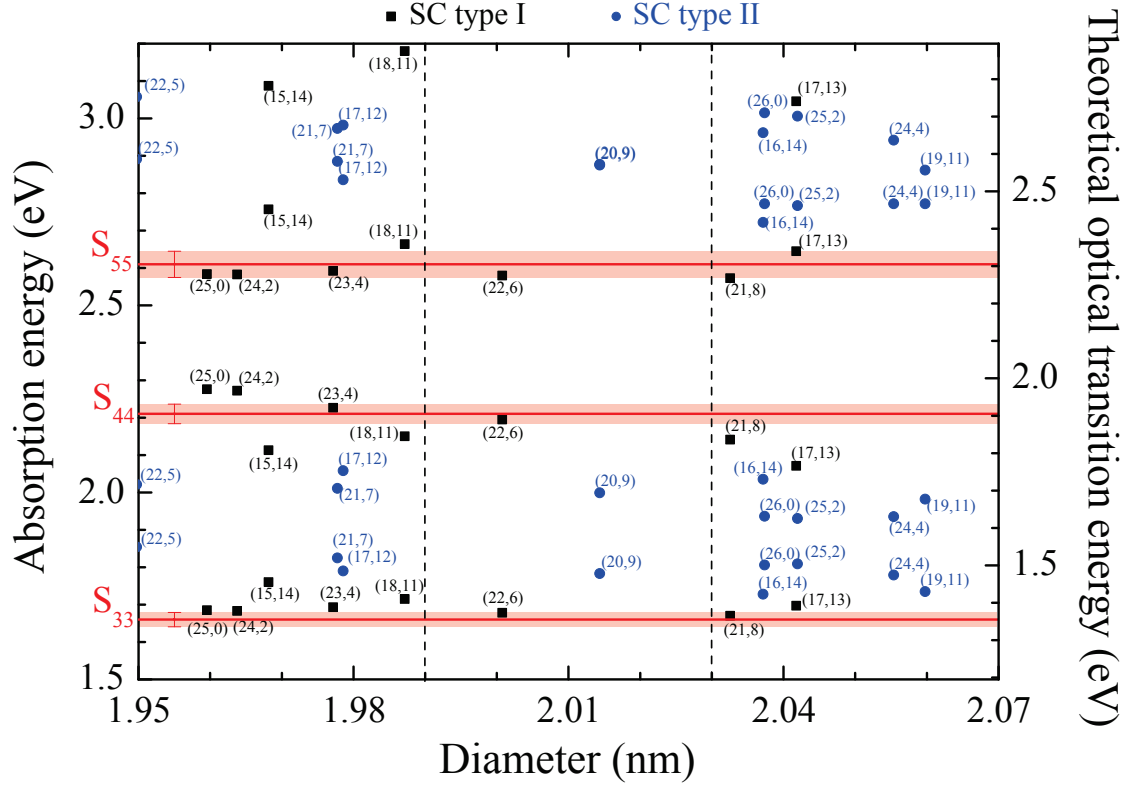


**Figure A.1:** Structure assignment CNT 1 (see Fig. IV.1.a,c for the corresponding absorption and Raman spectra): comparison between measured absorption energies (red lines) and theoretical optical transition energies as a function of nanotube diameter (black squares and blue dots, type I and type II semiconducting nanotubes respectively). The X-scale range corresponds to CNT 1 diameter (see text). Left scale corresponds to the energy in the experimental absorption spectrum and horizontal red bands show absorption peak positions with experimental error bars. Right scale is associated with the transitions calculated in [44] which undergo rigid shift of 0.31 eV. For the sake of clarity, the metallic tubes have been removed from the plot.

( $118 \pm 3 \text{ cm}^{-1}$ ), identical for few different excitation energies, yields a diameter  $d = 2.24 \pm 0.07 \text{ nm}$ . Hence, nanotubes in the range 2.17-2.31 nm are considered as potential candidates for structure assignment (Fig. A.3). In the absorption spectrum two energy transitions are observed at 1.64 and 1.79 eV (Fig. IV.3.a). The profile of the absorption feature around 2.62 eV can only be reproduced by two Lorentzian functions, suggesting the presence of two excitonic energy transitions (2.50 eV and 2.62 eV). The feature around 2.80 eV does not show a good agreement with a Lorentzian profile, but is rather well fitted with a phonon-side band model (cf. main text). Possible nanotube candidates can be discriminated with respect to the energy difference between the two low energy transitions ( $0.15 \pm 0.04 \text{ eV}$ ). Among them, the (23,9) can be ruled out based on the energy difference between the two high energy transitions ( $0.12 \pm 0.07 \text{ eV}$ ). The five remaining



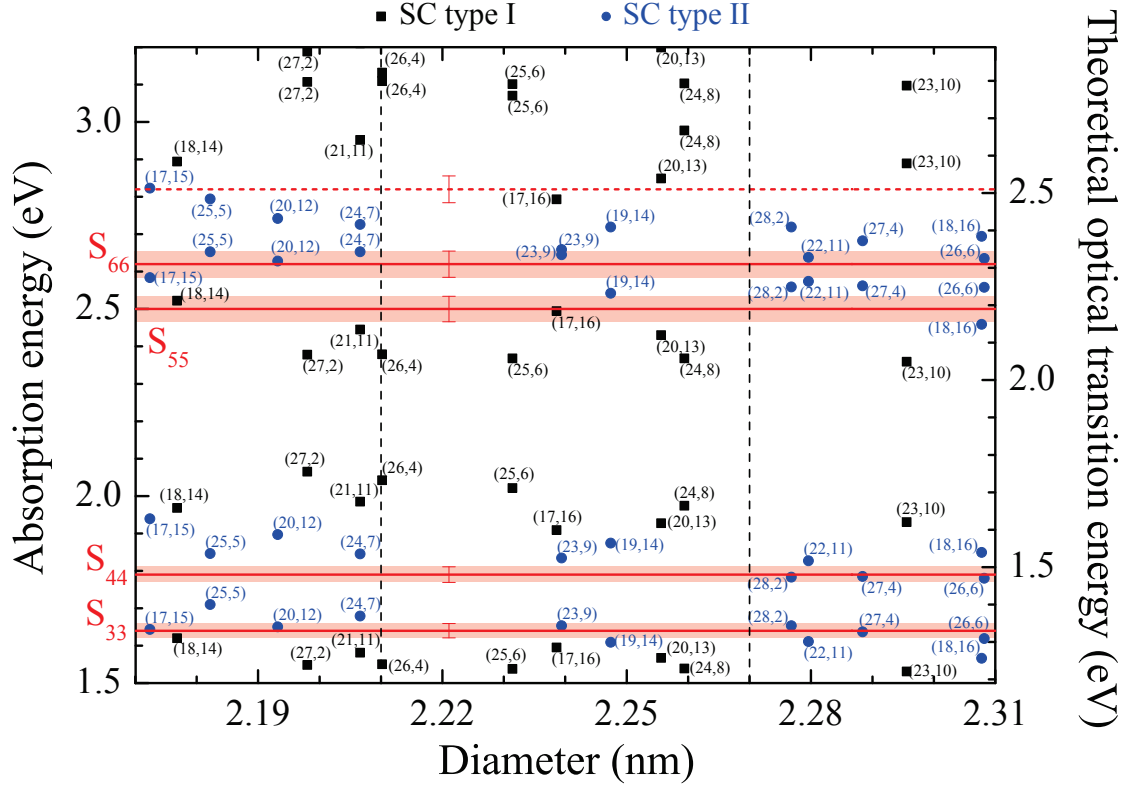


**Figure A.3:** Structure assignment CNT 3 (see Fig. IV.3.a,c for the corresponding absorption and Raman spectra): comparison between measured absorption energies (red lines) and theoretical optical transition energies as a function of nanotube diameter (black squares and blue dots, type I and type II semiconducting nanotubes respectively) The X-scale range corresponds to CNT 3 diameter (see text). Left scale corresponds to the energy in the experimental absorption spectrum and horizontal red bands show absorption peak positions with experimental error bars. Right scale is associated with the transitions calculated in [44] which undergo rigid shift of 0.31 eV. For the sake of clarity, the metallic and zigzag tubes have been removed from the plot.

#### Assignment CNT 4 (Fig. A.4)

The G-band profile of CNT 4 corresponds also to the signature of a chiral semiconducting SWNT. The RBM frequency is measured at  $\omega_{\text{RBM}} = 109 \pm 3 \text{ cm}^{-1}$  independently of excitation energy. The resulting diameter  $d = 2.49 \pm 0.09 \text{ nm}$  provides possible candidates in the range 2.4-2.58 nm (Fig. A.4). Fitting procedure applied to the absorption spectrum (see main text for details) yields energy transitions at 1.65, 1.79, 2.50, and 2.63 eV (Fig. IV.3.b). In fact, the profile of the absorption peak around 2.63 eV can only be reproduced by two Lorentzian functions whereas the feature around 2.80 eV is well fitted with phonon-side band profile. Possible nanotube candidates can be discriminated with respect to the energy difference between the two low energy transitions ( $0.145 \pm 0.045$





# Model for the absorption cross-section

# B

*A quantitative approach to the absorption cross-section of carbon nanotubes is possible by modeling the response of either a dielectric cylinder or a dielectric tube with finite thickness. Although the excitonic absorption features cannot be reproduced, we can estimate the evolution of the  $C_{\text{abs}}$  as a function of different parameters of the nanotubes, e. g. diameter and environment. The first problem is treated within the quasi-static approximation and the second one directly using Mie theory. Both complementary methods provide simple approaches applicable to a large range of nanotube species (small and large diameters, single- and multi-wall tubes). Moreover, optical conductivity  $\sigma_S$  and nanotube frequency dependent dielectric constant  $\varepsilon(\omega)$  are directly related to  $C_{\text{abs}}$ .*

## II–1 Nanowire and hollow cylinder models

### Nanowire

The parallel (perpendicular) absorption cross-section  $C_{\text{abs}}^{\parallel}$  ( $C_{\text{abs}}^{\perp}$ ) are calculated for an infinite cylinder of diameter  $d$  embedded in a dielectric environment (static dielectric permittivity  $\varepsilon_m$  and refractive index  $n_m$ ). An incident electric field  $\mathbf{E}_i$  (frequency  $\omega$ ) is impinging onto the cylinder in the direction perpendicular to its main axis (set  $\theta_{\text{exc}} = 90^\circ$  in Fig. III.17.c, or direction  $\hat{e}_i$  in Fig. III.17.b).  $\mathbf{E}_i$  is linearly polarized either parallel (//) or perpendicular ( $\perp$ ) to the cylinder. In the quasi-static approximation, i. e. under the condition that the  $d \ll \lambda$  ( $\lambda$  the wavelength of the field), the dielectric constant mismatch at the tube/medium interface derives the internal fields:

$$\mathbf{E}_{//} = \mathbf{E}_i, \quad \mathbf{E}_{\perp} = \frac{2\varepsilon_m}{\varepsilon(\omega) + \varepsilon_m} \mathbf{E}_i. \quad (\text{B.1})$$

Using the general expression of  $C_{\text{abs}}$  given in ref. [194], the absorption cross-sections per unit length for parallel and perpendicular polarization read:

$$C_{\text{abs}}^{\parallel} = \frac{\pi d^2 \omega}{4n_m c} 2n_1 n_2 \quad (\text{B.2a})$$

$$C_{\text{abs}}^{\perp} = \frac{\pi d^2 \omega}{4n_m c} n_1 n_2 \left| \frac{2\varepsilon_m}{\varepsilon(\omega) + \varepsilon_m} \right|^2, \quad (\text{B.2b})$$

where  $n_1$  and  $n_2$  stand for the real and imaginary parts of the nanowire's frequency-dependent refractive index. Using the relation between complex refractive index and real conductivity

$$\varepsilon_0(n_1 + in_2)^2 = \text{Re}(\varepsilon(\omega)) + i\frac{4\pi\sigma}{\omega}, \quad (\text{B.3})$$

as well as the sheet conductivity  $\sigma_S = \omega/\pi d$ , the absorption cross-sections per unit length simplify to

$$C_{\text{abs}}^{\parallel} = \frac{\pi d Z_0}{n_m} \sigma_S \quad (\text{B.4a})$$

$$C_{\text{abs}}^{\perp} = \frac{\pi d Z_0}{n_m} \sigma_S \left| \frac{2\varepsilon_m}{\varepsilon(\omega) + \varepsilon_m} \right|^2. \quad (\text{B.4b})$$

The same kind of derivation gives the scattering cross-section for parallel polarization:

$$C_{\text{sca}}^{\parallel} = \frac{\pi^3 d^2 Z_0^2}{2\lambda n_m} \sigma_S, \quad (\text{B.5})$$

where  $\lambda$  is the corresponding light wavelength.

The nanowire model within the quasi-static approximation provides an analytic formula linking absorption cross-section and sheet conductivity of the nanowire.

### **Hollow cylinder**

A more general description is possible using Mie theory applied to a hollow cylinder as discussed partially in Sec. III–2.2. The following analytic derivation is inspired by the book of Bohren and Huffman [124], and details can be found therein.

We consider an infinite hollow cylinder of thickness  $\delta_t$ , and dielectric parameters as mentioned in the previous paragraph. The properties of the incident electric field are identical to the previous paragraph, too. Briefly, the wave equation is expressed in cylindrical coordinates  $(\rho, \phi, z)$ , giving separate solutions  $\psi_n(\rho, \phi) = Z_n(\rho) e^{in\phi}$  ( $Z_n$  solution of Bessel equation,  $n$  integer) that are single-valued functions of  $\phi$ .<sup>a</sup> The electric fields (incident  $\mathbf{E}_i$  and scattered  $\mathbf{E}_s$ ) are expressed on the vector cylindrical harmonics basis which is generated by the functions  $\psi_n(\rho, \phi)$ . Then the boundary conditions at the two interfaces of the hollow cylinder set the relations between  $\mathbf{E}_i$ ,  $\mathbf{E}_s$ , the electric fields inside the dielectric material and in the tube's hole. After some derivations, one can express, in the far field limit, the scattered field as a linear function of the incident one (see relation (III.14)). Both  $T_1$  and  $T_2$  are expressed as a series of the proportionality coefficients of the development of  $\mathbf{E}_s$  on the basis of the vector harmonics (see ref. [124] for details); their general form is given in

$$T_1 = b_0^{\prime\prime} + 2 \sum_{p=1}^{+\infty} b_p^{\prime\prime} (\pm 1)^p, \quad T_2 = a_0^{\perp} + 2 \sum_{p=1}^{+\infty} a_p^{\perp} (\pm 1)^p, \quad (\text{B.6})$$

---

<sup>a</sup>For incident light propagating perpendicular to the tube, the system is invariant with respect to  $z$ , and the problem can be treated in 2D polar coordinates.

with  $+$  and  $-$  standing for detection in the forward or backward direction ( $\phi = 0$  and  $\phi = \pi$  in Fig. III.17.b).  $T_3$  and  $T_4$  are null for incident field propagating perpendicular to the nanotube axis. Then, we consider a cylindrical surface  $S_c$  of radius  $\rho_0 \gg d$  (far-field limit) and length  $L_0$ , centered on the same axis as the tube. For a non-absorbing medium surrounding the hollow cylinder,  $W_{\text{abs}}$  the rate at which energy is absorbed by the tube is proportional to the extinction and scattering rates ( $W_{\text{ext}}$  and  $W_{\text{sca}}$ , respectively):  $W_{\text{abs}} = W_{\text{ext}} + W_{\text{sca}}$ . Integrating the Poynting vectors of the incident and scattering fields over the surface  $S_c$  provide the expressions of the different cross-sections per unit length:

$$C_{\text{ext}}^{\parallel} = \frac{4}{k_1} \left( |b_0^{\parallel}|^2 + 2 \sum_{p=1}^{+\infty} |b_p^{\parallel}|^2 \right) \quad (\text{B.7a})$$

$$C_{\text{sca}}^{\parallel} = \frac{4}{k_1} \text{Re}(T_1) \quad (\text{B.7b})$$

$$C_{\text{ext}}^{\perp} = \frac{4}{k_1} \left( |a_0^{\perp}|^2 + 2 \sum_{p=1}^{+\infty} |a_p^{\perp}|^2 \right) \quad (\text{B.7c})$$

$$C_{\text{sca}}^{\perp} = \frac{4}{k_1} \text{Re}(T_2) \quad (\text{B.7d})$$

$$C_{\text{abs}}^{\parallel} = C_{\text{ext}}^{\parallel} - C_{\text{sca}}^{\parallel} \quad (\text{B.7e})$$

$$C_{\text{abs}}^{\perp} = C_{\text{ext}}^{\perp} - C_{\text{sca}}^{\perp}. \quad (\text{B.7f})$$

The derivation of the parameters  $a_p$  and  $b_p$  is performed numerically. The dielectric and environment parameters are identical to the ones described for the nanowire model (see previous paragraph), except for the refractive index of the medium inside the tube that can be changed (for sake of clarity it is kept to 1 in all the results presented here).<sup>b</sup>

## II-2 Results and interpretation

In this section, we describe some results obtained with the two models presented above. Three different studies are discussed regarding the evolution of the absorption cross-section with respect to the tube diameter, environment, and wall thickness. In all computations, the real part of the dielectric constant and the sheet conductivity of the (hollow) cylinder are set to 1 and  $8.3 \text{ G}_0$ , respectively.<sup>c</sup>

The first two studies focus on the diameter and environment dependence of  $C_{\text{abs}}$  in a SWNT of diameter  $d$ . In the hollow cylinder model, the wall thickness is set to  $0.335 \text{ nm}$ ,

<sup>b</sup>For future calculations, one can think of inserting molecules inside the tube.

<sup>c</sup>The choice of the dielectric constant of the nanotubes has little impact on the outcome of the Mie theory (a recent study yield  $3.5 \pm 0.2$  [56]). Rayleigh experiments estimated an uniform resonance conductivity of  $8.3 \text{ G}_0$  in SWNTs [14, 143].

i. e. the distance between the two planes in bilayer graphene. For parallel polarization, the nanowire model within the quasi-static approximation is exactly equivalent to the Mie theory applied to the tube (Fig. B.1a), in fact the electric field inside the nanotube is equal to the one outside. In other words,  $C_{\text{abs}}^{\parallel}$  and  $C_{\text{sca}}^{\parallel}$  scales as  $d$  (see (B.4a)) and  $d^2$  (see (B.5)), respectively. For SWNT, we observe that  $C_{\text{abs}}^{\parallel}$  is two order of magnitude bigger than  $C_{\text{sca}}^{\parallel}$ . Moreover,  $C_{\text{abs}}^{\perp}$  is one order of magnitude smaller than  $C_{\text{abs}}^{\parallel}$ . These results are in good agreement with our absorption results for free-standing SWNTs.

The effect on the environment is investigated for a SWNT of diameter 1.8 nm (Fig. B.1b). We observe a significant damping of  $C_{\text{abs}}^{\parallel}$  scaling as  $n_m^{-1}$ , while  $C_{\text{abs}}^{\perp}$  slightly increases. Already in water,  $C_{\text{abs}}^{\parallel}$  is divided by almost a factor of two. This graph underlies the importance of controlling the environment of carbon nanotubes to assess their intrinsic absorption cross-section.

The quasi-static approximation is applicable for small-diameter few-wall carbon nanotubes. However, for large-diameter multi-wall nanotubes,  $C_{\text{abs}}$  deviates from the simple scaling  $N\sigma_s$ , where  $N$  is the number of walls (the conductivity of each wall is set to  $8.3 G_0$ ). In the hollow cylinder model each added wall increase the outer radius by 0.335 nm. Fig. B.2 shows the evolution of both  $C_{\text{abs}}$  and  $C_{\text{sca}}$  with respect to the number of walls composing the nanotube (the inner diameter  $d_{\text{in}}$  is kept constant while the outer diameter is  $N$ -dependent). A strong increase of  $C_{\text{abs}}^{\parallel}$  is observed already for tubes with small number of walls ( $< 5$ ), and this effect is enhanced for bigger inner wall diameter (compare open and filled black dots).  $C_{\text{sca}}^{\parallel}$  becomes significant for  $\sim 5 - 10$  walls, which should be then taken into account in the (R)SMS absorption measurements. For large number of walls,  $C_{\text{abs}}^{\parallel}$  and  $C_{\text{sca}}^{\parallel}$  become comparable, as the latter presents stronger  $N$ -dependence. We notice that the optical cross-sections for perpendicular polarization are still one or two order of magnitude smaller, suggesting that strong depolarization are preserved in multi-wall nanotubes.

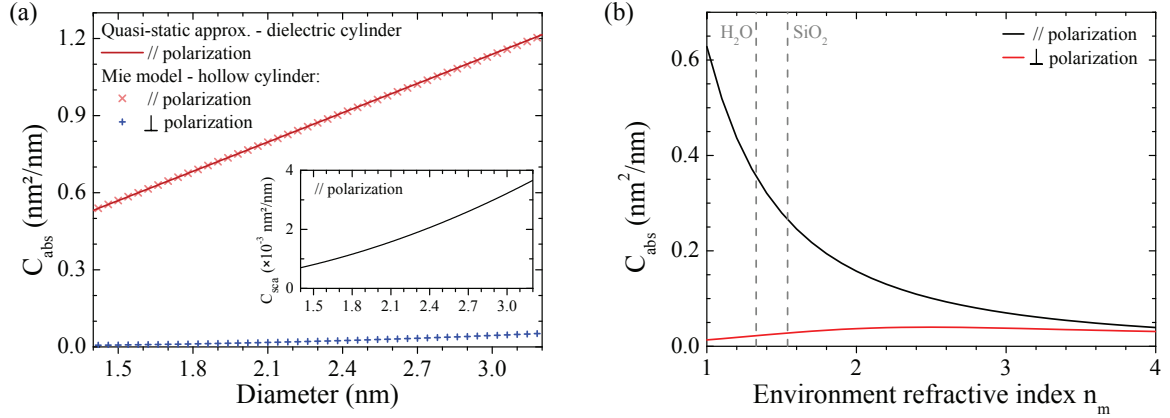


**Figure B.1:** Mie theory model for the absorption cross-section of SWNTs. Nanotubes are modeled as nanowires or hollow cylinder of diameter  $d$ . Computed  $C_{\text{abs}}$  as a function of (a) the diameter ( $n_m = 1$ ) and (b) the environment dielectric constant ( $d = 1.8$  nm). The real part of the dielectric constant and the sheet conductivity of the (hollow) cylinder are set to 1 and  $8.3G_0$ , respectively.

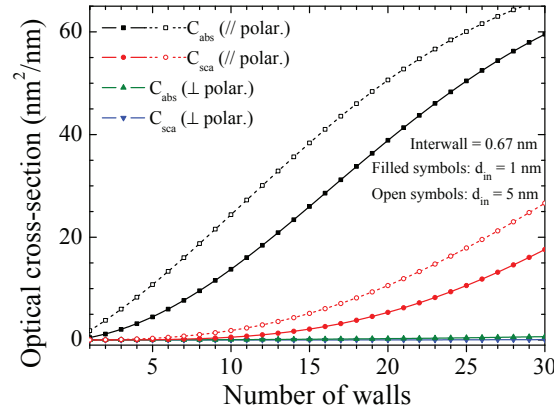


**Figure B.2:** Mie theory of hollow dielectric cylinder: computed absorption and scattering cross-sections *vs.* nanotube's number of walls. The inner diameter of the hollow cylinder is fixed and each wall is added by increasing the outer diameter by 0.67 nm (typical inter-wall distance in CNTs). The real part of the dielectric constant and the sheet conductivity of the (hollow) cylinder are set to 1 and  $8.3 G_0$ , respectively. The environment refractive index is  $n_m = 1$ .





# Absorption of mono- and bi-layers graphene



*Reflective spatial modulation spectroscopy provide direct to the absorption of graphene deposited on opaque substrates. We assessed the visible and near infra-red absorption of both mono- and bi-layer graphene prepared on commercial silicon substrates with a  $\approx 300$  nm layer of silicon oxide. In a first section, we demonstrate the potential of RSMS to image graphene surface and flake interfaces with higher contrast than conventional optical techniques. Preliminary absorption measurements are presented in the second section, as well as a first analysis of the results.*

## III–1 Sample preparation and characterization

Exfoliated graphene was prepared on a silicon wafer coated with a thermally grown  $\text{SiO}_2$  layer of thickness  $312 \pm 3$  nm. Such thickness gives a good visibility of graphene flakes with a conventional optical microscope, allowing identification of few-layer graphene area (see for example Fig. C.1.b, left panel) [35]. Raman spectroscopy and atomic force microscopy identified an isolated monolayer graphene flake ‘M1’ (AFM image presented in Fig. C.1.a, left panel) and a bilayer graphene ‘B2’ close to areas with different few-graphene layers (Fig. C.1.b, left panel).

Fig. C.1.c shows the Raman spectra of both samples. In graphene one observe in-plane two-times degenerated phonon mode (G-band) and inter-valley phonon modes (2D-band). The number of peak contained in the 2D-mode is characteristic of the number of carbon layer. In the 2D-phonon Raman process, a carrier is first scattered from the  $K$  (resp.  $K'$ ) valley to the  $K'$  (resp.  $K$ ) valley by a phonon, and then a defect/impurity induces back-scattering to the initial valley of the graphene band structure. The G-band phonon mode of each flake is observed at  $1582 \text{ cm}^{-1}$  with  $\text{FWHM} \sim 16 \text{ cm}^{-1}$ . Relatively small defect D-band (in comparison to G- and 2D-peaks) is observed for both graphene, suggesting limited environment-induced doping and/or contamination. The 2D-band profile of M1 is reproduced with a single peak at  $\sim 2582 \text{ cm}^{-1}$ , but a shoulder on the right-hand could be attributed to environmental effects, e.g. substrate interactions [99]. On the other hand, the bilayer 2D-phonon mode is characterized by four peaks measured at 2680, 2693, 2712, and  $2730 \text{ cm}^{-1}$  with linewidth  $\sim 25 \text{ cm}^{-1}$ . Additionally, the ratio of the 2D and G bands Raman intensity decreases from 3.5 for M1 to 2.1 for B2, which

confirms the samples assignment to monolayer and bilayer graphene.

Finally, the monolayer graphene flake is imaged with AFM in Fig. C.1.a (left panels). The step in the height profile measures the thickness of M1 ( $\sim 1.4$  nm). In multi-layer graphene, the distance between the carbon planes is around  $\sim 0.335$  nm. However, many AFM studies have shown similar step explained by the presence of a air-water layer in between the graphene and the substrate [195,196].

## **III–2 High-contrast imaging of graphene flakes**

In the past ten years, several production methods have been developed for the fabrication of graphene on-chip opto-electronic devices. They must present high throughput and should be able to prepare high-quality enough graphene for applications, e.g. the number of defect sites should be reduced to preserve the graphene high mobility. In parallel, several characterization and imaging techniques have been applied to the characterization and imaging of graphene. The imaging of the graphene layer would provide precious information about the number of defect/impurity sites (and eventually change in the number of layer) and thus the quality of graphene devices. Main exciting techniques are: optical microscopy (OM), scanning electron microscopy (SEM), and AFM. The first one has poor resolution. SEM can resolve details down to 1 nm but tends to add surface contamination. AFM, in non-contact mode, show highly detailed images of graphene flakes (resolution is limited to the size of the canteliver, see for instance Fig. C.1.a), but is too slow for large-surface rastering. Then, optical techniques should provide non-invasive imaging and faster surface characterization. Here we show that reflective spatial modulation spectroscopy can fulfill these requirements. Example of RSMS surface mapping are presented in Figs. C.1.a,b (right panels) for two different laser wavelengths. Details about spatial modulation and signal detection can be found in Sec. III–2 (modulation amplitude  $\sim 400–500$  nm, modulation frequency  $f = 1.5$  kHz, synchronous detection at  $f$  or  $2f$ ). All graphene flake edges non-parallel to the modulation direction (which is vertical in the images) are clearly resolved in the RSMS images, as well as surface impurities (see bright three peak spots). All AFM and OM surface features, as well as new ones, are observed with higher contrast in the RSMS absorption maps (see dashed lines Figs. C.1.a,b). Moreover, the relative reflectivity measured is of the order of  $10^{-3} - 10^{-2}$  attainable with conventional detection systems. Finally, RSMS allows fast surface rastering (in comparison to AFM for example for equivalent resolution), e.g.  $20\ \mu\text{m} \times 20\ \mu\text{m}$  image with 200 nm pixel spacing can be realized in less than  $\sim 20$  min. In conclusion, RSMS is an absorption-based high-contrast imaging technique for surface characterization of graphene supported on opaque substrates

## **III–3 Absorption spectroscopy**

The absorbance (absorption cross-section per unit of surface) of mono- and bi-layer graphene is measured on the flakes edges. In other words, one satellite peak is absent on

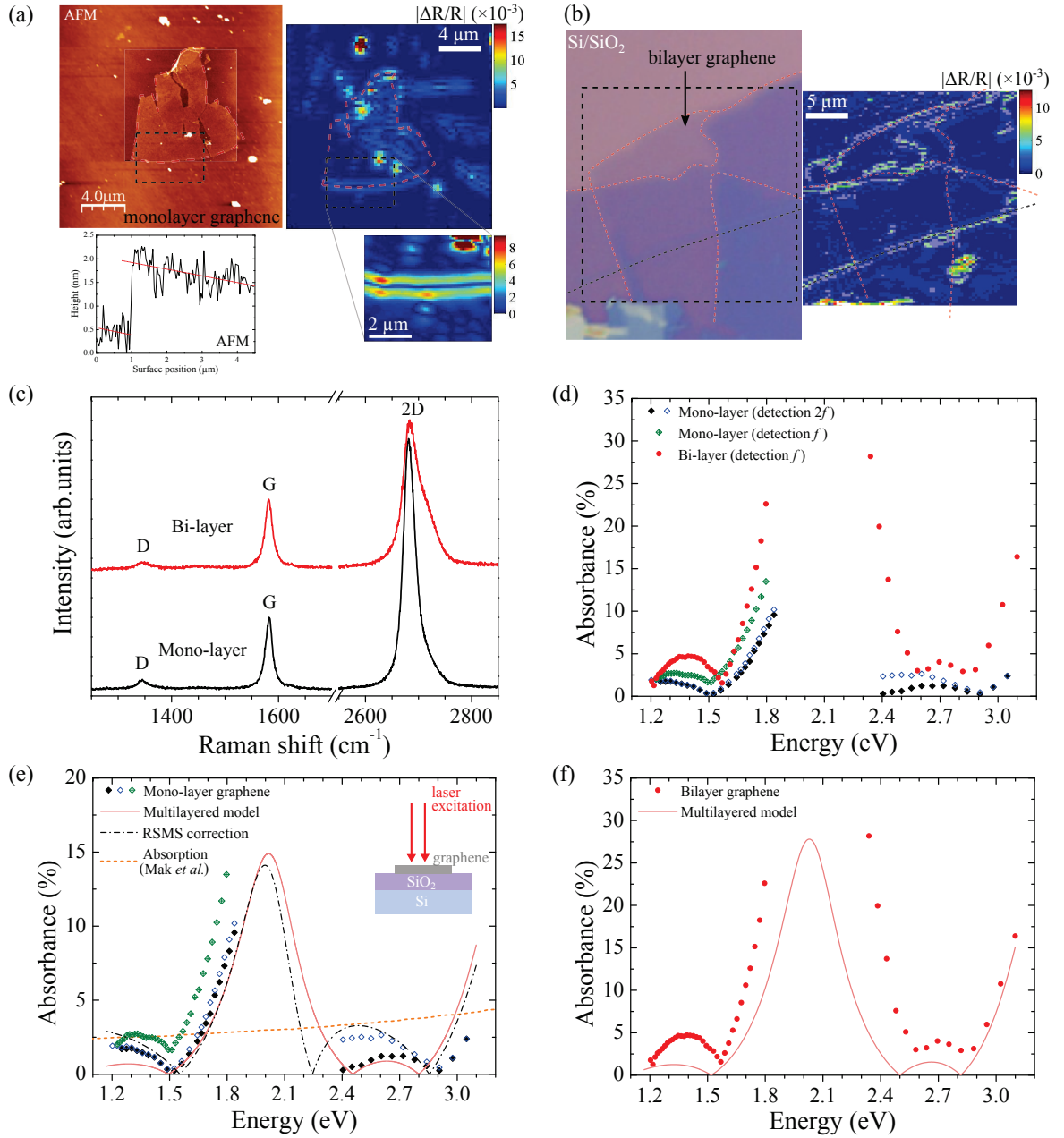


**Figure C.1:** Absorption spectroscopy and imaging of mono- and bi-layer graphene on Si/SiO<sub>2</sub> substrate. (a) AFM and RSMS imaging ( $\lambda = 720$  nm) of monolayer graphene flake. (b) Optical and RSMS imaging ( $\lambda = 530$  nm) of graphene flakes with different layers. Both RSMS maps are acquired for spatial modulation in the vertical direction and horizontal linear polarization. (c) Raman signal of the monolayer and bilayer graphene flakes. (d) Absorbance of graphene for different detection frequency (synchronous detection at  $f$  or  $2f$ ) and different polarization (all data measured for polarization // graphene edge, except empty blue squares for polarization  $\perp$  edge). Orange dashed line is the absorption of graphene on transparent substrate [141]. Modeling of the absorbance of (e) monolayer graphene and (f) bilayer graphene (see text for details).

the RSMS surface mapping when detecting at  $2f$  (each half period the laser spot is almost fully on the graphene, thus showing no modulation in the reflected signal). Therefore, synchronous detection at the modulation frequency seems more adapted for this study. Fig. C.1.d shows the absorbance of the graphene samples in the ranges 1.2-1.8 eV and 2.4-3.1 eV. In comparison to the optical absorption of monolayer graphene measured on transparent substrate (orange dashed curve in Fig. C.1.e) , the signals present strong variations accounted for the multi-layered substrate which induces important changes in the surface local fields depending on the laser energy (understood as Fabry-Pérot effects or modifications of the Fresnel surface coefficients).

### Multi-layered model

The three-layered model (silicon,  $\text{SiO}_2$ , graphene) is sketch on Fig. C.1e (inset). The monolayer (resp. bilayer) graphene thickness is set to 0.335 (resp. 0.67) nm and its complex refractive index is taken from the literature  $2.69 + 1.52i$  (resp.  $2.38 + 1.66i$ ) [35, 195]. The incident laser beam impinges onto the sample normal to the its surface. Mono- and bi-layer graphene computed absorbances are plotted in Fig. C.1.e (light red curve) and Fig. C.1.f, respectively. Both reproduce the general shape of the absorption spectra, but relatively important disagreement between data and model are observed (especially for bilayer graphene).

In the case of monolayer graphene, the three minima and the maxima of the absorption are well reproduced by our model. The differences in energy positions of the minima and amplitude can be accounted by two phenomena not included in our model: the intermediate air/water layer between graphene and substrate [195], and/or the high focusing of the laser beam. The latter introduce some leakage of the initial laser beam polarization to other polarization, as well as some changes in the surface local fields (i.e. , changes in the Fresnel coefficients) [126, 127]. Advance modeling of the surface field and Fresnel coefficients could provide a more accurate description of the results. The complex refractive index of graphene and its energy dependence is still under debate in the literature and introduces another source of uncertainty.

For bilayer graphene, although the multi-layer model is in good agreement with the overall experimental spectrum shape, absorption extrema and amplitude are poorly reproduced. More advanced model including the effects listed above for monolayer graphene could provide a better understanding to the absorption response of bilayer graphene supported on Si/ $\text{SiO}_2$  substrate.

### RSMS correction

In this paragraph, we test a different approach to reproduce the absorbance of monolayer graphene on substrate. The procedure, described in Sec. III–2.2.a, consists in applying corrections to the intrinsic absorption of graphene (measured experimentally on transparent substrates by Mak et al. [141]) according to equation III.16. Data are best reproduced for the complex phase  $\varphi_s \approx 150^\circ$  as shown in Fig. C.1e (black dash-dot curve). However, future improvement to the corrections should include advanced Fresnel coefficients including effects of strong laser beam focusing and possible development of

the correction term to higher order (including scattering fields of higher-order, the model is limited to the first order scattering of the incident beam as shown in Fig. III.16).



# Bibliography

---

- [1] S. Iijima. Helical microtubules of graphitic carbon. *Nature*, 354(6348):56–58, 1991.
- [2] S. Iijima and T. Ichihashi. Single-shell carbon nanotubes of 1-nm diameter. *Nature*, 363(6430):603–605, 1993.
- [3] P. Avouris, J. Appenzeller, R. Martel, and S.J. Wind. Carbon nanotube electronics. *Proc. IEEE*, 91(11):1772–1784, 2003.
- [4] P. Avouris, Z. Chen, and V. Perebeinos. Carbon-based electronics. *Nat. Nano.*, 2(10):605–615, 2007.
- [5] H. Park, A. Afzali, S.-J. Han, G. S. Tulevski, A. D. Franklin, J. Tersoff, J. B. Hannon, and W. Haensch. High-density integration of carbon nanotubes via chemical self-assembly. *Nat. Nano.*, 7(12):787–791, 2012.
- [6] D.-M. Sun, M. Y. Timmermans, A. Kaskela, A. G. Nasibulin, S. Kishimoto, T. Mizutani, E. I. Kauppinen, and Y. Ohno. Mouldable all-carbon integrated circuits. *Nat. Commun.*, 4:2302, 2013.
- [7] P. Avouris, M. Freitag, and V. Perebeinos. Carbon-nanotube photonics and optoelectronics. *Nat. Photon.*, 2(6):341–350, 2008.
- [8] E. Gaufrés, N. Izard, X. Le Roux, D. Marris-Morini, S. Kazaoui, E. Cassan, and L. Vivien. Optical gain in carbon nanotubes. *Appl. Phys. Lett.*, 96(23):231105, 2010.
- [9] S. Berciaud, L. Cognet, P. Poulin, R B. Weisman, and B. Lounis. Absorption spectroscopy of individual single-walled carbon nanotubes. *Nano Lett.*, 7(5):1203–1207, 2007.
- [10] S. Berciaud, C. Voisin, H. Yan, B. Chandra, R. Caldwell, Y. Shan, L. E. Brus, J. Hone, and T. F. Heinz. Excitons and high-order optical transitions in individual carbon nanotubes: A rayleigh scattering spectroscopy study. *Phys. Rev. B*, 81(4):041414, 2010.



- [11] S. Berciaud, V. V. Deshpande, R. Caldwell, Y. Miyauchi, C. Voisin, P. Kim, J. Hone, and T. F. Heinz. All-optical structure assignment of individual single-walled carbon nanotubes from rayleigh and raman scattering measurements. *phys. stat. sol. (b)*, 249(12):2436–2441, 2012.
- [12] D. Christofilos, J.-C. Blancon, J. Arvanitidis, A. San Miguel, A. Ayari, N. Del Fatti, and F. Vallée. Optical imaging and absolute absorption cross section measurement of individual nano-objects on opaque substrates: Single-wall carbon nanotubes on silicon. *J. Phys. Chem. Lett.*, 3(9):1176–1181, 2012.
- [13] G. Dukovic, F. Wang, D. Song, M. Y. Sfeir, T. F. Heinz, and L. E. Brus. Structural dependence of excitonic optical transitions and band-gap energies in carbon nanotubes. *Nano Lett.*, 5(11):2314–2318, 2005.
- [14] D. Y. Joh, J. Kinder, L. H. Herman, S.-Y. Ju, M. A. Segal, J. N. Johnson, K.-L. ChanGarnet, and J. Park. Single-walled carbon nanotubes as excitonic optical wires. *Nat. Nano.*, 6(1):51–56, 2011.
- [15] J Lefebvre and P Finnie. Polarized photoluminescence excitation spectroscopy of single-walled carbon nanotubes. *Phys. Rev. Lett.*, 98(16):167406, 2007.
- [16] K. Liu, J. Deslippe, F. Xiao, R. B Capaz, X. Hong, S. Aloni, A. Zettl, W. Wang, X. Bai, S. G Louie, E. Wang, and F. Wang. An atlas of carbon nanotube optical transitions. *Nat. Nano.*, 7(5):325–329, 2012.
- [17] J. Maultzsch, R. Pomraenke, S. Reich, E. Chang, D. Prezzi, A. Ruini, E. Molinari, M. S. Strano, C. Thomsen, and C. Lienau. Exciton binding energies in carbon nanotubes from two-photon photoluminescence. *Phys. Rev. B*, 72(24):241402, 2005.
- [18] T. Michel, M. Paillet, D. Nakabayashi, M. Picher, V. Jourdain, J. C. Meyer, A. A. Zahab, and J.-L. Sauvajol. Indexing of individual single-walled carbon nanotubes from raman spectroscopy. *Phys. Rev. B*, 80(24):245416, 2009.
- [19] M Paillet, T M., J C Meyer, V N Popov, L Henrard, S Roth, and J-L Sauvajol. Raman active phonons of identified semiconducting single-walled carbon nanotubes. *Phys. Rev. Lett.*, 96(25):257401, 2006.
- [20] M. Y. Sfeir, T. Beetz, F. Wang, Limin Huang, X. M. Henry Huang, M. Huang, J. Hone, S. O’Brien, J. A. Misewich, T. F. Heinz, Lijun Wu, Yimei Zhu, and L. E. Brus. Optical spectroscopy of individual single-walled carbon nanotubes of defined chiral structure. *Science*, 312(5773):554–556, 2006.
- [21] F. Wang, G. Dukovic, L. E Brus, and T. F Heinz. The optical resonances in carbon nanotubes arise from excitons. *Science*, 308(5723):838–841, 2005.
- [22] S. Berciaud, L. Cognet, and B. Lounis. Luminescence decay and the absorption cross section of individual single-walled carbon nanotubes. *Phys. Rev. Lett.*, 101(7):077402, 2008.

- 
- [23] D. Wang, M. T. Carlson, and H. H. Richardson. Absorption cross section and interfacial thermal conductance from an individual optically excited single-walled carbon nanotube. *ACS Nano*, 5(9):7391–7396, 2011.
- [24] M. M. J. Treacy, T. W. Ebbesen, and J. M. Gibson. Exceptionally high young’s modulus observed for individual carbon nanotubes. *Nature*, 381(6584):678–680, 1996.
- [25] C. Caillier, A. Ayari, V. Gouttenoire, A. San Miguel, V. Jourdain, M. Picher, and J.-L. Sauvajol. Gold contact to individual metallic carbon nanotubes: A sensitive nanosensor for high-pressure. *Appl. Phys. Lett.*, 97(17):173111, 2010.
- [26] C. Caillier, A. Ayari, V. Gouttenoire, J.-M. Benoit, V. Jourdain, M. Picher, M. Paillet, Sylvie Le Floch, S. T. Purcell, J.-L. Sauvajol, and A. San Miguel. An individual carbon nanotube transistor tuned by high pressure. *Adv. Funct. Mater.*, 20(19):3330–3335, 2010.
- [27] A. San Miguel, C. Cailler, D. Machon, E. B. Barros, A. L. Aguiar, and A. G. Souza Filho. Carbon nanotubes under high pressure probed by resonance raman scattering. In Elena Boldyreva and Przemyslaw Dera, editors, *High-Pressure Crystallography*, NATO Science for Peace and Security Series B: Physics and Biophysics, pages 435–446. Springer Netherlands, 2010.
- [28] C. A. Kuntscher, K. Thirunavukkuarasu, À. Pekker, K. Kamaràs, F. Hennrich, M. Kappes, and Y. Iwasa. Pressure-induced phenomena in single-walled carbon nanotubes. *phys. stat. sol. (b)*, 244(11):3982–3985, 2007.
- [29] W. Shan, J. Wu, W. Walukiewicz, J. W. Ager, K. M. Yu, E. E. Haller, K. Kissell, S. M. Bachilo, R. B. Weisman, and R. E. Smalley. Pressure dependence of optical transitions in semiconducting single-walled carbon nanotubes. *phys. stat. sol. (b)*, 241(14):3367–3373, 2004.
- [30] T. Hertel, R. E. Walkup, and P. Avouris. Deformation of carbon nanotubes by surface van der waals forces. *Phys. Rev. B*, 58:13870–13873, 1998.
- [31] Y. Y. Jiang, W. Zhou, T. Kim, Y. Huang, and J. M. Zuo. Measurement of radial deformation of single-wall carbon nanotubes induced by intertube van der waals forces. *Phys. Rev. B*, 77:153405, 2008.
- [32] J. Wu, W. Walukiewicz, W. Shan, E. Bourret-Courchesne, J. W. Ager, K. M. Yu, E. E. Haller, Kyle Kissell, S. M. Bachilo, R. B. Weisman, and R. E. Smalley. Structure-dependent hydrostatic deformation potentials of individual single-walled carbon nanotubes. *Phys. Rev. Lett.*, 93:017404, 2004.
- [33] S. Reich, S. Maultzsch, and Thomsen. *Carbon Nanotubes: Basic Concepts and Physical Properties*. Wiley-VCH, 2004.

- [34] R. Saito, G. Dresselhaus, and M.S. Dresselhaus. *Physical Properties of Carbon Nanotube*. Imperial College Press, 1998.
- [35] K. S. Novoselov, A. K. Geim, S. V. Morozov, D. Jiang, Y. Zhang, S. V. Dubonos, I. V. Grigorieva, and A. A. Firsov. Electric field effect in atomically thin carbon films. *Science*, 306(5696):666–669, 2004.
- [36] R. S. Ruoff, J. Tersoff, D. C. Lorents, S. Subramoney, and B. Chan. Radial deformation of carbon nanotubes by van der waals forces. *Nature*, 364(6437):514–516, 1993.
- [37] R. Saito, A. Grüneis, G.G. Samsonidze, G. Dresselhaus, M.S. Dresselhaus, A. Jorio, L.G. Cançado, M.A. Pimenta, and A.G. Souza Filho. Optical absorption of graphite and single-wall carbon nanotubes. *Appl. Phys. A*, 78(8):1099–1105, 2004.
- [38] J.-C. Charlier, X. Blase, and S. Roche. Electronic and transport properties of nanotubes. *Rev. Mod. Phys.*, 79:677–732, 2007.
- [39] T. W. Odom, J.-L. Huang, P. Kim, and C. M. Lieber. Atomic structure and electronic properties of single-walled carbon nanotubes. *Nature*, 391(6662):62–64, 1998.
- [40] J. W. G. Wilder, L. C. Venema, A. G. Rinzler, R. E. Smalley, and C. Dekker. Electronic structure of atomically resolved carbon nanotubes. *Nature*, 391(6662):59–62, 1998.
- [41] H. Kataura, Y. Kumazawa, Y. Maniwa, I. Umez, S. Suzuki, Y. Ohtsuka, and Y. Achiba. Optical properties of single-wall carbon nanotubes. *Synt. Met.*, 103(1-3):2555–2558, 1999.
- [42] C. F. Klingshirn. *Semiconductor Optics*. Springer, 1997.
- [43] E. B. Barros, A. Jorio, G. G. Samsonidze, R. B. Capaz, A. G. Souza Filho, J. M. Mendes Filho, G. Dresselhaus, and M. S. Dresselhaus. Review on the symmetry-related properties of carbon nanotubes. *Phys. Rep.*, 431(6):261–302, 2006.
- [44] V. N Popov. Curvature effects on the structural, electronic and optical properties of isolated single-walled carbon nanotubes within a symmetry-adapted non-orthogonal tight-binding model. *New J. Phys.*, 6:17, 2004.
- [45] H. Ajiki. Exciton states and optical properties of carbon nanotubes. *J. Phys. Cond. Matt.*, 24(48):483001, 2012.
- [46] H. Ajiki and T. Ando. Aharonov-bohm effect in carbon nanotubes. *Physica B*, 201(0):349 – 352, 1994.
- [47] L. X. Benedict, S. G. Louie, and M. L. Cohen. Static polarizabilities of single-wall carbon nanotubes. *Phys. Rev. B*, 52:8541–8549, 1995.

- 
- [48] M. F. Islam, D. E. Milkie, C. L. Kane, A. G. Yodh, and J. M. Kikkawa. Direct measurement of the polarized optical absorption cross section of single-wall carbon nanotubes. *Phys. Rev. Lett.*, 93(3):037404, 2004.
- [49] M. Y Sfeir, F. Wang, Limin Huang, Chia-Chin Chuang, J Hone, S. P O'brien, T. F Heinz, and L. E Brus. Probing electronic transitions in individual carbon nanotubes by rayleigh scattering. *Science*, 306(5701):1540–1543, 2004.
- [50] Y. Miyauchi, H. Ajiki, and S. Maruyama. Electron-hole asymmetry in single-walled carbon nanotubes probed by direct observation of transverse quasidark excitons. *Phys. Rev. B*, 81(12):121415, 2010.
- [51] S. Uryu and T. Ando. Exciton absorption of perpendicularly polarized light in carbon nanotubes. *Phys. Rev. B*, 74:155411, 2006.
- [52] Z. Wang, H. Zhao, and S. Mazumdar.  $\pi$ -electron theory of transverse optical excitons in semiconducting single-walled carbon nanotubes. *Phys. Rev. B*, 76:115431, 2007.
- [53] S. Kilina, S. Tretiak, S. K. Doorn, Z. Luo, F. Papadimitrakopoulos, A. Piryatinski, Avadh Saxena, and A. R. Bishop. Cross-polarized excitons in carbon nanotubes. *PNAS*, 105(19):6797–6802, 2008.
- [54] S. Uryu and T. Ando. Effect of electron-hole asymmetry on cross-polarized excitons in carbon nanotubes. *Phys. Rev. B*, 83:085404, 2011.
- [55] A. W. Tsen, Luke A. K. Donev, H. Kurt, L. H. Herman, and J. Park. Imaging the electrical conductance of individual carbon nanotubes with photothermal current microscopy. *Nat. Nano.*, 4(2):108–113, 2009.
- [56] M. Barkelid, G. A. Steele, and V. Zwiller. Probing optical transitions in individual carbon nanotubes using polarized photocurrent spectroscopy. *Nano Lett.*, 12(11):5649–5653, 2012.
- [57] S. Uryu and T. Ando. Environment effect on cross-polarized excitons in carbon nanotubes. *Phys. Rev. B*, 86(12):125412, 2012.
- [58] A. M. Rao, E. Richter, Shunji Bandow, B. Chase, P. C. Eklund, K. A. Williams, S. Fang, K. R. Subbaswamy, M. Menon, A. Thess, R. E. Smalley, G. Dresselhaus, and M. S. Dresselhaus. Diameter-selective raman scattering from vibrational modes in carbon nanotubes. *Science*, 275(5297):187–191, 1997.
- [59] S. M. Bachilo, M. S. Strano, C. Kittrell, R. H. Hauge, R. E. Smalley, and R. B. Weisman. Structure-assigned optical spectra of single-walled carbon nanotubes. *Science*, 298(5602):2361–2366, 2002.

- [60] M. J. O’Connell, S. M. Bachilo, C. B. Huffman, V. C. Moore, M. S. Strano, E. H. Haroz, K. L. Rialon, P. J. Boul, W. H. Noon, C. Kittrell, J. Ma, R. H. Hauge, R. B. Weisman, and R. E. Smalley. Band gap fluorescence from individual single-walled carbon nanotubes. *Science*, 297(5581):593–596, 2002.
- [61] R. Saito, G. Dresselhaus, and M. S. Dresselhaus. Trigonal warping effect of carbon nanotubes. *Phys. Rev. B*, 61:2981–2990, 2000.
- [62] S. K. Doorn, P. T. Araujo, K. Hata, and A. Jorio. Excitons and exciton-phonon coupling in metallic single-walled carbon nanotubes: Resonance raman spectroscopy. *Phys. Rev. B*, 78(16):165408, 2008.
- [63] R. B. Weisman and S. M. Bachilo. Dependence of optical transition energies on structure for single-walled carbon nanotubes in aqueous suspension: An empirical kataura plot. *Nano Lett.*, 3(9):1235–1238, 2003.
- [64] C. L. Kane and E. J. Mele. Electron interactions and scaling relations for optical excitations in carbon nanotubes. *Phys. Rev. Lett.*, 93(19):197402, 2004.
- [65] C. L. Kane and E. J. Mele. Ratio problem in single carbon nanotube fluorescence spectroscopy. *Phys. Rev. Lett.*, 90:207401, 2003.
- [66] V. Perebeinos, J. Tersoff, and P. Avouris. Scaling of excitons in carbon nanotubes. *Phys. Rev. Lett.*, 92(25):257402, 2004.
- [67] C. D. Spataru, S. Ismail-Beigi, L. X. Benedict, and S. G. Louie. Excitonic effects and optical spectra of single-walled carbon nanotubes. *Phys. Rev. Lett.*, 92:077402, 2004.
- [68] L. Lüer, S. Hoseinkhani, D. Polli, J. Crochet, T. Hertel, and G. Lanzani. Size and mobility of excitons in (6, 5) carbon nanotubes. *Nat. Phys.*, 5(1):54–58, 2009.
- [69] T. Ando. Excitons in carbon nanotubes. *Jpn. J. Appl. Phys.*, 66(4):1066–1073, 1997.
- [70] A. R. T. Nugraha, R. Saito, K. Sato, P. T. Araujo, A. Jorio, and M. S. Dresselhaus. Dielectric constant model for environmental effects on the exciton energies of single wall carbon nanotubes. *Appl. Phys. Lett.*, 97(9):91905, 2010.
- [71] E. Malić, M. Hirschulz, F. Milde, M. Richter, J. Maultzsch, S. Reich, and A. Knorr. Coulomb effects in single-walled carbon nanotubes. *phys. stat. sol. (b)*, 245(10):2155–2158, 2008.
- [72] J. Lefebvre and P. Finnie. Excited excitonic states in single-walled carbon nanotubes. *Nano Lett.*, 8(7):1890–1895, 2008.
- [73] E. Malić, J. Maultzsch, S. Reich, and A. Knorr. Excitonic rayleigh scattering spectra of metallic single-walled carbon nanotubes. *Phys. Rev. B*, 82:115439, 2010.

- 
- [74] E. Verdenhalven and E. Malié. Excitonic absorption intensity of semiconducting and metallic carbon nanotubes. *J. Phys. Cond. Matt.*, 25(24):245302, 2013.
- [75] M. S. Dresselhaus, G. Dresselhaus, R. Saito, and A. Jorio. Exciton photophysics of carbon nanotubes. *Annu. Rev. Phys. Chem.*, 58(1):719–747, 2007.
- [76] S. Tretiak. Triplet state absorption in carbon nanotubes:a td-dft study. *Nano Lett.*, 7(8):2201–2206, 2007.
- [77] R. Matsunaga, K. Matsuda, and Y. Kanemitsu. Optical spectroscopy of dark excitons and trions in carbon nanotubes. In *4th Workshop on Nanotube Optics and Nanospectroscopy (WONTON’11)*, 2011.
- [78] R. B. Capaz, C. D. Spataru, S. Ismail-Beigi, and S. G. Louie. Diameter and chirality dependence of exciton properties in carbon nanotubes. *Phys. Rev. B*, 74(12):121401, 2006.
- [79] R. Matsunaga, K. Matsuda, and Y. Kanemitsu. Evidence for dark excitons in a single carbon nanotube due to the aharonov-bohm effect. *Phys. Rev. Lett.*, 101:147404, 2008.
- [80] A. Srivastava, H. Htoon, V. I. Klimov, and J. Kono. Direct observation of dark excitons in individual carbon nanotubes: Inhomogeneity in the exchange splitting. *Phys. Rev. Lett.*, 101:087402, 2008.
- [81] C. Voisin, S. Berger, S. Berciaud, H. Yan, J.-S. Lauret, G. Cassabois, P. Roussignol, J. Hone, and T. F. Heinz. Excitonic signatures in the optical response of single-wall carbon nanotubes. *phys. stat. sol. (b)*, 249(5):900–906, 2012.
- [82] T. Gokus, L. Cognet, J. G. Duque, M. Pasquali, A. Hartschuh, and B. Lounis. Mono- and biexponential luminescence decays of individual single-walled carbon nanotubes. *J. Phys. Chem. C*, 114(33):14025–14028, 2010.
- [83] S. Cambré, S. M. Santos, W. Wenseleers, A. R. T. Nugraha, R. Saito, L. Cognet, and B. Lounis. Luminescence properties of individual empty and water-filled single-walled carbon nanotubes. *ACS Nano*, 6(3):2649–2655, 2012.
- [84] J. Jiang, R. Saito, Ge. G. Samsonidze, A. Jorio, S. G. Chou, G. Dresselhaus, and M. S. Dresselhaus. Chirality dependence of exciton effects in single-wall carbon nanotubes: Tight-binding model. *Phys. Rev. B*, 75:035407, 2007.
- [85] K. Sato, R. Saito, J. Jiang, G. Dresselhaus, and M.S. Dresselhaus. Chirality dependence of many body effects of single wall carbon nanotubes. *Vib. Spectro.*, 45(2):89–94, 2007.
- [86] A. G. Walsh, A. N. Vamivakas, Y. Yin, S. B. Cronin, M. S. ünlü, B. B. Goldberg, and A. K. Swan. Screening of excitons in single, suspended carbon nanotubes. *Nano Lett.*, 7(6):1485–1488, 2007.



- [87] H. Lin, J. Lagoute, V. Repain, C. Chacon, Y. Girard, J.-S. Lauret, F. Ducastelle, A. Loiseau, and S. Rousset. Many-body effects in electronic bandgaps of carbon nanotubes measured by scanning tunnelling spectroscopy. *Nat. Mater.*, 9(3):235–238, 2010.
- [88] P. T. Araujo, S. K. Doorn, S. Kilina, S. Tretiak, E. Einarsson, S. Maruyama, H. Chacham, M. A. Pimenta, and A. Jorio. Third and fourth optical transitions in semiconducting carbon nanotubes. *Phys. Rev. Lett.*, 98:067401, 2007.
- [89] T. Michel, M. Paillet, J. C. Meyer, V. N. Popov, L. Henrard, and J.-L. Sauvajol.  $E_{33}$  and  $E_{44}$  optical transitions in semiconducting single-walled carbon nanotubes: Electron diffraction and raman experiments. *Phys. Rev. B*, 75:155432, 2007.
- [90] K. Sato, R. Saito, J. Jiang, G. Dresselhaus, and M. S. Dresselhaus. Discontinuity in the family pattern of single-wall carbon nanotubes. *Phys. Rev. B*, 76:195446, 2007.
- [91] P. T. Araujo, A. Jorio, M. S. Dresselhaus, K. Sato, and R. Saito. Diameter dependence of the dielectric constant for the excitonic transition energy of single-wall carbon nanotubes. *Phys. Rev. Lett.*, 103:146802, 2009.
- [92] J. Lefebvre, J. M. Fraser, P. Finnie, and Y. Homma. Photoluminescence from an individual single-walled carbon nanotube. *Phys. Rev. B*, 69(7):075403, 2004.
- [93] J.-S. Lauret, C. Voisin, G. Cassaboiss, C. Delalande, P. Roussignol, O. Jost, and L. Capes. Ultrafast carrier dynamics in single-wall carbon nanotubes. *Phys. Rev. Lett.*, 90:057404, 2003.
- [94] C. Manzoni, A. Gambetta, E. Menna, M. Meneghetti, G. Lanzani, and G. Cerullo. Intersubband exciton relaxation dynamics in single-walled carbon nanotubes. *Phys. Rev. Lett.*, 94:207401, 2005.
- [95] F. Wang, D. J. Cho, B. Kessler, J. Deslippe, P. J. Schuck, S. G. Louie, A. Zettl, T. F. Heinz, and Y. R. Shen. Observation of excitons in one-dimensional metallic single-walled carbon nanotubes. *Phys. Rev. Lett.*, 99(22):227401, 2007.
- [96] S.K. Choi, J. Deslippe, R. B. Capaz, and S. G. Louie. An explicit formula for optical oscillator strength of excitons in semiconducting single-walled carbon nanotubes: Family behavior. *Nano Lett.*, 13(1):54–58, 2013.
- [97] J. Lefebvre, J.M. Fraser, Y. Homma, and P. Finnie. Photoluminescence from single-walled carbon nanotubes: a comparison between suspended and micelle-encapsulated nanotubes. *Appl. Phys. A*, 78(8):1107–1110, 2004.
- [98] M.S. Dresselhaus, G. Dresselhaus, R. Saito, and A. Jorio. Raman spectroscopy of carbon nanotubes. *Phys. Rep.*, 409(2):47–99, 2005.



- 
- [99] R. Saito, M. Hofmann, G. Dresselhaus, A. Jorio, and M. S. Dresselhaus. Raman spectroscopy of graphene and carbon nanotubes. *Adv. Phys.*, 60(3):413–550, 2011.
- [100] C. Fantini, A. Jorio, M. Souza, M. S. Strano, M. S. Dresselhaus, and M. A. Pimenta. Optical transition energies for carbon nanotubes from resonant raman spectroscopy: Environment and temperature effects. *Phys. Rev. Lett.*, 93:147406, 2004.
- [101] H. Telg, J. Maultzsch, S. Reich, F. Hennrich, and C. Thomsen. Chirality distribution and transition energies of carbon nanotubes. *Phys. Rev. Lett.*, 93(17):177401, 2004.
- [102] J. U. Lee, P. P. Gipp, and C. M. Heller. Carbon nanotube p-n junction diodes. *Appl. Phys. Lett.*, 85(1):145–147, 2004.
- [103] M. Zheng and B. A. Diner. Solution redox chemistry of carbon nanotubes. *J. Am. Chem. Soc.*, 126(47):15490–15494, December 2004.
- [104] A. Débarre, M. Kobylko, A. M. Bonnot, A. R., V. N. Popov, L. Henrard, and M. Kociak. Electronic and mechanical coupling of carbon nanotubes: A tunable resonant raman study of systems with known structures. *Phys. Rev. Lett.*, 101:197403, 2008.
- [105] J. C. Meyer, M. Paillet, Thierry M., A. Moréac, A. Neumann, G. S. Duesberg, S. Roth, and J.-L. Sauvajol. Raman modes of index-identified freestanding single-walled carbon nanotubes. *Phys. Rev. Lett.*, 95:217401, 2005.
- [106] F. Schöppler, C. Mann, T. C. Hain, F. M. Neubauer, G. Privitera, F. Bonaccorso, D. Chu, A. C. Ferrari, and T. Hertel. Molar extinction coefficient of single-wall carbon nanotubes. *J. Phys. Chem. C*, 115(30):14682–14686, 2011.
- [107] L. Oudjedi, G. Parra-Vasquez, A. and Nicholas, A. G. Godin, L. Cognet, and B. Lounis. Metrological investigation of the (6,5) carbon nanotube absorption cross section. *J. Phys. Chem. Lett.*, 4(9):1460–1464, 2013.
- [108] C. Roquelet, D. Garrot, J. S. Lauret, C. Voisin, V. Alain-Rizzo, P. Roussignol, J. A. Delaire, and E. Deleporte. Quantum efficiency of energy transfer in noncovalent carbon nanotube/porphyrin compounds. *Appl. Phys. Lett.*, 97(14):141918, 2010.
- [109] F. Vialla, C. Roquelet, B. Langlois, G. Delport, S. M. Santos, J.-S. Lauret, and C. Voisin. Chirality dependence of the absorption cross-section of carbon nanotubes revealed by energy transfer in nanotube/porphyrin compounds. In *5th Workshop on Nanotube Optics and Nanospectroscopy (WONTON'13)*, 2013.
- [110] Y. Oyama, R. Saito, K. Sato, J. Jiang, G. G. Samsonidze, A. Grüneis, Y. Miyauchi, S. Maruyama, A. Jorio, G. Dresselhaus, and M.S. Dresselhaus. Photoluminescence intensity of single-wall carbon nanotubes. *Carbon*, 44(5):873 – 879, 2006.

- [111] R. B. Weisman. New methods for measuring swent basic photophysical properties. In *5th Workshop on Nanotube Optics and Nanospectroscopy (WONTON'13)*, 2013.
- [112] K. Liu, X. Hong, and F. Wang. Towards seeing and identifying individual carbon nanotubes in device by light microscopy. In *5th Workshop on Nanotube Optics and Nanospectroscopy (WONTON'13)*, 2013.
- [113] Y. Ohno, S. Maruyama, and T. Mizutani. Environmental effects on photoluminescence of single-walled carbon nanotubes. In Jose M. Marulanda, editor, *Carbon Nanotubes*. InTech, 2010.
- [114] M. Steiner, M. Freitag, J. C. Tsang, V. Perebeinos, A. A. Bol, A. V. Failla, and P. Avouris. How does the substrate affect the raman and excited state spectra of a carbon nanotube? *Appl. Phys. A*, 96(2):271–282, 2009.
- [115] R. Arenal, P. Lothman, M. Picher, T. Than, M. Paillet, and V. Jourdain. Direct evidence of atomic structure conservation along ultra-long carbon nanotubes. *J. Phys. Chem. C*, 116(26):14103–14107, 2012.
- [116] D. Levshov, T. X. Than, R. Arenal, V. N. Popov, R. Parret, M. Paillet, V. Jourdain, A. A. Zahab, T. M., Yu. I. Yuzuyuk, and J.-L. Sauvajol. Experimental evidence of a mechanical coupling between layers in an individual double-walled carbon nanotube. *Nano Lett.*, 11(11):4800–4804, 2011.
- [117] T. X. Tinh, N. Van Chuc, V. Jourdain, M. Paillet, D.-Y. Kim, J.-L. Sauvajol, N. T. T. Tam, and P. N. Minh. Synthesis of individual ultra-long carbon nanotubes and transfer to other substrates. *J. Exp. Nano.*, 6(5):547–556, 2011.
- [118] T. W. Ebbesen and P. M. Ajayan. Large-scale synthesis of carbon nanotubes. *Nature*, 358(6383):220–222, 1992.
- [119] A. Thess, R. Lee, P. Nikolaev, H. Dai, P. Petit, J. Robert, C. Xu, Y. H. Lee, S. G. Kim, A. G. Rinzler, D. T. Colbert, G. E. Scuseria, D. Tománek, J. E. Fischer, and R. E. Smalley. Crystalline ropes of metallic carbon nanotubes. *Science*, 273(5274):483–487, 1996.
- [120] P. Nikolaev, M. J Bronikowski, R. Kelley Bradley, F. Rohmund, D. T Colbert, K.A Smith, and R. E Smalley. Gas-phase catalytic growth of single-walled carbon nanotubes from carbon monoxide. *Chem. Phys. Lett.*, 313(1-2):91–97, 1999.
- [121] A. Arbouet, D. Christofilos, N. Del Fatti, F. Vallée, J. R. Huntzinger, L. Arnaud, P. Billaud, and M. Broyer. Direct measurement of the single-metal-cluster optical absorption. *Phys. Rev. Lett.*, 93(12):127401, 2004.
- [122] V. Juvé, M. F. Cardinal, A. Lombardi, A. Crut, P. Maioli, J. Pérez-Juste, L. M. Liz-Marzà, N. Del Fatti, and F. Vallée. Size-dependent surface plasmon resonance broadening in nonspherical nanoparticles: Single gold nanorods. *Nano Lett.*, 0(0):null, 2013.

- 
- [123] A. Lombardi, M. P. Grzelczak, A. Crut, P. Maioli, I Pastoriza-Santos, L. M. Liz-Marzà, N. Del Fatti, and F. Vallée. Optical response of individual au-ag@sio<sub>2</sub> heterodimers. *ACS Nano*, 7(3):2522–2531, 2013.
- [124] C. F. Bohren and D. R. Huffman. *Absorption and Scattering of Light by Small Particles*. Wiley-VCH, 1998.
- [125] B. E. A. Saleh and M. C. Teich. *Fundamentals of Photonics*, pages 644–695. John Wiley & Sons, Inc., 2001.
- [126] L. H. Herman, C.-J. Kim, Z. Wang, M.-H. Jo, and J. Park. Depolarization effect in optical absorption measurements of one- and two-dimensional nanostructures. *Appl. Phys. Lett.*, 101(12):123102, 2012.
- [127] L. Novotny and B. Hecht. *Principles of nano-optics*. Cambridge University Press, 2006.
- [128] C. Biswas and Y. H. Lee. Graphene versus carbon nanotubes in electronic devices. *Adv. Funct. Mater.*, 21(20):3806–3826, 2011.
- [129] V. Perebeinos, J. Tersoff, and P. Avouris. Effect of exciton-phonon coupling in the calculated optical absorption of carbon nanotubes. *Phys. Rev. Lett.*, 94(2):027402, 2005.
- [130] F. Plentz, H. B. Ribeiro, A. Jorio, M. S. Strano, and M. A. Pimenta. Direct experimental evidence of exciton-phonon bound states in carbon nanotubes. *Phys. Rev. Lett.*, 95:247401, 2005.
- [131] Y. Miyauchi and S. Maruyama. Identification of an excitonic phonon sideband by photoluminescence spectroscopy of single-walled carbon-13 nanotubes. *Phys. Rev. B*, 74:035415, 2006.
- [132] O. N. Torrens, M. Zheng, and J. M. Kikkawa. Energy of k-momentum dark excitons in carbon nanotubes by optical spectroscopy. *Phys. Rev. Lett.*, 101(15):157401, 2008.
- [133] Y. Murakami, B. Lu, S. Kazaoui, N. Minami, T. Okubo, and S. Maruyama. Photoluminescence sidebands of carbon nanotubes below the bright singlet excitonic levels. *Phys. Rev. B*, 79:195407, 2009.
- [134] R. Matsunaga, K. Matsuda, and Y. Kanemitsu. Origin of low-energy photoluminescence peaks in single carbon nanotubes: K-momentum dark excitons and triplet dark excitons. *Phys. Rev. B*, 81(3):033401, 2010.
- [135] P. M. Vora, X. Tu, E. J. Mele, M. Zheng, and J. M. Kikkawa. Chirality dependence of the k-momentum dark excitons in carbon nanotubes. *Phys. Rev. B*, 81(15):155123, 2010.

- [136] V. N. Popov and P. Lambin. Resonant raman intensity of the totally symmetric phonons of single-walled carbon nanotubes. *Phys. Rev. B*, 73(16):165425, 2006.
- [137] R. W. Havener, A. W. Tsen, H. C. Choi, and J. Park. Laser-based imaging of individual carbon nanostructures. *NPG Asia Mater.*, 3(10):91–99, 2011.
- [138] T. Ando, Y. Zheng, and H. Suzuura. Dynamical conductivity and zero-mode anomaly in honeycomb lattices. *J. Phys. Soc. Jpn.*, 71(5):1318–1324, 2002.
- [139] K. F. Mak, M. Y. Sfeir, Y. Wu, Chun Hung Lui, J. A. Misewich, and T. F. Heinz. Measurement of the optical conductivity of graphene. *Phys. Rev. Lett.*, 101:196405, 2008.
- [140] R. R. Nair, P. Blake, A. N. Grigorenko, K. S. Novoselov, T. J. Booth, T. Stauber, N. M. R. Peres, and A. K. Geim. Fine structure constant defines visual transparency of graphene. *Science*, 320(5881):1308–1308, 2008.
- [141] K. F. Mak, L. Ju, F. Wang, and T. F. Heinz. Optical spectroscopy of graphene: From the far infrared to the ultraviolet. *Solid State Commun.*, 152(15):1341–1349, 2012.
- [142] Y. Takagi and S. Okada. Theoretical calculation for the ultraviolet optical properties of single-walled carbon nanotubes. *Phys. Rev. B*, 79:233406, 2009.
- [143] J. M. Kinder, G. Chan, and J. Park. Uniform peak optical conductivity in single-walled carbon nanotubes. *Phys. Rev. B*, 84(12):125428, 2011.
- [144] S. Piscanec, M. Lazzeri, J. Robertson, A. C. Ferrari, and F. Mauri. Optical phonons in carbon nanotubes: Kohn anomalies, peierls distortions, and dynamic effects. *Phys. Rev. B*, 75:035427, 2007.
- [145] V. N. Popov and P. Lambin. Non-adiabatic phonon dispersion of metallic single-walled carbon nanotubes. *Nano Res.*, 3(11):822–829, 2010.
- [146] H. Telg, J. G. Duque, M. Staiger, X. Tu, F. Hennrich, M. M. Kappes, M. Zheng, J. Maultzsch, C. Thomsen, and S. K. Doorn. Chiral index dependence of the g+ and g- raman modes in semiconducting carbon nanotubes. *ACS Nano*, 6(1):904–911, 2012.
- [147] J. G. Duque, H. Chen, A. K. Swan, A. P. Shreve, S. Kilina, S. Tretiak, X. Tu, M. Zheng, and S. K. Doorn. Violation of the condon approximation in semiconducting carbon nanotubes. *ACS Nano*, 5(6):5233–5241, 2011.
- [148] J. G. Duque, H. Telg, H. Chen, A. K. Swan, A. P. Shreve, X. Tu, M. Zheng, and S. K. Doorn. Quantum interference between the third and fourth exciton states in semiconducting carbon nanotubes using resonance raman spectroscopy. *Phys. Rev. Lett.*, 108:117404, 2012.

- 
- [149] J. S. Park, Y. Oyama, R. Saito, W. Izumida, J. Jiang, K. Sato, C. Fantini, A. Jorio, G. Dresselhaus, and M. S. Dresselhaus. Raman resonance window of single-wall carbon nanotubes. *Phys. Rev. B*, 74(16):165414, 2006.
- [150] T. Inoue, K. Matsuda, Y. Murakami, S. Maruyama, and Y. Kanemitsu. Diameter dependence of exciton-phonon interaction in individual single-walled carbon nanotubes studied by microphotoluminescence spectroscopy. *Phys. Rev. B*, 73(23):233401, 2006.
- [151] Y. Ohno, S. Kishimoto, T. Mizutani, T. Okazaki, and H. Shinohara. Chirality assignment of individual single-walled carbon nanotubes in carbon nanotube field-effect transistors by micro-photocurrent spectroscopy. *Appl. Phys. Lett.*, 84(8):1368–1370, 2004.
- [152] V. Perebeinos and P. Avouris. Phonon and electronic nonradiative decay mechanisms of excitons in carbon nanotubes. *Phys. Rev. Lett.*, 101(5):057401, 2008.
- [153] C. M. Aguirre, P. L. Levesque, M. Paillet, F. Lapointe, B. C. St-Antoine, P. Desjardins, and R. Martel. The role of the oxygen/water redox couple in suppressing electron conduction in field-effect transistors. *Adv. Mater.*, 21(30):3087–3091, 2009.
- [154] J. S. Soares, A. P. M. Barboza, P. T. Araujo, N. M. Barbosa Neto, D. Nakabayashi, N. Shadmi, T. S. Yarden, A. Ismach, N. Geblinger, E. Joselevich, C. Vilani, L. G. Cançado, L. Novotny, G. Dresselhaus, M. S. Dresselhaus, B. R. A. Neves, M. S. C. Mazzoni, and A. Jorio. Modulating the electronic properties along carbon nanotubes via tube-substrate interaction. *Nano Lett.*, 10(12):5043–5048, 2010.
- [155] M. Shim, T. Ozel, A. Gaur, and C. Wang. Insights on charge transfer doping and intrinsic phonon line shape of carbon nanotubes by simple polymer adsorption. *J. Am. Chem. Soc.*, 128(23):7522–7530, 2006.
- [156] Y. Homma, S. Chiashi, T. Yamamoto, K. Kono, D. Matsumoto, J. Shitaba, and S. Sato. Photoluminescence measurements and molecular dynamics simulations of water adsorption on the hydrophobic surface of a carbon nanotube in water vapor. *Phys. Rev. Lett.*, 110:157402, 2013.
- [157] S. Ghosh, S. M. Bachilo, R. A. Simonette, K. M. Beckingham, and R. B. Weisman. Oxygen doping modifies near-infrared band gaps in fluorescent single-walled carbon nanotubes. *Science*, 330(6011):1656–1659, 2010.
- [158] Y. Ohno, S. Iwasaki, Y. Murakami, S. Kishimoto, S. Maruyama, and T. Mizutani. Excitonic transition energies in single-walled carbon nanotubes: Dependence on environmental dielectric constant. *phys. stat. sol. (b)*, 244(11):4002–4005, 2007.
- [159] T. Ando. Effects of environmental dielectric screening on optical absorption in carbon nanotubes. *Physica E*, 43(3):798–803, 2011.

- [160] Y. Miyauchi, R. Saito, K. Sato, Y. Ohno, S. Iwasaki, T. Mizutani, J. Jiang, and S. Maruyama. Dependence of exciton transition energy of single-walled carbon nanotubes on surrounding dielectric materials. *Chem. Phys. Lett.*, 442(4-6):394–399, 2007.
- [161] A. G. Walsh, A. N. Vamivakas, Y. Yin, S. B. Cronin, M. S. Ünlü, B. B. Goldberg, and A. K. Swan. Scaling of exciton binding energy with external dielectric function in carbon nanotubes. *Physica E*, 40(7):2375–2379, 2008.
- [162] K. Arnold, S. Lebedkin, O. Kiowski, F. Hennrich, and M. M. Kappest. Matrix-imposed stress-induced shifts in the photoluminescence of single-walled carbon nanotubes at low temperatures. *Nano Lett.*, 4(12):2349–2354, 2004.
- [163] R. B. Capaz, C. D. Spataru, P. Tangney, M. L. Cohen, and S. G. Louie. Hydrostatic pressure effects on the structural and electronic properties of carbon nanotubes. *phys. stat. sol. (b)*, 241(14):3085, 2004.
- [164] M. Huang, Y. Wu, B. Chandra, H. Yan, Y. Shan, T. F. Heinz, and J. Hone. Direct measurement of strain-induced changes in the band structure of carbon nanotubes. *Phys. Rev. Lett.*, 100(13):136803, 2008.
- [165] P. Finnie, Y. Homma, and J. Lefebvre. Band-gap shift transition in the photoluminescence of single-walled carbon nanotubes. *Phys. Rev. Lett.*, 94(24):247401, 2005.
- [166] J. J. Crochet, J. D. Sau, J. G. Duque, S. K. Doorn, and M. L. Cohen. Electrodynamic and excitonic intertube interactions in semiconducting carbon nanotube aggregates. *ACS Nano*, 5(4):2611–2618, 2011.
- [167] K. Liu, X. Hong, M. Wu, F. Xiao, W. Wang, X. Bai, J. W. Ager, S. Aloni, A. Zettl, E. Wang, and F. Wang. Quantum-coupled radial-breathing oscillations in double-walled carbon nanotubes. *Nat. Commun.*, 4:1375, 2013.
- [168] V. N. Popov and L. Henrard. Breathinglike phonon modes of multiwalled carbon nanotubes. *Phys. Rev. B*, 65:235415, 2002.
- [169] T. Hertel, Axel H., V. Talalaev, K. Arnold, F. Hennrich, M. Kappes, S. Rosenthal, J. McBride, H. Ulbricht, and E. Flahaut. Spectroscopy of single- and double-wall carbon nanotubes in different environments. *Nano Lett.*, 5(3):511–514, 2005.
- [170] H. Hirori, K. Matsuda, and Y. Kanemitsu. Exciton energy transfer between the inner and outer tubes in double-walled carbon nanotubes. *Phys. Rev. B*, 78:113409, 2008.
- [171] D. Shimamoto, H. Muramatsu, T. Hayashi, Y. A. Kim, M. Endo, J. S. Park, R. Saito, M. Terrones, and M. S. Dresselhaus. Strong and stable photoluminescence from the semiconducting inner tubes within double walled carbon nanotubes. *Appl. Phys. Lett.*, 94(8):083106, 2009.



- 
- [172] S. Yang, A. N. Parks, S. A. Saba, P. L. Ferguson, and J. Liu. Photoluminescence from inner walls in double-walled carbon nanotubes: Some do, some do not. *Nano Lett.*, 11(10):4405–4410, 2011.
- [173] T. Koyama, Y. Miyata, K. Asaka, H. Shinohara, Y. Saito, and A. Nakamura. Ultrafast energy transfer of one-dimensional excitons between carbon nanotubes: a femtosecond time-resolved luminescence study. *Phys. Chem. Chem. Phys.*, 14:1070–1084, 2012.
- [174] Y. Tomio, H. Suzuura, and T. Ando. Interwall screening and excitons in double-wall carbon nanotubes. *Phys. Rev. B*, 85:085411, 2012.
- [175] D. Bouilly, J. Cabana, F. Meunier, M. Desjardins-Carrière, F. Lapointe, P. Gagnon, F. L. Larouche, E. A., M. Paillet, and R. Martel. Wall-selective probing of double-walled carbon nanotubes using covalent functionalization. *ACS Nano*, 5(6):4927–4934, 2011.
- [176] Y. Tomio, H. Suzuura, and T. Ando. Cross-polarized excitons in double-wall carbon nanotubes. *Phys. Rev. B*, 86:245428, 2012.
- [177] A. L. Aguiar, E. B. Barros, R. B. Capaz, A. G. Souza Filho, P. T. C. Freire, J. M. Filho, D. Machon, C. Caillier, Y. A. Kim, H. Muramatsu, M. Endo, and A. San-Miguel. Pressure-induced collapse in double-walled carbon nanotubes: Chemical and mechanical screening effects. *J. Phys. Chem. C*, 115(13):5378–5384, 2011.
- [178] C. Caillier, D. Machon, A. San-Miguel, R. Arenal, G. Montagnac, H. Cardon, M. Kalbac, M. Zukalova, and L. Kavan. Probing high-pressure properties of single-wall carbon nanotubes through fullerene encapsulation. *Phys. Rev. B*, 77(12):125418, 2008.
- [179] J. Elliott, J. Sandler, A. Windle, R. Young, and M. Shaffer. Collapse of single-wall carbon nanotubes is diameter dependent. *Phys. Rev. Lett.*, 92(9):095501, 2004.
- [180] M. Hasegawa and K. Nishidate. Radial deformation and stability of single-wall carbon nanotubes under hydrostatic pressure. *Phys. Rev. B*, 74(11):115401, 2006.
- [181] W. Yang, R. Z. Wang, X. M. Song, B. Wang, and H. Yan. Pressure-induced raman-active radial breathing mode transition in single-wall carbon nanotubes. *Phys. Rev. B*, 75:045425, 2007.
- [182] A. N. Imtani and V. K. Jindal. Characterizing single-walled carbon nanotubes by pressure probe. *Carbon*, 47(14):3247–3251, 2009.
- [183] A. Javey, J. Guo, Q. Wang, M. Lundstrom, and H. Dai. Ballistic carbon nanotube field-effect transistors. *Nature*, 424(6949):654–657, 2003.
- [184] M. S. Fuhrer, B. M. Kim, T. Dürkop, and T. Brintlinger. High-mobility nanotube transistor memory. *Nano Lett.*, 2(7):755–759, 2002.



- [185] J. B. Cui, R. Sordan, M. Burghard, and K. Kern. Carbon nanotube memory devices of high charge storage stability. *Appl. Phys. Lett.*, 81(17):3260–3262, 2002.
- [186] M. Radosavljević, M. Freitag, K. V. Thadani, and A. T. Johnson. Nonvolatile molecular memory elements based on ambipolar nanotube field effect transistors. *Nano Lett.*, 2(7):761–764, 2002.
- [187] W. Kim, A. Javey, O. Vermesh, Q. Wang, Y. Li, and H. Dai. Hysteresis caused by water molecules in carbon nanotube field-effect transistors. *Nano Lett.*, 3(2):193–198, 2003.
- [188] C. Caillier, A. Ayari, S. Le Floch, H. Féret, G. Guiraud, and A. San-Miguel. Measuring the electronic transport properties of individual nano-objects under high pressures. *High Pres. Res.*, 31(3):367–374, 2011.
- [189] S. M. Sze and K. K. Ng. *Physics of Semiconductor Devices*. John Wiley & Sons, Inc., 3 edition, 2006.
- [190] I. Heller, A. M Janssens, J. Männik, E. D Minot, S. G Lemay, and C. Dekker. Identifying the mechanism of biosensing with carbon nanotube transistors. *Nano Lett.*, 8(2):591–595, 2008.
- [191] A. L. Aguiar, A. San-Miguel, E. B. Barros, M. Kalbáč, D. Machon, Y. A. Kim, H. Muramatsu, M. Endo, and A. G. Souza Filho. Effects of intercalation and inhomogeneous filling on the collapse pressure of double-wall carbon nanotubes. *Phys. Rev. B*, 86:195410, 2012.
- [192] E. D. Minot, Y. Yaish, V. Sazonova, J.-Y. Park, M. Brink, and P. L. McEuen. Tuning carbon nanotube band gaps with strain. *Phys. Rev. Lett.*, 90:156401, 2003.
- [193] H. Grabert and M. H. Devoret. *Single Charge Tunneling: Coulomb Blockade Phenomena in Nanostructures*. Springer, 1 edition, 1992.
- [194] F. Vietmeyer, M. P. McDonald, and M. Kuno. Single nanowire microscopy and spectroscopy. *J. Phys. Chem. C*, 116(23):12379–12396, 2012.
- [195] V. G. Kravets, A. N. Grigorenko, R. R. Nair, P. Blake, S. Anissimova, K. S. Novoselov, and A. K. Geim. Spectroscopic ellipsometry of graphene and an exciton-shifted van hove peak in absorption. *Phys. Rev. B*, 81:155413, 2010.
- [196] C. Soldano, A. Mahmood, and E. Dujardin. Production, properties and potential of graphene. *Carbon*, 48(8):2127–2150, 2010.

# List of Figures

---

I.1	First observation of carbon nanotubes by Sumino Ijima . . . . .	7
I.2	Graphene honeycomb lattice . . . . .	9
I.3	Carbon nanotube classification . . . . .	10
I.4	Graphene band structure . . . . .	13
I.5	Construction of the nanotubes band structure: zone-folding approximation	15
I.6	Density of states of carbon nanotubes in the approximation of linear dispersion of graphene. . . . .	18
II.1	Sketch of the absorption energy transitions . . . . .	23
II.2	Calculated absorption for parallel and perpendicular polarization. . . . .	25
II.3	Absorption energy transitions vs. diameter: simplified Kataura plot . . .	26
II.4	Trigonal warping effect. . . . .	28
II.5	Kataura plot in the single-particle model . . . . .	30
II.6	Structure-assigned optical spectra of SWNTs and ratio problem . . . . .	32
II.7	Exciton states in single-wall carbon nanotubes. . . . .	34
II.8	Exciton dispersion in chrial single-wall carbon nanotubes. . . . .	35
II.9	Diameter dependency of exciton binding energy in semiconducting single-wall carbon nanotubes. . . . .	39
II.10	Sketch of the exciton size evolution with diameter and energy transition.	40
II.11	Presentation of different experimental and theoretical Kataura plots . . .	46
III.1	Sketch of the carbon nanotube vapor deposition synthesis technique . . .	54
III.2	Imaging of a single-wall carbon nanotube on Si/SiO <sub>2</sub> substrate (sample Si-4). . . . .	55
III.3	Carbon nanotubes grown on quartz ST-cut substrate (sample Q-3). . . . .	55
III.4	Freely suspended and supported CNTs on the sample FS-1. . . . .	57
III.5	SMS images of selected free-standing nanotubes on sample FS-2. . . . .	58
III.6	TEM and SEM imaging of home-made free-standing carbon nanotubes. .	59
III.7	Principle of spatial modulation spectroscopy . . . . .	62
III.8	Computed relative transmission signal for two excitation wavelengths and two modulation amplitudes . . . . .	64
III.9	Computed SMS response for different CNT orientation . . . . .	67
III.10	Spatial modulation spectroscopy experimental setup . . . . .	68

III.11	Calibration: laser beam size and spatial modulation amplitude . . . . .	70
III.12	Absorption-based imaging of an individual freely suspended SWNT . . .	72
III.13	Experimental relation between relative transmission and absorption cross-section in CNTs. . . . .	73
III.14	Experimental determination of the energy dependent sensitivity limit for free-standing CNTs. . . . .	74
III.15	Slab correction to the absorption cross-section for Si/SiO <sub>2</sub> substrates. . .	77
III.16	Model Mie theory: absorption and scattering by a small arbitrary object lying on a substrate . . . . .	77
III.17	Scattering behaviour for nanotubes. . . . .	79
III.18	Approximation slab correction to the absorption cross-section for Si/SiO <sub>2</sub> substrates. . . . .	80
III.19	Absorption imaging of individual CNTs on opaque substrate. . . . .	81
III.20	Comparison of RSMS imaging with other visualization techniques on opaque substrate. . . . .	82
IV.1	Absorption and Raman spectroscopy of individual free-standing type I semiconducting SWNTs. . . . .	87
IV.2	Principle of phonon-assisted absorption and fitting procedure of absorption spectra. . . . .	89
IV.3	Absorption and Raman spectroscopy of individual free-standing type II semiconducting SWNTs. . . . .	93
IV.4	Absorption properties of individual free-standing single-wall carbon nanotubes . . . . .	94
IV.5	Non-resonant absorption and conductivity in individual free-standing SC-SWNTs . . . . .	98
IV.6	Absorption and Raman spectroscopy of two free-standing bundles of SWNTs	100
IV.7	Absorption properties of semiconducting SWNTs included in free-standing bundles . . . . .	104
IV.8	Absorption and Raman scattering of the (18,5) SWNT supported on Si/SiO <sub>2</sub> substrate (Si-4 sample) . . . . .	107
IV.9	Polarization-dependent absorption of the (18,5) SWNT on Si/SiO <sub>2</sub> substrate (Si-4 sample). . . . .	107
IV.10	Absorption of (14,13) SWNT supported on Si/SiO <sub>2</sub> substrate and comparison with the freely suspended optical properties of the same nanotube.	109
IV.11	Sketch of exciton non-radiative decay mechanisms/pathways . . . . .	112
IV.12	Scaling of exciton energy with the dielectric environment. . . . .	114
IV.13	Absorption and Raman scattering of the quartz-supported carbon nanotubes. . . . .	115
V.1	Diameter identification of double-wall carbon nanotubes from resonant Raman spectroscopy . . . . .	121
V.2	Absorption and Raman spectroscopy of the free-standing double-wall nanotube DCNT 1 identified as (type-I SC)@(type-I SC) . . . . .	128

V.3	Absorption and Raman spectroscopy of the individual free-standing double-wall nanotube DCNT 2 identified as (type-I SC)@(type-II SC) . . . . .	131
V.4	Absorption and Raman spectroscopy of the individual free-standing double-wall nanotube DCNT 3 identified as SC@M . . . . .	134
V.4	Absorption and Raman spectroscopy of an individual free-standing DWNT of type SC@M (continuation) . . . . .	135
V.5	Substrate effects on the absorption properties of an individual DWNT . .	138
V.5	Substrate effects on the absorption properties of an individual DWNT (continuation) . . . . .	139
V.6	Bundling effects on the absorption properties of an individual DWNT . .	142
V.6	Environment-dependent absorption of an individual DWNT (continuation)	143
V.7	Absorption fitting of overlapping excitonic transitions in different environments . . . . .	144
V.8	Absorption properties of individual free-standing double-wall carbon nanotubes . . . . .	146
V.9	Non-resonant absorption and conductivity in individual free-standing DWNTs	147
VI.1	Carbon nanotube-based field effect transistor (CNT-FET) . . . . .	153
VI.2	Electrical transport measurements at high pressure: experimental setup .	154
VI.3	Pressure evolution of the CNT transistor characteristics . . . . .	156
VI.4	Analysis of the metallic CNT resistance behavior under pressure . . . . .	157
VI.5	Evolution of the gate voltage hysteresis under pressure . . . . .	157
VI.6	Pressure dependence of the the electron and hole mobilities in the FET device . . . . .	158
VI.7	Analysis of the p and n branches of the transistor characteristics under pressure . . . . .	159
VI.8	Observation of Coulomb blockade in individual carbon nanotubes bundles at low and high pressure . . . . .	161
A.1	Structure assignment CNT 1 . . . . .	171
A.2	Structure assignment CNT 2 . . . . .	172
A.3	Structure assignment CNT 3 . . . . .	173
A.4	Structure assignment CNT 4 . . . . .	174
B.1	Mie theory model for the absorption cross-section of SWNTs. . . . .	179
B.2	Mie theory of hollow dielectric cylinder: computed absorption and scattering cross-sections <i>vs.</i> hollow cylinder number of walls. . . . .	179
C.1	Absorption spectroscopy and imaging of mono- and bi-layer graphene on Si/SiO <sub>2</sub> substrate. . . . .	183



# Acronyms

---

## Materials

CNT	Carbon nanotube
SWNT	Single-wall carbon nanotube
DWNT	Double-wall carbon nanotube
MWNT	Multi-wall carbon nanotube
SC	Semiconducting
M	Metallic

## Electronic and optical properties

DOS	Density of states
JDOS	Joint density of states
VB	Valence band – index (–)
CB	Conduction band – index (+)
SP	Single particle model
FWHM	Full width at half maximum

## Experimental methods

SMS	Spatial modulation spectroscopy
RSMS	Reflective spatial modulation spectroscopy
PD	Photodiode
LIA	Lock-in amplifier
NA	Numerical aperture
RRS	Resonant Raman spectroscopy
RBM	Radial breathing mode
BLM	Breathing-like mode
PL	Photoluminescence
PLE	Photoluminescence excitation
AFM	Atomic force microscopy
TEM	Transmission electron microscopy

SEM      Scanning electron microscopy

FET      Field-effect transistor

**Synthesis of carbon nanotubes**

CVD      Chemical vapor deposition

HiPCO    High-pressure decomposition of iron pentacarbonyl (also CoMoCAT)



# List of notations

---

## Structure and properties of carbon nanotube

$d$	diameter	11
$L$	length	25
$(n,m)$	chiral index	9
$\theta_c$	chiral angle	9
$\Delta d$	interwall distance in a double-wall nanotube	120
$d_{\text{in}}$	inner tube diameter in a DWNT	119
$d_{\text{out}}$	outer tube diameter in a DWNT	119
$\mathbf{C}$	chiral or circumferential vector	8
$\mathbf{T}$	translational vector	11
$N_R$	greatest common divisor of $(2n + m)$ and $(2m + n)$	11
$N_L$	number of carbon atoms per unit length	11
$N_C$	number of carbon atoms in the nanotube unit cell	11
$u_{\text{cell}}$	number of graphene hexagons in the nanotube unit cell	15
$\varepsilon(\omega)$	nanotube dielectric constant	175
$\varepsilon_m$	dielectric constant of the nanotube environment	39
$\sigma_S$	nanotube optical sheet conductivity	97
$\nu$	nanotube family defined from $\text{mod}(n - m, 3)$	16

## Electronic structure

$(\mathbf{a}_1, \mathbf{a}_2)$	primitive basis vectors	8
$(\mathbf{b}_1, \mathbf{b}_2)$	primitive vectors of the reciprocal space	12
$a_0$	lattice constant of graphene	8
$a_{CC}$	carbon-carbon bond length	8
$E_g^\pm$	graphene conduction (+) and valence (-) bands dispersion	14
$\mathbf{r}, \mathbf{k}$	real space position and reciprocal space wave vector	
$\mathbf{k}_\parallel$	nanotube reciprocal lattice wave vector along its axis	15
$\mathbf{k}_\perp$	nanotube reciprocal lattice wave vector along its circumference	15
$k_{\perp,q}$	magnitude of $\mathbf{k}_\perp$	15
$(q, k)$	quantum numbers associated with $(\mathbf{k}_\parallel, \mathbf{k}_\perp)$	16
$(E_q^\pm(k), \mathbf{k}_q)$	energy dispersion and wave vector of subband $q$	16

**Spatial modulation spectroscopy technique**

$\delta y$	amplitude of the spatial modulation	62
$f$	frequency of the spatial modulation	62
$D_S$	size of the laser spot	68
$V_{LIA}$	lock-in amplifier effective voltage	69
$\Delta T/T$	relative change in the transmission signal	61
$\Delta R/R$	relative change in the reflection signal	76
$\theta_{CNT}$	angle between the nanotube and direction of spatial modulation	65
$\theta_{pol}$	angle between the nanotube and direction of linear polarization	86
$L_{ill}$	length of the nanotube segment illuminated by the incident light	65
$K_{2f}$	coefficients which relates $C_{abs}$ and $\Delta T/T$	65
$A_{slab}$	correction to $K_{2f}$ for substrate-supported nanotubes	76

**Absorption cross-section**

$C_{abs}$	absorption cross-section	45
$C_{abs}^{\parallel} C_{abs}^{\perp}$	$C_{abs}$ for parallel ( $\parallel$ ) or perpendicular ( $\perp$ ) polarization	86
$C_{sca}$	scattering cross-section	62
$C_{sca}^{\parallel} C_{sca}^{\perp}$	$C_{sca}$ for parallel ( $\parallel$ ) or perpendicular ( $\perp$ ) polarization	176
$C_{ext}$	extinction cross-section	62
$C_{ext}^{\parallel} C_{ext}^{\perp}$	$C_{ext}$ for parallel ( $\parallel$ ) or perpendicular ( $\perp$ ) polarization	177
$W_{abs}$	absorption rate	22
$C_{abs}^{exc}$	absorption cross section of an excitonic resonance	86
$C_{abs}^{peak}$	peak absorption cross-section	86
$C_{abs}^{nr}$	non resonant absorption cross-section	86
$\sigma_S^{nr}$	non resonant sheet conductivity	97
$C_{abs,NT}^{exc}$	$C_{abs}^{exc}$ in double-wall carbon nanotubes	129
$C_{abs,NT}^{peak}$	$C_{abs}^{peak}$ in double-wall carbon nanotubes	129
$C_{abs,SW}^{exc}$	$C_{abs}^{exc}$ associated with one nanotube in a DWNT	129

**Absorption resonances**

$E_{ij} S_{ij} M_{ij}$	absorption energy transition from subband $i$ to $j$	
$E_{ii}^{in} S_{ii}^{in} M_{ii}^{in}$	parallel absorption energy transition of the inner tube in a DWNT	
$E_{ii}^{out} S_{ii}^{out} M_{ii}^{out}$	parallel absorption energy transition of the inner tube in a DWNT	
$E_{SP}$	optical energy transitions in the single particle model	35
$E_{e-e}$	self-energy in the many-body model	32
$E_{e-h}$	electron-hole repulsion energy in the many-body model	32
$E_b$	binding energy of the ground state exciton ( $ 1u\rangle$ )	35
$\gamma$	exciton full width at half maximum	86
$l_\chi$	exciton size	32
$\mathbf{K}_{exc}$	exciton center of mass momentum	34
$f_C$	oscillator strength per C-atom of a nanotube	43
$f_{C,NT}$	oscillator strength per C-atom of a DWNT	129
$f_{C,SW}$	$f_C$ of one nanotube in a DWNT	129

**Phonon-assisted absorption**

$k'$	phonon momentum	90
$\omega_{iTO}$	frequency of the in-plane transverse optical phonon	90

**Raman spectroscopy**

$\omega_{\text{RBM}}$	radial breathing mode frequency in a SWNT	86
$\omega_{\text{LF}}$	low frequency BLM (in-phase) in a DWNT	123
$\omega_{\text{HF}}$	high frequency BLM (counterphase)	123
$\omega_{\text{out}}$	calculated counterphase BLM	119
$\omega_{\text{in}}$	calculated in-phase BLM	119
$I_{\text{out}} I_{\text{in}}$	Raman intensity of the breathing-like phonon modes	119

**Electrical transport**

$I_{\text{SD}}$	source-drain current	152
$V_{\text{SD}}$	source-drain bias voltage	152
$V_{\text{G}}$	gate voltage	152
$R_{\text{min}}$	resistance associated with the metallic response of the CNT-FET	155
$V_{\text{G,min}}^i V_{\text{G,min}}^d$	position of the current minimum while sweeping $V_{\text{G}}$	156
$\Delta V_{\text{G,min}}$	gate voltage hysteresis	156
$\mu_{\text{e}} \mu_{\text{h}}$	electron and hole effective mobility	158
$l_{\text{eff}}$	effective length measured in the Coulomb blockade regime	162

